DEVELOPMENT OF MULTIFUNCTIONAL NANOFIBROUS MATERIALS VIA ELECTROSPINNING

A DISSERTATION SUBMITTED TO

MATERIALS SCIENCE AND NANOTECHNOLOGY PROGRAM

OF THE GRADUATE SCHOOL OF ENGINEERING AND SCIENCE

OF BILKENT UNIVERSITY

IN PARTIAL FULFILLMENT OF THE REQUIREMENTS

FOR THE DEGREE OF

DOCTOR OF PHILOSOPHY

By

FATMA KAYACI

September, 2014

I certify that I have read this thesis and that in my opinion it is fully adequate, in scope and in quality, as a thesis of the degree of Doctor of Philosophy.

…….

Assoc. Prof. Dr. Tamer Uyar (Advisor)

I certify that I have read this thesis and that in my opinion it is fully adequate, in scope and in quality, as a thesis of the degree of Doctor of Philosophy.

…….

Assist. Prof. Dr. Necmi Bıyıklı

I certify that I have read this thesis and that in my opinion it is fully adequate, in scope and in quality, as a thesis of the degree of Doctor of Philosophy.

…….

Assoc. Prof. Dr. Ali Çırpan

I certify that I have read this thesis and that in my opinion it is fully adequate, in scope and in quality, as a thesis of the degree of Doctor of Philosophy.

…….

Assoc. Prof. Dr. Fatih Büyükserin

I certify that I have read this thesis and that in my opinion it is fully adequate, in scope and in quality, as a thesis of the degree of Doctor of Philosophy.

…….

Assist. Prof. Dr. Hasan Tarık Baytekin

Approved for the Graduate School of Engineering and Science:

…….

Prof. Dr. Levent Onural

Director of the Graduate School

ABSTRACT

DEVELOPMENT OF MULTIFUNCTIONAL NANOFIBROUS MATERIALS VIA ELECTROSPINNING

Fatma Kayacı
PhD in Materials Science and Nanotechnology
Supervisor: Assoc. Prof. Dr. Tamer Uyar
September, 2014

Electrospun nanofibers are very attractive for many applications including functional textile, biomedical, energy, sensor, biotechnology, food packaging and filtration due to their large surface area to volume ratio, pores in nano range, high encapsulation efficiency, low basis weight and design flexibility for physical/chemical modification. Cyclodextrins (CD) are applicable in several industries such as pharmaceutical, cosmetic, textile, functional food and filtration owing to their intriguing ability to form non-covalent host-guest inclusion complexes (IC) with a variety of molecules. Furhermore, atomic layer deposition (ALD) technique can be effectively used to deposit metal oxides onto temperature-sensitive polymeric substrates.

In this dissertation, initially, CD-IC of bioactive compounds (vanillin, eugenol, geraniol, triclosan) having antibacterial and/or antioxidant properties were incorporated into electrospun nanofibers via electrospinning. Higher thermal stability, controlled/sustained release, enhanced solubility and functionality of these compounds have been provided by CD-IC. These specific properties of CD-IC have been combined with high surface area and nanoporous structure of electrospun nanofibers. Thereby, the resulting functional nanofibrous materials can be quite applicable in active food packaging in order to prevent foodborne diseases by providing safety/quality of nutrition and extending shelf life of food. On the other hand, CD incorporated electrospun nanofibers have also been developed for efficient removal of unpleasant odors, hazardous organic waste molecules from air by taking advantages of not only high surface area and nanoporous structure of nanofibers but also IC capability of CD. Since CD are water soluble, CD polymer (CDP) coated onto nanofibers have been also obtained for molecular filtration of polyaromatic hydrocarbons from aqueous environment. Moreover, metal oxides (ZnO, TiO_2) have been deposited onto electrospun nanofibers via ALD in order to develop efficient and energy saving innovative nanofibrous membrane materials for water purification and waste treatment. Thus, organic pollutants in water have been effectively disintegrated by photocatalytic activity of these nanofibrous filtering materials having high surface area.

Overall, the multifunctional electrospun nanofibrous materials have been improved by incorporating CD-IC or CD into the fiber matrix; by coating either CDP or metal oxides (ZnO, TiO_2) onto fiber surface to enhance possible applications of nanofibers for filtration, food packaging, functional textiles, etc.

Keywords: electrospinning, nanofibers, cyclodextrin, inclusion complex, atomic layer deposition, photocatalytic activity

ÖZET
ELEKTROEĞİRME YÖNTEMİ İLE ÇOK FONKSİYONLU NANOLİFLERDEN OLUŞAN MALZEMELERİN GELİŞTİRİLMESİ

Fatma Kayacı
Malzeme Bilimi ve Nanoteknoloji, Doktora
Tez Danışmanı: Doç. Dr. Tamer Uyar
Eylül, 2014

Elektroeğirme yöntemi ile elde edilen nanolifler yüksek yüzey alanı, nano boyutta gözenekleri, yüksek kapsülleme verimi, düşük ağırlığı ve fiziksel/kimyasal modifikasyon çeşitliliği sebebiyle fonksiyonel tekstil, biyomedikal, enerji, sensör, biyoteknoloji ve gıda paketlemesi alanlarında ilgi çekmektedir. Siklodekstrinler (CD) değişik moleküller ile kovalent olmayan misafir-ev sahibi inküzyon kompleks (IC) oluşturabilme yetenekleri sayesinde ilaç, kozmetik, tekstil, fonksiyonel gıda ve filtrasyon endüstrilerinde kullanılabilirler. Bunların yanı sıra, atomik katman kaplama (ALD) tekniği sıcaklık hassasiyesti olan organik maddelere metal oksit kaplanması için etkin bir biçimde kullanılabilir.

Bu tezde, ilk olarak, antibakteriyel ve/veya antioksidan özellikleri olan biyoaktif bileşimlerin (vanilya, öjenol, geraniol, triklosan) CD-IC'leri elektrospin yöntemi sırasında nanoliflerin içerisine katılmıştır. CD-IC'ler sayesinde bu bileşimlerin ısıl dayanımı, kontrollü/devamlı salımı, çözünürlükleri ve etkinlikleri geliştirilmiştir. CD-IC'lerin bu özellikleri ile nanoliflerin yüksek yüzey alanı ve nanoboyutta gözenekli yapısı birleştirilmiştir. Bu nedenle elde edilen fonksiyonel nanolifler gıdalarda güven/kalite sağlayıp gıdaların raf ömürlerini uzatarak, gıda kaynaklı hastalıkları engellemek amacıyla paketleme malzemesi olarak oldukça kullanışlı olabilirler. Diğer taraftan, hem nanoliflerin yüksek yüzey alanı ve nanoboyutta gözenekli yapılarının hem de CD'lerin IC oluşturma kabiliyetlerinin avantajları kullanılarak havadan istenmeyen kokuların ve zararlı atık moleküllerin etkin bir şekilde uzaklaştırılması için CD içeren nanolifler geliştirilmiştir. CD'ler suda çözündüğü için, sulu ortamda poliaromatik hidrokarbonların moleküler filtrasyonunu sağlamak amacıyla CD polimeri (CDP) kaplanmış nanolifler de elde edilmiştir. Ayrıca, su saflaştrılması ve atık arıtımında etkili ve enerji tasarrufu sağlayan yenilikçi membran malzemeleri geliştirmek için elektrospin ile elde edilen nanoliflerin üzerine ALD tekniği ile metal oksitler (ZnO, TiO_2) kaplanmıştır. Böylece, yüksek yüzey alanına sahip bu nanoliflerin fotokatalitik özellikleri sayesinde su içerisindeki organik kirliliklerin bozunması sağlanmıştır.

Sonuç olarak, filtrasyon, gıda paketlemesi ve fonksiyonel tekstil alanlarında nanoliflerin kullanım potansiyellerini arttırmak amacıyla nanoliflerin içerisine CD-IC veya CD katarak, ya da yüzeylerine CDP veya metal oksit (ZnO, TiO_2) kaplayarak çok fonsiyonlu nanolif tabanlı malzemeler geliştirilmiştir.

Anahtar kelimeler: elektroeğirme, nanolifler, siklodekstrin, inklüzyon kompleks, atomik katman kaplama, fotokatalitik aktivite

ACKNOWLEDGEMENTS

Initially, I would like to thanks and gratitude to my supervisor Assoc. Prof. Dr. Tamer Uyar for his invaluable guidance, continuos support, encouragement, confidence and patience during my graduate studies. I extended my knowledge and vision due to his motivation to me in diverse research projects. I am also indebted to Dr. Sesha Vempati for his valuable mentor on my research studies regarding photocatalytic activity about which I have learned many things from him. I feel extremely grateful especially for the mankind and friendship he provided me. The members of my thesis committee, Assist. Prof. Dr. Necmi Bıyıklı, Assoc. Prof. Dr. Ali Çırpan, Assoc. Prof. Dr. Fatih Büyükserin and Assist. Prof. Dr. Hasan Tarık Baytekin, are gratefully acknowledged for their insightful comments.

I would also like to express my deep appreciation to Aslı Çelebioğlu for her generous help and contributions in all time during these five years. I could not have imagined this period without her kind friendship. Gratitude extends to Yelda Ertaş and Zeynep Aytaç not only for their collaboration, but also their valuable friendship. I am pleased to have very kind lab-mates: Şefika Eroğlu Özcan, A. Ekrem Deniz, Dr. N. Oya San, Dr. Anitha Senthamizan, Dr. V. Jagadeesh Babu and Ö. Faruk Sarıoğlu. Ruslan Garifullin has also deserved many thanks for various assistance.

I am sincerely thankful to Assist. Prof. Dr. Necmi Bıyıklı, Dr. Çağla Özgit-Akgün and İnci Dönmez for their efforts in research projects where we combined electrospinning and ALD processes. I also thank Assist. Prof. Engin Durgun and Dr. H. Sener Sen who have performed the CD and CD-IC modeling studies. Many thanks to Assoc. Prof. Turgay Tekinay and Özgün C.O. Umu for antibacterial study.

I am very grateful for having the opportunity to work with UNAM facilities, thereby I would like to thank to everyone contributed to the founding and working of UNAM.

Foremost, I want to express my gratitude to my parents: Zehra Kayacı and Ali Kayacı for their love, endless support, understanding, patience and prayers. I owe them a lot which cannot be paid. Very special thanks to Kürşad Kayacı and Osman Kayacı for their lovely brotherhood. I'm especially grateful to my dearest friend İlkay Keneş Yılmaz who is like a sister for me.

Finally, TÜBİTAK-BİDEB 2211 Ph.D. fellowship programme and TÜBİTAK project # 110M612 and 111M459 deserve great portion of acknowledgements due to their financial support.

Anneme ve Babama…

(Zehra & Ali Kayacı)

CONTENTS

LIST OF ABBREVIATIONS

CD	:	Cyclodextrins
IC	:	Inclusion complexes
CDP	:	Cyclodextrin polymer
ALD	:	Atomic layer deposition
PCA	:	Photocatalytic activity
AFD	:	Average fiber diameter
SEM	:	Scanning electron microscope
TEM	:	Transmission electron microscope
HRTEM	:	High resolution transmission electron microscope
SAED	:	Selected area electron diffraction
FFT	:	Fast Fourier transform
EDX	:	Energy dispersive X-ray
XRD	:	X-ray diffraction
FWHM	:	Full width at half maximum
^{1}H-NMR	:	Proton nuclear magnetic resonance
FTIR	:	Fourier transform infrared
ATR	:	Attenuated total reflectance
TGA	:	Thermogravimetric analyzer
DSC	:	Differential scanning calorimeter
GC-MS	:	Gas chromatography-mass spectrometry
BET	:	Brunauer– Emmett–Teller
DMA	:	Dynamic mechanical analyzer
HPLC	:	High performance liquid chromatography

PL	:	Photoluminescence
SE	:	Spectroscopic ellipsometry
PBT	:	Polybutylene terephthalate
PVA	:	Polyvinyl alcohol
PLA	:	Polylactic acid
PET	:	Polyester
PAN	:	Poly(acrylonitrile)
PSU	:	Polysulfone
PVP	:	Poly (vinylpyrrolidone)
EG	:	Eugenol
TR	:	Triclosan
TFA	:	Ttrifluoroacetic acid
ACN	:	Acetonitrile
DMF	:	N,N-dimethylformamide
DCM	:	Dichloromethane
HFIP	:	1,1,1,3,3,3-hexafluoro-2-propanol
DMSO-d_6	:	Deuterated dimethylsulfoxide
Rh-B	:	Rhodamine-B
MB	:	Methylene blue
DEZn	:	Diethylzinc
ZAD	:	Zinc acetate dihydrate
HMTA	:	Hexamethylene tetramine
DI	:	De-ionised
TTIP	:	Titanium (IV) isopropoxide

TDMAT	:	Tetrakis (dimethylamido) titanium
SHPI	:	Sodium hypophosphite hydrate
CTR	:	Citric acid
VOC	:	Volatile organic compounds
PAH	:	Polycyclic aromatic hydrocarbon
S. aureus	:	*Staphylococcus aureus*
E. coli	:	*Escherichia coli*
NP	:	Nanoparticles
QDs	:	Quantum dots
NC	:	Nanocoating
CSHJ	:	Core-shell heterojunction
VB	:	Valance band
CB	:	Conduction band
BGR	:	Bulk grain region
DR	:	Depletion region
V_O	:	Oxygen vacancy
Zn_i	:	Zinc interstitials
FX	:	Free exciton
˙OH	:	Hydroxyl radical
ppm	:	Parts per million
DFT	:	Density functional theory
$E_{complex}$	:	Complexation energy
tan δ	:	Loss tangent
T_g	:	Glass transition temperature

LIST OF FIGURES

LIST OF TABLES

CHAPTER 1

1. INTRODUCTION

1.1. Electrospinning

One-dimensional nanostructures such as nanofibers have distinctive properties which can offer good opportunities for developing advanced materials and devices [1-3]. Among the other nanofiber fabrication methods (drawing, template synthesis, phase separation, self-assembly), electrospinning has gained growing interest in the past decade, since this technique is quite versatile and cost-effective for producing functional nanofibers from variety of materials including synthetic or natural polymers, polymer blends, emulsions, suspensions, sol-gels, metal oxides, composite structures as well as non-polymeric systems, *etc.*[1-2, 4-10].

Basic electrospinning set-up has three main components; syringe pump, high voltage power supply and collector which is schematically shown in Figure 1. Electrospinning unit at UNAM is also given in Figure 2. In electrospinning process, the fluid (mostly polymer solution) in a syringe is pumped through a thin nozzle that serves as an electrode to which a high voltage is applied [1, 6-7]. A drop is formed on the tip of the nozzle due to surface tension of a fluid. When repulsive force induced by the charge distribution on the surface of the drop overcomes surface tension of the liquid, a fluid jet erupts from the droplet at the tip of the nozzle

resulting in the deformation of the liquid drop into a conical shape named as Taylor cone [1, 7]. During the movement of the liquid jet to the region of lower potential which in most cases, is a grounded collector, the solvent evaporates and solid fibers with diameter ranges from microns down to a few tens of nanometers are collected on the counter collector [1, 7].

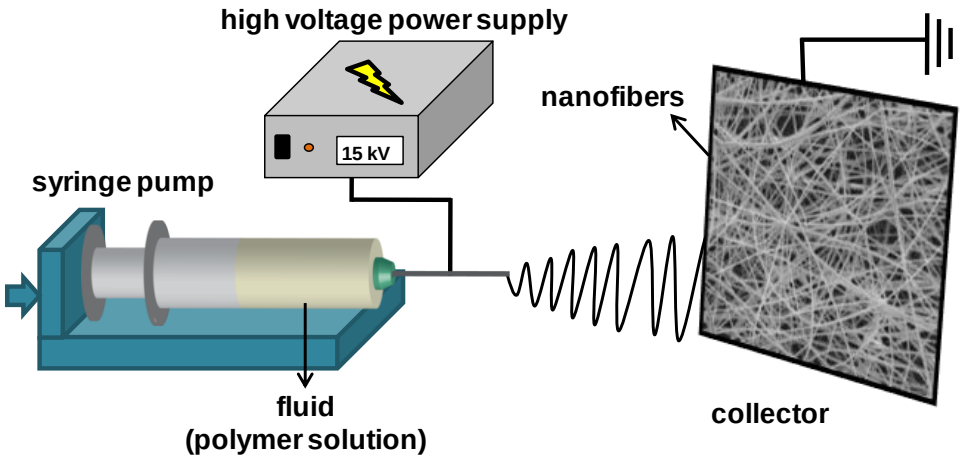

Figure 1. Schematic view of electrospinning. (Copyright © 2012, American Chemical Society. Reprinted with permission from Ref.[11])

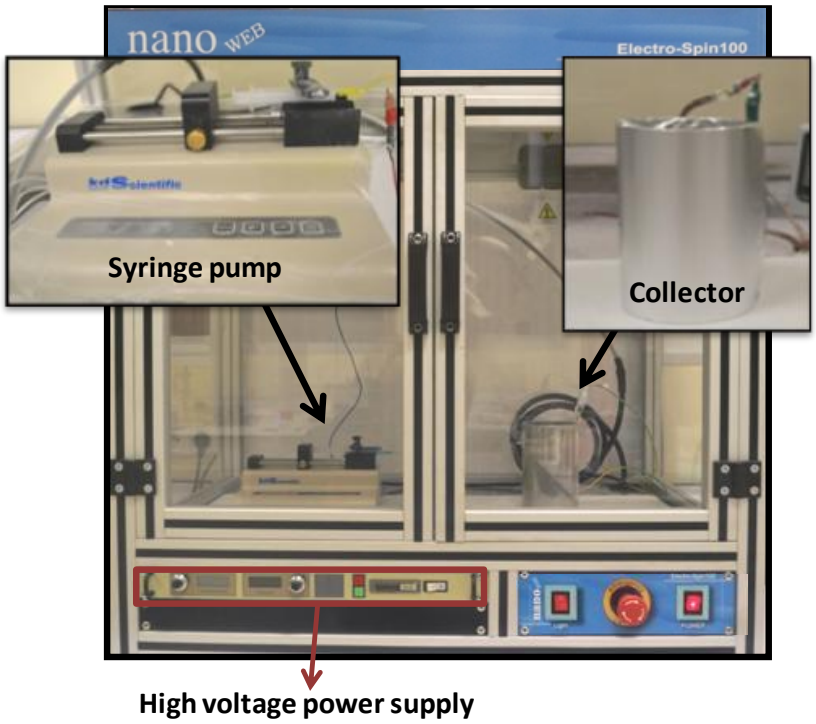

Figure 2. Electrospinning unit at UNAM.

By electrospinning, we can produce nanofibers that are one thousand times thinner than a human hair (see scanning electron microscope (SEM) image in Figure 3). The parameters that influence the morphology of the resultant electrospun fibers with their diameters may be broadly classified into polymer/solution parameters, processing conditions (applied voltage, distance between tip of the nozzle and collector, internal diameter of the needle, feeding rate for the fluid, type of collector) and ambient conditions (humidity, temperature, type of atmosphere and pressure) [1, 7, 12]. Among these polymer/solution parameters which include type of polymer (molecular weight, conformation of polymer chain), viscosity, conductivity and surface tension of the solution, polarity and dielectric effect of solvent have the most significant influence. It is possible to fabricate nanofibers with various morphology (beaded fibers, bead-free fibers) and different fiber diameters by varying these parameters.

Figure 3. The SEM image of the nylon 6,6 nanofibers collected on a human hair.

We obtained polybutylene terephthalate (PBT) nanofibers from different concentration of PBT solutions using trifluoroacetic acid (TFA) as a solvent to find optimal concentration for bead-free fibers. In order to show the effect of concentration of polymer solution on the morphology and diameter of nanofibers the SEM images with average fiber diameter (AFD) of these electrospun PBT nanofibers are given in Figure 4. If the concentration is high enough, bead structures are eliminated and bead-free and uniform nanofibers can be obtained due to required

level of viscosity. In general, thicker fibers are obtained from more concentrated solutions resulting in less stretching of the electrified jet.

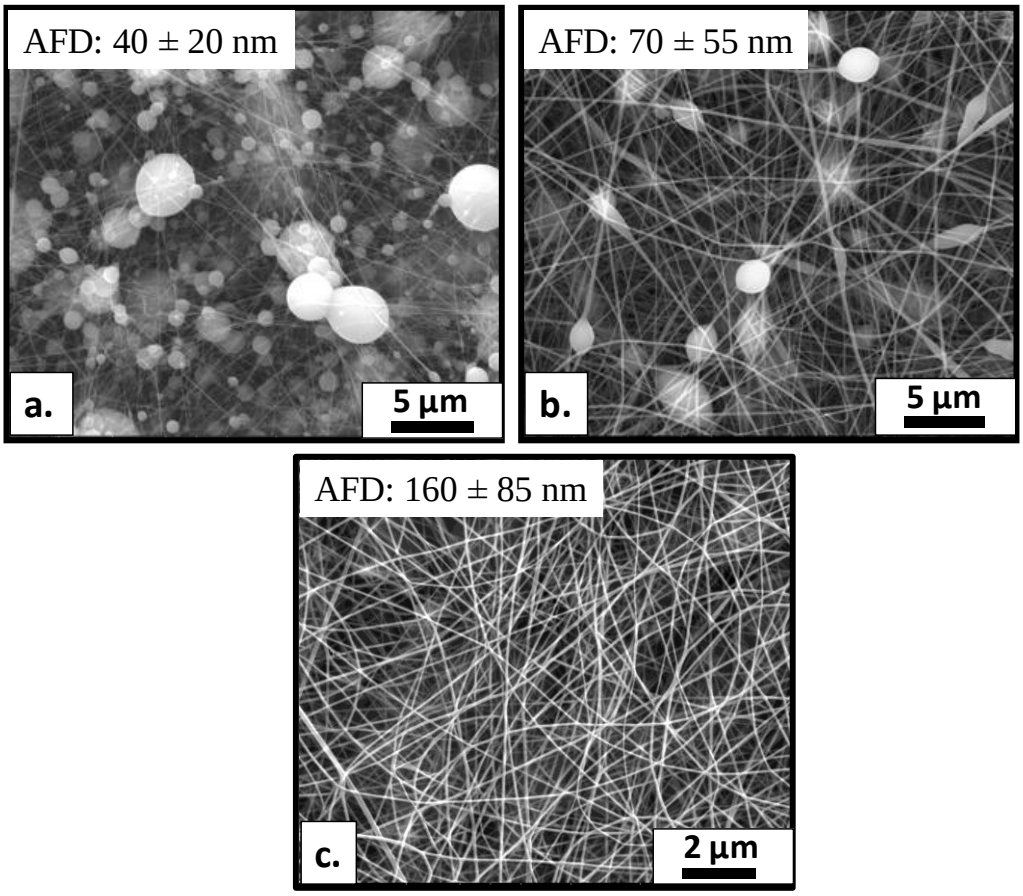

Figure 4. SEM images with AFD of the electrospun nanofibers obtained from different concentration of PBT solutions in TFA (a) 5%, (b) 8% and (c) 12.5% (w/v).

Although electrospun fibers are commonly circular in cross section, other shapes, in particular ribbon-like structures can be obtained [12]. We obtained nylon 6,6 nanofibers having both round and ribbon-like morphology by using different polymer concentration in formic acid (see Figure 5). Therefore, the formation ribbon-like morphology from the more concentrated solution is possibly due to collapse of the skin on the surface of liquid jet during rapid evaporation of solvent.

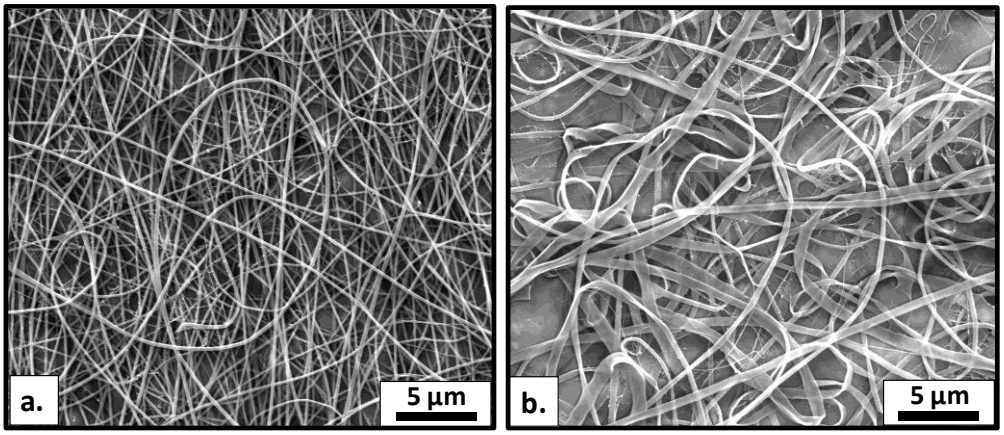

Figure 5. SEM images of electrospun nanofibers obtained from different concentration of nylon 6,6 solutions in formic acid (a) 10% and (b) 15% (w/v).

Electrospun nanofibers and their nanofibrous webs have remarkable characteristics including a very high specific surface area, pore sizes within the nanoscale and very light weight. Moreover, the control of the fiber surface morphology, fiber orientation and cross sectional configuration, and design flexibility for physical/chemical modification either during electrospinning or post-processing is quite feasible for obtaining multifunctional electrospun nanofibers. Therefore, the properties of electrospun nanofibers can be improved by incorporating functional additives and/or nanoparticles into the fiber matrix and/or onto fiber surface [6-7, 10, 12-20]. Due to their exceptional properties, it has been shown that electrospun nanofibers/nanowebs have potentials for various applications in the field of functional textiles [6], biomedical (wound dressing, tissue engineering, drug delivery) [1-2, 4, 6-7, 21], nanocomposites [1-2, 6-8, 22], energy (solar cells, fuel cells, supercapacitors, hydrogen storage, optoelectronics, transistors) [1-2, 6-7, 23], sensor [1-2, 6-7, 24], immobilization of catalysts/enzymes [6, 24] and environment [1-2, 6-7, 23, 25].

Electrospun nanofibers and their nanowebs have also shown some potential in biotechnology, controlled/sustained release systems and active food packaging due to their exceptionally large surface area and high encapsulation efficiency that can be effective for the stabilization of active agents. Electrospun nanofibers from biodegradable [26-28] or edible [29] polymers has received great attention in

functional food and active food packaging systems, recently. Moreover, food related applications and food packaging application were investigated for electrospun nanofibers based on food grade materials [30-31] and/or nanofibers incorporating active agents such as antibacterials [32-35], antioxidants [36-38], essential oils [33] or even probiotics [39]. Development of nanocomposite fabrics with the functional electrospun nanofibers that can supply antimicrobial protection or delivery of nutraceuticals to foods could improve the performance for bioactive packaging applications [40]. In Chapter 2, the development of electrospun nanofibers using cyclodextrin inclusion complexes (CD-IC) is reported in which these functional nanofibers can be applicable in the fields of biotechnology, controlled/sustained release systems and especially active food packaging. The resulting cyclodextrin functionalized electrospun zein nanofibers mentioned in the second part of Chapter 3 (3.2) may be also useful for food packaging application.

Moreover, It has been reported that functional electrospun nanofibrous materials can be easily obtained in the form of nonwoven membranes which can be readily used as a filtering material for particulate separation [25, 41], liquid filtration [25, 41-42], air filtration [23, 41, 43-53], waste vapor treatment [52, 54] as well as desalination [55] due to their high surface-to-volume ratio and nanoporous structure, high permeability, low basis weight. In addition, the design flexibility of electrospun nanofibers for specific surface functionality can yield better adsorptive capacity and selective separation performance [56-57]. More efficient and energy saving innovative membrane materials are very demanding for removal of volatile organic compounds, chemical and biological pollutants, warfare contaminants and toxic agents from air, water and surroundings [23, 44-45, 48, 50-53]. In Chapter 3, there is an overview of the researches in which we obtained multifunctional nanofibrous materials using cyclodextrins (CD; see the second part of Chapter 1 (1.2)) to promote their applicability in filtration. In the research studies mentioned in Chapter 4, the surface of the electrospun nanofibers was coated with nanostructures of metal oxides (ZnO, TiO_2) to achieve the photo degradation of organic contaminants in the aqueous solutions. Photocatalytic activity (PCA) of metal oxides is explained in detail in the third part of Chapter 1 (1.3).

1.2. Cyclodextrins

Cyclodextrins (CD) that are non-toxic cyclic oligosaccharides consisting of α(1,4)-linked glucopyranose units, are produced by the enzymatic (glocosyl transferase enzyme) degradation of starch [58-61]. There are three most commonly used native CD types; α-CD, β-CD, and γ-CD having 6, 7, and 8 glucopyranose units in their cyclic structure, respectively (Figure 6a) [58-60]. The depth of the cavity for these three CD having truncated cone shaped molecular structure is same which is ~8 Å, whereas the internal diameter of the cavity is different for α-CD, β-CD, and γ-CD, being ~6, 8 and 10 Å, respectively (Figure 6b) [58-60, 62].

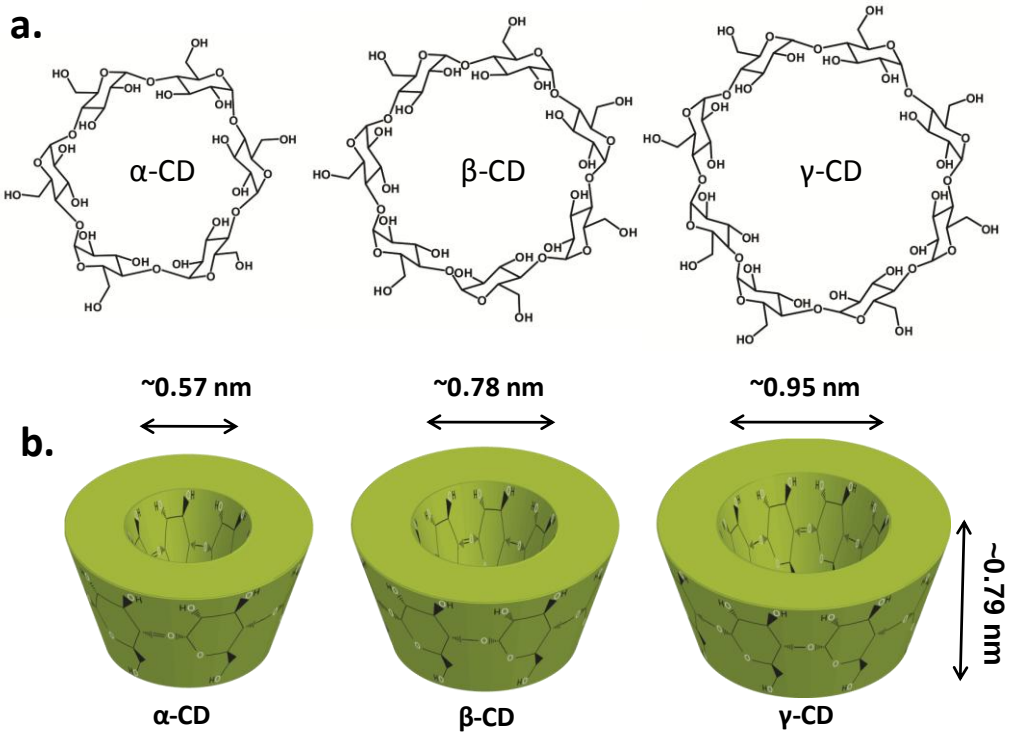

Figure 6. (a) Chemical structures, (b) schematic representations with approximate dimensions of α-CD, β-CD, and γ-CD.

The main properties of α-CD, β-CD, and γ-CD are summarized in Table 1 [58]. The possible formation of hydrogen bond between C-2-OH group of one glucopyranose unit and C-3-OH group of the adjacent glucopyranose unit can affect the aqueous solubility of CD (see Table 1). β-CD has a rather rigid structure due to a

complete secondary belt formed by these intramolecular hydrogen bonds; hence, it is the lowest water soluble among the three common CD [58]. On the other hand, the hydrogen belt is not complete in α-CD because of one glucopyranose unit having distorted position which resulting in only four fully established intramolecular hydrogen bonds instead of six; therefore, α-CD has a greater aqueous solubility compared to β-CD, but less than that of γ-CD having a non-coplanar and more flexible structure [58].

Table 1. Main properties of α-CD, β-CD, and γ-CD.

Properties	**α-CD**	**β-CD**	**γ-CD**
Number of glucopyranose units	6	7	8
Approximate cavity diameter (Å)	4.5-5.7	6.2-7.8	7.9-9.5
Approximate height of torus (Å)	7.9	7.9	7.9
Approximate cavity volume ($Å^3$)	174	262	427
Molecular weight (g/mol)	972	1135	1297
Solubility in water at 25 °C (g/100 mL)	14.5	1.85	23.2

The primary hydroxyl groups of the glucose residues are located at the narrow edge of the cone, whereas the secondary hydroxyl groups are at the wider edge (see Figure 6b). While these hydroxyl groups are orientated to the cone exterior, skeletal carbons and ether oxygens of the glucose residues are situated in the central cavity [58-59]. CD have a relatively hydrophobic inner cavity and hydrophilic outer surface owing to this unique chemical structure [58-59]. The relatively hydrophobic cavities of CD have remarkable ability to form non-covalent host-guest inclusion complexes (IC) with a variety of molecules in appropriate polarity and dimension. Figure 7 illustrates schematic representation of formation of CD-IC with host CD and guest molecule.

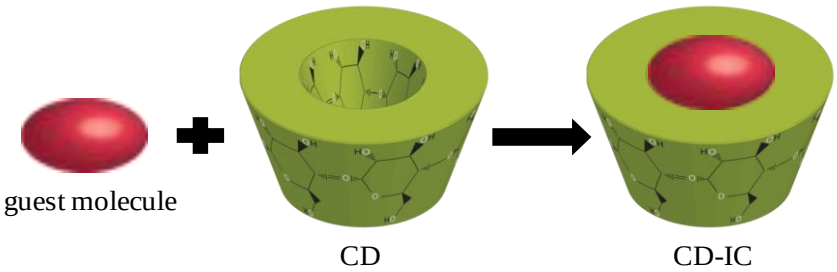

Figure 7. Schematic representation of CD-IC formation.

The main driving force of the inclusion complexation is the replacement of enthalpy-rich water molecules inside the apolar CD cavity with hydrophobic guest molecule [59]. CD-IC can be formed in solution (water is the most commonly used solvent) efficiently compared to the formation in the crystalline state. While the repulsive interactions between the hydrophobic guest and the aqueous environment decrease, hydrophobic interactions (apolar- apolar association) increased as the guest inserts into the apolar CD cavity [59]. Thereby lower energy in system is achieved with the decrease of CD ring strain.

The soluble CD in the solvent are available for complexation. However, as the amount of water is further increased, the CD and the guest do not get in contact easily [59]. The most commonly used techniques to form CD-IC are dry mixing, paste, slurry, co-precipitation, low-temperature drying [59-60]. The quantities of water employed are different among these techniques. Dry mixing is not efficient method because of mixing times ranging from hours to days with no added water [59-60]. Using a minimum amount of water (20-30% w/w) resulting in high viscosity make paste method not useful in the laboratory [59-60]. In the slurry method, up to 50% w/w water is used. Because of large amount of water employed, the large scale formation of IC with co-precipitation method is not frequent. However, this method is widely used in the laboratory, since it demonstrates feasibility of complexation of a particular guest [59-60]. Precipitation is not possible for soluble complexes, so freeze-drying is especially useful for these samples [59-60].

CD are extensively used in many industries (see Figure 8) such as pharmaceutical and medical, agricultural, textile, cosmetic and home/personel care and mostly food, since CD can form IC with a variety of molecules including drugs [62], pesticides [63-64], textile auxiliaries [65-67] and volatile and/or unstable additives such as essential oils [61, 68], flavors [69-70], antioxidants [71-72], antibacterials [73-80]; and inclusion complexation can enhance stability (against to heat, light, oxygen), solubility, bioavailability, functionality and controlled/sustained release of these guest molecules. In Chapter 2, I reported our research studies on

functionalized electrospun nanofibers with CD-IC of different active agents, and thus development of CD applications in such areas.

Moreover CD can also be used in separations, purification and filtration purposes due to their unique property to selectively form IC with unpleasant odors, hazardous and polluting organic compounds [81-87]. CD functionalized electrospun nanofibers were developed to combine this capability of CD and high surface area and nanoporous structure of nanofibers, and these research studies were reported in Chapter 3.

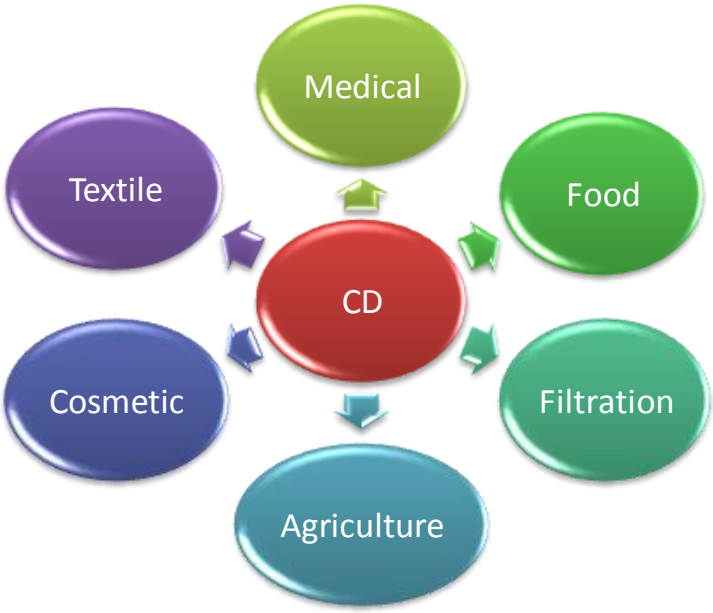

Figure 8. Industrial applications of CD.

The formation and stability of the CD-IC depend on various factors including the size/shape fit, chemical surroundings, and binding forces (hydrophobic interactions, van der Waals attractions, hydrogen bonding, electrostatic interactions, etc.) between the host CD and guest molecules [88-90]. In our most studies in Chapter 2 and Chapter 3, the capability of different types of CD (α-CD, β-CD, and γ-CD) to form IC with the same guest molecule were comparable and the different stability have been found for some resulting CD-IC depending on CD type.

1.3. Atomic Layer Deposition of Metal Oxides

Polymer-inorganic composite nanofibrous structures have intriguing properties which combine the advantages of polymers such as structural flexibility and light weight with the properties of inorganic materials such as high mechanical strength, high thermal stability and excellent electrical, magnetic, optical, catalytically properties, *etc.* These composite nanofibers have many potential applications in filtration [1, 22, 25], protective clothing [19], electronics [91], energy storage devices [92], sensors [93], microwave absorbers [94], *etc.* Morphological characteristics of the polymer-inorganic composite nanofibers are also very important for presenting their properties. For instance, core-shell nanofibers are quite attractive since their morphology could further enhance the material properties.

Different methods such as radio frequency sputtering [95] and metal-organic chemical vapor deposition [96], *etc.* were utilized on the electrospun inorganic nanofibers to produce inorganic-inorganic core-shell nanofibers. Moreover, inorganic-inorganic coaxial nanofibers were also fabricated by co-electrospinning of two different sol-gel systems [97]. On the other hand, polymer-polymer coaxial nanofibers have been extensively fabricated by using coaxial electrospinning setup [98-99] or they can also be obtained by single spinneret electrospinning of blends of the two different types of polymers [100]. Yet, the fabrication of polymer-inorganic core-shell nanofibers is somewhat challenging since the deposition of inorganic shell layer requires a high temperature process which can easily deform the polymeric core structure.

Low-temperatures used in atomic layer deposition (ALD) technique further allow inorganic deposition on temperature-sensitive organic substrates including polymeric films [101] and fibrous systems such as cotton [102-103], cellulose-based filter paper [102-105], nonwovens [106], synthetic [103-104] and natural fibers [107] and nanofibrillated cellulose [108]. ALD, which is a special type of low-temperature chemical vapor deposition, proceeds though the sequential pulses of two or more precursors separated by purging/evacuation periods [109]. ALD is therefore a cyclic process, and one ALD cycle consists of at least these steps (see Figure 9): exposure

of the first precursor, purging and/or evacuation to remove excess precursor molecules (non-reacted) and gaseous by-product(s), exposure of the second precursor, and again purging and/or evacuation to remove non-reacted precursor molecules and gaseous by-product(s).

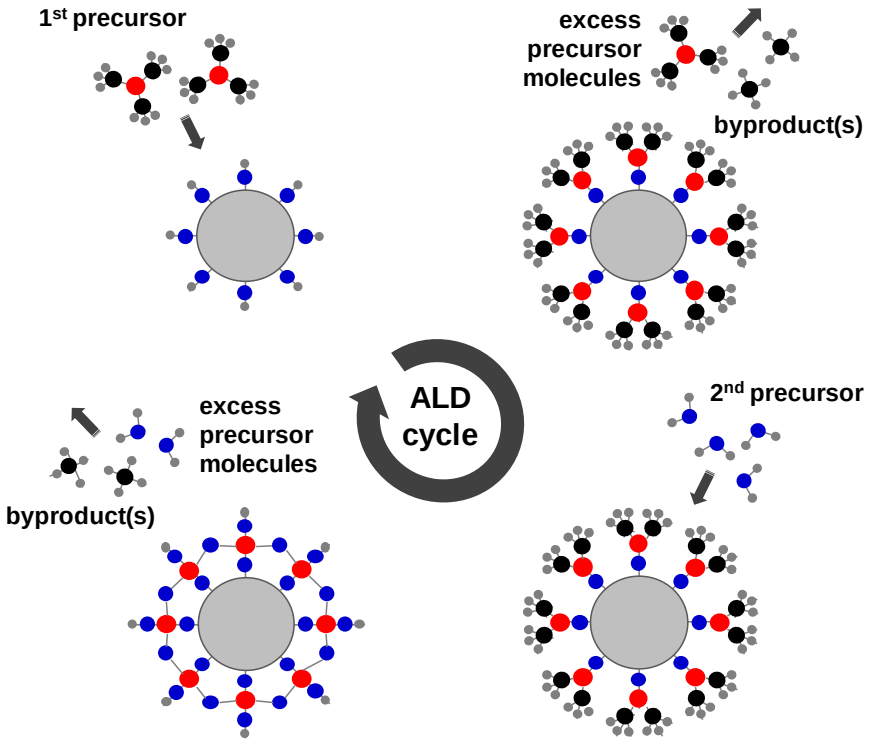

Figure 9. Schematic representation of the processing steps for one ALD cycle. (Copyright © 2012, American Chemical Society. Reprinted with permission from Ref.[11])

Same amount of material is deposited in each cycle, which is known as the growth per cycle. As the substrate is exposed to a certain precursor, gaseous precursor molecules saturate the surface by reacting with available surface sites, creating new sites for the following precursor. Unless decomposition occurs, precursor molecules do not tend to react with themselves, and hence the gas-solid reaction taking place at the substrate surface terminates when all the available reactive surface sites are occupied. This results in a unique self-limiting growth mechanism of ALD, which gives rise to unique properties such as high uniformity and conformality over large areas, as well as sub-nanometer precise thickness control [109-111]. ALD process provides repeatability and flexibility so that very thin

conformal layers of metals, metal oxides or metal nitrides can be coated onto different types of three-dimensional substrates [109-111]. Moreover, ALD a powerful method for coating particles [112] and synthesizing complex nanostructures.

Electrospun nanofibers can be used as a template for producing hollow nanofibers using ALD technique. For instance, Al_2O_3 microtubes with precise wall thickness control were fabricated by ALD of Al_2O_3 onto electrospun poly(vinyl alcohol) fibers, in which the polymeric fiber core was removed by calcination [113]. Similarly tubes or hollow fibers of various sizes and materials (Al_2O_3/ZnO/Al_2O_3 multilayer [114], TiO_2 [115], $CoFe_2O_4$ and Fe_2O_3-particle doped TiO_2 [116], ZnO [117-118], SnO_2 [119]) were synthesized by first depositing the inorganic shell by ALD and then removing the polymeric electrospun nanofiber templates by calcination. We also used electrospun nanofibers template-based synthesis to obtain AlN [120] and HfO_2 [121] hollow nanofibers. Moreover, the high surface area nanostructured Al_2O_3 tubes were also prepared by dissolution of ALD-coated electrospun PVA fibers without using calcination [122].

ALD has also been utilized to coat and protect electrospun nylon-6 nanofibers [123]. Nevertheless, to the best of our knowledge, the focus on the fabrication of polymer-inorganic core-shell nanofibers by combination of electrospinning and ALD has been very limited in the literature [123]. The combination of ALD and electrospinning was also used to prepare TiO_2-coated $NiFe_2O_4$-fibers [116] and inorganic-inorganic core-shell nanofibers of TiO_2-ZnO [124] and SnO_2-ZnO [125].

In Chapter 4, our research studies focused on the production of mostly polymer-ZnO (4.2, 4.3, 4.4, 4.5) nanofibers having different ZnO morphology and TiO_2-ZnO/ZnO-TiO_2 core-shell heterojunction nanofibers (4.6) by combination of electrospinning and ALD and the investigation of photocatalytic activity (PCA) of the resulting nanofibrous samples. Photocatalytic activity of metal oxides is explained in detail in the next part of this Chapter (1.4).

1.4. Photocatalytic Activity of Metal Oxides

Water pollution is a growing environmental issue which threatens the human health severely, consequently, development of novel materials for water purification and waste treatment is an important requirement [126-127]. Disintegration of organic pollutants by photocatalytic activity (PCA) of semiconductors is one of the widely researched [11, 128-137] topics because of its importance in water and environmental purification in the background of unavoidable and ever increasing industrialization [138-140]. Functional nanomaterials [141] having photocatalytic properties along with their very high surface area have been widely investigated, since these nanostructures are quite effective for the degradation of organic contaminants under UV light and sunlight. For instance, metal oxides such as ZnO [142-145] and TiO_2 [146-149] are very well known for their PCA and therefore, these materials in their structured forms of nanoparticles [144, 148], nanorods [142, 145, 147] and nanofibers [144, 149] are studied intensely for water purification purposes. Therefore, organic molecules are adsorbed on the surface as a monolayer at a distance of 1 Å. These adsorbed molecules are oxidized through a process mediated by hydroxyl radical (·OH) [139-140]. Under suitable illumination electrons can be excited from the valance band (VB) to reach the conduction band (CB), leaving behind holes in the VB [150-151]. If these separated charges can migrate to the surface of the semiconductor before they recombine, then they have a chance to participate in the redox reactions to form hydroxyl radical (˙OH) [152].

Photocatalysis process is shown as follows after Izumi et al. [139] and Matthews [140]. The key for the photocatalysis is the formation of ˙OH, which can be through (a) *electron* generated at CB (e_{CB}^-) and/or (b) *hole* generated at VB (h_{VB}^+). Process (a) contains multiple steps (see below), which are mediated by superoxide anions ($˙O_2^-$) as proposed by Izumi et al. [139] Initially, molecular oxygen traps the e_{CB}^- and forms $˙O_2^-$ ions (a1-1), while the second step involves formation of H_2O_2 (a2-1 through a2-4) followed by its cleavage by superoxide anions (a3-1, 2 or 3) as shown below.

$$e_{CB}^{-} + O_2 \rightarrow {}^{\bullet}O_2^{-} \text{ …..(a1-1)}$$

$${}^{\bullet}O_2^{-} + H^{+} \rightarrow {}^{\bullet}HO_2 \text{ ….. (a2-1)}$$

$$2{}^{\bullet}HO_2 \rightarrow H_2O_2 + O_2 \text{ ….. (a2-2)}$$

$${}^{\bullet}O_2^{-} + {}^{\bullet}HO_2 \rightarrow {}^{\bullet}HO_2^{-} + O_2 \text{ ….. (a2-3)}$$

$${}^{\bullet}HO_2^{-} + H^{+} \rightarrow H_2O_2 \text{ ….. (a2-4)}$$

$$H_2O_2 + {}^{\bullet}O_2^{-} \rightarrow {}^{\bullet}OH + OH^{-} + O_2 \text{ ….. (a3-1) (OR)}$$

$$H_2O_2 + e_{CB}^{-} \rightarrow {}^{\bullet}OH + OH^{-} \text{ ….. (a3-2) (OR)}$$

$$H_2O_2 \xrightarrow{h\nu} 2\ {}^{\bullet}OH \text{ ….. (a3-3)}$$

On the other hand, in process (b), [140] ˙OH radicals are formed majorly from the h_{VB}^{+} in the presence of either adsorbed H_2O (b-1) or the OH^{-} groups on the surface (b-2).

$$h_{VB}^{+} + H_2O \rightarrow {}^{\bullet}OH + H^{+} \text{ ….. (b-1)}$$

$$h_{VB}^{+} + HO^{-} \rightarrow {}^{\bullet}OH \text{ ….. (b-2)}$$

Finally, in any case the ˙OH radical oxidises the dye (˙OH + dye → oxidised products) when generated by a photo-*electron* or photo-*hole*.

In order to increase the efficiency of a semiconductor catalyst one needs to isolate [153] or at least delay the recombination of photogenerated *electron* and *hole* [138, 148, 154-161]. To achieve this, lattice defects are induced in the semiconductor [138, 148, 155, 157-161] apart from the fabrication of heterojunctions (either with noble metals [154-156] or another semiconductors [153, 162]). In connection to the lattice defects, depending on the type and energetic location of the defect, their character is determined to capture either an *electron* or a *hole*, thereby the recombination process is delayed [138-140, 148, 153, 155, 157-161]. As a consequence the captured or free charge carrier participates in the PCA, in which the catalysis takes place at CB, VB and the defect site if available on the surface [153, 157]. Also note that the defects form intermediate bands within the band gap which allow the visible light harvest especially in the case of wide band gap semiconductors [138, 150-151, 153, 157, 163]. The lattice defects connected to PCA are basically

intrinsic (vacancies, interstitials, anti-site) or extrinsic (induced by impurities) in nature [138, 148, 153, 155, 157-161, 163-164].

In principle, there are a number of defect states within the band gap (3.36 eV) of ZnO nanostructures [11, 128, 130-131, 137, 165-166] that have attracted a lot of attention among a list of semiconductors employed in photocatalysis, due to their easy processability via a variety of methods [131, 151, 167-168], versatility in nanostructuring [131, 151, 167-168], non-toxicity, abundance, low cost, etc. The donor defects are zinc interstitials (Zn_i: Zn_i^+, Zn_i^{++}, Zn_i^* (neutral)), Oxygen vacancies (V_Os: V_O^+, V_O^{++}, and V_O^*(neutral)), and the acceptor defects are zinc vacancies V''_{Zn} and V'_{Zn} [169-170]. At higher oxygen partial pressures V_{Zn} and O_i may also be thermodynamically stabilized [171]. However, which defect (Zn_i or V_O) dominates in native/undoped ZnO is still under debate [163]. The energetic locations of defects of Zn_i [172], external Zn_i (ex-Zn_is) [163] and V_O^*(bulk grain region (BGR)), V_O^{++} (depletion region (DR)) [173] is schematized in Figure 10 for a typical band gap of 3.36 eV [151].

On the other hand, fibrous membranes made of nanofibers show remarkable photocatalytic properties due to their unique morphological features including high surface area and nanoporosity [144, 149, 174-175]. Nevertheless, the metal oxide nanofibers are quite brittle and do not show any structural flexibility, which may cause significant problems during their handling and usage as a membrane material. For this reason, the development of flexible nanofibrous membranes or textiles having photocatalytic properties is still on demand for self-cleaning and water purification and waste treatment [149, 176]. The initial four parts of Chapter 4 (4.1, 4.2, 4.3, 4.4) reported on the studies that we obtained different morphology and/or crystal structures of ZnO on the polymeric electrospun nanofibers and investigated the PCA of the resulting samples.

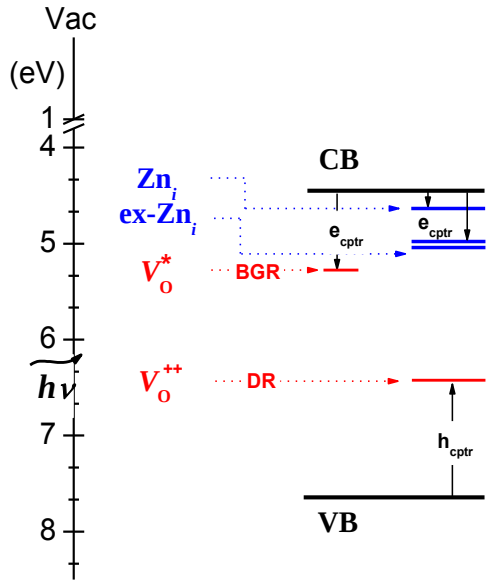

Figure 10. Schematic diagram depicting the energetic locations of the various defects in the band gap of ZnO. (e_{cptr} and h_{cptr}: *electron* and *hole* capture). (Copyright © 2014, Elsevier. Reprinted with permission from Ref.[157])

On the other hand, oxidative degradation of environmental pollutants or chemical conversions with heterostructure-catalysts are well known for their efficiency where the photo-generated charge carriers are driven apart before the recombination,[137, 148, 154-156, 177-182] while understanding the catalysis mechanism is vital for the design of new functional materials to be a part of environmentally friendly technology. In the use of heterostructures, an electron reservoir from a noble metal [148, 154-156] or another semiconductor (heterojunction) [162, 178, 183] is brought into contact. The former case is exploited in core-shell [148, 155, 181] and nanocomposite [137, 154, 156] formats in which the photo-*electrons* from the CB of the semiconductor are transferred to the noble metal and then to the catalysis process, while the *holes* react from the VB of the semiconductor. In the latter case, photo-generated *e/h* pairs diffuse across the heterojunction and *electron* and/or *hole* take part in catalysis from CB and VB of each semiconductor, respectively [178-180]. In the last part of Chapter 4 (4.5), I reported on such combination where we have considered two potential materials which have attracted a lot of attention in PCA (i.e. TiO_2 [148, 179-180, 182] and ZnO [11, 130, 137, 156, 165, 181, 184-186]) and fabricated ZnO-TiO_2 and TiO_2-ZnO as core-shell nanofibers, respectively.

CHAPTER 2

2. NANOFIBERS INCORPORATING CYCLODEXTRIN INCLUSION COMPLEXES

The work described in this chapter was published in part as:

(1) **Kayaci, F.**; Uyar, T., Solid inclusion complexes of vanillin with cyclodextrins: their formation, characterization, and high-temperature stability. *Journal of agricultural and food chemistry* 2011, *59* (21), 11772-11778. *DOI: 10.1021/jf202915c.*

(2) **Kayaci, F.**; Uyar, T., Encapsulation of vanillin/cyclodextrin inclusion complex in electrospun polyvinyl alcohol (PVA) nanowebs: prolonged shelf-life and high temperature stability of vanillin. *Food chemistry* 2012, *133* (3), 641-649. *DOI: 10.1016/j.foodchem.2012.01.040*.

(3) **Kayaci F.**; Ertas Y.; Uyar T., Enhanced Thermal Stability of Eugenol by Cyclodextrin Inclusion Complex Encapsulated in Electrospun Polymeric Nanofibers. *Journal of Agricultural and Food Chemistry* 2013, 61 (34), 8156–8165. DOI: 10.1021/jf402923c.

(4) **Kayaci, F.**; Sen, H. S.; Durgun, E.; Uyar, T., Functional electrospun polymeric nanofibers incorporating geraniol–cyclodextrin inclusion complexes: High thermal stability and enhanced durability of geraniol. *Food research international* 2014, *62*, 424-431. *DOI: 10.1016/j.foodres.2014.03.033.*

(5) **Kayaci, F.**; Umu, O. C.; Tekinay, T.; Uyar, T., Antibacterial electrospun poly (lactic acid)(PLA) nanofibrous webs incorporating triclosan/cyclodextrin inclusion complexes. *Journal of agricultural and food chemistry* 2013, *61* (16), 3901-3908. *DOI: 10.1021/jf400440b.*

2.1. Summary

In the recent years, the interest to new technologies for active food packaging to prevent foodborne diseases, provide safety/quality of nutrition and extend shelf life of food has increased significantly [187-188]. Incorporation of bioactive compounds with antibacterial and/or antioxidant properties [189], such as essential oils [190-191], bacteriocins [192], organic acids [193] and enzymes [194] have been studied for designing active food packaging materials. However, these bioactive compounds are mostly volatile and temperature sensitive, therefore, their incorporation into polymeric films often faces with problems since packaging films are produced by melt extrusion at high temperatures.

As it mention in the first part of Chapter 1 (1.1), very recently, electrospun nanofibrous webs from especially biodegradable [26-28] or edible [29] polymers have received great consideration as an active food packaging material due to their very large surface area to volume ratio, nanoscale porosity and high encapsulation efficiency of active compounds. Moreover, electrospinning of nanofibers is mostly performed from solution-based systems at room temperature, hence, homogeneous mixing of additives in the fiber matrix can be easily achieved and the evaporation of volatile additives can be prevented. It has been shown that functional nanofibers incorporating bioactive compounds such as antibacterials [32-35], antioxidants [36-38], essential oils [33] or even probiotics [39] can be effectively obtained by electrospinning method. Nevertheless, such food additives even may encounter problems related to quick release even during the electrospinning process or during the storage of the nanofiber matrix because of their volatile nature and sensitivity to heat, light and oxygen. As it mention in the second part of Chapter 1 (1.2), cyclodextrin inclusion complexes (CD-IC) is very effective for the stabilization/protection and controlled/sustained release of these functional additives, and can enhance their solubility and functionality [72, 195].

The incorporation of CD-IC into electrospun polymeric nanofibrous matrix is quite interesting, since these functional nanofibers/nanowebs have not only high surface area and nanoporous structure, but also the specific properties of CD-IC [35,

196-198]. Thereby, we incorporated the CD-IC of some active compounds such as vanillin, eugenol, geraniol, triclosan into nanofibers during electrospinning [199-202]. Figure 11 indicated the schematic representations of the formation of CD-IC and electrospinning of polymer solution including CD-IC (polymer/CD-IC). The resulting functional nanofibers would be quite applicable in functional foods and active food packaging.

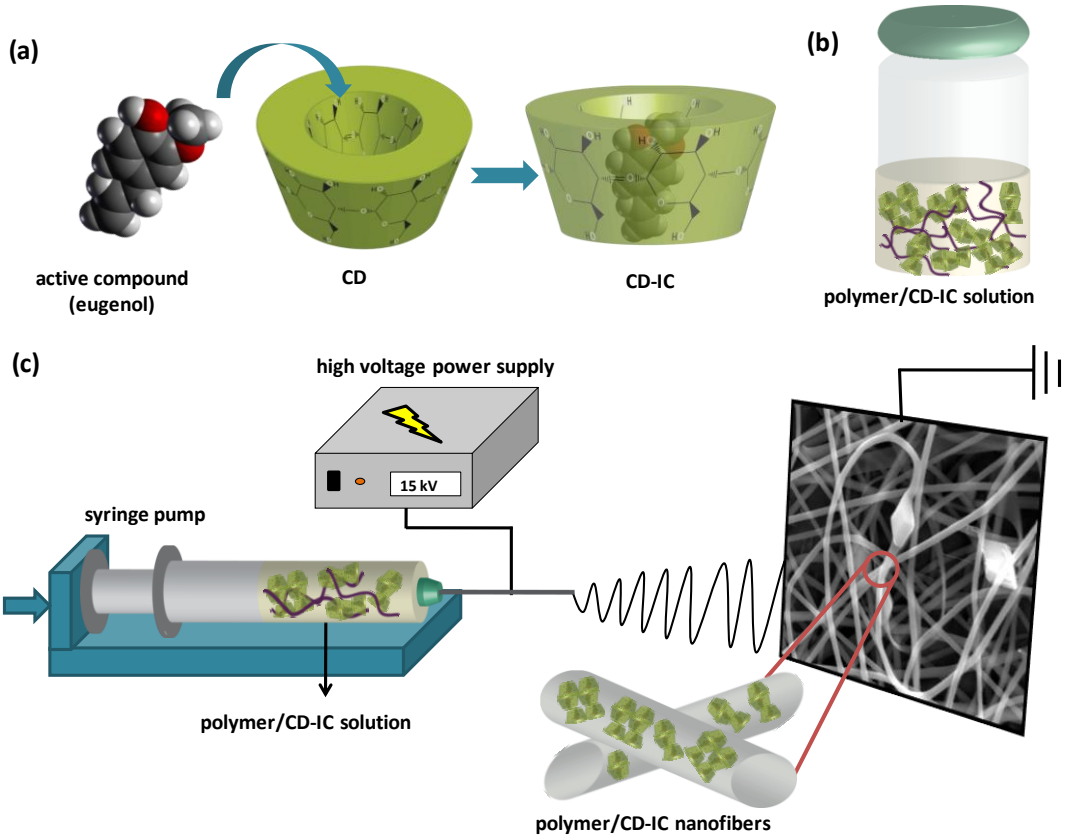

Figure 11. Schematic representations of (a) formation of CD-IC, (b) polymer/CD-IC solution and (c) electrospinning of nanofibers from polymer/CD-IC solution. (Copyright © 2013, American Chemical Society. Reproduced with permission from Ref.[199])

Vanillin (4-hydroxy-3-methoxybenzaldehyde) which is the major component of natural vanilla is widely used as a flavoring additive in the food industry [203-205]. It can also be used as a food preservative due to its antioxidant and

antimicrobial properties [204-205]. Moreover, vanillin is used as a fragrance constituent in cosmetics and textile industries [66, 205]. However, a short shelf-life is a significant problem for vanillin due to its thermal instability and volatile nature. Very few studies have been reported for the formation of vanillin/CD-IC by using β-CD and these CD-IC were mostly studied in solutions [204, 206-209]. However, to date, the solid vanillin/CD-IC systems have not been studied in detail and the inclusion complexation of vanillin with different types of CD has not been evaluated in the solid state. In order to enhance the thermal stability and sustained release of vanillin, we formed solid vanillin/CD-IC by using α-CD, β-CD and γ-CD by a freeze-drying method and co-precipitation method (only for γ–CD) [70]. Thereafter, encapsulation of vanillin/CD-IC in polyvinyl alcohol (PVA) nanofibers was performed via electrospinning [202]. PVA was selected as a polymeric matrix, since it is a proper polymer type for food packaging [210]. I reported these related studies in the next part of this Chapter (2.2).

Eugenol (EG) is a natural fragrance and flavor extracted from plants having antibacterial [79], antifungal [211] and antioxidant [212] properties which make this compound more attractive in food industry as a preservative and germicide. However, the use of EG has some limitations due to its low stability since it is easily oxidized or decomposed in the presence of oxygen, light or heat [213]. So, the approach of molecular encapsulation by forming CD-IC of EG was considered in order to improve its stability against oxygen [214-215], light [214-215] and/or heat [80, 214, 216-217]. In our study reported third part of this Chapter (2.3), electrospun PVA nanofibers encapsulating EG/CD-IC were obtained via electrospinning to improve the thermal stability, and slow release of EG in the fiber matrix [199]. Here, three types of native CD (α-CD, β-CD, and γ-CD) were used to investigate the effect of CD type on the IC formation capability with EG and the stability of EG in the CD-IC.

Geraniol, a natural component of plant essential oils, having rose-like odor and taste is generally used as a fragrance/flavor in food industry to treat infectious diseases and/or preserve the food [218]; therefore, geraniol is shown several

remarkable properties such as insect repellent, antimicrobial, antioxidant, anti-inflammatory and anticancer etc. [219]. It is acknowledged as generally-recognized-as-safe by Food and Drug Administration [220]. However sustainability of geraniol is a major challenge because of its volatile nature. In our study, as a first step we prepared solid CD-IC of geraniol (geraniol/CD-IC) by using α-CD, β-CD, and γ-CD. Our collaborators, Dr. H. Sener Sen and Assist. Prof. Engin Durgun have also performed the modeling studies for inclusion complexation between geraniol and CD using ab initio techniques. Both experimentally and theoretically, we observed that γ-CD has shown higher complexation efficiency compared to other CD types. Then, geraniol/γ-CD-IC was encapsulated in PVA nanofibers via electrospinning in order to enhance thermal stability and durability of geraniol in the nanofibrous webs [200]. This study was reported fourth part of this Chapter (2.4).

Triclosan (TR) is a practically water-insoluble antibacterial agent; therefore, its antibacterial activity can be enhanced with increasing the solubility by forming CD-IC [73-78]. We first tried to form solid TR/CD-IC by using three types of CD (α-CD, β-CD, γ-CD). Then, the prepared TR/CD-IC were incorporated in polylactic acid (PLA) nanofibers via electrospinning [201]. PLA is a well-known biodegradable, biocompatible and non-toxic natural polymer used in food packaging [221-223]. The antibacterial properties of the resulting PLA/TR/CD-IC electrospun nanofibrous webs were investigated by our collaborators Assoc. Prof. Turgay Tekinay and Özgün C.O. Umu. I reported this study the final part of this Chapter (2.5).

2.2. Formation of Solid Vanillin/Cyclodextrin-Inclusion Complexes and Nanofibers Incorporating These Complexes

2.2.1. Solid Inclusion Complexes of Vanillin with Cyclodextrins: Their Formation, Characterization and High Temperature Stability

2.2.1.1. Experimental

Materials: Vanillin (4-hydroxy-3-methoxybenzaldehyde, $C_8H_8O_3$; molecular weight, 152.15; melting point, 81–83 ^oC, 99% purity) was obtained from Sigma-Aldrich. Cyclodextrins (α-CD, β-CD, and γ-CD) were purchased from Wacker Chemie AG (Germany). All materials were used without any purification. Water used for the preparation of the complexes was from Millipore Milli-Q ultrapore water system.

Preparation of vanillin/cyclodextrin inclusion complexes (vanillin/CD-IC): The IC of vanillin with α-CD, β-CD and γ-CD were prepared by adding equimolar amount of vanillin to an aqueous solution of α-CD, β-CD and γ-CD. The amount of the water used was determined according to the solubility of CD in water at 25 °C, that is, 14.5, 1.85 and 23.2 g/100 mL for α-CD, β-CD and γ-CD, respectively [58-59]. First, 0.25 g of α-CD dissolved in 1.725 mL water and, then, 0.039 g of vanillin was added into the aqueous α-CD solution and the vanillin/α-CD solution was mixed overnight at room temperature. The vanillin/α-CD solution became slightly turbid but precipitation did not occur. For vanillin/β-CD-IC, 0.25 g of β-CD was dissolved in 14 mL of water, and then 0.034 g of vanillin was added into this clear β-CD aqueous solution. The vanillin/β-CD solution became clear after mixing it overnight at room temperature and no precipitation was observed. In the case of vanillin/γ-CD-IC, 0.25 g of γ-CD was dissolved in 1.08 mL water and 0.029 g of vanillin was added into this solution. The vanillin/γ-CD solution first became clear and then highly turbid and precipitation took place after mixing overnight at room temperature. Thereafter, all three vanillin/CD solutions were frozen at -80 ^oC and then lyophilized in a freeze dryer (Labconco) to obtain solid vanillin/CD-IC. In addition, the IC of vanillin with

γ-CD was also prepared by a co-precipitation method. Similarly, 0.029 g of vanillin was added to aqueous solution of γ-CD (0.25 g of γ-CD dissolved in 1.08 mL water) and stirred overnight. The resulting suspension was filtered through a borosilicate filter (por 2), and then the filtrate was washed with water several times to remove uncomplexed vanillin and γ-CD and then dried overnight under the hood. After drying, the vanillin/γ-CD-IC solid sample was crushed in a mortar to obtain a fine powder. For comparison, physical mixtures of vanillin/CD having 1:1 molar ratio were prepared in the solid state by admixing vanillin and CD and ground with a pestle in an agar mortar.

Characterization and measurements: A Fourier transform infrared (FTIR) spectrometer (VERTEX70, Bruker) was used to obtain the infrared spectra of the samples. The FTIR measurements were performed by blending the samples with potassium bromide and pellets were formed under high pressure. The spectra were recorded between 4000 and 400 cm^{-1} with a resolution of 4 cm^{-1} at total scans of 64. The proton nuclear magnetic resonance (^{1}H-NMR, Bruker DPX-400) spectra were recorded at 400 MHz at 25 °C. About 20 g/L vanillin/CD-IC were dissolved in DMSO-d_6 to evaluate the stoichiometries of the complexes. Integration of the resonance peak given in parts per million (ppm) of the samples was calculated by using NMR software. The X-ray diffraction (XRD, PANalyticalX'Pert Powder diffractometer) patterns for the samples were collected by using Cu Kα radiation in a range of $2\theta = 5^o$- 30^o. The thermal properties of the vanillin/CD-IC, vanillin/CD physical mixtures and the pure vanillin were investigated by using a differential scanning calorimeter (DSC, Q2000, TA Instruments) and a thermogravimetric analyzer (TGA, Q500, TA Instruments). For DSC analyses, the samples were initially equilibrated at 25 ^{o}C and then heated to 250 ^{o}C at a 20 ^{o}C/min heating rate under N_2 as a purge gas. TGA measurements were performed from room temperature to 500 ^{o}C at a heating rate of 20 ^{o}C/min under N_2 atmosphere.

Headspace gas chromatography-mass spectrometry (GC-MS) analyses were performed on an Agilent Technologies 7890A gas chromatograph coupled to an Agilent Technologies 5975C inert MSD with triple-axis detector. The headspace GC-

MS experiments were carried out by using CTCPAL auto-sampler. Different amounts of CD-IC (0.0185 g vanillin/α-CD-IC, 0.0211 g vanillin/β-CD-IC and 0.238 g vanillin/γ-CD-IC) were placed separately in 20 mL headspace glass vials in order to have the same amount of vanillin (0.0025 g) in each vial. For comparison, the same amount of vanillin/CD physical mixtures were placed separately in 20 mL headspace glass vials for the headspace GC-MS measurements. The tops of the all vials were tightened in order to prevent the escape of the vanillin. Every sample was agitated at 250 rpm at different incubation temperatures in the order 35 ^{o}C, 50 ^{o}C, 75 ^{o}C and 100 ^{o}C for 30 min by using agitator and then analyzed by headspace GC-MS. One thousand microliters of vapor was injected to GC-MS by using headspace injector (MSH 02-00B, volume = 2.5 mL, scale = 60mm). The syringe temperature was kept the same with incubation temperature. The separation of compounds was performed on an HP-5MS (Hewlett-Packard, Avondale, PA) capillary column (30 m × 0.25 mm ID, 0.25 μm film thickness). Column temperature was held at 50 °C for 2 min and increased to 250 °C at the rate of 20 °C/min and equilibrated at this temperature for 3 min. Helium was used as a carrier gas at a flow rate of 1.2 mL/min. Thermal desorption was carried out in the splitless mode during 2 min. The temperatures of the ion source and the transfer line were 230°C and 280 °C, respectively. The GC-MS analyses were carried out in the complete scanning mode (SCAN) in the 50-550 mass range. The vanillin peak was identified by comparing its mass spectrum with that of the vanillin in Flavor 2 and NIST 0.5 libraries. The retention time of vanillin was 8.76 min, and the major peaks of the vanillin were 151 and 152 mass over charge.

2.2.1.2. Results and Discussion

In this study, we prepared solid IC of vanillin with three types of CD (α-CD, β-CD and γ-CD) by using a freeze-drying method; in addition, a co-precipitation method was also used in the case of vanillin/γ-CD-IC. Initially, the presence of the guest molecule (vanillin) in the CD-IC was confirmed by the FTIR studies. The characteristic absorption bands of CD are observed at around 1030, 1080 and 1155 cm^{-1} corresponding to the coupled C–C/C–O stretching vibrations and the

asymmetric stretching vibration of the C–O–C glycosidic bridge in the FTIR spectra of pure CD (Figure 12a). The FTIR spectra of the vanillin/CD-IC are depicted in Figure 12b, and the FTIR spectrum of pure vanillin is also given for comparison. The FTIR spectrum of pure vanillin exhibited characteristic peaks at 1510, 1590 and 1665 cm^{-1} corresponding to stretching absorption of benzene ring and stretching of C=O of the aldehyde group [224]. The overlapping of absorption peaks of CD and vanillin makes the identification of the individual components rather complicated in vanillin/CD-IC. Yet, the absorption bands of vanillin at 1512, 1595 and 1670 cm^{-1} were observed for all vanillin/CD-IC, which indicated that vanillin is present in the samples. In addition, it was noted that the characteristic absorption bands of vanillin were shifted slightly for vanillin/CD-IC when compared to pure vanillin, suggesting the host-guest interactions between CD and vanillin in these samples. This is very typical for CD-IC and FTIR peak shifts were commonly reported for various CD-IC systems [225-226].

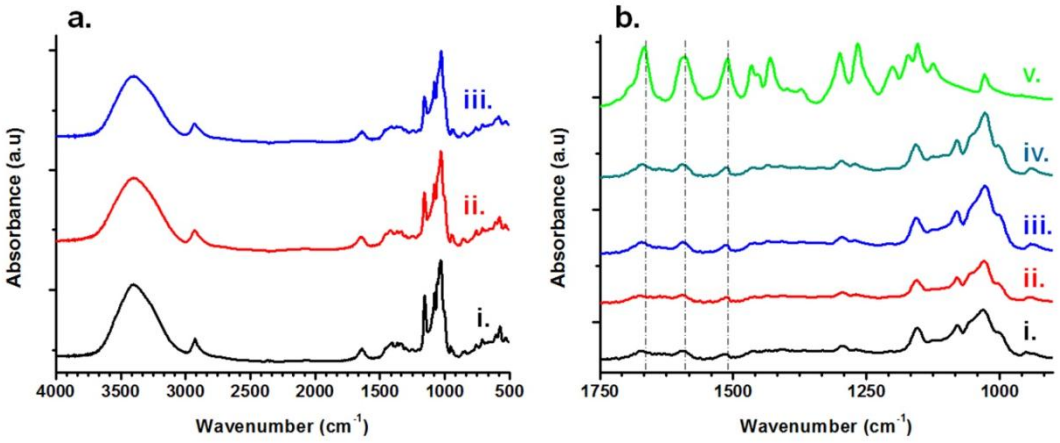

Figure 12. FTIR spectra of (a) as-received (i) α-CD, (ii) β-CD, (iii) γ-CD and (b) (i) vanillin/α-CD-IC, (ii) vanillin/β-CD-IC, (iii) vanillin/γ-CD-IC, (iv) vanillin/γ-CD-IC (co-precipitation) and (v) vanillin. (Copyright © 2011, American Chemical Society. Reprinted with permission from Ref. [70])

The presence of vanillin in the CD-IC and their stoichiometries were determined by ^{1}H-NMR studies (Figure 13). The peaks for vanillin observed at about 3.8, 6.9, 7.4 and 9.8 ppm correspond to different protons in vanillin [207, 209]. The

quantity of vanillin in the CD-IC was calculated by integrating the peak ratio of the characteristic chemical shifts corresponding to vanillin and CD. The integration of the CD peak at 4.8 ppm [208] and the vanillin peak at 9.8 ppm were taken into account to calculate the stoichiometry of the host and guest molecules in the CD-IC samples. It was found that vanillin/β-CD-IC and vanillin/γ-CD-IC have a 1:1 (vanillin/CD) molar ratio whereas the ratio of vanillin/α-CD was 0.625:1, suggesting that the 1:1 initial molar ratio used for the formation of CD-IC was not conserved in the case of vanillin/α-CD-IC. This suggests that α-CD was not very effective in encapsulating vanillin, which is possibly because of the small dimension of α-CD cavity. Additionally, the chemical shifts for pure vanillin and the vanillin/α-CD system were almost the same in the NMR spectrum, indicating that vanillin and α-CD were decomplexed in the DMSO-d_6 solvent system. However, we observed differences in chemical shifts (about 0.1 ppm shift) for vanillin peaks in vanillin/β-CD and vanillin/γ-CD samples when compared to pure vanillin, which is due to the presence of complexation.

XRD studies were performed to investigate the crystalline structure of vanillin/CD-IC. The as-received CD have cage-type packing structure in which the cavity of each CD molecule is blocked by neighboring CD molecules (Figure 14a) [227-228]. The inclusion complexation is generally confirmed by the formation of channel-type arrangement of the CD molecules in which CD molecules are aligned and stacked on top of each other by forming cylindrical channels (Figure 14b) [85, 227-228].

The XRD patterns of as-received CD (Figure 15a) and vanillin/CD-IC (Figure 15b) have characteristic diffraction peaks in the range of 2θ=5-30°. Vanillin is a crystalline material having a distinct diffraction centered at $2\theta \cong 13°$ (Figure 15b). The XRD data show that the as-received CD (α-CD, β-CD, and γ-CD) have cage-type packing structure which is consistent with the literature findings [85, 229-230]. The XRD patterns of vanillin/CD-IC are very different from those of as-received CD.

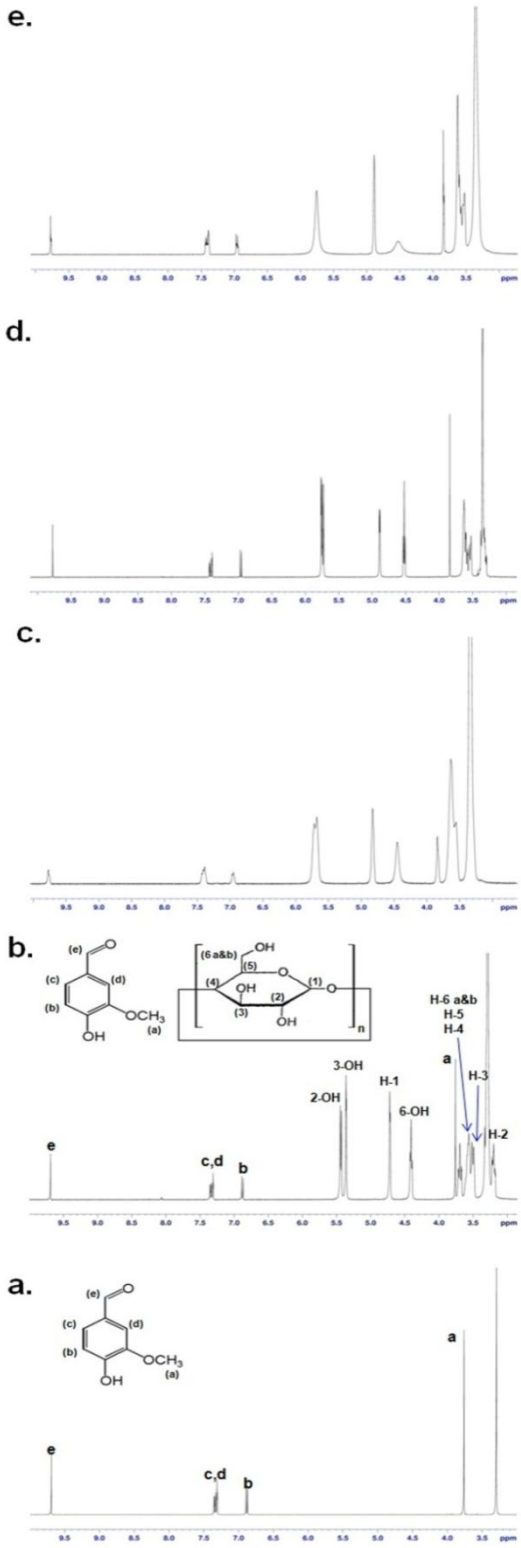

Figure 13. ^{1}H-NMR spectra of (a) vanillin, (b) vanillin/α-CD-IC, (c) vanillin/β-CD-IC, (d) vanillin/γ-CD-IC, (e) vanillin/γ-CD-IC (co-precipitation). (Copyright © 2011, American Chemical Society. Reprinted with permission from Ref. [70])

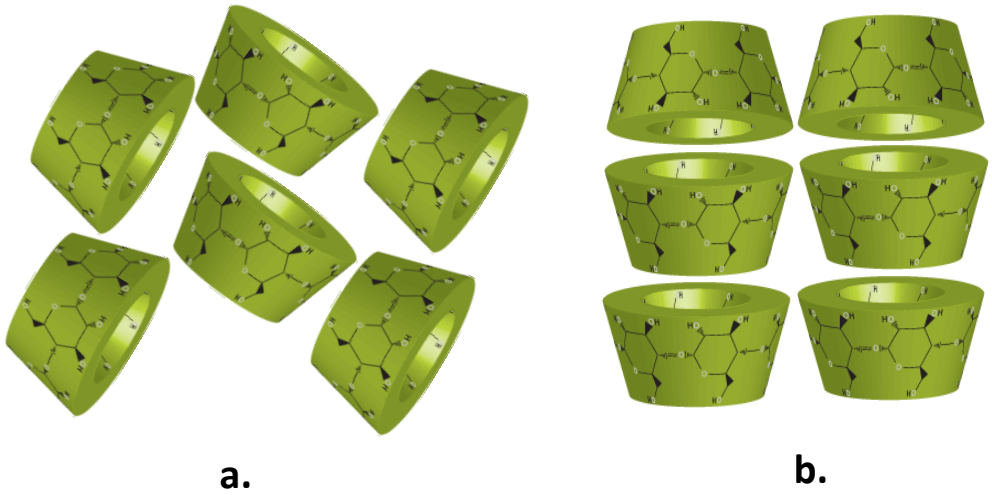

Figure 14. Schematic representations of packing structures of (a) cage-type and (b) channel-type CD crystals. (Copyright © 2013, American Chemical Society. Reprinted with permission from Ref.[199])

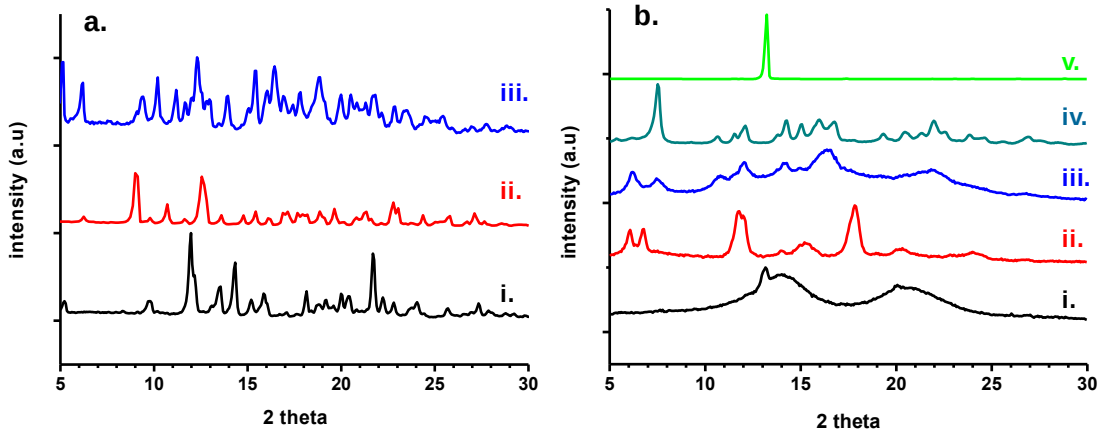

Figure 15. XRD patterns of as-received (a) (i) α-CD, (ii) β-CD, and (iii) γ-CD; (b) (i) vanillin/α-CD-IC, (ii) vanillin/β-CD-IC, (iii) vanillin/γ-CD-IC, (iv) vanillin/γ-CD-IC (co-precipitation), and (v) vanillin. (Copyright © 2011, American Chemical Society. Reprinted with permission from Ref. [70])

The XRD of the vanillin/α-CD-IC shows two broad halo diffraction patterns, indicating that the material was mostly amorphous; yet, a distinct peak at 2θ ≅ 13° and a weak peak at 2θ ≅ 20° were present. The α-CD having channel-type structure has two prominent peaks centered at 2θ ≅ 13° and 2θ ≅ 20° [230]. As mentioned above, vanillin has a major diffraction peak at 2θ≅13° (Figure 15b). The overlapping

of vanillin and the α-CD channel-type diffraction peaks makes the peak assignment rather complicated. The supplementary thermal analyses by DSC, which will be discussed in the following section, indicated that some free vanillin was present in vanillin/α-CD-IC sample. Therefore, the peak at 2θ≅13° was both due to the presence of some uncomplexed free vanillin and the α-CD channel-type packing. In short, the XRD data of vanillin/α-CD-IC suggests that some free vanillin is present in vanillin/α-CD-IC and the sample was mostly amorphous having some amount of channel-type structure.

The XRD pattern of vanillin/β-CD-IC shows two major peaks centered at 2θ ≅ 11.8° and 2θ ≅ 17.8°, indicating that the β-CD adopts a channel-type packing; [229] in addition, no peak at 2θ ≅ 13° for free vanillin was observed, suggesting that complete complexation of vanillin with β-CD was successful. In the case of vanillin/γ-CD-IC obtained by co-precipitation technique, the XRD pattern has a major peak at 2θ ≅ 7.5° along with minor diffractions at 2θ ≅ 14.2°, 15°, 16°, 16.8° and 22°, confirming the tetragonal channel-type packing of γ-CD (26,27). The XRD pattern of vanillin/γ-CD-IC obtained by freeze-drying is similar to that of the vanillin/γ-CD-IC obtained by co-precipitation method; yet, the peaks are relatively broad, indicating that the material was partially amorphous. In addition, the peak at 2θ ≅ 6.2° corresponding to channel structure with hexagonal packing was also observed [85]. The tetragonal channel packing transforms to hexagonal packing upon removal of water residing in the interstitial sites when vacuum dried [85]. Hence, in the case of freeze-drying method, vanillin/γ-CD-IC having a mixture of tetragonal and hexagonal channel-type packing was obtained. Similar to vanillin/β-CD-IC, the vanillin peak at 2θ ≅ 13° was absent, indicating that uncomplexed vanillin was not present in both vanillin/γ-CD-IC samples. The XRD data suggested that both co-precipitation and freeze-drying methods were successful for obtaining solid vanillin/γ-CD-IC.

The solid vanillin/CD-IC were further characterized by DSC (Figure 16a) to verify whether the vanillin was included inside the CD cavities or not. For instance, thermal transitions such as the melting point for guest molecule would be observed if

there were any uncomplexed guest molecules present in the CD-IC [231-233]. The DSC thermograms of vanillin/CD physical mixtures have shown an endothermic peak at around 77 ^{o}C which corresponds to the melting point of vanillin (Figure 16b). The DSC thermogram of pure vanillin is also given for comparison, showing a melting point of 82 ^{o}C. On the other hand, the DSC thermogram of vanillin/β-CD-IC did not show any melting peak for free vanillin, suggesting that the vanillin was fully complexed with the β-CD. Similarly, the melting peak of free vanillin was also absent in the DSC thermograms of vanillin/γ-CD-IC samples obtained by freeze-drying and co-precipitation methods, confirming that both techniques resulted in pure vanillin/γ-CD-IC. The absence of vanillin melting point in DSC and the absence of diffraction peak at 2θ ≅ 13° in XRD for solid vanillin/β-CD-IC and vanillin/γ-CD-IC samples comprise strong evidence for the complete inclusion complexation of vanillin with β-CD and γ-CD. However, in the case of vanillin/α-CD-IC, a small endothermic peak at around 75 ^{o}C was observed in the DSC thermogram due to presence of some free vanillin in this sample. The DSC data also correlate with the XRD data as discussed in the previous section, where the XRD of vanillin/α-CD-IC has a diffraction peak for some uncomplexed vanillin crystals.

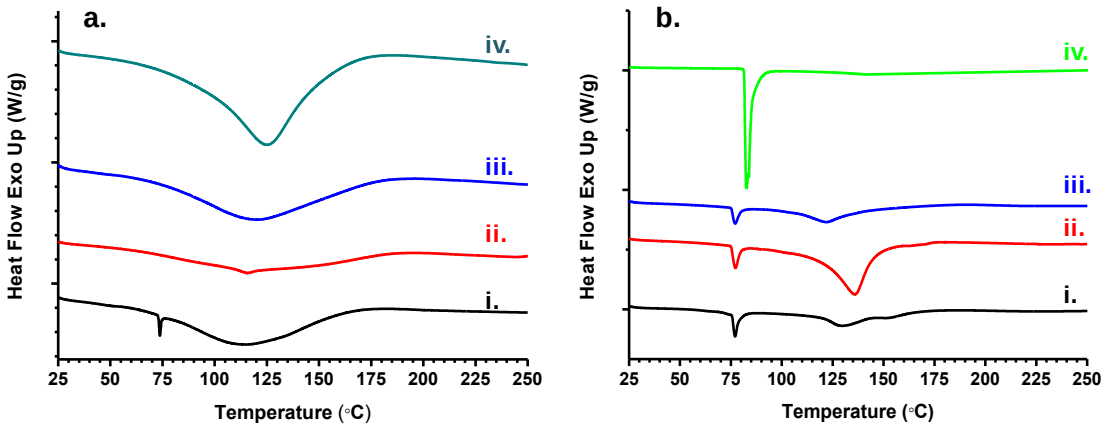

Figure 16. DSC thermograms of (a) (i) vanillin/α-CD-IC, (ii) vanillin/β-CD-IC, (iii) vanillin/γ-CD-IC, and (iv) vanillin/γ-CD-IC (co-precipitation) and (b) (i) vanillin/α-CD physical mixture (ii) vanillin/β-CD physical mixture (iii) vanillin/γ-CD physical mixture (iv) vanillin. (Copyright © 2011, American Chemical Society. Reprinted with permission from Ref. [70])

For CD-IC, the thermal stability and the evaporation of the volatile guest molecules shift to higher temperature upon inclusion complexation due to guest-host interactions [85, 234]. Hence, TGA was carried out for vanillin/CD-IC to determine the thermal stability and evaporation of the vanillin included inside the CD cavities (Figure 17). The TGAs of vanillin/CD physical mixtures and pure vanillin were also performed for comparison (Figure 17). The TGA thermogram of pure vanillin has a major weight loss observed in the range of 80-200 ^{o}C, showing that vanillin has a volatile nature. TGA thermograms of vanillin/CD-IC showed three weight losses; the initial weight loss below 100 ^{o}C is due to water loss, the second weight loss between 150 and 300 ^{o}C is due to the evaporation/degradation of vanillin, and the major weight loss above 300 ^{o}C corresponds to the main thermal degradation of CD. The TGA thermograms of vanillin/CD-IC showed that thermal degradation of vanillin occurred over a much higher temperature range (150-300 ^{o}C) when compared to pure vanillin (80-200 ^{o}C), confirming that the thermal stability of vanillin increased due to the inclusion complexation with CD. For vanillin/CD physical mixtures, three weight losses were observed: the one below 100 ^{o}C is attributed to removal of water and the second one in the range of 80-200 ^{o}C corresponds to the evaporation of vanillin, and the one above 300 ^{o}C is due to the main thermal degradation of CD. The temperature range for evaporation of vanillin for vanillin/CD physical mixtures is similar to pure vanillin. However, in the case of vanillin/CD-IC, the thermal stability of vanillin shifted to a much higher temperature owing to the strong interactions between vanillin and CD cavity in the CD-IC.

The amount of vanillin was calculated for solid vanillin/CD-IC samples from the TGA data. For vanillin/β-CD-IC, the amount of vanillin was ~11% (w/w, with respect to β-CD), which correlates the initial amount of vanillin used for the complexation. This corresponds to a 1:1 molar ratio complexation between the β-CD and vanillin, correlating with the NMR data; the initial amount of vanillin was preserved and no loss of guest molecule occurred during the formation and storage of vanillin/β-CD-IC. The amount of vanillin was calculated as ~10% (w/w, with respect to γ-CD) for both vanillin/γ-CD-IC samples obtained by freeze-drying and co-precipitation method. Similar to vanillin/β-CD-IC, vanillin/γ-CD-IC samples have

also a 1:1 molar ratio complexation between the γ-CD and vanillin as observed in the NMR study, and the initial amount of vanillin was preserved during the formation and storage of these samples. In the case of vanillin/α-CD-IC, the amount of vanillin was calculated as ~8% (w/w, with respect to CD) which is lower than the initial weight % (~13%, w/w). As DSC and XRD data confirmed, some uncomplexed vanillin was present in the sample and it is likely that free vanillin could not be preserved during the storage of vanillin/α-CD-IC sample.

The temperature stability and release characteristics of vanillin/CD-IC were also studied by headspace GC-MS. The vanillin/CD physical mixtures were also analyzed for comparison. The release of the vanillin from each sample was quantified from the corrected peak area calculated at 8.76 min from each chromatogram. The relative release of vanillin at different incubation temperatures (35, 50, 75 and 100 ^{o}C) was calculated by dividing the corrected peak areas obtained at different temperatures with the one obtained at 35 °C for each sample. The relative release of the vanillin with increasing temperature is summarized in Table 2. It is evident that the release of vanillin was much slower for vanillin/CD-IC at all temperatures when compared to the vanillin/CD physical mixtures. In addition, it was observed that as the temperature was increased, the relative amount of vanillin released was in the order vanillin/α-CD > vanillin/β-CD > vanillin/γ-CD for CD-IC samples, indicating that the strength of interaction between vanillin and the CD cavity was in the order γ-CD > β-CD > α-CD. Moreover, in the case of vanillin/γ-CD-IC, it was noted that co-precipitation method was more effective for the stabilization and sustained release of vanillin at high temperature (100 ^{o}C) when compared to the freeze-drying method. In the co-precipitation method, the vanillin/γ-CD IC sample was washed several times to remove uncomplexed and/or loosely complexed vanillin; however, the vanillin/γ-CD IC sample obtained by the freeze-drying method may contain some amount of loosely complexed vanillin, and this may be why CD IC prepared by the co-precipitation method were more effective for the stabilization of vanillin at high temperature.

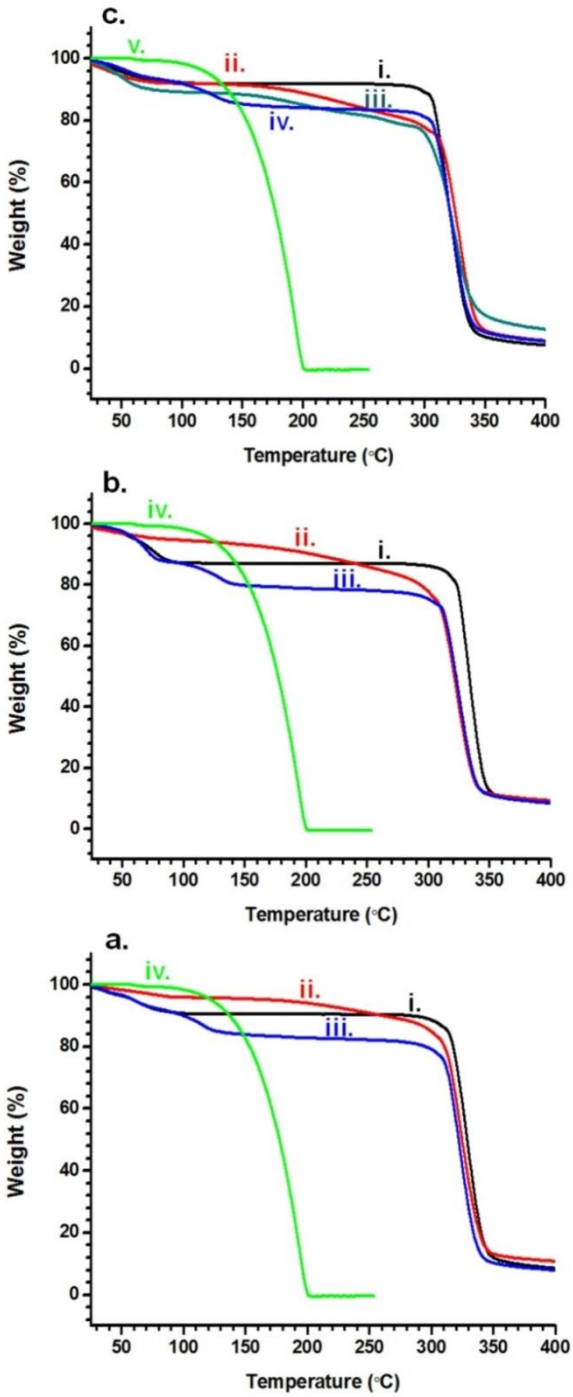

Figure 17. TGA thermograms of (a) (i) α-CD (ii) vanillin/α-CD-IC (iii) vanillin/α-CD physical mixture (iv) vanillin; (b) (i) β-CD, (ii) vanillin/β-CD-IC, (iii) vanillin/β-CD physical mixture, and (iv) vanillin; and (c) (i) γ-CD, (ii) vanillin/γ-CD-IC, (iii) vanillin/γ-CD-IC (co-precipitation), (iv) vanillin/γ-CD physical mixture, and (v) vanillin. (Copyright © 2011, American Chemical Society. Reprinted with permission from Ref. [70])

Table 2. Corrected peak areas[a] calculated at 8.76 min from headspace GC-MS chromatograms for vanillin/CD-IC and vanillin/CD physical mixtures agitated at different incubation temperatures. (Copyright © 2011, American Chemical Society. Reprinted with permission from Ref. [70])

Samples	35 °C	50 °C	75 °C	100 °C
vanillin/α-CD-IC	× 1	× 52	× 736	× 3002
vanillin/α-CD physical mixture	× 1	× 75	× 981	× 4898
vanillin/β-CD-IC	× 1	× 11	× 108	× 1119
vanillin/β-CD physical mixture	× 1	× 41	× 519	× 2083
vanillin/γ-CD-IC	× 1	× 10	× 51	× 912
vanillin/γ-CD-IC (co-precipitation)	× 1	× 10	× 63	× 283
vanillin/γ-CD physical mixture	× 1	× 45	× 385	× 1486

[a] All of the peak area values were divided by the peak area obtained at 35°C for each sample.

In short, the headspace GC-MS studies showed that the temperature release profile of vanillin was different for each CD-IC sample and highly dependent on the type of CD. The reason for the formation of a more stable inclusion complex between vanillin and γ-CD is possibly because of the bigger cavity size of γ-CD, resulting in a better fit and size match between the vanillin molecule and the γ-CD cavity.

2.2.1.3. Conclusions

In conclusion, the formation of solid CD-IC was successfully achieved between vanillin and three types of CD (α-CD, β-CD and γ-CD). The inclusion complexation of vanillin with β-CD and γ-CD having a 1:1 molar ratio was quite successful, whereas α-CD has shown poor complexation ability. Vanillin has a volatile nature; however, higher thermal stability and sustained release of vanillin at high temperatures were attained by forming vanillin/CD-IC. The thermal evaporation/degradation of vanillin shifted to a much higher temperature range (150-300 ^{o}C) for vanillin/CD-IC samples when compared to pure vanillin (80-200 ^{o}C) or vanillin/CD physical mixtures. Additionally, the headspace GC-MS analyses showed that the relative amount of vanillin released as a function of temperature was the

lowest for vanillin/γ-CD-IC and the highest for vanillin/α-CD-IC, suggesting that the strength of interaction between vanillin and the CD cavity was in the order γ-CD > β-CD > α-CD. In brief, CD-IC of a widely-used flavor/fragrance; vanillin, were achieved with improved thermal stability, and such solid vanillin/CD-IC can be quite applicable in food industry, active food packaging and textile industry, etc.

2.2.2. Encapsulation of Vanillin/Cyclodextrin Inclusion Complex in Electrospun Polyvinyl alcohol (PVA) Nanowebs: Prolonged Shelf-life and High Temperature Stability of Vanillin

2.2.2.1. Experimental

Materials: Polyvinyl alcohol (PVA) (M_w: 85,000–124,000, Aldrich, 87-89% hydrolyzed) and vanillin (99% purity, melting point: 81-83 ^oC, Sigma-Aldrich), deuterated dimethylsulfoxide (DMSO-d_6) (Merck, deuteration degree min. 99.8% for NMR spectroscopy) were used in this study. Cyclodextrins (α-CD, β-CD, and γ-CD) were purchased from Wacker Chemie AG, Germany. All materials were used without any purification. The water was from Millipore Milli-Q ultrapure water system.

Preparation of the solutions: The inclusion complexes (IC) of vanillin with α-CD, β-CD, and γ-CD were prepared by mixing equimolar (1:1 molar ratio) amount of vanillin with CD in water. In the solutions, the vanillin content was 5% (w/w) with respect to the PVA content and the CD amount was adjusted to 32% (w/w) for α-CD, 37% (w/w) for β-CD and 43% (w/w) for γ-CD, with respect to PVA. The α-CD and γ-CD were dissolved in water at room temperature whereas β-CD was dissolved in water at 75 °C for 5 min because of its low water solubility, and then, the vanillin was added to the aqueous solutions of CD. After mixing the solutions overnight at room temperature, the vanillin/α-CD solution became slightly turbid, the vanillin/β-CD solution became clear and the vanillin/γ-CD solution became highly turbid. PVA solutions were prepared separately by mixing PVA pellets in water for 2 h at 75 °C,

and the solutions were cooled down to room temperature. Then, the vanillin/α-CD and vanillin/γ-CD-IC solutions were added to the polymer solutions and stirred for additional 4 h at room temperature. On the other hand, total water amount was used to dissolve β-CD so PVA pellets were directly added to vanillin/β-CD-IC aqueous solution and stirred 2 h at 75 °C. In all cases, the PVA concentration was 12% (w/v, with respect to solvent (water)) in PVA/vanillin/CD-IC solutions. PVA/vanillin/CD-IC nanofibers were subsequently electrospun from the resultant solutions at room temperature. For comparison, we also have electrospun nanofibers from the solution of PVA and PVA/vanillin without CD.

Electrospinning: The prepared solutions were loaded individually in a 3 mL syringe. The syringe (needle inner diameter = 0.8 mm) was fixed horizontally on the syringe pump (Model: KDS 101, KD Scientific, USA) and the solutions were electrospun by using high voltage power supply (AU Series, Matsusada Precision, Japan). The electrospinning of the solutions was performed at the following parameters; applied voltage = 15 kV, tip-to-collector distance = 10 cm and the solution flow rate = 1 mL/h. A grounded stationary cylindrical metal collector covered by a piece of aluminum foil was used as a collector for the fiber deposition. The electrospinning setup was enclosed in Plexiglas box and the electrospinning was carried out at 24 ^{o}C at 30 % relative humidity. The nanowebs were dried at room temperature in the suction hood for 24 h in order to let the uncomplexed vanilllin evaporate if any present.

Measurements and characterization: The viscosity of the solutions was measured with rheometer (Physica MCR 301, Anton Paar) equipped with a cone/plate accessory (spindle type CP 40-2) at a constant shear rate of 100 s^{-1} at 22 ^{o}C. The conductivity of the solutions was measured with Multiparameter meter InoLab® Multi 720 (WTW) at room temperature. The morphology and the fiber diameter of the electrospun nanofibers were analyzed by scanning electron microscope (SEM) (Quanta 200 FEG, FEI). The nanofiber samples were coated with 5 nm Au/Pd (PECS-682) prior to SEM imaging. The average fiber diameter (AFD) for the samples was calculated by analyzing around 100 fibers from the SEM images.

The X-ray diffraction (XRD) (PANalyticalX'Pert Powder diffractometer) data for the CD, nanowebs and vanillin were collected by using Cu Kα radiation in a range of 2θ = 5- 30^{o}. Thermal properties of the samples were investigated by using differential scanning calorimeter (DSC) (Q2000, TA Instruments) and thermogravimetric analyzer (TGA) (Q500, TA Instruments). For DSC analyses, the samples were initially equilibrated at 25 ^{o}C and then heated to 250 ^{o}C at a 20 ^{o}C/min heating rate under nitrogen gas. TGA measurements were performed for electrospun nanowebs after 1 day of their storage. The TGA data were recorded from room temperature to 600 ^{o}C at a heating rate of 20 ^{o}C/min under nitrogen atmosphere. The proton nuclear magnetic resonance (^{1}H-NMR) (DPX-400, Bruker) spectra were recorded at 400 MHz at 25 °C. About 20 g/L nanoweb sample was dissolved in DMSO-d_6 in order to determine the presence of vanillin in the nanoweb samples.

Stability test: PVA/vanillin and PVA/vanillin/CD-IC nanowebs were stored in the open air in the laboratory (22 ^{o}C at 25 % relative humidity) for a certain period of time. After 1 day and 8 days of their storage, small samples of nanowebs were analyzed by TGA in order to determine the amount of the remaining vanillin in the samples. The amount of vanillin present in the nanowebs was calculated from the TGA data, that is, the % weight loss took place between 80-175 ^{o}C and 100-200 ^{o}C in TGA thermogram of PVA/vanillin and PVA/vanillin/α-CD-IC and PVA/vanillin/β-CD-IC was considered as the % weight of vanillin present in the samples, respectively. In the case of PVA/vanillin/γ-CD-IC, the weight loss was continuous between 125 and 250 ^{o}C, therefore, the calculation of the % weight of vanillin was kind of difficult since there was an overlapping of PVA degradation as well starting from 250 ^{o}C, so, to be on the safe side, % weight loss took place up to 240 ^{o}C was considered as the % weight of vanillin present in this sample.

The nanowebs were also analyzed by TGA after 50 days of their storage, but, the weight loss between 80 and 225 ^{o}C was insignificant and the interpretation of the TGA data was difficult. Therefore, the presence of vanillin in the nanowebs after 50 days of their storage was detected by ^{1}H-NMR studies. The quantity of vanillin in the nanowebs was calculated by integrating the peak ratio of the characteristic chemical

shifts corresponding to vanillin and CD. The integration of the CD peak at 5.8 ppm and vanillin peak at 9.8 ppm were taken into account in order to calculate the stoichiometry of the vanillin and the CD molecules in the nanowebs. The % weight of vanillin in the nanowebs was calculated from the molar stoichiometry between the vanillin and the CD determined from the ^{1}H-NMR spectra. It was assumed that the initial amount of CD was preserved before and after the electrospinning, that is, the amount of CD in the PVA solution before the electrospinning was considered same as the amount of CD in the PVA nanowebs after the electrospinning.

2.2.2.2. Results and Discussion

In this study, encapsulation of vanillin/CD-IC in PVA nanoweb was achieved via electrospinning technique. PVA nanofiber matrix was chosen since PVA is a biodegradable and non-toxic synthetic polymer, and PVA is applicable in food packaging [235-237]. Several studies have also shown that PVA has good electrospinnability in which drugs [238], enzymes [239] or nanoparticles [240] can be easily incorporated in electrospun PVA nanofibers.

The PVA nanofibers containing vanillin/α-CD-IC, vanillin/β-CD-IC and vanillin/γ-CD-IC were electrospun from the aqueous solution mixture of PVA and vanillin/CD-IC. For a comparison study, PVA and PVA/vanillin nanofibers without CD were also electrospun. The representative SEM images and the fiber diameter distribution along with AFD of pure PVA, PVA/vanillin and PVA/vanillin/CD-IC nanowebs are depicted in Figure 18. Uniform and bead-free nanofibers were obtained from PVA, PVA/vanillin PVA/vanillin/α-CD-IC and PVA/vanillin/β-CD-IC systems. In the case of PVA/vanillin/γ-CD-IC nanoweb, the nanofibers were mostly uniform, but, in some areas, it was observed that aggregates of vanillin/γ-CD-IC crystals were present and distributed in the fiber matrix. Mostly, the fiber diameters were between 100 and 250 nm for all the samples, yet, small variations were observed among the samples. The variations of the fiber diameters observed for the nanofibers are possibly owing to differences in viscosity and conductivity of the solutions, hence, we have investigated the rheological behavior and conductivity of the solutions. Table 3 summarizes the solution properties and AFD of the electrospun

nanofibers. PVA/vanillin/CD-IC solutions have shown higher viscosity when compared to pure PVA solution which was possibly due to the interactions between the PVA polymer chains and the CD molecules. Similarly, the viscosity of the PVA/vanillin was higher than pure PVA solution. The conductivity of PVA/vanillin/CD-IC and PVA/vanillin solutions was lower than the PVA solution. In general, higher solution viscosity and lower solution conductivity resulted in less stretching of the electrified jet and therefore thicker nanofibers were obtained in electrospinning [241-242]. For PVA/vanillin system, slightly thicker fibers were obtained when compared to pure PVA system because of the higher solution viscosity and lower solution conductivity. In the case of PVA/vanillin/CD-IC systems, the solutions have higher viscosity and lower conductivity compared to pure PVA solution, yet, fiber diameters of PVA, PVA/vanillin/α-CD-IC and PVA/vanillin/β-CD-IC were very similar to each other and thinner fibers were obtained from PVA/vanillin/γ-CD-IC. This result seems to contradict with the general observation for the electrospinning, but, PVA/vanillin/CD-IC solutions were rather inhomogeneous and complex when compared to PVA homopolymer solution and we observed that the electrospinning of these solutions did not follow the general trend observed in electrospinning in terms of fiber diameter thickness.

Table 3. The solution properties and AFD of the resulting electrospun nanofibers. (Copyright © 2012, Elsevier. Reprinted with permission from Ref.[202])

Solutions	Viscosity (Pa·s)	Conductivity (μS/cm)	AFD (nm)
PVA	0.157	798	185 ± 50
PVA/vanillin	0.662	784	245 ± 45
PVA/vanillin/α-CD-IC	0.233	667	180 ± 35
PVA/vanillin/β-CD-IC	0.588	489	190 ± 40
PVA/vanillin/γ-CD-IC	0.192	536	140 ± 20

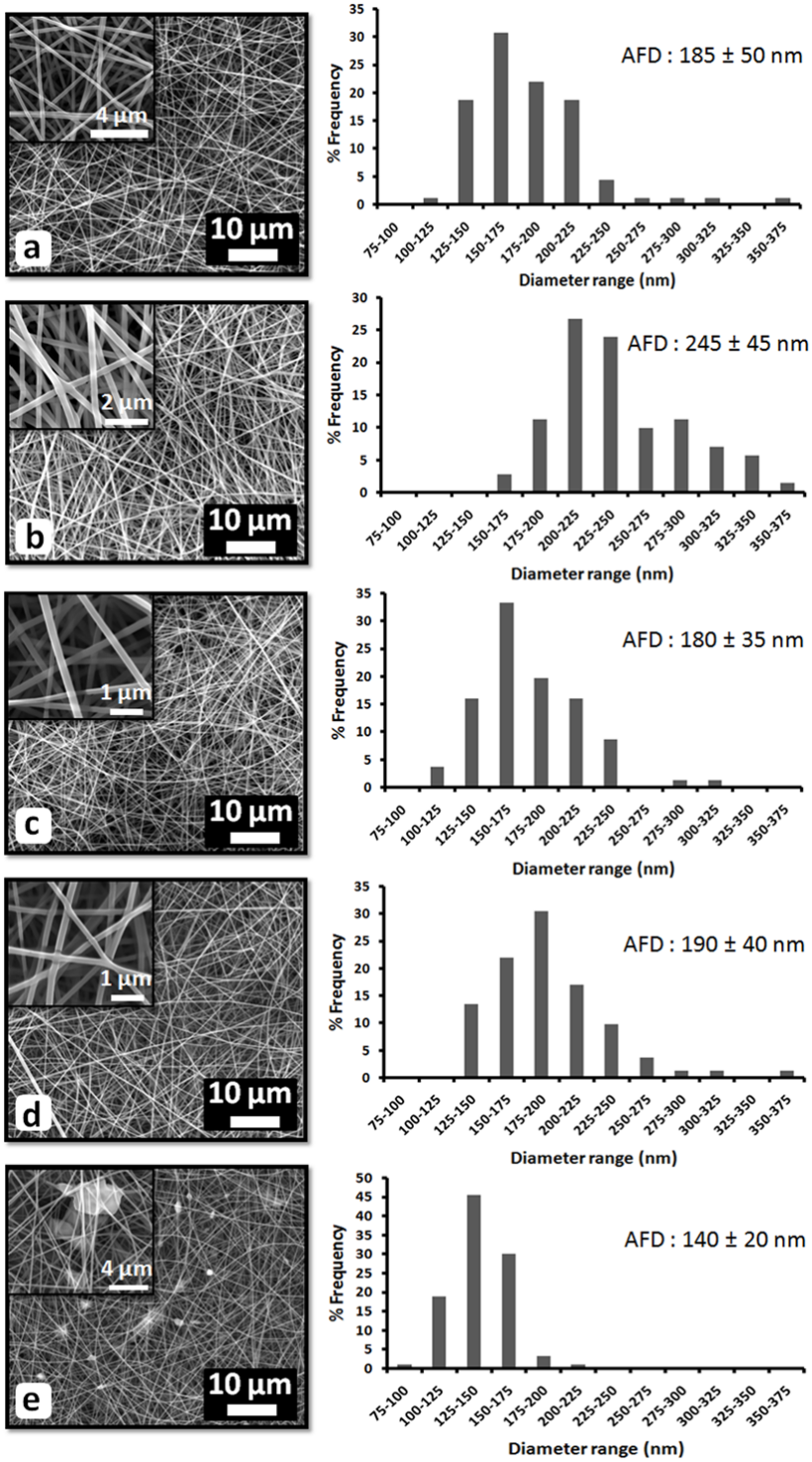

Figure 18. SEM images and fiber diameter distribution of the electrospun nanowebs obtained from solutions of (a) PVA, (b) PVA/vanillin, (c) PVA/vanillin/α-CD-IC (d) PVA/vanillin/β-CD-IC and (e) PVA/vanillin/γ-CD-IC. The insets show the high magnification images. (Copyright © 2012, Elsevier. Reprinted with permission from Ref.[202])

The XRD patterns of as-received CD, pure vanillin powder and the nanowebs of PVA, PVA/vanillin and PVA/vanillin/CD-IC are depicted in Figure 19a and b. Vanillin is a crystalline material having a sharp diffraction peak centered at $2\theta \cong 13^{o}$. The electrospun PVA nanoweb has a semi-crystalline nature showing a broad diffraction pattern centered at $2\theta \cong 20^{o}$. The XRD pattern of PVA/vanillin nanoweb is very similar to PVA nanoweb having a broad diffraction pattern and no diffraction peak for crystalline vanillin was observed suggesting that vanillin molecules were distributed in the fiber matrix without any crystalline aggregates.

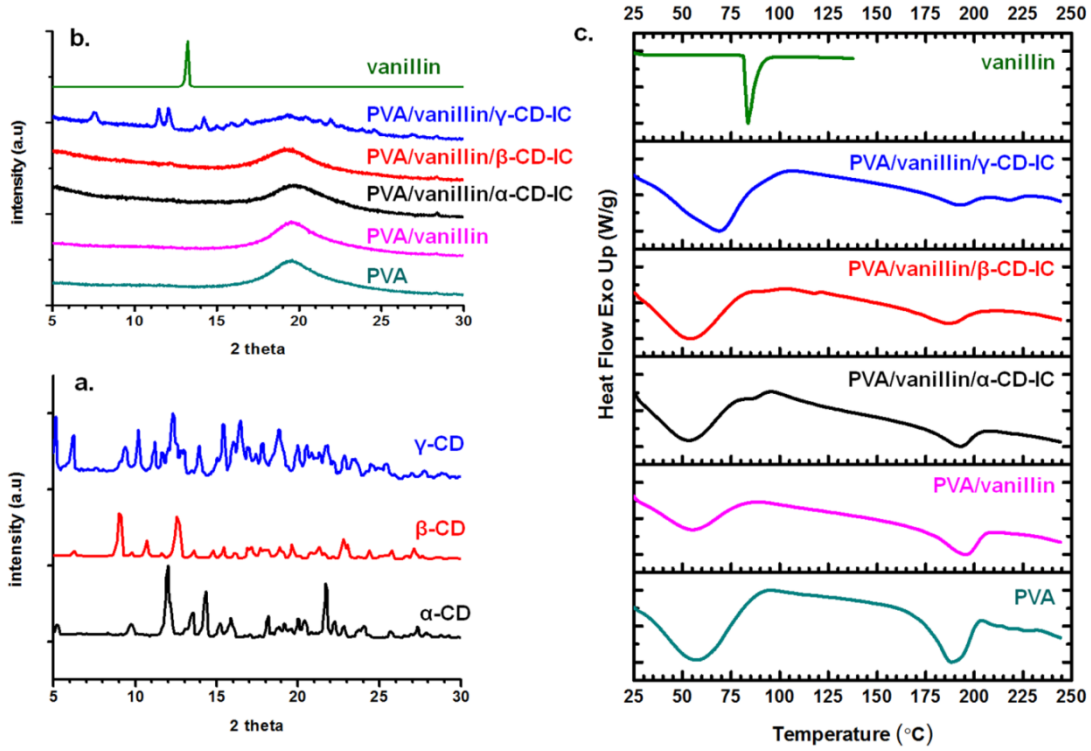

Figure 19. XRD patterns of (a) as-received CD, (b) vanillin and the electrospun nanowebs, (c) DSC thermograms of vanillin and the electrospun nanowebs. (Copyright © 2012, Elsevier. Reprinted with permission from Ref.[202])

The XRD patterns of PVA/vanillin/CD-IC nanowebs have broad diffraction centered at $2\theta \cong 20^{o}$ due to the PVA indicating that the presence of CD-IC did not significantly affect the semi-crystalline nature of the PVA matrix. In the XRD patterns of CD-IC, the diffraction peaks for the guest molecules would be absent

since the guest molecules would reside in the CD cavity and they are separated from each other by the CD molecules and therefore, they cannot form crystals [227]. For PVA/vanillin/CD-IC nanowebs, no diffraction peak for crystalline vanillin was observed in the XRD patterns suggesting that vanillin was complexed with CD or even there may be some free vanillin present in the nanowebs, the uncomplexed vanillin should be present without crystalline aggregates as in the case of PVA/vanillin nanoweb.

The as-received CD (α-CD, β-CD, and γ-CD) are crystalline materials having cage-type packing structure [227] and have characteristic diffraction peaks in the range of 2θ = 5-30° (Figure 19a). However, PVA/vanillin/α-CD-IC and PVA/vanillin/β-CD-IC nanowebs have shown no diffraction peaks for CD suggesting that vanillin/CD-IC were dispersed in the PVA nanofiber matrix without forming any crystalline aggregates. The SEM images of PVA/vanillin/α-CD-IC and PVA/vanillin/β-CD-IC nanofibers were also smooth showing no sign of CD-IC aggregates, and consequently, the SEM findings correlates with the XRD data. In the case of PVA/vanillin/γ-CD-IC nanoweb, the diffraction peaks at $2\theta \cong$ 7.5°, 11°, 12°, 14°, 17° and 22° were observed elucidating that channel-type packing structure [233] of vanillin/γ-CD-IC was present in the PVA nanofiber matrix. The inclusion complexation is generally confirmed by the formation of channel-type arrangement of the CD molecules in which CD molecules are aligned and stacked on top of each other by forming cylindrical channels [227]. As discussed above, these crystalline vanillin/γ-CD-IC aggregates were also clearly observed in the SEM images of the nanoweb. In brief, the XRD studies of PVA/vanillin/CD-IC nanowebs reveal the incorporation of vanillin/CD-IC in PVA nanofiber matrix for γ-CD since CD molecules adopt channel-type packing structures. However, in the case of α-CD and β-CD no distinct XRD diffraction patterns were observed for any type of CD crystal aggregates, for that reason, XRD did not give any valid information for the presence of vanillin/CD-IC in these samples, however, as discussed below, the thermal characterizations of these nanowebs revealed the presence of vanillin/CD-IC in PVA nanofiber matrix.

The thermal properties of the PVA/vanillin and PVA/vanillin/CD-IC nanowebs were investigated by the DSC studies (Figure 19c). The DSC studies for pure vanillin and PVA nanoweb were also performed for comparison. The DSC thermogram of pure vanillin has shown a main endothermic peak at around 82 ^{o}C which corresponds to the melting point of vanillin. PVA nanoweb has shown a broad endothermic peak between 30 and 100 ^{o}C due to loss of water and an endothermic peak at around 188 ^{o}C corresponding to the melting temperature of PVA itself. The DSC thermograms of PVA/vanillin and PVA/vanillin/CD-IC nanowebs are similar to PVA nanowebs showing water loss between 30 and 100 ^{o}C and a melting peak of polymer matrix at around 192 ^{o}C. There is a slight shift of T_m to higher temperature for PVA/vanillin/CD-IC and PVA/vanillin nanowebs and this is possibly because of the interactions between the polymer matrix and CD and vanillin.

Typically, for CD-IC, the thermal transitions such as the melting point for guest molecule could not be observed when they are included inside the CD cavity [70, 232, 243]. The DSC thermograms of the PVA/vanillin/CD-IC nanowebs did not show any significant melting peak for vanillin, except, DSC thermogram of PVA/vanillin/α-CD-IC has shown small endothermic peak at around 80 ^{o}C which may be due to presence of some free vanillin in this sample. So, the absence of vanillin melting peak in DSC of PVA/vanillin/β-CD-IC and PVA/vanillin/γ-CD-IC nanowebs could be because the vanillin was fully complexed with the CD. Even there was any uncomplexed vanillin in PVA/vanillin/CD-IC nanowebs, the vanillin was present without any crystalline aggregation. In the case of PVA/vanillin nanoweb, the DSC thermogram also did not show any melting peak for vanillin suggesting that the vanillin molecules were dispersed in the fiber matrix without any crystalline aggregation. In short, The DSC data correlates with the XRD data as discussed in the previous section where the vanillin was mostly present in the PVA fiber matrix without any crystal aggregates for PVA/vanillin and PVA/vanillin/CD-IC nanowebs.

Thermogravimetric analysis (TGA) is a useful technique in order to investigate the volatility and thermal stability of fragrances/flavors. Here, we have

investigated the thermal characteristics of vanillin present in PVA/vanillin and PVA/vanillin/CD-IC nanowebs (Figure 20a). The TGA studies were also performed for pure vanillin and PVA nanoweb for comparison. In the TGA thermogram of pure vanillin, the weight loss was started at around 80 ^{o}C showing an onset point at around 150 ^{o}C indicating that vanillin has a volatile nature. The main thermal degradation of PVA nanoweb started at around 250 ^{o}C. TGA thermogram of PVA/vanillin showed three weight losses; the initial weight loss below 100 ^{o}C is due to water loss, the second weight loss between 80 and 175 ^{o}C is due to the evaporation of vanillin, and the major weight loss started at around 250 ^{o}C corresponds to the main thermal degradation of PVA. For PVA/vanillin/α-CD-IC nanoweb, water loss below 100 ^{o}C, weight loss between 100 and 190 ^{o}C due to vanillin evaporation and the major weight loss started around 270 ^{o}C corresponding to the main degradation of PVA and CD were observed. In the TGA thermogram of PVA/vanillin/β-CD-IC nanoweb, the weight loss due to the vanillin evaporation was observed between 100-180 ^{o}C. In the case of PVA/vanillin/γ-CD-IC nanoweb, the weight loss was continuous between 125 and 250 ^{o}C indicating that the release of vanillin occurred at much higher temperature range. It was noted that the main degradation temperature of PVA shifted to slightly higher temperature with the presence of CD which may be because of the hydrogen bonding interaction between the hydroxyl groups of CD and PVA and this may resulted in higher thermal stability for PVA. More importantly, the thermal stability of vanillin in PVA/vanillin/CD-IC nanowebs was shifted to higher temperature when compared to PVA/vanillin nanoweb. In CD-IC, the thermal evaporation of the volatile guest molecules shifts to higher temperatures due to the interactions with the CD cavity [70, 244], and as anticipated, enhanced thermal stability for vanillin was observed for PVA/vanillin/CD-IC nanowebs due to the complexation between vanillin and CD.

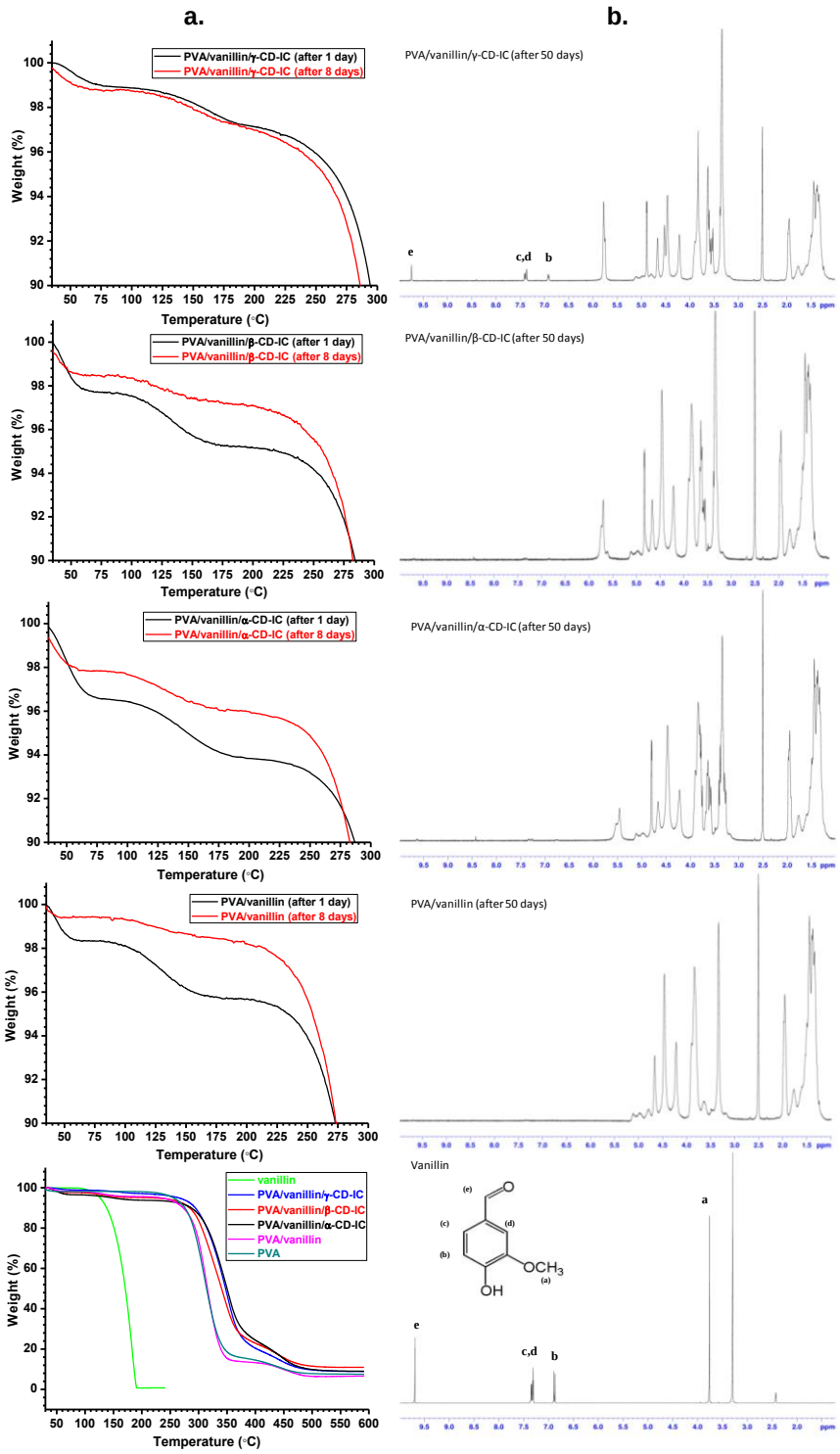

Figure 20. (a) TGA thermograms of the electrospun nanowebs after 1 and 8 days of storage period, (b) ^{1}H-NMR solution spectra of vanillin and the electrospun nanoweb samples dissolved in DMSO-d_6 after 50 days of storage. (Copyright © 2012, Elsevier. Reprinted with permission from Ref.[202])

The loss of vanillin was observed at slightly higher temperature for PVA/vanillin/α-CD-IC and PVA/vanillin/β-CD-IC nanowebs when compared to PVA/vanillin nanoweb suggesting that the interaction between vanillin and α-CD or β-CD is not that strong. However, in the case of PVA/vanillin/γ-CD-IC nanoweb, the loss of vanillin was observed at higher temperature range (between 125 and 250 ^{o}C) indicating that the interaction between vanillin and γ-CD was much stronger compared to α-CD and β-CD.

The durability of vanillin in PVA/vanillin and PVA/vanillin/CD-IC nanowebs was also studied. At different storage time periods; after 1, 8 and 50 days of storage of the nanowebs at room temperature, the TGA and NMR studies were performed in order to determine the remaining amount of the vanillin in the nanowebs. Table 4 summarizes the initial amount of vanillin in the PVA solutions before the electrospinning and remaining amount of vanillin in the nanowebs after certain days. For PVA/vanillin, around ~45% of the vanillin was evaporated after the first day of nanoweb production. The loss of vanillin could take place both during the electrospinning of PVA/vanillin solution and during the storage of the nanoweb. After the 8 days of storage, only about ~20% of the vanillin was left in PVA/vanillin nanoweb indicating that PVA nanoweb without CD-IC could not preserve volatile vanillin.

Table 4. Initial amount of vanillin in the solutions and remaining amount of vanillin in the nanowebs after certain days obtained by TGA and NMR results. (Copyright © 2012, Elsevier. Reprinted with permission from Ref.[202])

Samples	% weight of vanillin (% weight loss of vanillin)			
	initial	after 1 day[a]	after 8 days[a]	after 50 days[b]
PVA/vanillin	4.76 (0 %)	2.65 (44 %)	0.92 (81 %)	-
PVA/vanillin/α-CD-IC	3.65 (0 %)	2.65 (27 %)	1.48 (60 %)	-
PVA/vanillin/β-CD-IC	3.52 (0 %)	2.41 (32 %)	1.19 (66 %)	-
PVA/vanillin/γ-CD-IC	3.39 (0 %)	2.97 (12 %)	2.71 (20 %)	~1.98 (42 %)

a Measured by TGA

b Measured by NMR

In the case of PVA/vanillin/CD-IC nanowebs, the preservation of vanillin was very effective compared to PVA/vanillin nanoweb. For PVA/vanillin/α-CD-IC nanoweb, the loss of vanillin (with respect to initial amount of vanillin) was ~25% and ~60% after 1 day and 8 days of storage, respectively. For PVA/vanillin/β-CD-IC nanoweb, the loss of vanillin amount was ~30% and ~65% after 1 day and 8 days of storage, respectively. In the case of PVA/vanillin/γ-CD-IC nanoweb, the loss of vanillin amount was minimal when compared to PVA/vanillin/α-CD-IC and PVA/vanillin/β-CD-IC nanowebs which was ~10% and ~20% after 1 day and 8 days of storage, respectively. TGA results indicated that γ-CD was more effective for stabilization of vanillin when compared to α-CD and β-CD. The reason for forming more stable IC between vanillin and γ-CD is possibly because of the bigger cavity size of γ-CD resulting better fit and size match between the guest molecule and the host CD cavity. This also correlates with our recent findings where γ-CD forms more stable IC with vanillin in the solid state [70].

We have also analyzed the nanowebs by TGA after 50 days of their storage, but, the weight loss between 80 and 225 ^{o}C was insignificant and the analyses of the TGA data was rather difficult. Therefore, we performed ^{1}H-NMR studies to check the presence of vanillin in the nanowebs after 50 days of their storage (Figure 20b). Vanillin was not detected for PVA/vanillin nanoweb indicating that the all the vanillin was evaporated from the sample after 50 days of storage. For PVA/vanillin/α-CD-IC and PVA/vanillin/β-CD-IC nanowebs, trace amount of vanillin was detected but since the intensity of the vanillin peaks were very weak, we were unable to integrate the peaks and therefore could not able to calculate the amount of vanillin in the sample. In the case of PVA/vanillin/γ-CD-IC nanoweb, the vanillin peak was present and the molar ratio of vanillin to γ-CD was calculated as 1:1.7 which corresponds that the amount of vanillin was around 1.98 % weight of the total sample. This corresponds to ~40% loss of vanillin from PVA/vanillin/γ-CD-IC nanoweb after 50 days of its storage. The initial amount of vanillin was about ~3.4% and ~60% of the vanillin was remaining in the nanoweb after 50 days of its storage. This finding elucidates that PVA/vanillin/γ-CD-IC nanoweb is quite effective for the prolonged durability of vanillin. In short, our studies showed that high temperature

stability and prolonged shelf-life of vanillin was achieved PVA/vanillin/CD-IC nanowebs whereas vanillin in PVA nanoweb without CD-IC could not be preserved effectively. In addition, we observed that the prolonged shelf-life of vanillin was highly dependent on the type of CD; γ-CD was more effective for stabilization of vanillin over longer time period when compared to α-CD and β-CD.

2.2.2.3. Conclusions

PVA nanowebs incorporating vanillin/CD-IC were successfully produced via electrospinning technique with the goal to obtain functional nanowebs containing flavor/fragrance molecules with enhanced thermal stability and durability. Three types of CD; α-CD, β-CD and γ-CD were used for the formation of vanillin/CD-IC and these vanillin/CD-IC were encapsulated in electrospun PVA nanowebs. Vanillin has a volatile nature; however, higher thermal stability and prolonged shelf-life for vanillin were attained for PVA/vanillin/CD-IC nanowebs whereas PVA nanoweb without the CD-IC could not efficiently preserve the vanillin. The thermal evaporation/degradation of vanillin shifted to higher temperature for PVA/vanillin/CD-IC nanowebs when compared to PVA/vanillin. In addition, we observed that the PVA/vanillin/CD-IC nanowebs are quite effective for the prolonged shelf-life of vanillin. For PVA/vanillin/γ-CD-IC nanoweb, the loss of vanillin amount was minimal when compared to PVA/vanillin/α-CD-IC and PVA/vanillin/β-CD-IC nanowebs and about 60% of the initial amount of vanillin was preserved after 50 days of storage. This reveals that the durability of vanillin was significantly dependent on the CD type, that is, γ-CD was much more effective for stabilization of vanillin over longer time period when compared to α-CD and β-CD.

In brief, vanillin/CD-IC was encapsulated in electrospun PVA nanofibers and higher thermal stability and prolonged shelf-life was achieved for vanillin. Vanillin is a widely-used flavor/fragrance; therefore, PVA/vanillin/CD-IC nanowebs can be quite applicable in food industry, active food packaging and textile industry, etc. Moreover, our results should be of interest to food, biomedical, textile and personal care industries since CD-IC functionalized nanowebs may have practical applications

depending on the type the functional components used such as flavors, antimicrobials, antioxidants, drugs, and bioactive agents, etc.

2.3. Enhanced Thermal Stability of Eugenol by Cyclodextrin Inclusion Complex Encapsulated in Electrospun Polymeric Nanofibers

2.3.1. Experimental

Materials: Polyvinyl alcohol (PVA, 88 % hydrolyzed, M_w: 125,000 g/mol, SP^2-Scientific Polymer Products) and eugenol (EG, 99% purity, Sigma-Aldrich), deuterated dimethylsulfoxide (DMSO-d_6, deuteration degree min. 99.8% for NMR spectroscopy, Merck) were used in this study. Cyclodextrins (α-CD, β-CD, and γ-CD) were purchased from Wacker Chemie AG. All materials were used without any purification. The water was from Millipore Milli-Q ultrapure water system.

Preparation of the solutions: 1:1 molar ratio of EG with CD (α-CD, β-CD, and γ-CD) was used to prepare the inclusion complexes (IC) of EG. Firstly, α-CD (0.158 g, 1.6×10^{-4} mol) and γ-CD (0.21 g, 1.6×10^{-4} mol) were dissolved in 1.1 and 0.9 mL of water, respectively, at room temperature for 10 minutes. The amount of water used for these solutions was determined according to the solubility of CD in water at 25 °C, that is, 14.5 and 23.2 g/100 mL for α-CD and γ-CD, respectively.[29] On the other hand, β-CD (0.185 g, 1.6×10^{-4} mol) was dissolved in 2 mL water at 75 °C for 10 minutes because of its lower water solubility (1.85g/100 mL) compared to other CD types.[29] Then EG (24 μL, 0.026 g, 1.6×10^{-4} mol) was added to each clear CD aqueous solution. After mixing the solutions overnight at room temperature, EG/β-CD-IC and EG/γ-CD-IC solutions became highly turbid due to the formation and suspension of solid IC (Figure 21a). On the other hand, EG/α-CD solution was clear and yellow EG molecules were visibly observed (Figure 21a), indicating that the IC

could not be formed between EG and α-CD under the chosen experimental conditions and the solvent system.

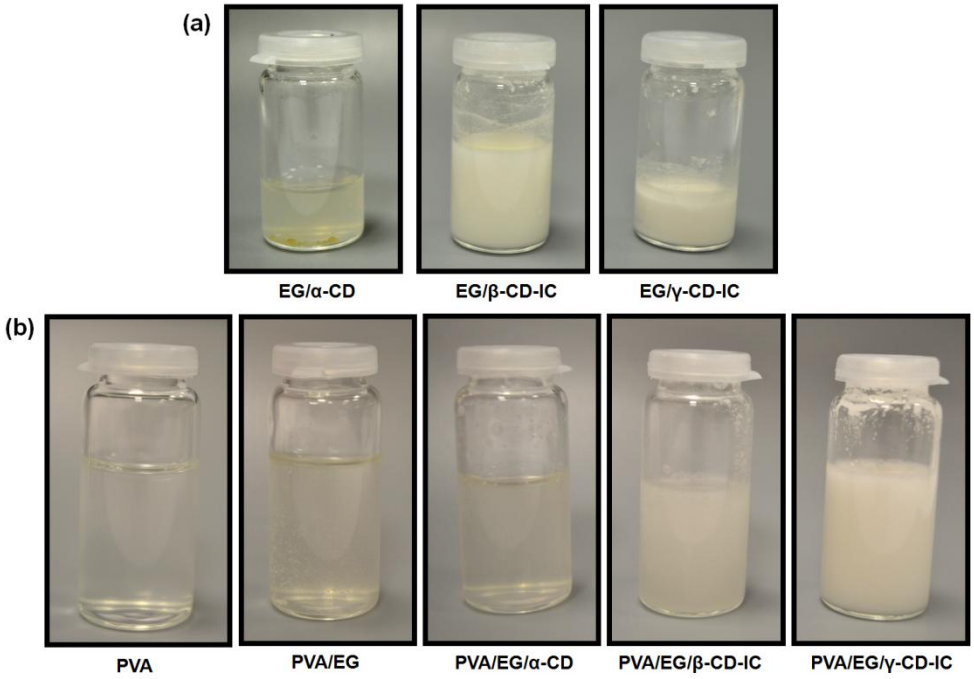

Figure 21. The phographs of the solutions of (a) EG/α-CD, EG/β-CD-IC and EG/γ-CD-IC, (b) PVA, PVA/EG, PVA/EG/α-CD, PVA/EG/β-CD-IC and PVA/EG/γ-CD-IC. (Copyright © 2013, American Chemical Society. Reprinted with permission from Ref.[199])

Afterwards, PVA solutions were prepared by mixing PVA pellets in water for 2 h at 75 °C, and the solutions were left at room temperature to cool down. After that, PVA solutions were mixed with EG/α-CD, EG/β-CD-IC and EG/γ-CD-IC solutions, individually and stirred for additional 2 h at room temperature. PVA/EG/α-CD solution was clear, whereas the solutions of PVA/EG/β-CD-IC and PVA/EG/γ-CD-IC were turbid, indicating solid EG/β-CD-IC and EG/γ-CD-IC were suspended in aqueous PVA solutions. In addition, we also prepared solutions of PVA and PVA/EG without CD for comparison. The photographs of resulting solutions are given in Figure 21b. For all solutions, the PVA concentration was kept 12% (w/v) with respect to solvent (water). The EG amount in the solutions was 5% (w/w), and

the amount of CD was adjusted to 33% (w/w) for α-CD, 39% (w/w) for β-CD and 44% (w/w) for γ-CD, with respect to PVA.

PVA/γ-CD solution was also prepared by using the same ratio to investigate the possible complexation of PVA with γ-CD. Firstly, PVA solution was prepared by mixing PVA pellets (12% (w/v) with respect to solvent (water)) in water for 2 h at 75 °C, and the solution was left at room temperature to cool down. Then, 44% (w/w) γ-CD with respect to PVA was added into this PVA solution. After mixing the solution overnight at room temperature, PVA/γ-CD solution became clear. Thereafter, PVA/γ-CD solution, were frozen at -80 ^{o}C and then lyophilized in a freeze dryer (Labconco) in order to obtain solid PVA/γ-CD.

Electrospinning: First, each solution was placed in a 3 mL syringe having metallic needle with 0.8 inner diameter. The syringe was positioned horizontally on the syringe pump (KD Scientific, KDS 101) and the electrode of the high voltage power supply (Spellman, SL Series) was clamped to the metallic needle tip. The electrospinning parameters were adjusted as 15 kV applied voltage, 10 cm of tip-to-collector distance and 1 mL/h flow rate of the solution. Electrospun nanofibers were deposited on the grounded stationary cylindrical collector covered by a piece of aluminum foil. Electrospinning was performed at 23 ^{o}C and at 18 % relative humidity in an enclosed Plexiglas box. Finally, the resulting electrospun nanofibers were left in the suction hood at room temperature for 24 h in order to allow the evaporation of uncomplexed EG if any exist.

Characterization and measurements: Rheometer (Physica MCR 301, Anton Paar) equipped with a cone/plate accessory (spindle type CP 40-2) was used at a constant shear rate of 100 1/sec, at 22 ^{o}C to measure the viscosity of the solutions. The conductivity of the solutions was measured with Multiparameter meter InoLab® Multi 720 (WTW) at room temperature. Scanning electron microscope (SEM, Quanta 200 FEG, FEI) was used to analyze the morphology and fiber diameter of the electrospun nanofibers. Before SEM imaging, nanofiber samples were coated with 5 nm Au/Pd (PECS- 682). The average fiber diameter (AFD) of the each sample was calculated by analyzing around 100 fibers from the SEM images. Fourier transform

infrared (FTIR) spectroscopy (Bruker-VERTEX 70) was used in order to examine the existence of EG in the electrospun nanowebs. For FTIR analyses, the pellets were prepared by blending a piece of sample with potassium bromide and then applying high pressure. The FTIR spectra were recorded with a resolution of 4 cm^{-1} from 400 to 4000 cm^{-1} of scanning wavenumber by taking 64 scans for each sample. The proton nuclear magnetic resonance (^{1}H-NMR, DPX-400, Bruker) spectra were recorded for about 20 g/L of the samples dissolved in DMSO-d_6 at 400 MHz and 25 °C to confirm the presence of EG in the electrospun nanowebs and to determine the molar stoichiometry of EG/CD. Integration of the resonance peaks given in parts per million (ppm) of the samples was calculated by using NMR software. The X-ray diffraction (XRD, PANalyticalX'Pert Powder diffractometer) measurements were carried out by using Cu Kα radiation in a range of $2\theta=5^o$-30^o to investigate the crystalline structure of the samples. Thermogravimetric analyzer (TGA, Q500, TA Instruments) was used to investigate the thermal properties of the samples. The TGA analysis was performed at a 20 ^{o}C/min heating rate by starting from room temperature to 300 ^{o}C for EG and to 550 ^{o}C for the nanowebs under nitrogen gas.

The release characteristic of EG from the nanofibers were investigated by headspace gas chromatography-mass spectrometry (GC-MS) analyses that were carried out by using Agilent Technologies 7890A gas chromatography coupled to an Agilent Technologies 5975C inert MSD with a triple-axis detector. The headspace GC-MS experiments were performed with a CTCPAL auto sampler by placing 16,6 mg of each nanoweb to 20 mL of headspace glass vials, and top of the all vials were firmly closed to avoid the escape of EG. The incubation temperature was determined as 50 ^{o}C, 75 ^{o}C and 100 ^{o}C and each sample was shaken sequentially at this temperature for 30 min at 250 rpm by using an agitator. Headspace injector (MSH 02-00B, volume = 2.5 mL, scale = 60 mm) injected 1 mL of the vapor of the samples to the GC-MS. HP-5MS (Hewlett- Packard, Avondale, PA) capillary column with 30 m×0.25 mm inner diameter and 0.25 μm film thickness was used for the separation of compounds. The temperature of the column first was kept at 70 ^{o}C for 2 min and then raised to 230 ^{o}C at the rate of 20 ^{o}C/min. Finally it was equilibrated at this temperature for 3 min. In these measurements, helium was used as a carrier gas at a

flow rate of 1.2 mL/min. Splitless mode was used in thermal desorption. Ion source and the transfer line temperatures were adjusted to 230 ^{o}C and 280 ^{o}C, respectively. The GC-MS analyses were performed in the complete scanning mode (SCAN) in the 50-550 mass range and the characteristic EG peak was determined by comparing its obtained mass spectrum with the EG spectrum in the Flavor 2 library. The peak areas of the major peak of EG having 164.1 mass over charge were identified. The experiment was repeated three times for each sample (PVA/EG, PVA/EG/α-CD, PVA/EG/β-CD-IC and PVA/EG/γ-CD-IC nanofibers) to determine standard deviation.

2.3.3. Results and Discussion

In this study, eugenol/CD-IC solutions (EG/β-CD-IC and EG/γ-CD-IC) including suspended solid IC (Figure 21a) were mixed with polyvinyl alcohol (PVA) solutions. Then, PVA nanofibers encapsulating EG/β-CD-IC and EG/γ-CD-IC were successfully obtained from the resulting solutions (Figure 21b) via electrospinning technique.

On the other hand, EG did not form IC with α-CD under the applied experimental conditions, therefore yellow EG molecules were clearly observed in EG/α-CD solution (Figure 21a). However EG/α-CD solution was also mixed with PVA solution, and we obtained PVA nanofibers incorporating EG/α-CD mixture for a comparison study. We also produced electrospun nanofibers of PVA, PVA/EG without CD-IC for comparison. Figure 22 shows the representative SEM images and the fiber diameter distributions with AFD of PVA, PVA/EG, PVA/EG/α-CD, PVA/EG/β-CD-IC and PVA/EG/γ-CD-IC nanofibers. The electrospun nanofibers of PVA, PVA/EG and PVA/EG/α-CD were uniform. However, the aggregates of EG/β-CD-IC and EG/γ-CD-IC crystals were present and randomly distributed in PVA fiber matrix in PVA/EG/β-CD-IC and PVA/EG/γ-CD-IC samples. The variations of fiber diameters were observed among the samples possibly due to differences in viscosity and conductivity of the solutions. Table 5 summarizes the properties of the solutions and the morphological characteristics of the resulting electrospun nanofibers with their AFD and fiber diameter ranges. The viscosity of the PVA/EG, PVA/EG/α-CD,

PVA/EG/β-CD-IC and PVA/EG/γ-CD-IC solutions was higher than pure PVA solution possibly due to the interactions between the PVA polymer chains and the EG and CD molecules. On the other hand, PVA/EG, PVA/EG/α-CD and PVA/EG/β-CD-IC and PVA/EG/γ-CD-IC solutions showed lower conductivity than that of the PVA solution. Both higher viscosity and lower conductivity of the solutions generally result in less stretching of the electrified jet and therefore thicker nanofibers are obtained in electrospinning [7, 10, 242]. As anticipated, slightly thicker nanofibers having fiber diameter around 500 nm were obtained for PVA/EG, PVA/EG/α-CD PVA/EG/β-CD-IC and PVA/EG/γ-CD-IC systems when compared to pristine PVA nanofibers having AFD of 360±50 nm owing to the higher solution viscosity and lower solution conductivity. Although PVA/EG solution had the highest viscosity, slightly thinner nanofibers were obtained compared to PVA nanofibers containing CD, since the conductivity of the PVA/EG solution was higher than that of PVA/EG/CD solutions. Moreover, the thickest nanofibers were obtained from PVA/EG/β-CD-IC system having lowest conductivity, since the polymer solution is being less stretched as a result of the less repulsion of the charges present at the surface. In brief, these findings are parallel with the general observation for electrospinning where viscosity and conductivity of the solutions are the key parameters to affect the fiber diameters of the electrospun nanofibers [7, 10, 242].

Table 5. The properties of the solutions used for electrospinning and morphological characteristics of the resulting electrospun nanofibers.

Solutions	Viscosity (Pa·s)	Conductivity (μS/cm)	AFD (nm)	Fiber diameter range (nm)
PVA	0.66	638	360±50	240-480
PVA/EG	1.78	618	440±90	210-860
PVA/EG/α-CD	1.25	584	520±120	310-930
PVA/EG/β-CD-IC	1.13	538	610±110	270-1140
PVA/EG/γ-CD-IC	1.10	578	540±150	310-1170

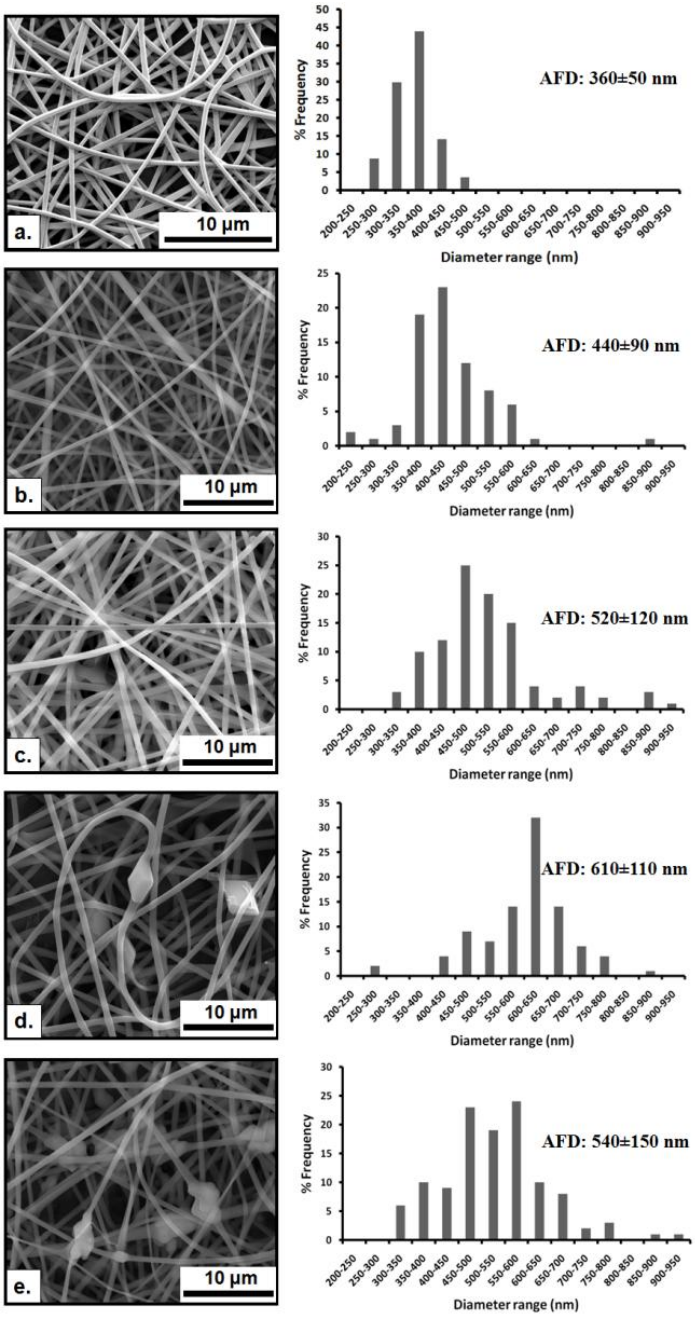

Figure 22. SEM images and fiber diameter distributions with average fiber diameters (AFD) of the electrospun nanofibers obtained from solutions of (a) PVA, (b) PVA/EG, (c) PVA/EG/α-CD, (d) PVA/EG/β-CD-IC and (e) PVA-EG/γ-CD-IC. (Copyright © 2013, American Chemical Society. Reprinted with permission from Ref.[199])

The FTIR spectra of β-CD, EG and the nanofibers are depicted in Figure 23a. Since FTIR spectra of three native CD are similar, just β-CD is given as an example. The FTIR spectrum of EG has characteristic peaks in the region of 720-1640 cm^{-1}

assigned to C=C region and aromatic ring present in EG [245-246]. In the FTIR spectrum of β-CD, the characteristic absorption peaks of CD were observed at around 1024, 1076, and 1153 cm^{-1} assigned to the coupled C-C/C-O stretching vibrations and the asymmetric stretching vibration of the C-O-C glycosidic bridge [70]. The broad absorption band in the region of 1000-1140 cm^{-1} in the FTIR spectra of PVA and PVA/EG nanofibers correspond to the stretching vibration of C–O and C–O–C groups in PVA [247]. This region becomes sharper for PVA/EG/α-CD, PVA/EG/β-CD-IC and PVA/EG/γ-CD-IC nanofibers especially due to the presence of distinct characteristic peaks of CD in the same region. These peaks confirmed the existence of CD in these nanofibers.

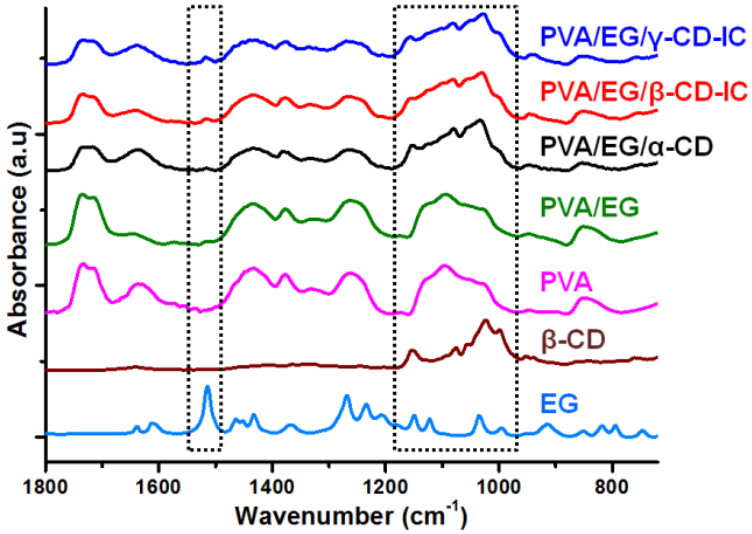

Figure 23. FTIR spectra of EG, β-CD and the electrospun nanofibers. (Copyright © 2013, American Chemical Society. Reprinted with permission from Ref.[199])

The overlapping of absorption peaks of PVA, CD and EG makes the identification of the individual compounds rather complicated in the spectra of the nanofibers. However, the sharpest absorption peak of EG at about 1514 cm^{-1} which is corresponding to C=C stretching of the aromatic moiety was observed for all nanofibers except for pure PVA nanofibers. This confirmed the presence of the EG in the PVA/EG, PVA/EG/α-CD and PVA/EG/β-CD-IC and PVA/EG/γ-CD-IC nanofiber samples. Moreover, it was noted that the characteristic peak of EG at 1514 cm^{-1} was shifted to 1517 cm^{-1} for PVA/EG/β-CD-IC and PVA/EG/γ-CD-IC

nanofibers, whereas no shift was observed in the case of PVA/EG and PVA/EG/α-CD nanofibers. The FTIR peak shift for the guest molecules is generally reported for the CD-IC systems due to the interaction between host CD cavity and guest molecules [201, 231]. Here, our FTIR data suggested that the host-guest interactions were present between host CD (β-CD and γ-CD) and EG which confirmed the inclusion complexation [248].

The presence of the EG and CD in the nanofibers was also confirmed by the ^{1}H-NMR studies of the samples (Figure 24). We performed ^{1}H-NMR study to calculate the ratio of EG/CD in the nanofibers by integrating the peak ratio of the characteristic resonances corresponding to EG and CD. For this calculation, the evident peaks for EG at about 6.7 and 6.6 ppm (H-c,f,e) [249] which are not overlapped with the peaks of PVA and CD, were chosen. The intensity of these EG peaks were very weak in the NMR spectrum of PVA/EG nanofibers so the integration of the EG peaks was not possible. This finding indicated that the most of EG evaporated from this sample during the electrospinning of PVA/EG solution and/or during the storage of the nanofibers in suction hood for 24 hour. This result was also verified by the TGA studies as discussed in the following sections. On the other hand, the peaks of CD protons (OH-2,3) at about 5.5 ppm (α-CD) and 5.7 ppm (β-CD) [70] that are not overlapped with the peaks of PVA and EG were taken into account to calculate the ratio of EG and CD molecules in the nanofibers. However, the peak at about 5.8 ppm (OH-2,3) in the NMR spectrum of γ-CD overlaps with the EG peak at 5.9 ppm (H-h). Therefore, in order to determine the integration of the γ-CD peaks (OH-2,3), the integration of EG peak assigned to one proton was subtracted from the integration of this overlapped peak. As a result, it was found that EG/α-CD, EG/β-CD and EG/γ-CD have stoichiometric ratio as 0.4:1, 0.6:1 and 0.8:1, respectively, in the PVA nanofibers. The results suggested that the 1:1 initial molar ratio used for the electrospinning process was not conserved especially in the case of PVA/EG/α-CD containing uncomplexed EG. The highest amount of EG observed in PVA/EG/γ-CD-IC nanoweb indicated that γ-CD was the most favorable CD type for the complexation with higher amount of EG, possibly due to its proper and larger cavity size compared to α-CD and β-CD.

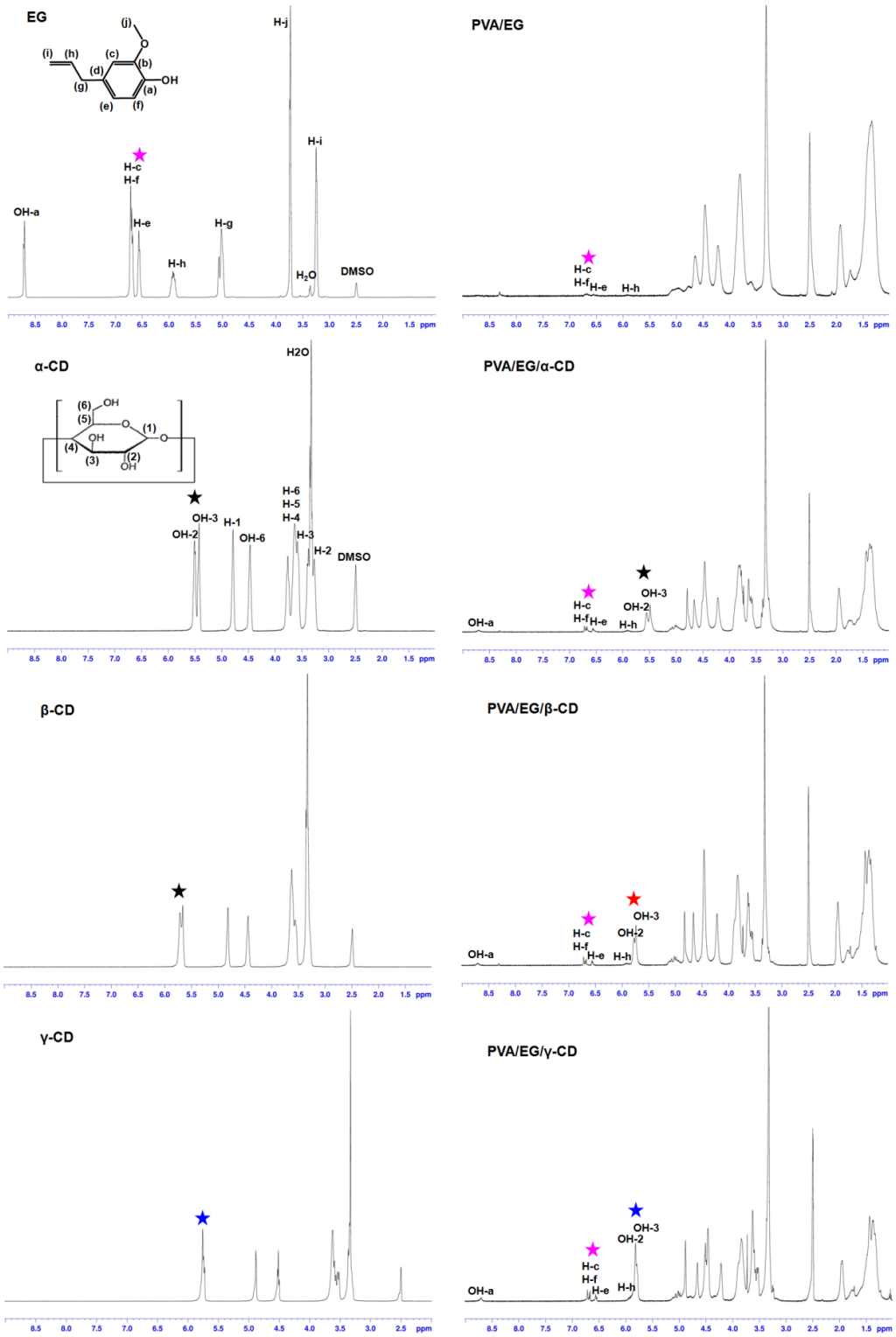

Figure 24. [1]H-NMR spectra of EG, CD and the electrospun nanofibers. (Protons used for calculation of EG/CD ratio, are shown by star sign; pink: EG, black: α-CD, red: β-CD, blue: γ-CD). (Copyright © 2013, American Chemical Society. Reprinted with permission from Ref.[199])

We have investigated the crystalline structures of the samples by using XRD. The XRD patterns of as-received CD are given in Figure 25a, and that of nanofibers are depicted in Figure 25b. The as-received crystalline CD (α-CD, β-CD, and γ-CD) have characteristic diffraction peaks in the range of 2θ=5-30° due to their cage-type packing structure as reported in the literature [228, 230]. PVA nanofibers represented a broad diffraction pattern centered at $2\theta \cong 20^{o}$ owing to its semi-crystalline nature. Similar broad diffraction pattern was also observed in the XRD pattern of PVA/EG nanofibers which indicated that EG molecules were distributed in the PVA nanofiber matrix without forming any phase separated crystal aggregates. The XRD pattern of PVA/EG/α-CD nanofibers had also broad diffraction centered at $2\theta \cong 20^{o}$, since EG/α-CD was dispersed in the PVA nanofiber matrix without forming any crystalline aggregates. Consequently, the XRD data correlates with SEM images of smooth PVA/EG and PVA/EG/α-CD nanofibers that showed no sign of EG or EG/α-CD aggregates. For the PVA/EG/β-CD-IC sample, the intense diffraction peak at $2\theta \cong 12^{o}$ in the XRD pattern indicated that channel-type packing structure of EG/β-CD-IC crystals [70, 197]was present in the PVA nanofiber matrix. In the case of PVA/EG/γ-CD-IC nanowebs, salient diffraction peaks at 2θ≅ 7.5°, 11°, 12° along with slightly intense diffraction peaks at 2θ≅14°, 17° and 22° were observed elucidating that channel-type crystals of EG/γ-CD-IC [70, 85, 230] were present in the PVA nanofiber matrix. The channel-type arrangement of the CD molecules in which CD molecules are aligned and stacked on top of each other by forming cylindrical channels is generally used to confirm the formation of IC [70, 85, 197, 227-228, 230]. The complexation of PVA with γ-CD that mentioned in the study of Hernandez et al. [250] is not valid in our system. Therefore, the cavities of γ-CD were not available to complex with PVA, since they had already formed IC with EG, and then mixed with PVA. Nevertheless we prepared solid PVA/γ-CD to investigate crystalline structure of it. The XRD pattern of solid PVA/γ-CD sample (data not shown) had broad diffraction centered at $2\theta \cong 20^{o}$, and we did not observe any characteristic peak of γ-CD, since γ-CD was dispersed in the PVA matrix without forming any crystalline aggregates. This result also confirmed the IC could not form between PVA and γ-CD, in our experimental conditions. As a result, XRD studies

revealed that EG/β-CD-IC and EG/γ-CD-IC channel-type crystals were encapsulated in PVA nanofiber matrix. As discussed above, these crystalline EG/β-CD-IC and EG/γ-CD-IC aggregates were also clearly observed in the SEM images of PVA/EG/β-CD-IC and PVA/EG/γ-CD-IC nanofibers.

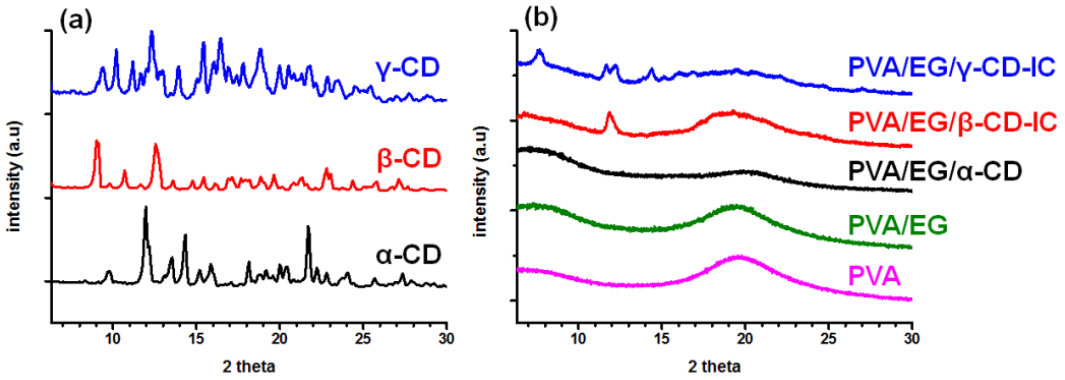

Figure 25. XRD patterns of (a) as-received CD and (b) the electrospun nanofibers. (Copyright © 2013, American Chemical Society. Reprinted with permission from Ref.[199])

The thermal stability of EG encapsulated in the PVA/EG, PVA/EG/α-CD, PVA/EG/β-CD-IC and PVA/EG/γ-CD-IC nanofibers was investigated by the thermogravimetric analyzer (TGA) (Figure 26). The TGA studies of pure EG and PVA nanofibers were also performed for comparison. In the TGA thermogram of pure EG, the weight loss was started at around 70 ^{o}C, and EG was completely evaporated before 200 ^{o}C which confirms its volatile nature. In the TGA thermogram of PVA nanofibers, the initial weight loss until 100 ^{o}C, and the major weight loss at above 250 ^{o}C were observed due to dehydration of water and thermal degradation of PVA, respectively. For PVA/EG nanofibers, three weight loss steps were recorded in the TGA thermograms; the initial weight loss is owing to water loss, the second weight loss around between 70-140 ^{o}C is due to the evaporation of EG, and the main weight loss started at around 250 ^{o}C corresponds to the main degradation of PVA. Although 5% (w/w, with respect to PVA) of EG was used for the preparation of all nanofiber samples, from the TGA data only 0.8% weight loss of EG (w/w, with respect to PVA) was observed in PVA/EG nanofibers. Therefore, around 85% of EG has already been lost during the electrospinning of PVA/EG solution and/or during the storage of the PVA/EG nanofibers in suction hood for 24 hour. As also

mentioned in the previous section, the integration of NMR peaks of EG in this sample even could not be calculated because of its low amount. The TGA thermogram of PVA/EG/α-CD nanofibers has shown three-step weight losses at comparable temperature range as PVA/EG nanofibers. The evaporation temperature of the EG in PVA/EG and PVA/EG/α-CD nanofibers was very similar to evaporation temperature of pure EG. It is known that the thermal degradation/evaporation of the volatile guest molecules shifts to higher temperatures in CD-IC owing to the interactions with the CD cavity [70, 234, 244]. Our result suggested that PVA nanofiber matrix could not enhance the thermal stability of EG without CD-IC, and so could not effectively preserve the EG at high temperature. Similar to PVA/EG, EG was in uncomplexed state in PVA/EG/α-CD nanofibers, therefore, the thermal stability of EG could not be improved. However, TGA thermogram of PVA/EG/α-CD nanofibers showed 2.45% weight loss of EG which corresponds to 33% (w/w) lost of EG from the initial amount used for this sample. Although α-CD and EG was not in the complex state, the remaining amount of EG in PVA/EG/α-CD nanofibers was much higher than the PVA/EG nanofibers. The presence of α-CD somehow preserve higher amount of EG in the nanofiber sample and this may be because of some interaction (maybe hydrogen bondings) between α-CD and EG.

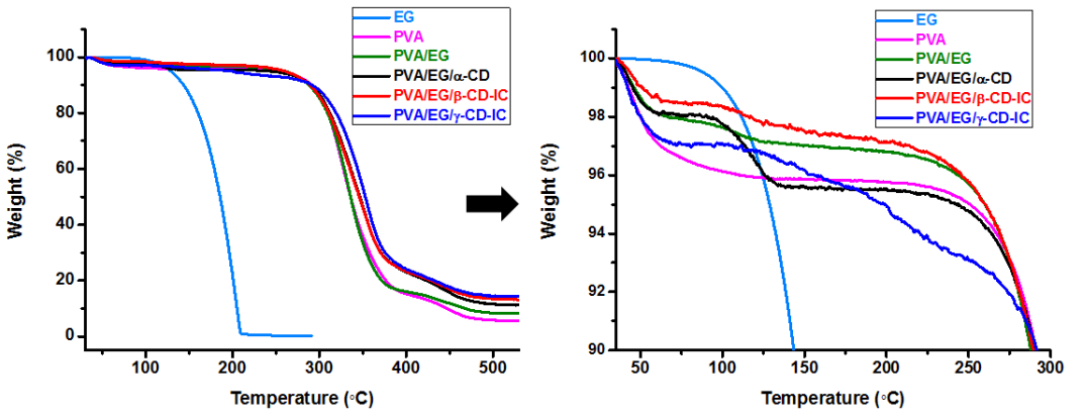

Figure 26. TGA thermograms of EG and the electrospun nanofibers. (Copyright © 2013, American Chemical Society. Reprinted with permission from Ref.[199])

On the other hand, higher thermal stability of EG was observed for PVA nanofibers incorporating EG/CD-IC compared to PVA/EG and PVA/EG/α-CD

nanofibers. For PVA/EG/β-CD-IC nanofibers, the weight loss of EG started at around 100 ^{o}C. In the case of PVA/EG/γ-CD-IC nanofibers, the weight loss of EG was observed up to 120 ^{o}C, elucidating that the thermal stability of EG was improved more significantly for this sample compared to PVA/EG/β-CD-IC. The higher thermal stability of EG in PVA/EG/γ-CD-IC nanofibers suggested that the strength of interaction between EG and the γ-CD cavity was stronger when compared to β-CD, as also confirmed by headspace GC-MS analyses discussed in the following section. Moreover, in PVA/EG/CD-IC samples, the evaporation of EG possibly continued above 250 ^{o}C where main degradation of CD and PVA started, and therefore, we could not use TGA thermograms for determining the actual weight content of EG in the PVA/EG/CD-IC (PVA/EG/β-CD-IC and PVA/EG/γ-CD-IC) nanofibers. So, as previously discussed, ^{1}H-NMR analyses were performed for calculation of actual EG content in these samples. However, as it seen in Figure 26, the % EG weight loss was higher for PVA/EG/γ-CD-IC compared to PVA/EG/β-CD-IC signifying that the amount of EG presented in this sample was higher, as also confirmed by ^{1}H-NMR analysis.

Headspace GC-MS technique was used to investigate the thermal stability and release characteristics of EG in the nanofibers. Therefore, the release ratio of EG at 50 ^{o}C, 75 ^{o}C and 100 ^{o}C from each sample was determined from the corrected area of the major peak of EG in each headspace GC-MS chromatogram, and the results are summarized in Figure 27. The headspace GC-MS analyses clearly showed that the amount of released EG is higher when the temperature increases from 50 ^{o}C to 100 ^{o}C. According to ^{1}H-NMR data, the relative amount of EG was in the order PVA/EG/γ-CD-IC > PVA/EG/β-CD-IC > PVA/EG/α-CD > PVA/EG. Both PVA/EG/α-CD and PVA/EG contain uncomplexed EG, but, the relative amount of released EG was higher for PVA/EG/α-CD compared to PVA/EG since the actual EG content presented in the PVA/EG/α-CD nanofibers was more than that of PVA/EG nanofibers as confirmed by ^{1}H-NMR and TGA data. Although PVA/EG/β-CD-IC nanofibers contain much higher amount of EG compared to PVA/EG, it was observed that the release of EG from PVA/EG/β-CD-IC sample was comparable to PVA/EG sample indicating that presence of EG/β-CD-IC in PVA nanofibers

enhanced the slow release of EG at higher temperature. In the case of PVA/EG/γ-CD-IC nanofibers, the least amount of EG was released although this sample has the highest amount of EG compare to other samples. The slow release of EG at each temperature from PVA/EG/γ-CD-IC nanofibers clearly showed that the enhanced durability and higher thermal stability was achieved for EG due to inclusion complexation with γ-CD. This elucidated that γ-CD is the most effective native CD type for the high temperature stabilization of EG in our systems. This finding was also correlated with the results of the TGA study. In short, the higher temperature stable IC was formed between EG and γ-CD. This is possibly due to bigger cavity size of γ-CD which resulting in a better fit and size match between the EG molecule and the γ-CD cavity. In short, both TGA and headspace GC-MS studies revealed that the CD-IC provided higher thermal stability and slow release of EG in the nanofibers, in addition, the choice of CD type is also important for better thermal stability of EG.

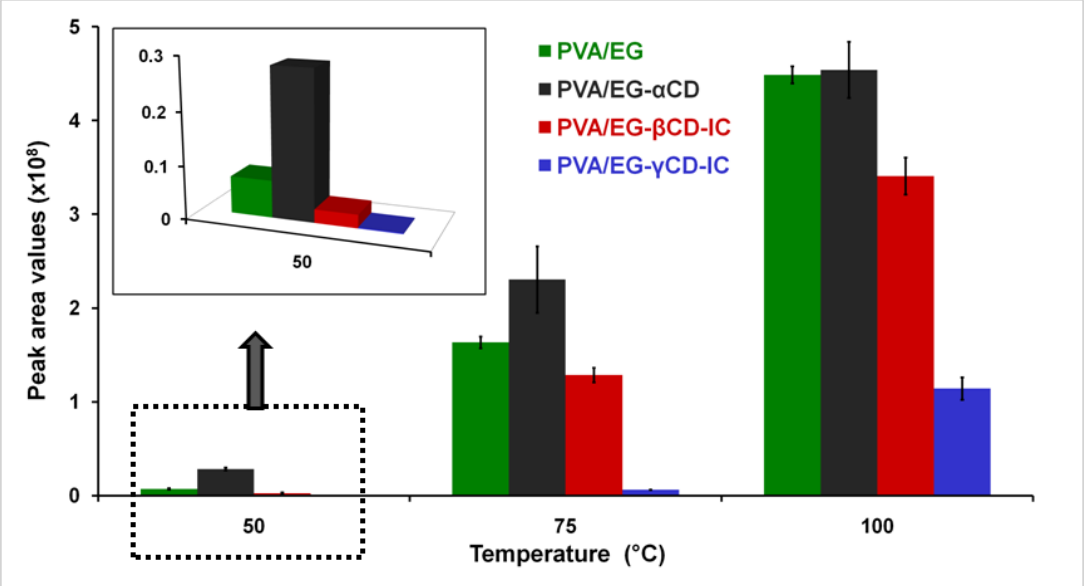

Figure 27. The peak areas of EG in headspace GC-MS chromatogram of electrospun nanofibers agitated at 50 °C, 75 °C and 100 °C for 30 min. (Copyright © 2013, American Chemical Society. Reprinted with permission from Ref.[199])

2.3.4. Conclusions

In conclusion, in order to obtain functional nanofibers/nanowebs containing EG with enhanced thermal stability and durability, PVA nanofibers encapsulating EG/CD-IC were successfully produced via electrospinning technique. Here, three types of CD; α-CD, β-CD and γ-CD were used for the formation of EG/CD-IC, and our results showed that the size/shape fit between the host CD and guest EG molecule is an important factor for forming inclusion complexation. EG could not be complexed with a small cavity size of α-CD. Hence, PVA nanofibers encapsulating EG only and EG/α-CD could not preserve the EG due to its high volatile nature. On the other hand, thermal evaporation of EG in PVA/EG/β-CD-IC and PVA/EG/γ-CD-IC nanofibers shifted to higher temperature when compared to pure EG, moreover, much slower release of EG at elevated temperature (50 ^{o}C, 75 ^{o}C and 100 ^{o}C) was achieved for PVA/EG/β-CD-IC and PVA/EG/γ-CD-IC nanofibers due to inclusion complexation. In addition, higher thermal stability and the slower release of EG was observed for PVA/EG/γ-CD-IC indicating that γ-CD was the most suitable host for EG when compared to α-CD and β-CD. EG is widely used bioactive compound as a fragrance and flavoring in food industry due to its antibacterial, antioxidant and antifungal properties, and so, these functional electrospun PVA nanofibers encapsulating EG/CD-IC and having very high surface area, nanoporous structure and the properties of EG/CD-IC may have practical application in food industry and active food packaging, etc.

2.4. Functional Electrospun Polymeric Nanofibers Incorporating Geraniol-Cyclodextrin Inclusion Complexes: High Thermal Stability and Enhanced Durability of Geraniol

2.4.1. Experimental

Materials: Cyclodextrins (α-CD, β-CD, and γ-CD, Wacker Chemie AG), geraniol (trans-3,7-dimethyl-2,6-octadien-1-ol, 98% purity, Sigma-Aldrich), polyvinyl alcohol (PVA, M_w: 85,000–124,000, 87-89% hydrolyzed, Sigma-Aldrich) and deuterated dimethylsulfoxide (DMSO-d_6, deuteration degree min. 99.8% for NMR spectroscopy, Merck) were used in this study without any purification. The water used as solvent was obtained from Millipore Milli-Q ultrapure water system.

Preparation of solid geraniol/cyclodextrin inclusion complexes (geraniol/CD-IC): The geraniol/CD-IC were prepared by co-precipitation method by using α-CD, β-CD, and γ-CD. Equimolar ratio (1:1) of geraniol with CD was used. First, 0.159 g (1.0×10^{-3} mol), 0.136 g (8.8×10^{-4} mol) and 0.119 g (7.7×10^{-4} mol) geraniol were dispersed in water, and then 1 g of α-CD (1.0×10^{-3} mol), β-CD (8.8×10^{-4} mol), and γ-CD (7.7×10^{-4} mol) were added in these geraniol dispersions, respectively. The amount of water used as solvent was determined according to the solubility of CD in water at 25 °C, that is, 14.5, 1.85 and 23.2 g/100 mL for α-CD, β-CD and γ-CD, respectively [58-59]. After mixing the solutions overnight at room temperature, the resulting three suspensions were filtered through a borosilicate filter (por. 3). Thereafter, the filtrates were washed with water several times in order to remove uncomplexed molecules if any present, and then dried overnight under the hood. Lastly, the resulting solid geraniol/CD-IC were crushed in a mortar to obtain fine powder.

Preparation of the electrospinning solutions: Among the three CD types, we observed that γ-CD has higher complexation efficiency with geraniol under the chosen experimental conditions; hence, we have selected geraniol/γ-CD-IC to

incorporate into PVA nanofibers via electrospinning technique. Firstly, 12% (w/v) PVA was dissolved in water by stirring for 2 h at 80°C, and the solution was left at room temperature to cool down. After that, geraniol/γ-CD-IC fine powder was dispersed in this polymer solution, and then the solution was stirred for additional 5 h at room temperature. The amount of geraniol/γ-CD-IC was adjusted as 50% (w/w), so as to include 5% (w/w) geraniol in the solution as regards the PVA content. For a comparison study, PVA and PVA/geraniol solutions without CD-IC were also prepared to obtain PVA and PVA/geraniol nanofibers. Table 6 summarizes the compositions of the solutions used for electrospinning.

Electrospinning: Each prepared solution was located in a 5 mL syringe having a metallic needle of 0.7 mm inner diameter, and the syringe was placed horizontally on the syringe pump (KD Scientific, KDS 101). The solutions were pumped with flow rate of 1 ml/h, and tip-to-collector distance was set to 10 cm. When voltage of 15 kV was applied by using high voltage power supply (Matsusada Precision, AU Series) to the metal needle, the nanofibers were deposited on the grounded stationary cylindrical metal collector (height: 15cm, diameter: 9 cm) covered with a piece of aluminum foil. The electrospinning was carried out at about 22 ^{o}C and 25% relative humidity in enclosed Plexiglas box. Then, the resulting nanofibers were kept in the suction hood at room temperature for 24 h to remove the residual solvent and uncomplexed geraniol if any present.

Characterization and measurements: The crystalline structures of the samples were investigated by X-ray diffraction (XRD, PANalyticalX'Pert Powder diffractometer) with Cu Kα radiation in a range of $2\theta=5^{o}$-30^{o}. About 20 g/L of the samples were dissolved in DMSO-d_6 for proton nuclear magnetic resonance (^{1}H-NMR, DPX-400, Bruker) study, and then ^{1}H-NMR spectra were recorded at 400 MHz and 25 °C. Thermogravimetric analyzer (TGA, Q500, TA Instruments) was used to investigate the thermal stability of geraniol, and the analyses were performed from room temperature to 250 ^{o}C (geraniol), 500 ^{o}C (γ-CD and geraniol/CD-IC) or 600 ^{o}C (electrospun nanofibers) at a 20 ^{o}C/min heating rate, with purge gas of N_2. Rheometer (Physica MCR 301, Anton Paar) equipped with a cone/plate accessory

(spindle type: CP 40-2) was used to measure the viscosity of the solutions used for electrospinning, at a constant shear rate of 100 s^{-1} and 22 ^{o}C. Scanning electron microscope (SEM, Quanta 200 FEG, FEI) was used to analyze the morphology and fiber diameter of the electrospun nanofibers that were sputtered with 5 nm Au/Pd (PECS-682) prior to SEM imaging. Average fiber diameter (AFD) of the samples was calculated by measuring around 100 fiber diameters of each sample.

Computational Method: The first-principles calculations based on density functional theory (DFT) [251-252] were performed by using the Vienna Ab initio simulation package [253-254]. The exchange-correlation was approximated within the generalized gradient approximation [255] with addition of Van der Waals correction [256]. The element potentials were described by projector augmented-wave method [257] using a plane-wave basis set with a kinetic energy cutoff of 500 eV. The initial structures of α-CD [258-259], β-CD [260], and γ-CD [261] were taken from Cambridge Structural Database [262]. All structures were relaxed using the Kosugi algorithm with simultaneous minimization of the total energy and interatomic forces. The convergence on the total energy and force was set to 10^{-5} eV and 10^{-2} eV/Å, respectively.

2.4.2. Results and Discussion

The co-precipitation method was applied to prepare the solid geraniol/CD-IC by using three types of native CD (α-CD, β-CD and γ-CD). Initially, the crystalline structures of the solid geraniol/CD-IC were investigated by XRD. The as-received CD were also analyzed by XRD for comparison. The characteristic diffraction patterns of as-received CD (Figure 28a) correspond to cage-type packing (Figure 14) [228, 230]. The channel-type packing in which CD molecules are aligned and stacked on top of each other, is generally observed for the IC, and therefore the presence of channel-type packing (Figure 14) is a strong evidence for the successful CD-IC formation [228, 230]. Here, we observed that the XRD patterns of geraniol/CD-IC (Figure 28b) are very different from that of as-received CD.

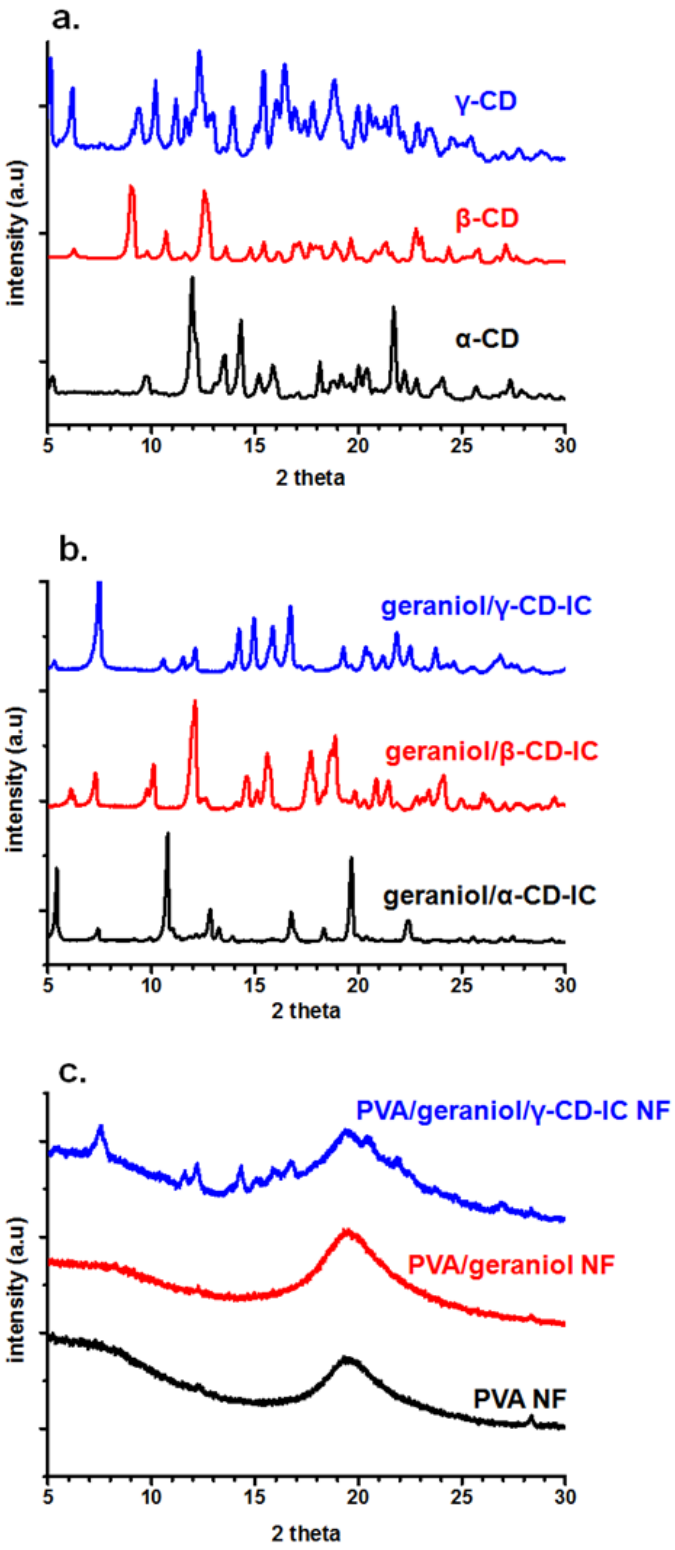

Figure 28. XRD patterns of (a) as-received CD, (b) geraniol/CD-IC and (c) the electrospun nanofibers (NF). (Copyright © 2014, Elsevier. Reprinted with permission from Ref.[200])

The distinct peak at 2θ≅19.7° in the XRD pattern of geraniol/α-CD-IC confirmed the channel-type packing of α-CD in this sample [70, 230]. In the case of geraniol/β-CD-IC, the XRD peaks at 2θ≅12° and 2θ≅17.7° were owing to channel-type packing of β-CD [70]. Furthermore, the characteristic peaks of tetragonal channel-type packing of γ-CD at 2θ≅7.6°, 14°, 15°, 15.9°, 16.7° and 21.9° were observed in the XRD pattern of geraniol/γ-CD-IC [85, 230]. As a result, channel-type packing of α-CD, β-CD, and γ-CD that were observed in the XRD patterns of solid geraniol/CD-IC confirmed that the inclusion complexation of geraniol with each type of CD was successful.

The thermal stability of geraniol in geraniol/CD-IC was investigated by TGA. The TGA thermograms of CD (γ-CD) and pure geraniol were also given for comparison (Figure 29a). The TGA data of α-CD and β-CD were not given, since the thermograms were quite similar to that of γ-CD. In TGA thermogram of γ-CD, initial weight loss at below 100 ^{o}C was due to water loss, and the major weight loss at around 300 ^{o}C corresponded to degradation of γ-CD. On the other hand, evaporation of pure geraniol was in the range of 70-230 ^{o}C as observed in its TGA thermogram. In the case of TGA thermogram of geraniol/CD-IC (Figure 29a), three steps of weigh losses were observed. That is, the initial water loss at below 100 ^{o}C and the main degradation of CD at 300 ^{o}C were recorded, additionally, the evaporation of geraniol complexed with CD was observed at above 120 ^{o}C till to 300 ^{o}C at which main degradation of CD occurred. The evaporation temperature of pure geraniol shifted from 70-230 ^{o}C to 120-300 ^{o}C when complexed with CD and this was due to the host-guest interaction in the CD-IC samples. The enhanced thermal stabilities of the guest molecules complexed with the CD cavities were also reported for other CD-IC systems [70, 234, 244]. In brief, the TGA data suggested the inclusion complexation of geraniol with α-CD, β-CD, and γ-CD. The evaporation temperature of geraniol in all three CD-IC samples was between 120-300 ^{o}C, and we did not see any significant difference among the CD-IC samples except for the % weight loss in this temperature range. It is possible that the evaporation of geraniol could continue above 300 ^{o}C where the main degradation of CD started. So, we did not use TGA thermograms for calculating the actual weight content of geraniol in the CD-IC,

instead, this was investigated by ^{1}H-NMR study as discussed in the following section.

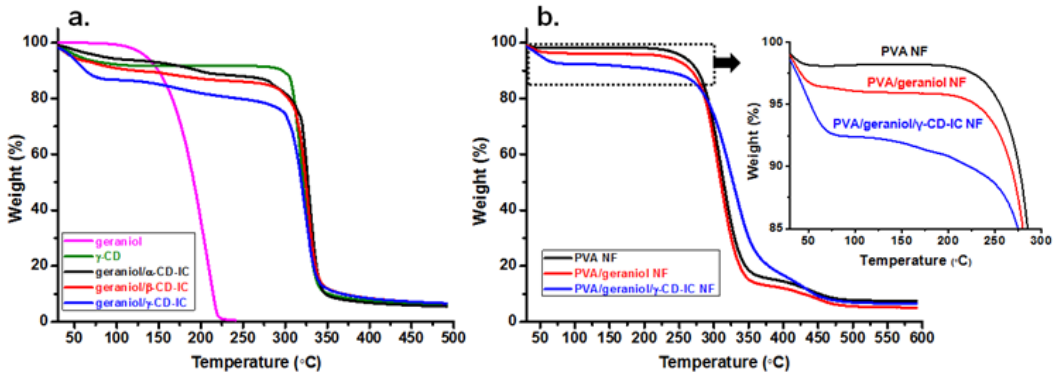

Figure 29. TGA thermograms of (a) geraniol, γ-CD, geraniol/CD-IC and (b) the electrospun nanofibers (NF). (Copyright © 2014, Elsevier. Reprinted with permission from Ref.[200])

The structural characterization of geraniol/CD-IC sample was studied by using ^{1}H-NMR. Initially, the characteristic peaks correspond to protons of pure CD and geraniol, were determined from their ^{1}H-NMR spectra (data not shown). The three geraniol/CD-IC samples were studied by ^{1}H-NMR, and only ^{1}H-NMR spectrum of geraniol/γ-CD-IC as the representative of geraniol/CD-IC is shown in Figure 30. All ^{1}H-NMR spectra of geraniol/CD-IC indicated characteristic peaks of not only CD but also geraniol, confirming the presence of both geraniol and CD in these samples. Moreover, ^{1}H-NMR spectroscopy is a useful tool for quantitative calculation of guest molecule in CD-IC system. We found out that the molar ratio of geraniol:CD was 0.78:1, 0.9:1 and 1:1 for geraniol/α-CD-IC, geraniol/β-CD-IC and geraniol/γ-CD-IC, respectively. The calculation was done by the integrations of the CD peak at about 5.8 ppm (OH-2&3) and geraniol peak at 5.3 ppm (H-b). This result indicated that initial molar ratio (geraniol:CD = 1:1) used for the preparation of geraniol/CD-IC was only preserved for geraniol/γ-CD-IC. However, α-CD and β-CD could not complex with all geraniol that was used, and some uncomplexed geraniol was removed from the geraniol/α-CD-IC and geraniol/β-CD-IC during sample preparation.

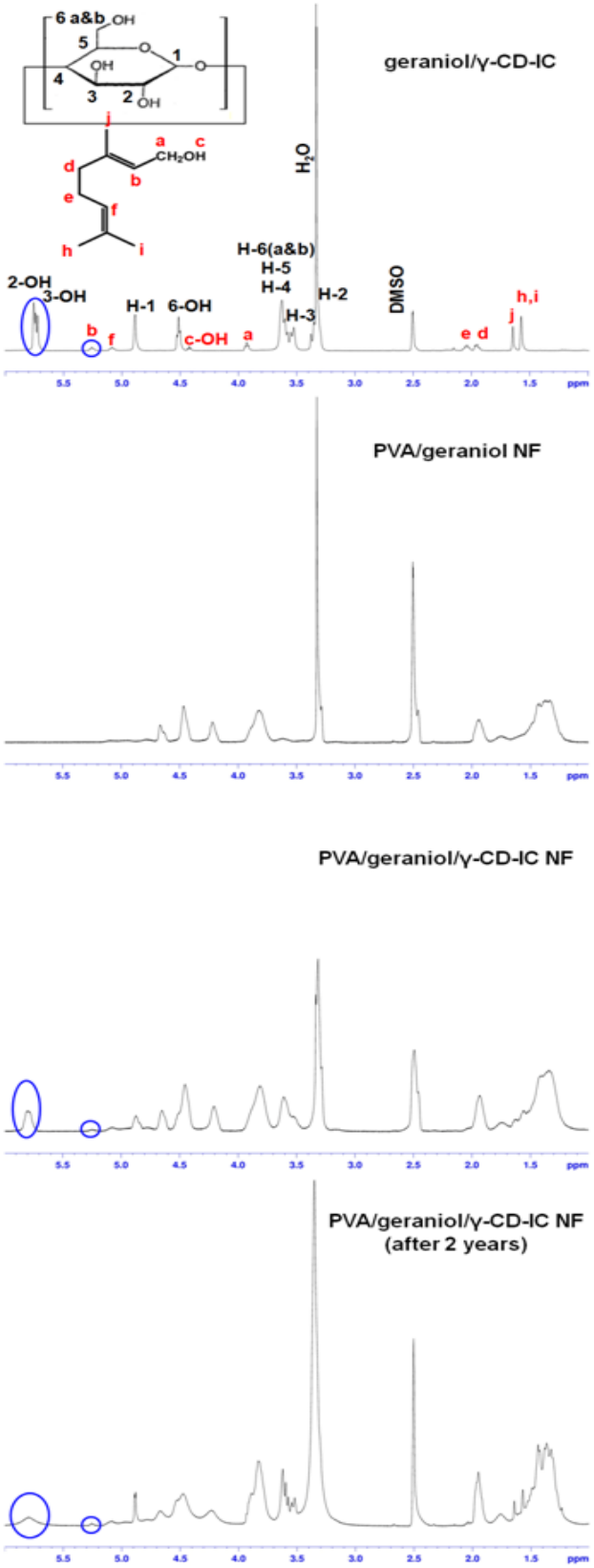

Figure 30. NMR spectrum of geraniol/γ-CD-IC and the electrospun nanofibers (NF). (Copyright © 2014, Elsevier. Reprinted with permission from Ref.[200])

As shown in Figure 6, the cavity size of CD are different and in the order of γ-CD > β-CD > α-CD. So, the higher complexation efficiency of γ-CD with geraniol might be due to the larger dimension of γ-CD cavity which may have a better size match with different conformers of geraniol molecule. Hence, in the next part of this study, geraniol/γ-CD-IC was selected and incorporated into the electrospun nanofibers.

The inclusion process between CD and geraniol is investigated by using ab initio techniques as explained in methods section. Firstly, the initial geometries of α-CD, β-CD, and γ-CD and various conformers of geraniol molecule are fully optimized separately in vacuum. In order to form a complex, geraniol molecule with two possible orientations (OH-end and CH_3-end) is introduced into CD cavity through the wide and narrow rims. In order to analyze the energy variation, the geraniol is initially positioned 6 Å away from the center of the CD cavity, which is chosen as the origin and moved in 1 Å steps towards the center [263]. At each step, the whole system is optimized without imposing any constraints and thus any conformational changes are allowed. For the lowest energy configuration (Figure 31), the complexation energy for each CD type is calculated as

$$E_{complex} = (E_{CD} + E_{geraniol}) - E_{geraniol+CD}$$

where E_{CD}, $E_{geraniol}$ and $E_{geraniol+CD}$ is the total energy (including van der Waals interaction) of CD (α-CD, β-CD, and γ-CD), geraniol, and geraniol/CD-IC, respectively.

In the case of geraniol/α-CD, the inclusion of geraniol mildly deforms the structure of α-CD. This indicates that even the most slender possible conformer of geraniol is large to fit in α-CD cavity. Complexation energy ($E_{complex}$) is calculated as 16.21 kcal/mol but in order to fit inside the cavity of α-CD, geraniol has to overcome an energy barrier. Accordingly, geraniol may form a complex at the edge the wide rim (which is a local energy minimum) instead as shown in Figure 31a with 10.03 kcal/mol complexation energy. The β-CD and γ-CD cavity is large enough to accommodate geraniol without any deformation (Figure 31b-c). For β-CD and γ-CD, $E_{complex}$ is 25.83 and 20.75 kcal/mol, respectively and there is no energy barrier for

inclusion process. The contribution to complexation energy is mainly due to van der Waals interaction and also extra hydrogen bonds are formed between hydroxyl group of the geraniol and primary hydroxyl group of CD at the narrow rim. The discussions are for the most slender geraniol conformer only but other conformers can be present as well. For instance, as γ-CD has the largest cavity it is more flexible to accommodate conformers of geraniol with different sizes (Figure 31c).

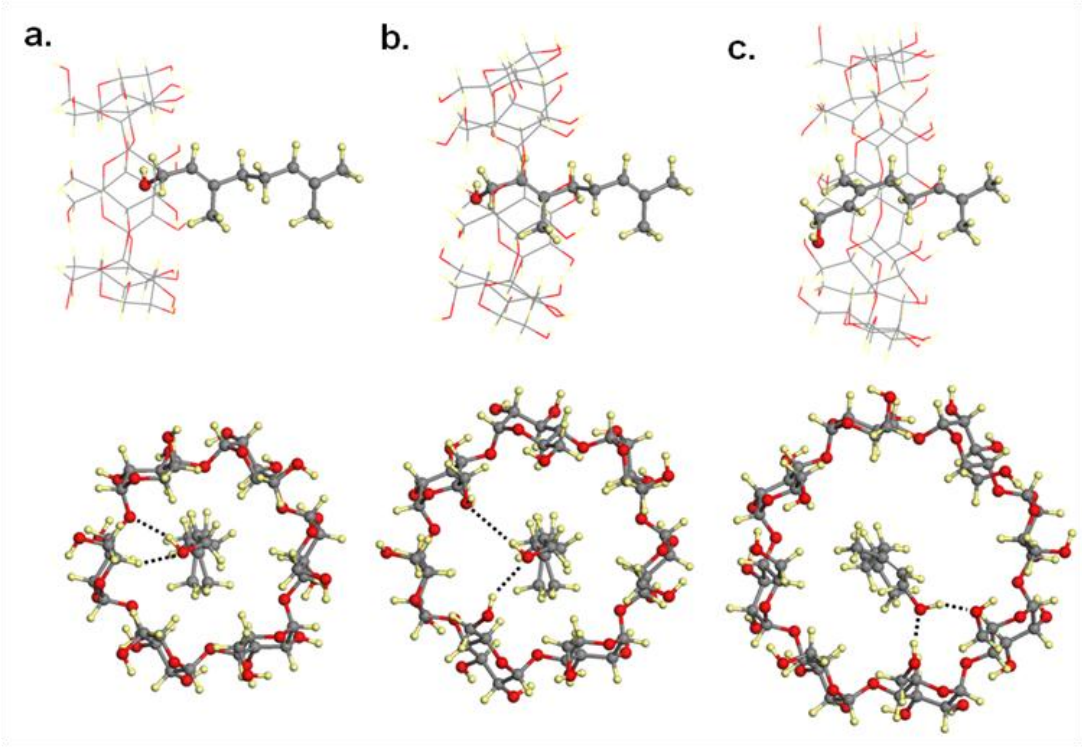

Figure 31. Side and top view of optimized structures of geraniol a) geraniol/α-CD-IC, b) geraniol/β-CD-IC, c) geraniol/γ-CD-IC. Extra hydrogen bonds are shown by dashed lines. Gray, red, and yellow spheres represent carbon, oxygen, and hydrogen atoms, respectively. (Copyright © 2014, Elsevier. Reprinted with permission from Ref.[200])

Finally, our modeling results show that, even the most slender conformer of geraniol does not fit into α-CD yielding relatively low complexation energy. This also indicates the possibility of complex formation outside the cavity. For β-CD and γ-CD, $E_{complex}$ is high which is in agreement with our experimental observations. Even though the largest $E_{complex}$ is obtained for β-CD for the slender geraniol

conformer, the large cavity of γ-CD allows accommodation of various conformers of geraniol and makes it the best candidate for inclusion complexation.

In the next part of the study, geraniol/γ-CD-IC crystals were incorporated in the PVA nanofibers via electrospinning in order to produce functional nanofibrous material. The geraniol/γ-CD-IC fine powder was dispersed in the PVA solution, and then this solution was electrospun to encapsulate the geraniol/γ-CD-IC in PVA nanofibers. We also produced electrospun PVA and PVA/geraniol nanofibers without CD-IC under the same electrospinning conditions for comparative study. Figure 32 indicates the representative SEM images of PVA, PVA/geraniol and PVA/geraniol/γ-CD-IC nanofibers. Moreover, Table 6 summarizes the viscosity of the solutions used for the electrospinning with AFD of the resulting electrospun nanofibers. PVA and PVA/geraniol nanofibers were uniform and bead-free, whereas the some aggregates of geraniol/γ-CD-IC crystals in PVA/geraniol/γ-CD-IC nanofibers were seen in SEM images in which the presence of CD-IC crystals were also confirmed by the XRD as discussed in the following section. The viscosities of PVA and PVA/geraniol solutions were very similar to each other, hence AFD of the nanofibers obtained from these solutions were almost same. On the other hand, higher viscosity was found for PVA/geraniol/γ-CD-IC solution compared to PVA and PVA/geraniol solutions possibly owing to the interaction between the geraniol/γ-CD-IC and PVA polymer chains. Therefore, less stretching of the PVA/geraniol/γ-CD-IC solution possibly occurred during electrospinning process due to its higher viscosity; accordingly, higher AFD was observed for PVA/geraniol/γ-CD-IC (290±70 nm) system when compared to PVA (195±50 nm) and PVA/geraniol (200±40 nm) systems. This result correlates with general observation that is obtaining of thicker nanofibers from the solution having higher viscosity [7, 241].

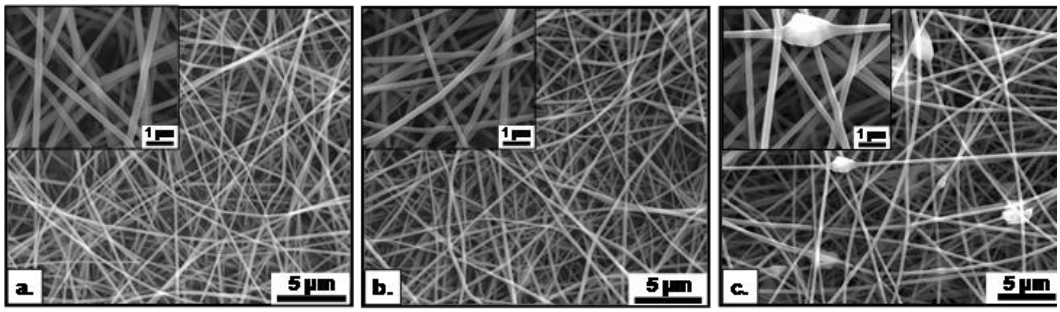

Figure 32. Representative SEM images of (a) PVA, (b) PVA/geraniol and (c) PVA/geraniol/γ-CD-IC nanofibers. (Copyright © 2014, Elsevier. Reprinted with permission from Ref.[200])

Table 6. The compositions and viscosity of the solutions used for electrospinning and morphological characteristics of the electrospun nanofibers.

Solutions	% PVA[a] (w/v)	% geraniol /CD-IC[b] (w/w)	% geraniol[b] (w/w)	viscosity (Pa·s)	AFD (nm)
PVA	12	-	-	0.237	195±50
PVA/geraniol	12	-	5	0.264	200±40
PVA/ geraniol /γ-CD-IC	12	50	5	0.372	290±70

[a] with respect to the solvent (water).
[b] with respect to the polymer (PVA).

We have investigated the crystalline structure of the resulting nanofibers by using XRD. The XRD patterns of both PVA and PVA/geraniol nanofibers (Figure 28c) have very similar broad diffraction centered at $2\theta \cong 20^{o}$ due to semi-crystalline nature of PVA matrix. The XRD pattern of PVA/geraniol/γ-CD-IC nanofibers (Figure 28c) has also broad diffraction centered at $2\theta \cong 20^{o}$, indicating the presence of geraniol/γ-CD-IC did not affect the semi-crystalline nature of the polymeric matrix. Furthermore, the characteristic diffraction peaks of channel-type packing of γ-CD observed in the XRD pattern of PVA/geraniol/γ-CD-IC nanofibers have been demonstrated the existence of geraniol/γ-CD-IC crystals in this sample (Figure 28c). It was deduced that channel-type packing of geraniol/γ-CD-IC were conserved during the solution preparation and electrospinning process, and then these crystalline aggregates of geraniol/γ-CD-IC were successfully encapsulated within the

PVA nanofibers matrix, as it was also clearly observed in the SEM image of PVA/geraniol/γ-CD-IC nanofibers (Figure 32c).

TGA thermograms of PVA, PVA/geraniol and PVA/geraniol/γ-CD-IC nanofibers are given in Figure 29b. The major weight loss of TGA thermogram of PVA nanofibers started at about 250 ^{o}C owing to thermal degradation of PVA. The geraniol could not be detected in TGA thermogram of PVA/geraniol nanofibers, since no difference was observed between the TGA thermograms of PVA and PVA/geraniol nanofibers. This result indicated that the loss of geraniol possibly took place during the electrospinning of PVA/geraniol solution or storage of these nanofibers in suction hood at RT for 24 h, and eventually; volatile geraniol could not be preserved without CD-IC. In the case of PVA/geraniol/γ-CD-IC nanofibers, the evaporation of complexed geraniol was observed at between 120-250 ^{o}C till the degradation of PVA starts. As a result, TGA data further confirmed the existence of geraniol/γ-CD-IC in PVA nanofibers matrix. The calculation of the quantity of geraniol in the nanofibers samples was not done from TGA data, since there might be overlapping of degradation temperature of PVA and γ-CD with the evaporation of complexed geraniol. So, we carried out ^{1}H-NMR study in order to calculate the actual content of remaining geraniol in the nanofibers, and this data is discussed in the following section.

We performed ^{1}H-NMR study to calculate the amount of geraniol in PVA/geraniol/γ-CD-IC nanofibers (Figure 30). The γ-CD peak at 5.8 ppm (OH-2&3) and geraniol peak at 5.3 ppm (H-b) which are not overlapped with the characteristic peaks of PVA were used to calculate the molar ratio of geraniol:CD in PVA/geraniol/γ-CD-IC nanofibers sample. The molar ratio of geraniol to γ-CD was detected as 1:1 which is the same ratio of geraniol:CD in geraniol/γ-CD-IC. It was assumed that the initial amount of geraniol in the PVA/geraniol/γ-CD-IC solution was preserved during the electrospinning process by means of inclusion complexation. The characteristic peak of geraniol at about 5.3 ppm (H-b) was not observed in the case of ^{1}H-NMR spectrum of PVA/geraniol nanofibers. This result correlated with TGA data, confirmed that all geraniol was evaporated from this sample during either the

electrospinning process or storage of the nanofibers in the suction hood for 24 h after production. So, it was obvious that PVA nanofibers could not protected geraniol molecules without CD-IC.

We have also performed the durability test for PVA/geraniol/γ-CD-IC nanofibers sample with the open air experiments to show the durability of geraniol in the electrospun nanofibers sample despite of the volatile nature of geraniol. The presence of geraniol quantity in the PVA/geraniol/γ-CD-IC nanofibers after two years of their storage in the open air in the laboratory (at about 22 ^{o}C and 25% relative humidity) was determined by ^{1}H-NMR study. The geraniol peak was still present, and it was even observed that the molar ratio of geraniol:γ-CD was 0.87:1 which was very close to the 1:1 initial molar ratio. This result showed that very small amount of geraniol (~10%) has evaporated from the PVA/geraniol/γ-CD-IC nanofibers even after two years of its storage. It was evident that the prolonged durability of geraniol in the nanofibers sample was provided by CD inclusion complexation. Hence, PVA/geraniol/γ-CD-IC nanofibers can be applicable in food packaging application since geraniol has antimicrobial and antioxidant properties and therefore PVA/geraniol/γ-CD-IC nanofibers can preserve the food effectively for a long time due to prolonged durability of geraniol.

2.4.3. Conclusions

As a first step, solid geraniol/CD-IC were obtained using α-CD, β-CD and γ-CD by co-precipitation method. The XRD patterns showed that complexation was achieved for all three types of CD. The TGA data indicated that complexed geraniol with CD had higher thermal evaporation (about 120-300 ^{o}C) compared to pure geraniol (70-230 ^{o}C).

Our ab initio modeling results show that, geraniol-CD complexation energy ($E_{complex}$) is higher for β-CD and γ-CD compared to α-CD. Although the largest $E_{complex}$ was obtained for β-CD for the slender geraniol conformer, the large cavity of γ-CD allows accommodation of various conformers of geraniol and makes it the best candidate for inclusion complexation. Due to higher complexation efficiency of γ-

CD with geraniol compared to other CD types, geraniol/γ-CD-IC was selected and incorporated in the electrospun PVA nanofibers. As a second part of this study, PVA nanofibers incorporating geraniol/γ-CD-IC were obtained successfully by electrospinning of PVA solution containing geraniol/γ-CD-IC dispersion. Bead-free and uniform nanofibers were obtained for PVA and PVA/geraniol nanofibrous samples, whereas the SEM images of PVA/geraniol/γ-CD-IC nanofibers showed that the aggregates of geraniol/γ-CD-IC crystals were present and encapsulated in PVA nanofibrous matrix. Furthermore, the presence of CD-IC crystals in the PVA/geraniol/γ-CD-IC nanofibers was also confirmed by the XRD data. The geraniol could not be detected in either TGA thermogram or NMR spectra of PVA/geraniol nanofibers. It was evident that the geraniol was not preserved in PVA nanofibers without CD-IC owing to its volatile nature. On the other hand, enhanced thermal stability of geraniol was observed in the TGA thermogram of PVA/geraniol/γ-CD-IC nanofibers. Besides, NMR result of PVA/geraniol/γ-CD-IC nanofibers indicated that the initial 1:1 molar ratio of geraniol:γ-CD in geraniol/γ-CD-IC did not change during the electrospinning process or after the storage. More importantly, the molar ratio of geraniol:γ-CD was found as 0.87:1 even after storage of these nanofibers for two years at ~22 ^{o}C and ~25% relative humidity. Only ~10% loss of geraniol was evaporated from PVA/geraniol/γ-CD-IC nanofibers confirming that the loss of geraniol was minimal after such a long storage period. The prolonged durability of geraniol was obviously observed owing to the CD inclusion complexation. PVA is a biodegradable synthetic polymer which is applicable in food packaging, and geraniol is widely used fragrance/flavor having many specific properties such as antimicrobial, antioxidant. Hence, the electrospun PVA/geraniol/γ-CD-IC nanofibers having very high surface area and nanoporous structure, as well as having geraniol with enhanced durability and thermal stability assisted by CD-IC may be quite applicable in functional food packaging and other food or medical related applications.

2.5. Antibacterial Electrospun Polylactic acid (PLA) Nanofibrous Webs Incorporating Triclosan/Cyclodextrin Inclusion Complexes

2.5.1. Experimental

Materials: Polylactic acid (PLA), a commercial polylactide resin identified as Ingeo^{TM} biopolymer was donated by NatureWorks LLC Company (product code: 4043D). Triclosan (TR) (≥97% (HPLC), Sigma-Aldrich), N,N-dimethylformamide (DMF, Pestanal, Riedel), chloroform (99-99.4% (GC), Sigma-Aldrich) and deuterated dimethylsulfoxide (DMSO-d_6, deuteration degree min. 99.8% for NMR spectroscopy, Merck) were purchased. Cyclodextrins (α-CD, β-CD, and γ-CD) were purchased from Wacker Chemie AG. All of these materials were used as-received. The water used as solvent was obtained from Millipore Milli-Q ultrapure water system.

Preparation of solid triclosan/cyclodextrin inclusion complexes (TR/CD-IC): The formation of solid inclusion complexes (IC) of TR with α-CD, β-CD, and γ-CD were performed by co-precipitation method. In all cases, the molar ratio of TR:CD was used as 0.5:1. Initially, 0.149 g (5.1×10^{-4} mol), 0.128 g (4.4×10^{-4} mol), and 0.112 g (3.9×10^{-4} mol) TR were stirred in 2 ml water for the IC formation of TR with α-CD, β-CD, and γ-CD, respectively. Since TR is not water-soluble, a suspension was obtained each vial. Then, 1g of α-CD (1×10^{-3} mol), β-CD (8.8×10^{-4} mol), and γ-CD (7.8×10^{-4} mol) was dissolved in 4.9 ml, 52 ml and 2.3 ml water at 60 °C, respectively. The total amount of the water used was determined according to the solubility of CD in water at 25 °C, that is, 14.5, 1.85 and 23.2 g/100 mL for α-CD, β-CD and γ-CD, respectively [58-59]. The resulting CD solution was added into aqueous TR suspension by drop-wise. Finally, each of TR/CD solution was mixed at 60 °C for 1 hour, and then stirred overnight at room temperature. TR/α-CD solution was not turbid subsequent to stirring overnight, and TR particles were suspended indicating that TR did not form IC with α-CD; therefore we eliminated the use of TR/α-CD in this study. On the other hand, turbid TR/β-CD and TR/γ-CD solution

were obtained after mixing overnight, and precipitation was observed for both of these solutions, elucidating the formation of IC between TR and β-/γ-CD. The resulting TR/CD suspensions were filtered by using a borosilicate filter (por. 3) to obtain solid TR/CD-IC. The filtrate was washed with water several times in order to remove uncomplexed CD and then dried overnight under the hood. Lastly, the solid TR/β-CD-IC and TR/γ-CD-IC were crushed in a mortar in order to obtain fine white powder, and weighted about 0.59 g and 0.60 g, respectively. The yield was around 50%, since excess amount of CD was used for the complexation (molar ratio of TR:CD was 0.5:1). From the NMR study as discussed in the later section, it was found that the complexation molar ratio of TR:CD was 1:1, therefore, the uncomplexed CD molecules did not precipitate out and/or might be removed from the samples during washing and filtration process.

Preparation of the solutions used for electrospinning: TR/β-CD-IC and TR/γ-CD-IC were incorporated in PLA nanofibers via electrospinning. The amount of TR/β-CD-IC (44%, w/w) and TR/γ-CD-IC (50%, w/w) was adjusted as to include 5% (w/w) TR with respect to PLA content. First, the TR/CD-IC crystals were dispersed in chloroform/DMF (9/1, v/v) solvent system by stirring for 30 min at room temperature. Then PLA was added to these dispersions and completely dissolved by mixing for 5 h at room temperature. On the other side, we have also prepared solutions of PLA and PLA/TR without CD under the same conditions for comparison. PLA and PLA/TR solutions were clear and transparent, whereas PLA/TR/CD-IC solutions were turbid due to the dispersion of TR/CD-IC crystals within the PLA solution. For all solutions, the PLA concentration was 8% (w/v) with respect to solvent (chloroform/DMF (9/1, v/v)).

Electrospinning: Each prepared solution was placed in a 10 mL syringe fitted with a metallic needle having 0.55 mm inner diameter and 0.8 mm outer diameter, and the syringe was fixed horizontally on the syringe pump (KD Scientific, Model:101). The electrode of the high voltage power supply (Matsusada Precision, AU Series) was clamped to the metal needle tip, while the stationary cylindrical collector covered by a piece of aluminum foil was grounded. Tip-to-collector distance was kept 10 cm,

and the solutions were pumped with flow rate of 1 ml/h. When voltage of +15 kV was applied to the metal needle tip, the nanofibers were deposited on the collector. The electrospinning apparatus was in an enclosed Plexiglas box, and the electrospinning was performed at 24 ^{o}C and 20% relative humidity. The collected nanofibers were left in the suction hood at room temperature for 24 h to remove the residual solvent if any present.

Characterizations and measurements: The characterizations of solid TR/CD-IC were carried out by proton nuclear magnetic resonance (^{1}H-NMR), Fourier transform infrared (FTIR) spectroscopy, X-ray diffraction (XRD), differential scanning calorimetry (DSC) and thermogravimetric analyzer (TGA). Pure triclosan and as-received CD were also characterized for comparison. In order to determine the stoichiometries of the TR/CD, ^{1}H-NMR (DPX-400, Bruker) spectra were recorded at 400 MHz and 25 °C by dissolving about 20 g/L sample in DMSO-d_6. For FTIR analyses, a small amount of sample was mixed with potassium bromide (FTIR grade) in a mortar and then pellet was obtained using press by applying high pressure. The infrared spectra of the samples were obtained by using FTIR spectroscopy (Bruker-VERTEX 70). The FTIR spectra were recorded from 750 to 1800 cm^{-1}, at a resolution of 4 cm^{-1} by taking 64 scans for each sample. XRD (PANalyticalX'Pert Powder diffractometer) data of the samples were obtained by using Cu K-α radiation in a range of $2\theta=5^{o}$-30^{o}. DSC (Q2000, TA Instruments) and TGA (Q500, TA Instruments) were used to investigate thermal properties of the samples. DSC analyses were carried out under nitrogen atmosphere, the samples were equilibrated at 0 ^{o}C, and then heated to 200 ^{o}C with a heating rate of 20 ^{o}C/min. TGA analyses were performed from room temperature to 450 ^{o}C at a 20 ^{o}C/min heating rate, and N_2 was used as a purge gas. The viscosity of the solutions used for electrospinning was measured by using Rheometer (Physica MCR 301, Anton Paar) equipped with a cone/plate accessory (spindle type CP 40-2) at 22 ^{o}C, with a constant shear rate of 100 1/sec. Scanning electron microscope (SEM) (Quanta 200 FEG, FEI) was used for the morphological investigation of electrospun nanofibers. Prior to SEM imaging, nanofiber samples were sputtered with 5 nm Au/Pd (PECS-682). Around 100 fiber diameters were measured from the SEM images to calculate the average fiber

diameter (AFD) and to determine fiber diameter range of each sample. XRD data of the nanofibers were also recorded in a range of $2\theta=5^{o}$-30^{o}.

Antibacterial activity test: Antibacterial properties of the electrospun nanofibrous webs were investigated against gram-positive bacteria; *Staphylococcus aureus* (*S. aureus*, ATCC 25923) and gram-negative bacteria; *Escherichia coli* (*E. coli*, RSHM 888, National Type Culture Collection Laboratory, Ankara, Turkey). This test was done in vitro using disc agar diffusion method. 100µL of the cultures that contain 10^{12}/ml *S. aureus* or $5x10^{12}$/ml *E. coli* were spread onto LB agar. The samples which are named as PLA/TR, PLA/TR/β-CD-IC and PLA/TR/γ-CD-IC were cut into circular discs having a diameter of about 1 cm. Then the nanofibrous webs were put on the agar, the agar plates were incubated at 37ºC for 24 h, and the inhibition zone diameters were measured.

2.5.2. Results and Discussion

In this study, we aimed to prepare solid CD-IC with triclosan (TR) by using three types of CD (α-CD, β-CD, and γ-CD). The formation of IC between α-CD and TR was unsuccessful possibly because of the small cavity size of α-CD which is not suitable host for the guest of TR molecules, or the chosen experimental conditions and the aqueous solvent system were not appropriate to form the CD-IC. However, the formation of IC between β-CD and TR (TR/β-CD-IC), and between γ-CD and TR (TR/γ-CD-IC) were successful and solid white powder of TR/β-CD-IC and TR/γ-CD-IC were obtained by filtration.

The molar stoichiometry of TR/CD in the solid TR/β-CD-IC and TR/γ-CD-IC was determined by ^{1}H-NMR (Figure 33). Initially, ^{1}H-NMR study was performed for pure CD and TR to detect the characteristic peaks corresponded to their protons, and it was observed that the peaks for TR were not overlapped with the peaks of CD (data not shown). The stoichiometry of the CD and TR in the CD-IC samples was calculated by taking the integrations of the CD peak at 4.8 ppm (H-1) and TR peak at 7.3 ppm (H-b). It was found that stoichiometric ratio of TR:β-CD and TR:γ-CD was around 1:1 for TR/β-CD-IC and TR/γ-CD-IC samples. At the beginning, excess

amount of CD was used (initial molar ratio of TR:CD 0.5:1) for the complexation process, however, the molar ratio of TR:CD was found 1:1 for TR/CD-IC samples.

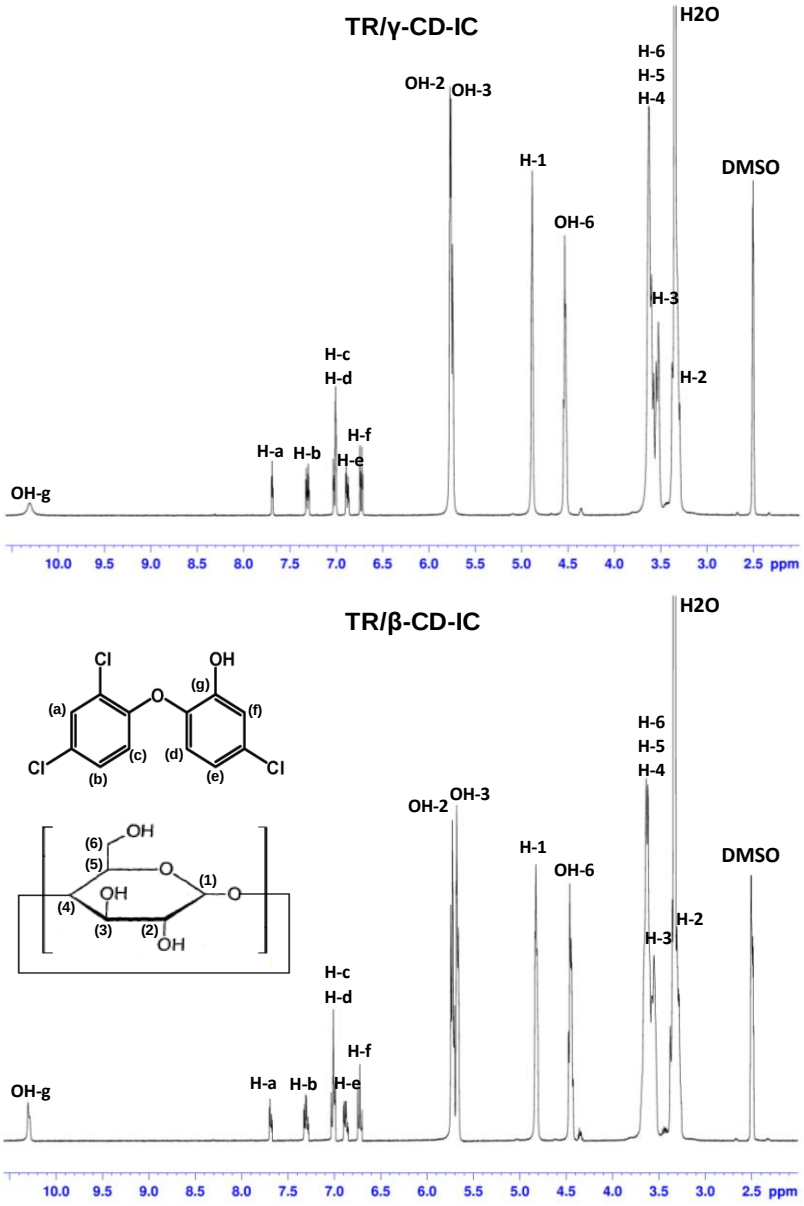

Figure 33. ^{1}H NMR spectra of TR/CD-IC dissolved in DMSO-d_6. (Copyright © 2013, American Chemical Society. Reprinted with permission from Ref.[201])

The chemical structures of TR/CD-IC samples were investigated by FTIR spectroscopy, and pure TR and CD were also studied for comparison (Figure 34). The characteristic absorption peaks of pure CD were observed at around 1030, 1080,

and 1157 cm^{-1} due to the coupled C-C/C-O stretching vibrations and the asymmetric stretching vibration of the C-O-C glycosidic bridge [70]. The FTIR spectrum of pure TR exhibited three characteristic peaks at 1505, 1472 and 1418 cm^{-1} corresponding to skeletal vibrations relating C–C stretching in the benzene ring [76]. Additionally, the peaks in the region from 1300 to 1000 and 900 to 750 cm^{-1} in the spectrum of pure TR were consequent of in-plane and out-of-plane bending of the aromatic ring C–H bonds, respectively, while the peaks at 1102 and 1084 cm^{-1} were related with to C–Cl absorption [76]. In the case of TR/β-CD-IC and TR/γ-CD-IC samples, characteristic peaks of TR and CD were observed, confirming the presence of both TR and CD in these samples. In addition, the characteristic peaks of TR at 1505, 1472 and 1418 cm^{-1} shifted to 1507, 1474 and 1419 cm^{-1}, respectively for the TR/CD-IC samples. This suggests the host-guest interactions between CD and TR, since inclusion complexation causes FTIR peak shifts as also reported for TR/CD-IC samples in the literature [75, 231].

The crystalline structures of the CD-IC (TR/β-CD-IC and TR/γ-CD-IC), pure TR and CD were investigated by XRD. The XRD patterns of as-received β-CD and γ-CD (Figure 4a) showed characteristic diffraction peaks in the range of $2\theta=5^{o}$-30^{o} for cage-type packing structure which are consistent with the literature findings [228, 230]. The inclusion complexation is generally confirmed the characteristic XRD peaks of CD molecules having channel-type arrangement in which CD molecules are aligned and stacked on top of each other by forming cylindrical channels [228, 230]. Moreover, XRD patterns of CD-IC show no diffraction peaks of guest molecules which are isolated from each other by the CD cavities, and therefore cannot form crystals [70, 231].

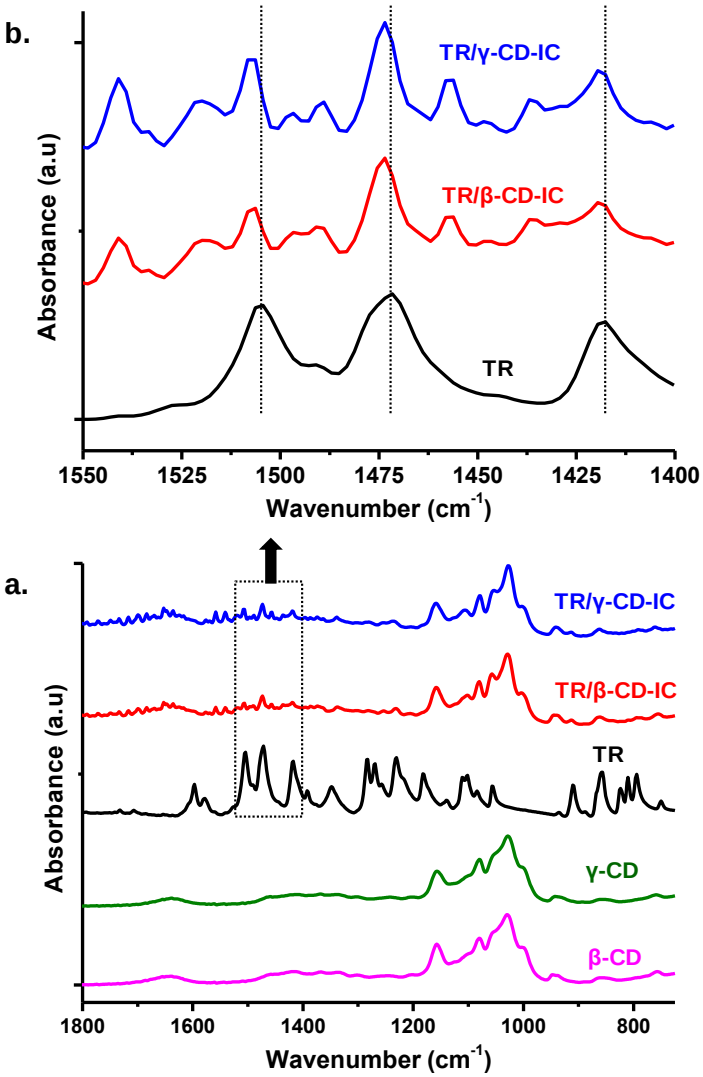

Figure 34. (a) FTIR spectra of as-received CD, pure TR and solid TR/CD-IC and (b) enlarged region of FTIR spectra between 1550 and 1400 cm^{-1} of pure TR and solid TR/CD-IC. (Copyright © 2013, American Chemical Society. Reprinted with permission from Ref.[201])

TR is a crystalline material and the XRD pattern of TR has major diffraction peaks at 2θ≅8.2°, 24.4° and 25.4° (Figure 35a). The peaks centered at 2θ≅12° and 2θ≅17.8° were observed in the XRD pattern of TR/β-CD-IC (Figure 35a) owing to channel-type packing of β-CD which indicated the inclusion complexation of TR with β-CD [70]. However, along with the β-CD peaks, the sharp diffraction peak of TR centered at 2θ≅8.2° was also present in the XRD pattern of TR/β-CD-IC because of the existence of some uncomplexed TR in this sample. The DSC analyses which

will be discussed in the following section also confirmed that the presence of free TR in TR/β-CD-IC sample. In the case of the XRD pattern of TR/γ-CD-IC (Figure 35a), a major peak at 2θ≅7.6° along with minor diffractions at 2θ≅14.4°, 15°, 16°, 16.9° and 22° were observed, confirming the tetragonal channel-type packing of γ-CD [85, 230]. In addition, the absence of the TR peak at 2θ≅8.2° indicated that complete complexation was achieved between TR and γ-CD. In short, the XRD data revealed that some of TR used for the preparation of TR/β-CD-IC could not complex with β-CD, while all TR used for the preparation of TR/γ-CD-IC was fully complexed with γ-CD.

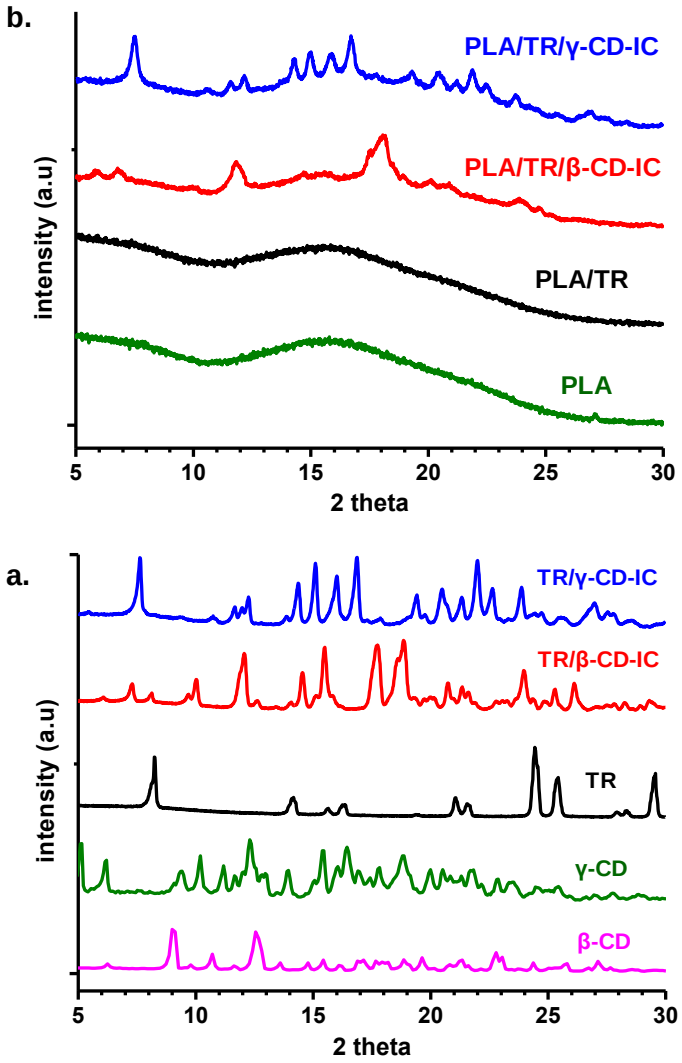

Figure 35. XRD patterns of (a) as-received CD, pure TR and solid TR/CD-IC, (b) the resulting electrospun nanowebs. (Copyright © 2013, American Chemical Society. Reprinted with permission from Ref.[201])

The solid TR/β-CD-IC and TR/γ-CD-IC were further characterized by DSC that is a useful technique to verify whether or not the guest molecules are included inside the CD cavities [72, 232]. Typically, if any uncomplexed guest molecules present in the CD-IC systems, melting point of guest molecules is observed in DSC thermograms of CD-IC [70, 232-233]. The DSC thermograms of pure TR and solid TR/β-CD-IC and TR/γ-CD-IC were given in Figure 36. The melting point of pure TR was observed at 59 ^{o}C. The small endothermic peak at around 55 ^{o}C was also observed in the DSC thermogram of TR/β-CD-IC, indicating the presence of some free TR in this sample. This DSC data correlates with the XRD data of TR/β-CD-IC having a diffraction peak for some uncomplexed TR crystals. However, the melting peak of free TR was absent in the DSC thermogram of TR/γ-CD-IC, elucidating that the TR was fully complexed with the γ-CD. Correspondingly, the complete inclusion complexation of TR with γ-CD was also confirmed by the absence of diffraction peak of TR at 2θ≅8.2° in the XRD data of solid TR/γ-CD-IC as discussed in the previous section.

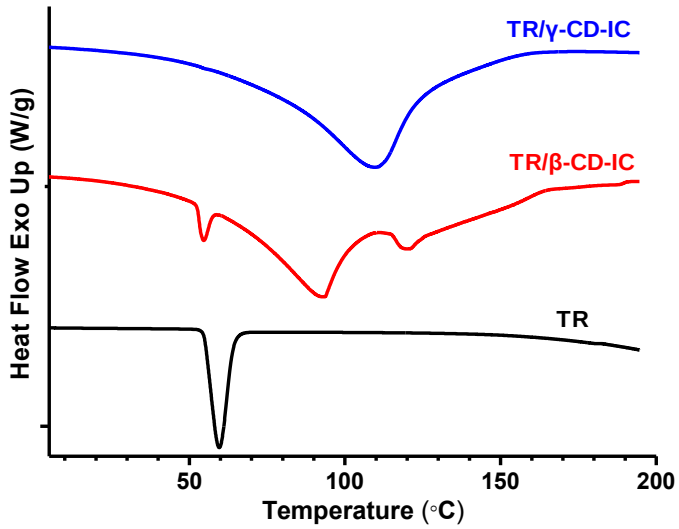

Figure 36. DSC thermograms of pure TR and solid TR/CD-IC. (Copyright © 2013, American Chemical Society. Reprinted with permission from Ref.[201])

In addition, we investigated the thermal characteristics of TR/β-CD-IC and TR/γ-CD-IC by TGA. The TGA studies of CD and pure TR were also performed for comparison. TGA curve of CD had two weight losses; below 100 ^{o}C and above 300

^{o}C corresponded to water loss and main degradation of CD, respectively (Figure 37a). TGA thermogram of pure TR indicated one major weight loss in the range of 120-270 ^{o}C (Figure 37b). The water loss below 100 ^{o}C and the main degradation of CD above 300 ^{o}C were also observed in TGA thermograms of CD/TR-IC samples (Figure 37b). Yet, additional weight losses due to the evaporation/degradation of TR were present in these samples.

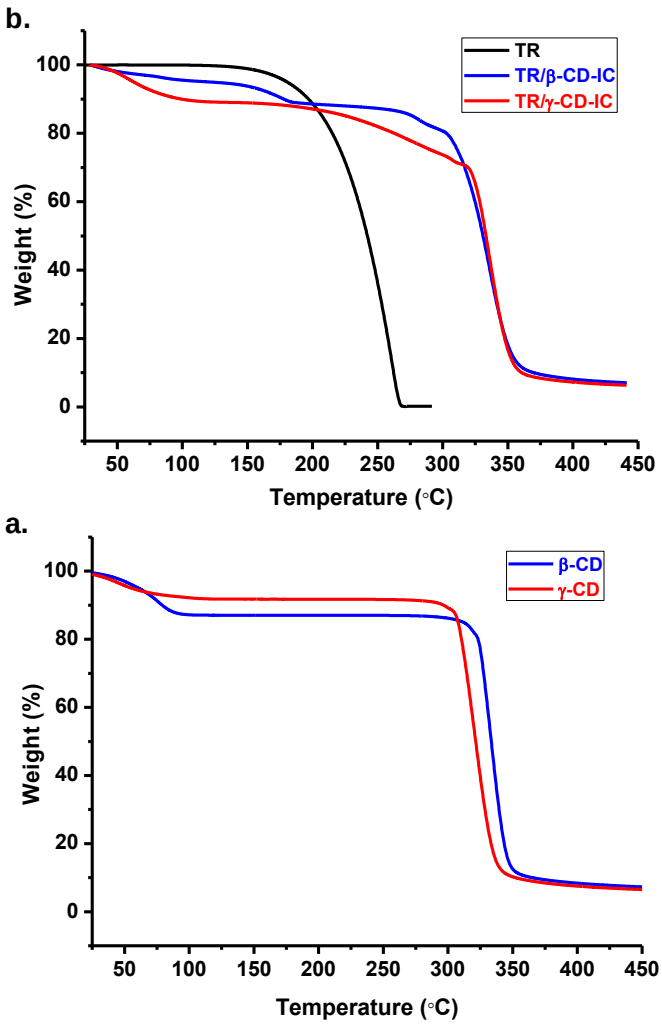

Figure 37. TGA thermograms of (a) as received CD and (b) pure TR and solid TR/CD-IC. (Copyright © 2013, American Chemical Society. Reprinted with permission from Ref.[201])

For TR/β-CD-IC, the weight loss of TR was observed in two steps; initial weight loss between 120-205 ^{o}C was owing to uncomplexed free TR molecules. The second weight loss corresponding to the degradation of complexed TR with β-CD occurred

at above 275 ^{o}C till to 315 ^{o}C at which main degradation of CD also occurred, indicating the higher thermal stability of TR due to the inclusion complexation. In general, the host-guest interactions in CD-IC increase the thermal stability of the guest molecules included in the CD cavity [70, 234, 244]. The amount of uncomplexed TR was calculated as ~6% (w/w, with respect to TR/β-CD-IC) from the TGA thermogram of TR/β-CD-IC. The amount of TR in TR/β-CD-IC was determined as ~20% (w/w) from the stoichiometric ratio of TR:β-CD (1:1), therefore, around 70% (w/w) of TR was in the complex state with β-CD in TR/β-CD-IC. In the case of TR/γ-CD-IC, thermal degradation/evaporation of TR took place between 200-325 ^{o}C which was much higher than that of the pure TR. In brief, it was observed that the thermal stability of complexed TR was shifted to much higher temperature due to stronger interaction between TR and CD cavity in the CD-IC.

In the next part of this study, the incorporation of TR/β-CD-IC and TR/γ-CD-IC in PLA nanofibers was achieved by electrospinning of the solution mixture of PLA and TR/CD-IC. For comparison, PLA and PLA/TR nanofibers were also produced via electrospinning under the same conditions. The representative SEM images of the resulting nanofibers are depicted in Figure 38. Uniform and bead-free nanofibers were obtained from PLA and PLA/TR. However, the nanofibers were not uniform in the case of PLA/TR/β-CD-IC and PLA/TR/γ-CD-IC samples, since the aggregates of TR/CD-IC crystals were present and distributed within the nanofiber matrix as confirmed by XRD results discussed in the following section.

The viscosity of the solutions used for the electrospinning and AFD with fiber diameter range of the resulting nanofibers are given in Table 7. The viscosities of PLA and PLA/TR solutions were very similar to each other, and so small variations were observed among the AFD and fiber diameter range of these samples. Higher viscosity was observed for the PLA/TR/CD-IC solutions when compared to pure PLA solution which is possibly owing to the presence of TR/CD-IC crystals in the PLA solution and/or the interactions between the TR/CD-IC and PLA polymer chains. Therefore, thicker fiber diameters were observed in PLA/TR/CD-IC nanofibers due to less stretching of the solutions having higher viscosity. In addition,

the standard deviation of AFD of these nanofibers were higher compared to uniform PLA and PLA/TR nanofibers possibly because of rather complex structure of PLA/TR/CD-IC nanofibers (Table 7).

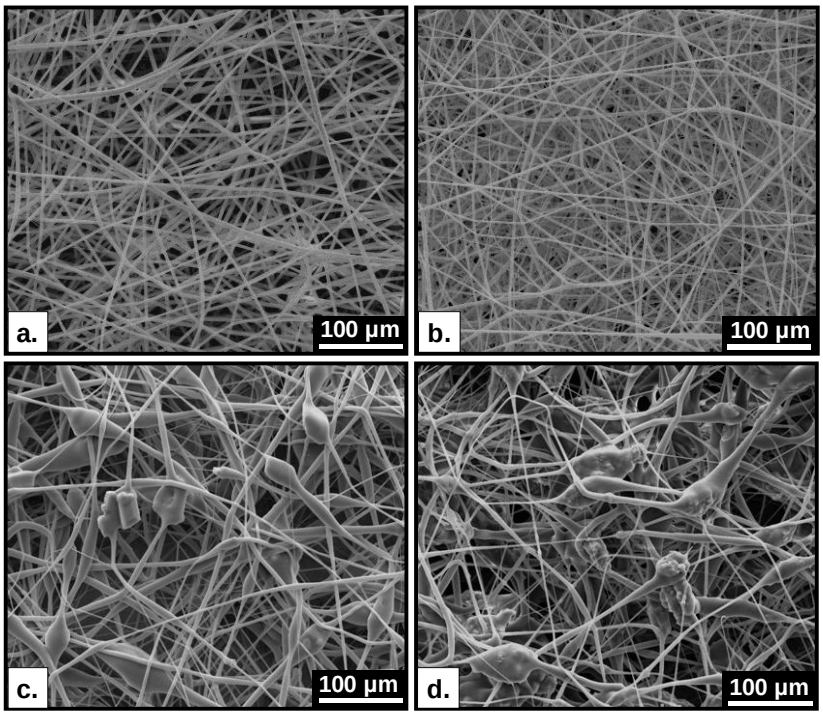

Figure 38. Representative SEM images of the electrospun nanowebs obtained from solutions of (a) PLA, (b) PLA/TR, (c) PLA/TR/β-CD-IC and (d) PLA/TR/γ-CD-IC. (Copyright © 2013, American Chemical Society. Reprinted with permission from Ref.[201])

Table 7. The solution viscosity, fiber diameter and inhibition zone results taken after 24 h incubation at 37 °C against *E. coli* and *S. aureus* bacteria for PLA/TR, PLA/TR/β-CD-IC and PLA/TR/γ-CD-IC.

Solutions	Viscosity (Pa·s)	Fiber diameter range (nm)	AFD (nm)	Zone of *E.coli* inhibition diameter (cm)	Zone of *S.aureus* inhibition diameter (cm)
PLA	0.106	140-900	650 ± 160	-	-
PLA/TR	0.115	250-950	560 ± 150	3.0 ± 0.20	2.83 ± 0.28
PLA/TR/β-CD-IC	0.135	210-1580	640 ± 480	3.7 ± 0.15	3.50 ± 0.00
PLA/TR/γ-CD-IC	0.176	260-2070	940 ± 500	3.3 ± 0.00	2.90 ± 0.17

Crystalline structures of the resulting nanowebs of PLA, PLA/TR and PLA/TR/CD-IC were investigated by XRD (Figure 35b). The XRD pattern of PLA/TR sample was very similar to PLA nanoweb having a broad diffraction pattern without any characteristic diffraction peaks for TR. This indicated that TR molecules were distributed in the fiber matrix without any crystalline aggregates. Supaphol et al. also reported similar finding where crystalline drug molecules became amorphous when they were incorporated in electrospun nanofibers [238]. In the case of PLA/TR/CD-IC nanowebs, the diffraction peaks for channel-type packing structure of β-CD and γ-CD were observed in the XRD patterns of PLA/TR/β-CD-IC and PLA/TR/γ-CD-IC nanowebs, respectively. The XRD data confirmed that channel-type packing of TR/CD-IC was well preserved during the solution preparation and electrospinning process and these crystalline aggregates of TR/β-CD-IC and TR/γ-CD-IC were dispersed within the PLA nanofiber matrix. This result correlates with SEM images which clearly revealed the presence of TR/CD-IC crystalline aggregates in PLA nanofibers.

Antibacterial activities of PLA/TR, PLA/TR/β-CD-IC and PLA/TR/γ-CD-IC nanowebs were tested against gram-positive bacteria; *Staphylococcus aureus* and gram-negative bacteria; *E. coli*. As given in Figure 39, PLA/TR nanoweb caused an inhibition in the growth of both *S. aureus* and *E. coli* due to well-known antibacterial property of TR. More importantly, the inhibition zones were wider for the PLA/TR/CD-IC nanowebs suggesting that both PLA/TR/β-CD-IC and PLA/TR/γ-CD-IC nanowebs have better antibacterial properties compared to the PLA/TR system (Table 7). Similar results were also reported by Tonelli et al. where TR/β-CD crystals incorporated in poly(caprolactone) (PCL) films have shown improved effectiveness against *E. coli* when compared to PCL film with TR only [264]. This is possibly because of the enhanced solubility of TR into agar medium by CD-IC. It was also noted that PLA/TR/β-CD-IC sample had better inhibition levels against both of the bacteria when compared to PLA/TR/γ-CD-IC sample and this may be caused by presence of uncomplexed TR in the PLA/TR/β-CD-IC sample, which can be released readily at the initial stage.

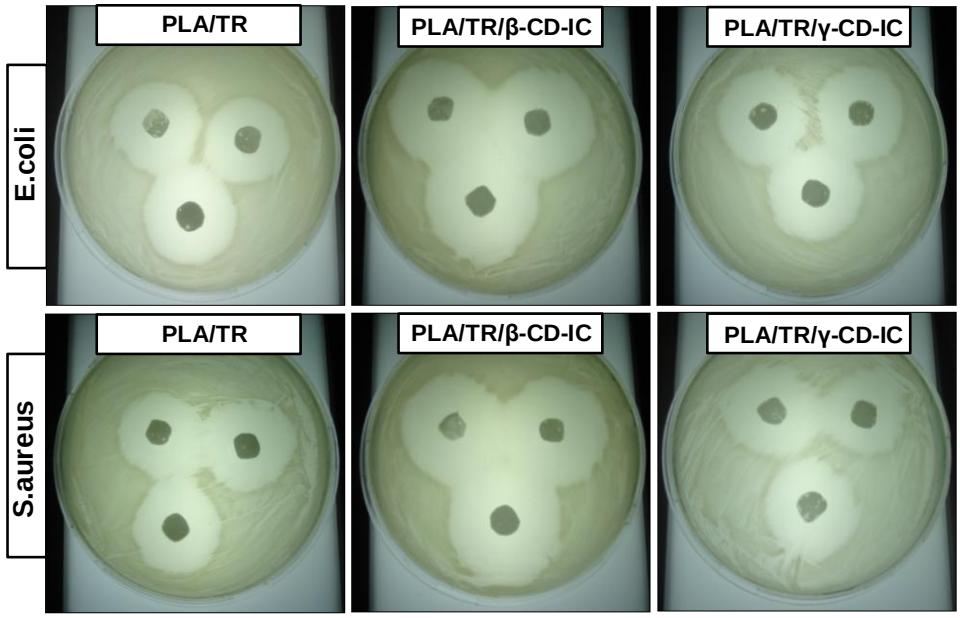

Figure 39 The photographs of antibacterial test of the electrospun nanowebs after 24 h incubation at 37 °C. (Copyright © 2013, American Chemical Society. Reprinted with permission from Ref.[201])

2.5.3. Conclusions

In conclusion, we successfully incorporated TR/CD-IC into electrospun PLA nanofibers in order to obtain nanofibrous webs having antibacterial property. TR did not form IC with α-CD, however, the complexation of TR with β-CD and γ-CD were succeeded, and 1:1 molar ratio of TR:CD was determined. By forming CD-IC, higher thermal stability was achieved for TR. More importantly, PLA/TR/CD-IC nanowebs have shown better antibacterial activity against *S. aureus* and *E. coli* when compared to PLA/TR nanoweb, since CD-IC can increase the solubility of TR which resulted in efficient release of this antibacterial agent from the nanowebs. PLA is a bio-derived biodegradable thermoplastic aliphatic polyester which is applicable in food packaging; therefore, PLA/TR/CD-IC electrospun nanowebs having very high surface area and nanoporous structure as well as having efficient antibacterial property facilitated by TR/CD-IC may be applicable in active food packaging.

CHAPTER 3

3. CYCLODEXTRIN FUNCTIONALIZED ELECTROSPUN NANOFIBERS

The work described in this chapter was published in part as:

(1) **Kayaci, F.**; Uyar, T., Electrospun zein nanofibers incorporating cyclodextrins. *Carbohydrate Polymers* 2012, *90* (1), 558-568. *DOI: 10.1016/j.carbpol.2012.05.078.*

(2) **Kayaci, F.**; Sen, H. S.; Durgun, E.; Uyar, T., Electrospun Nylon 6,6 Nanofibers Functionalized with Cyclodextrins for Removal of Toluene Vapor. *Journal of Applied Polymer Science* (submitted).

(3) **Kayaci, F.**; Uyar, T., Electrospun polyester/cyclodextrin nanofibers for entrapment of volatile organic compounds. *Polymer Engineering & Science* 2014. *DOI: 10.1002/pen.23858*.

(4) **Kayaci, F.**; Aytac, Z.; Uyar, T., Surface modification of electrospun polyester nanofibers with cyclodextrin polymer for the removal of phenanthrene from aqueous solution. *Journal of Hazardous Materials* 2013, *261*, 286-294. *DOI: 10.1016/j.jhazmat.2013.07.04*.

3.1. Summary

Our particular interest is the functionalization of electrospun polymeric nanofibers with cyclodextrins (CD) in order to combine their properties (see initial two parts of Chapter 1 (1.1 and 1.2)). Figure 40 indicated the schematic representation of the electrospinning of polymer/CD solution. Up to date, several studies have been carried out dealing with incorporation of CD in electrospun nanofibers for different purposes such as crosslinking of fiber matrix [265], molecular filtration [54, 266-268] and CD was also used as a reducing and stabilizing agent for gold [269] and silver [270] nanoparticles formation.

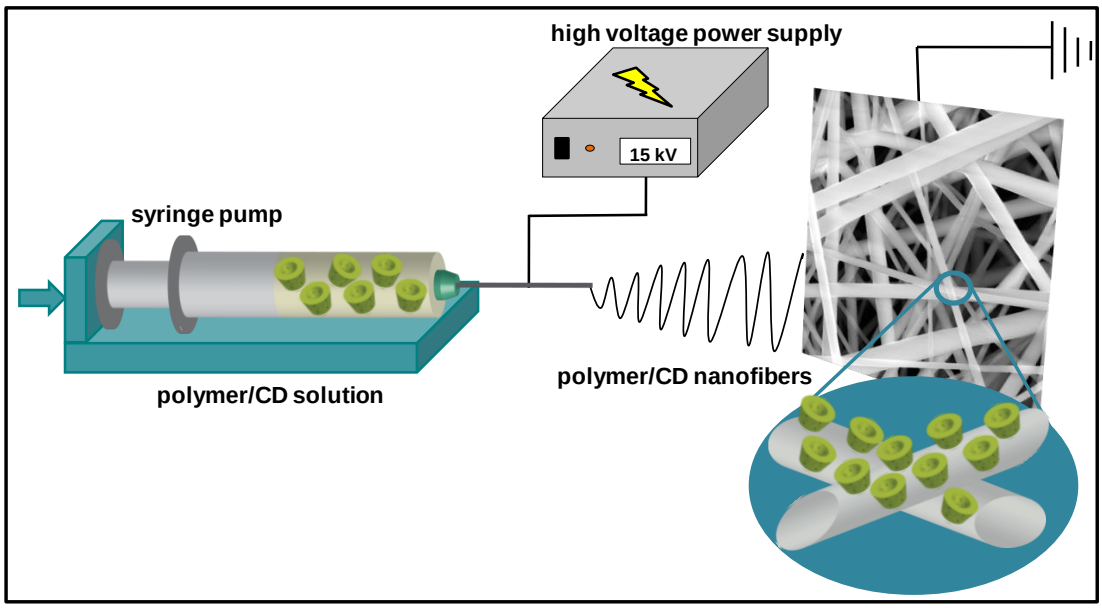

Figure 40. Schematic representatio of electrospinning of polymer/CD solution. (Copyright © 2014 Society of Plastics Engineers. Reproduced with permission from Ref.[271])

In the recent years, biopolymers from renewable resources such as zein have gained attention due to economical and environmental reasons [272-273]. Zein, the major protein of corn and a by-product of the bioethanol industry, is quite applicable as a biomaterial due to its non-toxic, biocompatible, biodegradable and film forming characteristics. Zein films and zein micro/nano particles can be used for encapsulation of essential oils, aromas and flavors, controlled release of active

additives and as a active food packaging material, etc. [274-278]. In the recent years, electrospinning of zein nanofibers have received some attentions as well [28, 279-285]. These studies mostly related to the optimization of the electrospinning parameters of zein nanofibers [28, 282-283], crosslinking of zein nanofibers [280-281, 284] and blending of zein with some other type of biopolymers [279, 285-286]. In addition, β-carotene which is a bioactive antioxidant [37] and (–)-epigallocatechin gallete that is a plant polyphenol [34] were incorporated into electrospun zein nanofiber matrix for the stabilization of these active additives.

In the next part of this Chapter (3.2), I report on the electrospinning of zein nanofibers incorporating CD. Electrospun zein/CD nanofibers were obtained by using three types of CD; α-CD, β-CD and γ-CD and the weight loadings of these CD were varied from 10% up to 50% (w/w) with respect to zein. This study mainly deals with the optimization of electrospinning of zein/CD nanofibers and their morphological, structural, surface and thermal characterizations [287]. These electrospun zein/CD nanofibers may have the potential to be used as active food packaging materials owing to very high surface area of zein nanofibers and surface associated CD molecules, since these CD molecules have inclusion complexation capability with various molecules and therefore removal of unpleasant odors from the surroundings can be achieved by CD.

Air pollution is undoubtedly major threat to the human health as industrialization and world population is growing day by day [141, 288]. In addition to aerosols, volatile organic compounds (VOC) into air are of the major pollutants daily inhaled, and can cause serious sicknesses such as fatigue, headache, and even cancer [288-292]. The necessity of removal of VOC from indoor and outdoor environments is of a high importance for a healthier life. Air filters can remove VOC by mostly adsorption [52, 291]. As it mention in the first part of Chapter 1 (1.1), the nanofibrous membranes obtained via electrospinning are desirable filtering materials due to their exclusive properties such as very high surface area to volume ratio, high adsorption capability, nanoporous structure, high permeability, low basis weight [23, 43-45, 48-49, 52, 293-294]. The design flexibility of the nanofibers with

chemical/physical functionalization either during electrospinning or post-processing may even promote their applicability in filtration [19, 51, 53, 295-297].

The electrospun nanofibrous membranes functionalized with active agents such as CD can provide efficient separation or purification performances, since CD functionalized nanofibers can entrap organic waste compounds from the surroundings [51, 54, 266-268, 298-301]. As it mention in the second part of Chapter 1 (1.2), CD have also shown potentials as a filtering material due to their capacity to remove organic waste molecules by inclusion complexation [81, 86]. Recently, several studies were reported for the removal of organic molecules from liquid media [266-268, 298-301] and vapor phase [54] by electrospun nanofibers incorporating CD. However, CD are water soluble, so physically bounded CD onto nanofibers could leach out from the nanofiber matrix during the filtration in aqueous medium. Yet, removal of VOC by CD functionalized nanofibers is possible without any leaching problem [54] since the nanofibrous membranes are not subjected to water, so these nanofibers can be promising filtering material for air filtration.

We have successfully produced the CD functionalized electrospun nylon 6,6 nanofibers (nylon 6,6/CD) by using α-CD, β-CD and γ-CD in two different % weight loading (25% and 50%, w/w, with respect to nylon 6,6) for the removal of toluene vapor as a model VOC from the environment. The modeling studies for formation of inclusion complex (IC) between CD and toluene were also performed using ab initio techniques by our collaborators, Dr. H. Sener Sen and Assist. Prof. Engin Durgun. We prepared a paper on this study, and submitted to Journal of Applied Polymer Science. Electrospun nylon 6,6 nanofibrous membranes have been indicated as a suitable material for filtration application in the literature [11, 302-303], which is the reason of the selection of the nylon 6,6 as a nanofibrous polymeric matrix in this study. This study was explained in the third part of this chapter (3.3).

In our research study mentioned in the fourt part of this chapter (3.4), for the entrapment of aniline vapor as a model VOC from the environment, polyester (PET) nanofibers incorporating CD by means of electrospinning [271]. Three types of native CD; α-CD, β-CD and γ-CD were used to functionalize PET nanofibers. PET

is a suitable polymer type for filtration application, and surface associated CD molecules onto PET nanofibers can entrap VOC from the surroundings for air filtration purpose.

As it mentioned in the previous section, CD are water soluble, therefore, they cannot be used directly as a filtering material for the removal of organic pollutants from water and wastewater. So, crosslinked and water-insoluble CD based polymers were synthesized for capturing organic pollutants from the surroundings [87]. Alternatively, CD molecules could be permanently immobilized by chemically grafting onto polymeric fibers [304-307], or the surface of the fibers could be modified by crosslinked CD polymer [308-310] for filtration purposes or delivery of additives. On the other hand, for the nanofibers incorporating CD in mentioned previous two studies, although most of the CD molecules were buried inside the fiber matrix, some CD molecules were present on the fiber surface, and only these surface associated CD molecules were effective for the removal of organic molecules from vapor phase. Consequently, permanent CD modification onto electrospun nanofibers would be ideal for designing novel filtering materials for water purification and wastewater treatment. Even though surface modifications of fibers and nonwoven fabrics by CD grafting [304, 306-307] or coating with crosslinked CD polymer [308-311] were reported, to the best of our knowledge, the surface modification of electrospun polymeric nanofibers with crosslinked CD polymer was not reported previously.

We have achieved the surface modification of the PET nanofibers with CD polymer (CDP) [299]. Water-insoluble and crosslinked CDP coating onto PET nanofibers was formed by the polymerization reaction between CD and crosslinking agent (see Figure 41). For a comparative study, three types of CD (α-CD, β-CD and γ-CD) were used in order to form CDP coating onto PET nanofibers. Water-insoluble crosslinked CDP coating was permanently adhered onto the PET nanofibers. The filtration performance of the PET/CDP nanofibrous mats was investigated by removal of a model polycyclic aromatic hydrocarbon (phenanthrene) from aqueous solution (see Figure 41). This study was reported in the last part of this Chapter (3.5).

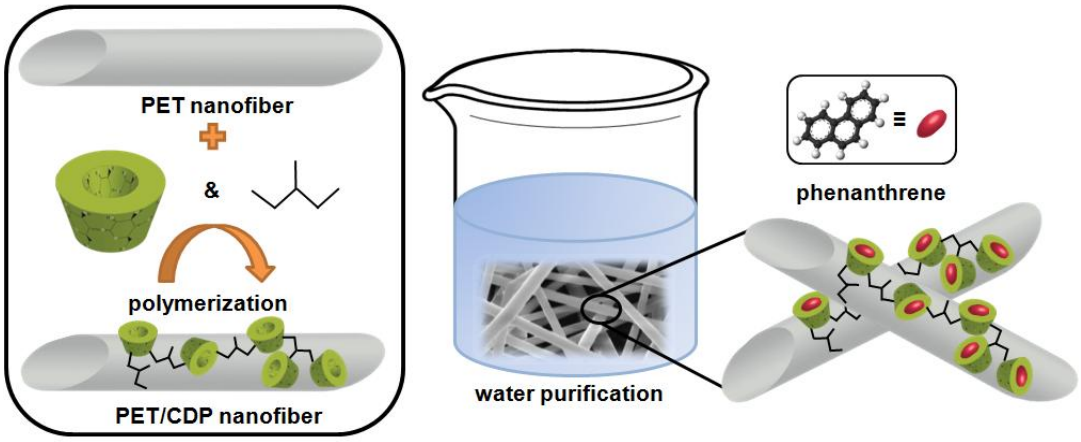

Figure 41. Schematic representations of the formation of PET/CDP nanofibers and removal of phenanthrene from aqueous solution using these nanofibrous mat. (Copyright © 2013, Elsevier. Reprinted with permission from Ref.[299])

3.2. Electrospinning of Zein Nanofibers Incorporating Cyclodextrins

3.2.1. Experimental

Materials: Zein from maize (Sigma-Aldrich) and N,N-dimethylformamide (DMF, Pestanal, Riedel) were purchased. The α-CD, β-CD and γ-CD were purchased from Wacker Chemie AG (Germany). All materials were used as-received without any purification.

Preparation of the Solutions: First, 40%, 50% and 60% (w/v) zein was dissolved in DMF and electrospinning of zein solutions without CD was performed. For the electrospinning of zein/CD solutions, 10%, 25% and 50% (w/w, with respect to zein) CD (α-CD, β-CD and γ-CD) were dissolved in DMF and then, 40%, 50% and 60% zein (w/v, with respect to solvent of DMF) was added to each CD solution separately and stirred for 1 h at room temperature. Homogeneous and clear solutions were obtained for all of the zein/β-CD compositions. On the other hand, the zein solutions containing 25% (w/w) α-CD was slightly turbid and also the solutions containing

50% (w/w) α-CD and γ-CD were highly turbid. After the preparation of the solutions, the resulting zein and zein/CD solutions were electrospun.

Electrospinning: The solutions were placed in a 3 mL syringe fitted with a metallic needle having inner diameter of 0.8 mm. The syringe was fixed horizontally on the syringe pump (Model: SP 101IZ, WPI). Several parameters were applied in order to optimize the electrospinning of the solutions and the optimal parameters were chosen as follows. Voltage of 15 kV was applied to the metal needle tip by using high voltage power supply (AU Series, Matsusada Precision Inc.). The polymer solution was pumped with flow rate of 0.5 mL/h during electrospinning and the tip-to-collector distance was set to 12 cm. The grounded stationary cylindrical metal collector (height: 15 cm, diameter: 9 cm) covered with aluminum foil was used for the deposition of the electrospun nanofibers. The electrospinning process was carried out at 24 ^{o}C and 30% relative humidity in enclosed Plexiglas box.

Measurements and characterization: The viscosity of the solutions was measured by using Anton Paar Physica MCR 301 Rheometer equipped with cone/plate accessory using the spindle type CP40-2 at 22 ^{o}C and a constant shear rate of 100 s^{-1}. The conductivity measurement of the solutions was performed by using Multiparameter meter InoLab®Multi 720 (WTW) at room temperature.The morphology and the diameter of the nanofibers were examined by using scanning electron microscope (SEM) (FEI–Quanta 200 FEG). The nanofibers were coated with 5 nm Au/Pd prior to SEM imaging. Around 100 fiber diameters were measured from the SEM images to determine the average fiber diameter (AFD) of the nanofibers. X-ray diffraction (XRD) data of the nanofibers were collected by using PANalytical X'Pert Powder diffractometer with Cu Kα radiation in a range $2\theta = 5^{o}$-30^{o}. Surface characterizations of the nanofibers were performed by attenuated total reflectance Fourier transform infrared spectroscopy (ATR-FTIR) (Bruker, VERTEX 70) and K-Alpha-Monochromated high-performance X-ray photoelectron spectrometer (XPS) (Thermo). The ATR-FTIR spectra were recorded from 700 to 4000 cm^{-1} with a resolution of 4 cm^{-1} by taking 64 scans for each sample, and these spectra were obtained with FTIR spectrometer equipped with a liquid nitrogen

cooled mercury cadminium telluride detector by using ATR set up containing a germanium crystal. XPS was used by means of a flood gun charge neutralizer system equipped with a monochromated Al K-α x-ray source (hν = 1486.6 eV). Wide energy survey scans were obtained over the 0–1360 eV binding energy range at a detector pass energy of 150 eV in order to determine the surface elemental composition of the nanofibers. The high resolution spectra were recorded for C 1s region at pass energy of 50 eV.

The thermal properties of the nanofibers were investigated by using differential scanning calorimetry (DSC) (TA Q2000) and thermal gravimetric analyzer (TGA) (TA Q500). DSC analyses were carried out with about 5 mg of samples under the N_2 as a purge gas. Initially, the samples were equilibrated at 25 ^oC then they were heated to 200 ^oC at 10^o C/min. TGA was performed from room temperature to 500 ^oC at a heating rate of 20 ^oC/min under the nitrogen atmosphere.

3.2.2. Results and Discussion

In the literature, the electrospinning of zein nanofibers was mostly carried out by using ethanol/water mixture solvent system which resulted in ribbon-like fiber morphology due to the rapid skin formation and collapse of the fiber core because of the very fast evaporation of the solvent [28, 282-283]. However, round-shaped zein nanofibers can be obtained by using solvent systems having high boiling points such as DMF [279]. In our study, the electrospinning of zein nanofibers was carried out by using DMF as a solvent system. The reason of choosing DMF is because thinner and more uniform zein fibers can be obtained [279] when compared to ethanol/water system [28, 282-283], and more importantly the other reason is that DMF is a very good solvent for CD, and therefore we were able to prepare zein/CD homogeneous solutions in most cases.

The characteristics (composition, viscosity and conductivity) of the zein and zein/CD solutions and the morphologies of the electrospun nanofibers and their AFD are summarized in Table 8. Zein solutions having different concentrations were electrospun in order to find the optimal polymer concentration for obtaining bead-

free uniform nanofibers. The representative SEM images of zein nanofibers electrospun from 40%, 50% and 60% (w/v) zein solution in DMF are depicted in Figure 42. At lower zein concentration (40% (w/v)), vastly micron size irregular spherical beaded structures were obtained due to the low viscosity of the polymer solution. As the concentration of zein solution was increased to 50% (w/v), the number of beads was decreased significantly and the shape of beads became more elongated and nanofibers having AFD of 80±35 nm were obtained. Uniform and bead-free zein nanofibers having AFD of 170±30 nm were obtained when 60% (w/v) zein solution was electrospun indicating that 60% (w/v) is the optimal zein concentration for producing uniform zein nanofibers at the applied electrospinning conditions. Our results correlate with the literature findings where the bead-free uniform zein nanofibers were produced above 50% (w/v) zein concentration when DMF was used a solvent system [279]. This behavior is very typical for the electrospinning of polymeric solutions where the transition from beaded structure to bead-free nanofibers is observed by increasing the polymer concentration. Higher polymer concentration resulted in higher solution viscosity due to the presence of more polymer chain entanglements and therefore the beaded structures are eliminated since the electrified polymer jet can be stretched fully yielding bead-free nanofibers [7, 242].

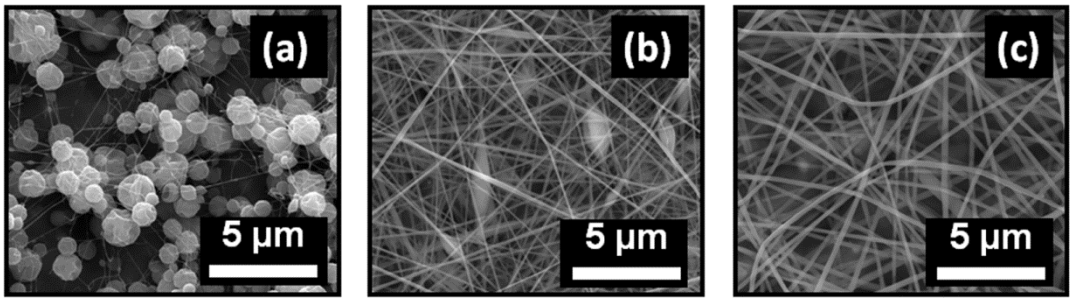

Figure 42. Representative SEM images of electrospun zein nanofibers obtained from zein solutions in DMF at a concentration of (a) 40%, (b) 50% and (c) 60% (w/v). (Copyright © 2012, Elsevier. Reprinted with permission from Ref.[287])

Table 8. Properties of zein and zein/CD solutions and the resulting zein and zein/CD nanofibers.

Solutions	Viscosity (Pa·s)	Conductivity (μS/cm)	Fiber morphology	AFD (nm)
zein40	0.0332	435	Nanofibers with many beads	-
zein50	0.0859	344	Nanofibers with few beads	80 ± 35
zein60	0.206	264	Bead-free nanofibers	170 ± 30
zein40/α-CD10	0.0421	359	Nanofibers with many beads	-
zein40/β-CD10	0.0428	357	Nanofibers with many beads	-
zein40/γ-CD10	0.0439	333	Nanofibers with few beads	60 ± 10
zein40/α-CD25	0.0522	270	Nanofibers with few beads	60 ± 20
zein40/β-CD25	0.0562	283	Nanofibers with few beads	70 ± 20
zein40/γ-CD25	0.0732	267	Nanofibers with few beads	60 ± 10
zein40/α-CD50	0.0849	96.8	Nanofibers with beads and aggregation CD crystals	-
zein40/β-CD50	0.0727	78.8	Nanofibers with beads	-
zein40/γ-CD50	0.101	115.6	Nanofibers with beads and aggregation CD crystals	-
zein50/α-CD10	0.125	286	Bead-free nanofibers	90 ± 20
zein50/β-CD10	0.171	278	Bead-free nanofibers	100 ± 25
zein50/γ-CD10	0.212	268	Bead-free nanofibers	110 ± 30
zein50/α-CD25	0.212	138	Nanofibers with aggregation CD crystals	185 ± 45
zein50/β-CD25	0.208	167	Bead-free nanofibers	150 ± 30
zein50/γ-CD25	0.239	161	Bead-free nanofibers	155 ± 35
zein50/α-CD50	0.39	74.3	Nanofibers with aggregation CD crystals	240 ± 85
zein50/β-CD50	0.381	97.8	Nanofibers with aggregation CD crystals	360 ± 140
zein50/γ-CD50	0.354	126.5	Nanofibers with aggregation CD crystals	265 ± 110
zein60/α-CD10	0.329	211	Bead-free nanofibers	225 ± 30
zein60/β-CD10	0.292	200	Bead-free nanofibers	185 ± 40
zein60/γ-CD10	0.218	189.4	Bead-free nanofibers	170 ± 40
zein60/α-CD25	0.69	89.8	Nanofibers with aggregation CD crystals	375 ± 80
zein60/β-CD25	0.441	113	Bead-free nanofibers	410 ± 130
zein60/γ-CD25	0.664	109.6	Bead-free nanofibers	380 ± 240
zein60/α-CD50	1.56	41.6	No fiber formation	-
zein60/β-CD50	1.02	85.6	No fiber formation	-
zein60/γ-CD50	0.752	85.8	No fiber formation	-

[a] With respect to solvent (DMF).
[b] With respect to polymer (zein).

The zein/CD solutions were clear and homogeneous except for the solutions containing higher weight percentage of α-CD and γ-CD. The zein/β-CD solutions were clear in all compositions whereas the zein/CD solutions containing 50% (w/w) α-CD and γ-CD were highly turbid, and zein/CD solutions containing 25% (w/w) α-CD were slightly turbid. The turbidity was observed possibly because of the precipitation of the α-CD and γ-CD at higher % loading, and it is anticipated that the electrospinning of these zein/CD solutions would contain CD aggregates in the fiber matrix. In the case of clear zein/CD solutions, the homogeneous distribution of the CD in the fiber matrix is expected for the electrospun zein/CD nanofibers containing lower amount of CD. The SEM imaging of the electrospun zein/CD nanofibers gave some insightful information for the presence of CD aggregates in the fiber matrix. The representative SEM images of the electrospun zein/CD nanofibers are depicted in Figure 43. It was observed that the addition of CD to zein solutions improved the electrospinnability, and less beaded structures and/or bead-free nanofibers were obtained at lower zein concentrations when compared to zein solutions without CD.

The electrospinning of 40% (w/w) zein solutions containing CD resulted in nanofibers having much less beaded structure when compared to 40% (w/w) pristine zein solution. Figure 43a shows the SEM images of electrospun zein/CD nanofibers obtained from 40% (w/v) zein solution containing 10%, 25% and 50% (w/w, with respect to zein) CD (α-CD, β-CD and γ-CD). The electrospinning of 40% (w/w) zein solutions containing 10% (w/w) CD resulted in reduction of beads to some extent (Figure 43(a1-a3)). In the case of zein40/γ-CD10 sample, the elimination of beads is much more pronounced which is possibly because of the higher solution viscosity compared to zein40/α-CD10 and zein40/β-CD10 solutions. Furthermore, it was clearly observed that the addition of 25% (w/w) CD to the 40% (w/v) zein solutions improved the electrospinnability of the zein/CD solutions, and yielded nanofibers with much less beads having more elongated structures (Figure 43(a4-a6)). This is possibly because of the higher solution viscosity of zein/CD systems where the beaded structures are mostly eliminated due to the more stretching of electrified solution jet.

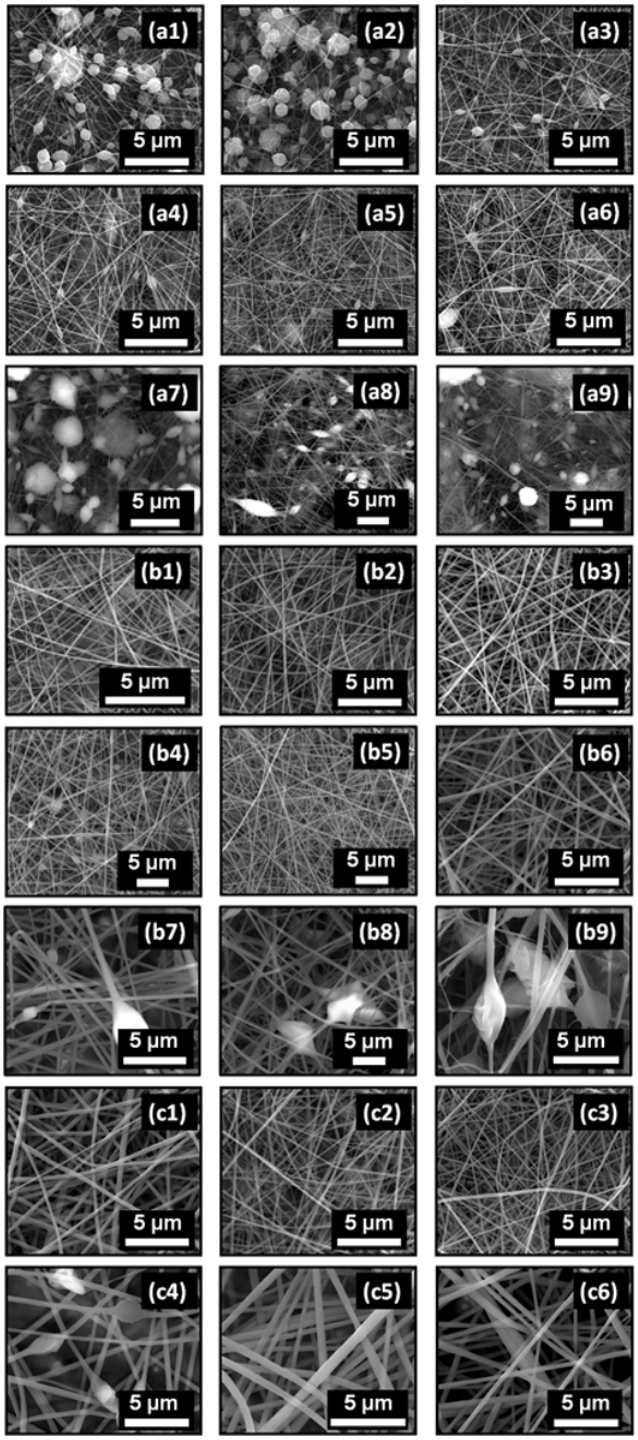

Figure 43. Representative SEM images of electrospun nanofibers of (a1) zein40/α-CD10, (a2) zein40/β-CD10, (a3) zein40/γ-CD10, (a4) zein40/α-CD25, (a5) zein40/β-CD25, (a6) zein40/γ-CD25, (a7) zein40/α-CD50, (a8) zein40/β-CD50 and (a9) zein40/γ-CD50; (b1) zein50/α-CD10, (b2) zein50/β-CD10, (b3) zein50/γ-CD10, (b4) zein50/α-CD25, (b5) zein50/β-CD25, (b6) zein50/γ-CD25, (b7) zein50/α-CD50, (b8) zein50/β-CD50 and (b9) zein50/γ-CD50; (c1) zein60/α-CD10, (c2) zein60/β-CD10, (c3) zein60/γ-CD10, (c4) zein60/α-CD25, (c5) zein60/β-CD25 and (c6) zein60/γ-CD25. (Copyright © 2012, Elsevier. Reprinted with permission from Ref.[287])

However, even the addition of 50% (w/w) CD resulted in more viscous solutions, the electrospinning of these zein/CD yielded nanofibers having irregular structures (Figure 43(a7-a9)) suggesting that uniform zein/CD nanofibers cannot be produced when the high weight % of CD was used, and these CD aggregates possibly could not be stretched out along the fiber matrix during the electrospinning process. The irregular structures consisting of not only beads but also CD aggregates were much more prominent in zein40/α-CD50 and zein40/γ-CD50 nanofibers when compared to zein40/β-CD50, since the zein40/α-CD50 and zein40/γ-CD50 solutions were highly turbid prior to electrospinning indicating that CD aggregates were already present in the solution, and these CD aggregates possibly could not be stretched out along the fiber matrix during the electrospinning process. In the case of zein40/β-CD50, the beads were less in number since the zein40/β-CD50 solution was clear, and some CD aggregates were possibly formed during the electrospinning process when the solvent evaporation took place.

The electrospinning of 50% (w/v) zein solution yielded nanofibers with few beads as mentioned above (Figure 42b), however, bead-free nanofibers were obtained from 50% (w/v) zein solution with the addition of 10% and 25% (w/w) CD (α-CD, β-CD and γ-CD) except for zein50/α-CD25 system (Figure 43b). In the case of zein50/α-CD25 nanofibers, some irregular structures were observed which is because of the presence of α-CD aggregates as discussed later in the XRD section. Similar to 40% (w/v) zein system, the addition of 50% (w/w) CD in 50% (w/v) zein solution yielded nanofibers having irregular structures due to the aggregation of CD crystals as confirmed by XRD results. It was clear that the addition of CD in certain ratios (10% and 25% w/w, except for 25% α-CD) to the 50% (w/v) zein solutions assisted to eliminate the bead formation and provided bead-free zein/CD nanofibers without increasing polymer concentration. We observed similar effect on the morphology of the electrospun PS [312], PMMA [313] and PEO [314] nanofibers containing CD in our recent studies.

The electrospinning of 60% zein (w/v) solutions containing 10% and 25% (w/w) CD resulted in bead-free nanofiber morphology except for zein60/α-CD25

system (Figure 43c). The zein60/α-CD25 nanofibers have some bead-like structures similar to zein50/α-CD25 system which is possibly due to CD aggregates. Furthermore, 60% zein (w/v) solution containing 50% (w/w) CD could not be electrospun due to very high viscosity of the solutions.

In brief, the addition of CD to zein solutions significantly affected the electrospinning, and bead-free nanofibers were obtained from lower zein concentrations for zein/CD systems when compared to pure zein solution. This is mostly due to the higher viscosity of the zein/CD solutions, and higher solution viscosity resulted in more uniform fibers when electrospun [7, 242]. In addition, the morphologies of the zein/CD nanofibers containing different kind of CD (α-CD, β-CD and γ-CD) have shown slight variations among each other because of the differences in viscosity and conductivity of these solutions. Table 8 summarizes the AFD of the zein and zein/CD nanofibers. It was observed that the AFD increases as the content of the CD increases since the presence of CD causes a viscosity increase of the solutions while it reduces the conductivity of the solutions. Therefore, zein/CD solutions having higher viscosity and lower conductivity values yielded thicker fibers due to the less stretching of the electrified jet [7, 242].

The XRD patterns of electrospun zein nanofibers and zein/CD nanofibers were depicted in Figure 44 and the XRD patterns of as-received CD were also shown for comparison. Zein nanofibers have shown two broad peaks having maxima at $2\theta = 8.99°$ (9.8 Å) and at $2\theta = 19.38°$ (4.58 Å). It is reported that the larger d-spacing around 10 Å is associated with the mean distance of approach of neighboring helices (the spacing of the inter-helix packing of zein chains) whereas the shorter d-spacing at around 4.5 Å is related to the average backbone distance within α-helix structure of zein [285].

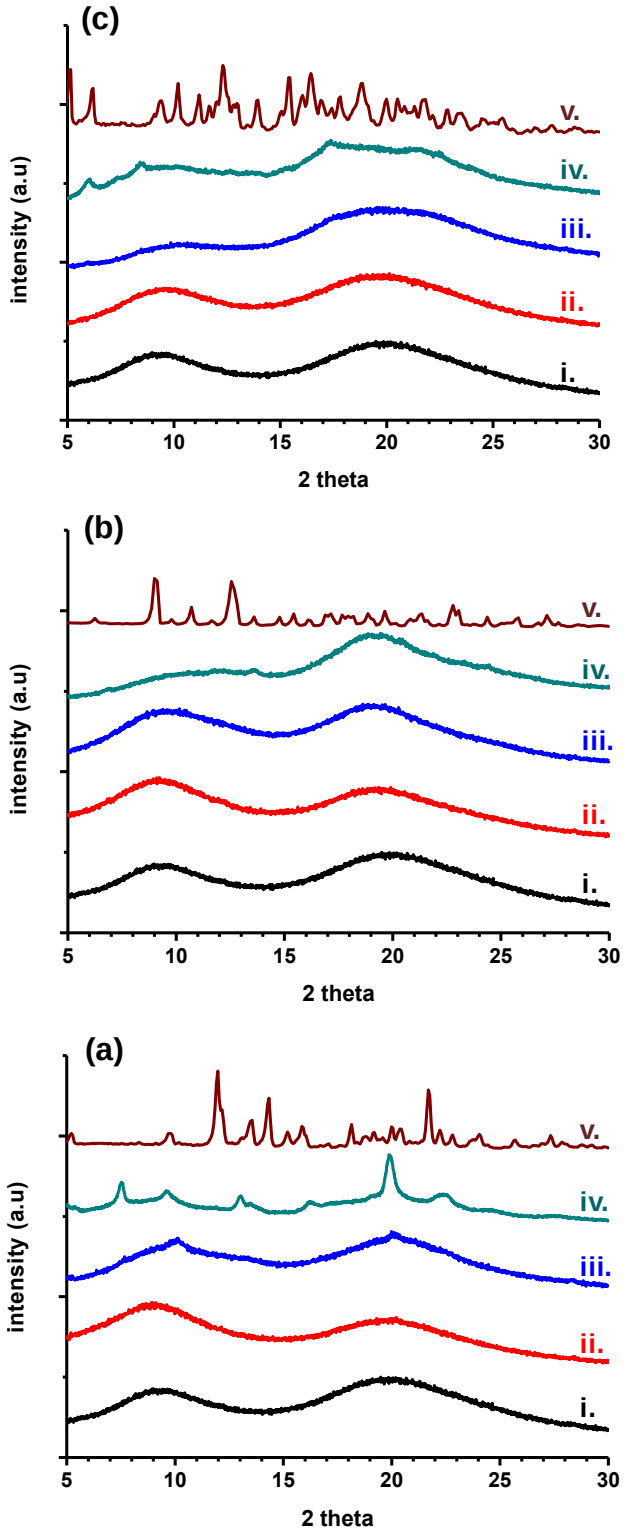

Figure 44. XRD patterns of (a) (i) zein50, (ii) zein50/α-CD10, (iii) zein50/α-CD25, (iv) zein50/α-CD50 and (v) α-CD ; (b) (i) zein50, (ii) zein50/β-CD10, (iii) zein50/β-CD25, (iv) zein50/β-CD50 and (v) β-CD ; (c) (i) zein50, (ii) zein50/γ-CD10, (iii) zein50/γ-CD25, (iv) zein50/γ-CD50 and (v) γ-CD. (Copyright © 2012, Elsevier. Reprinted with permission from Ref.[287])

CD (α-CD, β-CD and γ-CD) are crystalline materials having distinct diffraction patterns at 2θ = 5-30° (Figure 44). CD generally have two types of crystal structures; in 'cage-type' the cavity of each CD molecule is blocked by the adjacent CD molecules whereas the CD molecules are aligned and stacked on top of each other in the 'channel-type' structure. The XRD of as-received CD have shown diffraction patterns for 'cage-type' crystalline structures as reported in the literature [227-228, 230].

Some structural changes were observed for the zein/CD nanofibers depending on the weight percentage and type of CD. The XRD of zein50/α-CD10 nanofibers have shown two broad halo diffraction patterns centered at 2θ = 8.94° (9.9 Å) and at 2θ = 20.18° (4.4 Å) which is very similar to the zein nanofibers. The diffraction peaks for the α-CD crystals were absent in this sample indicating that α-CD molecules were distributed in the zein fiber matrix without forming any phase separated crystal aggregates. For zein50/α-CD25 and zein50/α-CD50 nanofibers, the decrease of the peak at 2θ = 8.99° suggested that the spacing of the inter-helix packing of zein chains was disturbed and the zein molecular aggregates were somehow destroyed with the presence of α-CD at higher weight percentages. Moreover, slightly intense diffraction peaks were observed for zein50/α-CD25 nanofibers suggesting that some aggregation of α-CD crystals was present in this sample. The α-CD crystalline peaks were much more pronounced for the zein50/α-CD50 sample. This finding correlates with the SEM images where the bead-like structures for zein50/α-CD25 and irregular structures for zein50/α-CD50 were observed for these samples due to the presence of some α-CD aggregates. The XRD pattern corresponds to channel-type packing of α-CD since the salient diffraction peak 2θ ≅ 20° is characteristic for the α-CD channel channel-type [227-228, 230]. In general, the 'channel-type' packing of CD is associated with the inclusion complex (IC) state. For instance, *Tonelli et al.* reported that protein based polymer such as bombyx mori silk fibroin can form an IC with γ-CD [315]. However, here we did not anticipate the inclusion complexation of zein with α-CD due to the small size cavity of α-CD. As mentioned in the experimental part, the zein50/α-CD25 and zein50/α-CD50 solutions were turbid and it is most likely that α-CD precipitated as 'channel-

type' crystals in the zein/DMF solution system. We have also observed similar situations for electrospun PS containing α-CD where the α-CD precipitated as 'channel-type' crystals without forming inclusion complexation [312]. Additionally, the XRD of zein50/β-CD50 and zein50/γ-CD50 have also shown some diffraction peaks due to the presence of some CD crystalline aggregates but these diffractions did not correspond to channel-type packing suggesting that CD were not in the complex state with zein chains in zein50/CD50 nanofibers. In XRD, the typical channel-type β-CD has two major peaks at 2θ≅ 11.5° and 18° [229]. and the characteristic diffraction for channel-type γ-CD has one major peak at 2θ≅ 7.5° with minor reflections at 2θ≅ 14°, 15°, 16°, 16.8° and 22° [85]. However, for zein50/β-CD50 and zein50/γ-CD50 nanofibers, the diffraction peaks were different than the channel-type packing as discussed below.

In XRD, it was observed that the diffraction patterns of zein50/β-CD10 and zein50/β-CD25 nanofibers were very similar to that of pure zein nanofibers (Figure 44b). In the case of zein50/β-CD50 nanofibers, the intensity of first peak at around 2θ = 9.0° was lowered significantly indicating that the inter-helix packing of zein molecular aggregates were substantially disturbed. In addition, very weak diffraction peaks at around 2θ = 6.9°, 13.6° and 24.4° were observed for this sample possibly because of the presence of some β-CD aggregates in the fiber matrix. However, these peaks did not correspond to either cage-type packing or channel-type packing indicating that the regular packing of β-CD was disturbed by the zein chains. For zein50/β-CD10 and zein50/β-CD25 nanofibers, no crystalline peaks were observed suggesting that β-CD molecules were distributed in the fiber matrix without forming any crystal aggregates.

In the case of zein/γ-CD nanofiber samples, the incorporation of γ-CD into zein fiber matrix has a very similar structural effect as seen for zein/α-CD and zein/β-CD. The XRD pattern of zein50/γ-CD10 nanofibers was similar to pure zein nanofibers showing two distinct broad halo at around 2θ = 9° and 2θ = 20° (Figure 44c). The incorporation of 25% and 50% (w/w) γ-CD to fiber matrix resulted in disruption of inter-helix packing of zein chains as deduced from the XRD patterns of

zein50/γ-CD25 and zein50/γ-CD50 since the peak at around 2θ = 9° was considerably weakened. In addition, certain diffraction peaks at around 2θ = 6°, 8.4° and 17.4° were observed for zein50/γ-CD50 sample suggesting that some crystalline γ-CD aggregates were present in this sample as observed in the SEM image of this sample. Yet, these peaks somewhat different than the cage-type packing or channel-type packing suggesting that γ-CD packing was disturbed by the zein chains which was similarly observed for the zein50/β-CD50.

In brief, it was observed that the shorter d-spacing ca 4.5 Å correlated to the average backbone distance in α-helix structure of zein did not change with the addition of CD, while the intensity of the larger d-spacing around 9 Å associated with the mean distance of approach of neighboring helices decreased significantly as the content of CD increased from 10% thru 50% (w/w) in zein/CD nanofibers. This result implied the structural changes depending on the side-chain packing were observed for zein with the addition of CD. Moreover, XRD data suggested that CD were mostly distributed in the zein fiber matrix without forming crystalline aggregates at lower weight percentages (10% of α-CD, and 10% and 25% of β-CD and γ-CD), but, incorporation of 25% α-CD and 50% of all three types of CD yielded some crystalline CD aggregates in the zein fiber matrix.

The surface analyses of zein/CD nanofibers were performed by using surface sensitive techniques, ATR-FTIR and XPS, in order to corroborate the presence of CD on the surface of the zein nanofibers. The ATR-FTIR spectra of the electrospun zein nanofibers and zein/CD nanofibers are shown in Figure 45(a1-a3). Zein protein backbone has two characteristic vibrational bands; amide I and amide II bands. The characteristic absorption band of amide I corresponds to the C=O stretching, while that of amide II corresponds N–H bending and C–N stretching [37, 285]. The characteristic absorption bands at 1653 and 1540 cm^{-1} indicated the presence of amide I and amide II, respectively for pure zein nanofibers (Figure 45(a1-a3)).

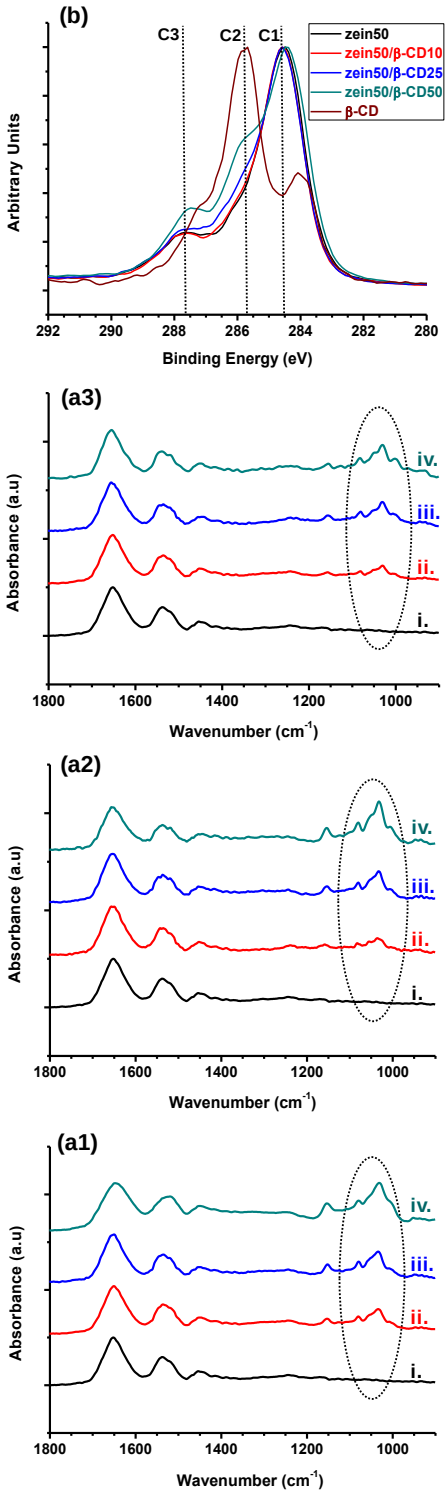

Figure 45. ATR-FTIR spectra of electrospun nanofibers of (a1) (i) zein50, (ii) zein50/α-CD10, (iii) zein50/α-CD25 and (iv) zein50/α-CD50, (a2) (i) zein50, (ii) zein50/β-CD10, (iii) zein50/β-CD25 and (iv) zein50/β-CD50, (a3) (i) zein50, (ii) zein50/γ-CD10, (iii) zein50/γ-CD25 and (iv) zein50/γ-CD50; (b) Overlay of XPS C1s spectra of the zein, zein/β-CD nanofibers and pure β-CD. (Copyright © 2012, Elsevier. Reprinted with permission from Ref.[287])

The characteristic peak of coupled C–C/C–O stretching vibrations and the antisymmetric stretching vibration of the C–O–C glycosidic bridge of CD were observed for zein/CD nanofibers at 1028, 1080 and 1150 cm^{-1}, respectively [313]. It was also clear that the intensity of CD related peaks was increased as the CD content increased from 10% thru 50% w/w in the zein/CD nanofibers. The ATR-FTIR data confirmed the successful incorporation of CD in the zein nanofibers and some CD were present on the surface of the zein/CD nanofibers.

In ATR-FTIR study, it was observed that the amide I and amide II peaks were slightly shifted to lower wavenumber for zein/CD nanofibers when compared to pure zein nanofibers. For instance, the amide I peak was observed at 1651, 1650 and 1648 cm^{-1} for zein50/α-CD10, zein50/α-CD25 and zein50/α-CD50, respectively. Similarly, the amide II peak was shifted to lower wavenumber as the weight % of the α-CD was increased from 10% thru 50%. That is, absorption peak of amide II was observed at 1536, 1535 and 1520 cm^{-1} for zein50/α-CD10, zein50/α-CD25 and zein50/α-CD50, respectively. The peak shift of amide I and amide II to lower wavenumbers for zein/CD nanofibers suggested the presence of interaction between zein and α-CD, and the interaction became more pronounced for nanofiber samples having higher loading of α-CD. In the case of zein/β-CD and zein/γ-CD nanofiber samples, the shift in the amide I was not that significant but the amide II peak was shifted to around 1535 cm^{-1} suggesting the presence of interaction between CD molecules and zein chains for these samples as well. But, the peak shift for amide I and amide II was much more significant in the case of zein/α-CD nanofibers compared to zein/β-CD and zein/γ-CD nanofibers possible because α-CD has smaller size which can interact more with the zein chains.

As observed in the SEM imaging, the more uniform nanofibers were obtained in the case of β-CD, therefore, more detailed surface analyses and thermal characterizations were carried out for zein/β-CD nanofibers. The in-depth surface chemistry analyses for zein/β-CD nanofibers were performed by X-ray photoelectron spectroscopy (XPS) in order to determine to what extent β-CD molecules are present on the surface of the zein fiber. Table 2 shows elementary compositions based on

wide energy survey spectra of the β-CD, zein nanofibers and zein/β-CD nanofibers. Oxygen content outer surface of the samples was increased with the increasing the amount of β-CD (from 10% to 50% (w/w)) used in the electrospinning of nanofibers. High energy resolution C 1s spectra were also recorded to get more detailed information about surface chemistry of the zein/β-CD nanofibers. The overlays of the C 1s spectra of the zein nanofibers, zein/β-CD nanofibers and β-CD that are normalized are given in Figure 45b. There are three different components for all of the C 1s high-resolution spectra. The position of one is at around 284.5 eV, C1, is assigned to aliphatic carbons, C–C and/or C–H [266-267, 277, 312]. It is a prominent peak for pure zein nanofibers. The component C2 at about 285.7 eV is arisen from either C–O–C or C–OH; and C3 (correlated to O–C–O) located at around 287.7 were found in both zein nanofibers and β-CD [266-267, 277]. The peaks are more distinctive for β-CD, therefore the relative concentrations of C2 and C3 increased with increasing amount of the β-CD used in the preparation of zein/β-CD nanofibers. It is found that the increase in oxygen content is due to the presence of C–O–C / C–OH and/or O–C–O on the surface of zein nanofibers. The presence of the β-CD on the surface of the zein/β-CD nanofibers is confirmed with these results. On the other hand, the β-CD concentration of the probed volume is calculated as approximately 4%, 7% and 13% for zein/β-CD10, zein/β-CD25 and zein/β-CD50, respectively from the elementary compositions in Table 9. The surface content of CD for all three zein/β-CD samples is lower than the CD content of the solutions they were prepared from. This indicates that the some of the CD molecules located on the fiber surface whereas some CD molecules are buried in the bulk of the fiber matrix. Zein is a useful food packaging material [274, 277], and CD have inclusion complexation capability with variety of molecules including aromas, colors, antioxidants, antibacterials, odors, and other functional ingredients [58-60], therefore, zein/CD nanofibers and their nanowebs may have the potentials to be used as active food packaging [316-317] materials owing to surface associated CD molecules and their high surface areas.

Table 9. Atomic concentrations generated from XPS wide energy survey scans.

samples	C (%)	O (%)	N (%)
β-CD	36.61	63.39	-
zein50	78.19	13.04	8.77
zein50/β-CD10	77.06	15.14	7.8
zein50/β-CD25	75.43	16.25	8.32
zein50/β-CD50	72.62	18.64	8.74

The thermal characteristics of the zein/β-CD nanofibers were studied by differential scanning calorimetry (DSC) and thermogravimetric analyzer (TGA). Figure 46(a1,a2) displays the DSC thermograms of zein nanofibers and zein/β-CD nanofibers containing 10%, 25% and 50% (w/w) β-CD. Zein nanofibers and zein/β-CD nanofibers have shown a broad endothermic peak having a peak maximum at around 100 °C in the DSC thermogram indicating that the samples contain some amount of water. The glass transition temperature (T_g) of the samples were also detected from the DSC thermograms. The T_g of the pure zein nanofibers was observed at around 154 °C which is in close agreement with the T_g value reported in the literature for zein [28, 318]. The T_g values for zein50/β-CD10, zein50/β-CD25 and zein50/β-CD50 nanofibers were observed at around 158 °C, 165 °C and 172 °C, respectively. It was clear that the higher T_g values were observed as the weight loadings of β-CD was increased from 10% thru 50%. The addition of CD in the zein nanofibers caused an increase in the T_g values which is possibly due to the less chain mobility of zein in the presence of CD.

Figure 46b shows the TGA thermograms of pure β-CD, zein nanofibers and zein/β-CD nanofibers. The TGA of pure β-CD has an initial weight loss (~12%) below 100 °C and major weight loss between 325-350 °C owing to water loss and main degradation of β-CD, respectively [16]. Similarly, water loss for zein nanofibers and zein/β-CD nanofibers were also observed but the water weight percentage was around 3-5% (w/w) indicating that less amount of water was present in the nanofibers. In addition, another minor weight loss regime between 125-200 °C was

observed for zein nanofibers and zein/β-CD nanofibers. This weight loss is possibly due to the presence of remaining solvent (DMF) in the nanofiber samples. The major weight loss for the zein nanofibers was recorded at around 275-350 °C which is consistent with the main degradation temperature reported for the electrospun zein nanofibers [319-320]. Since the degradation temperature for zein and β-CD was overlapped, we observed a single but broader weight loss for zein/β-CD nanofibers. Moreover, we observed that the thermal degradation of zein/CD nanofibers was shifted slightly to higher temperature with increasing β-CD content. Hence, zein/β-CD nanofibers have shown slightly higher degradation temperature compared to pure zein nanofibers indicating that the incorporation of the CD molecules in the zein fiber matrix resulted in higher thermal stability.

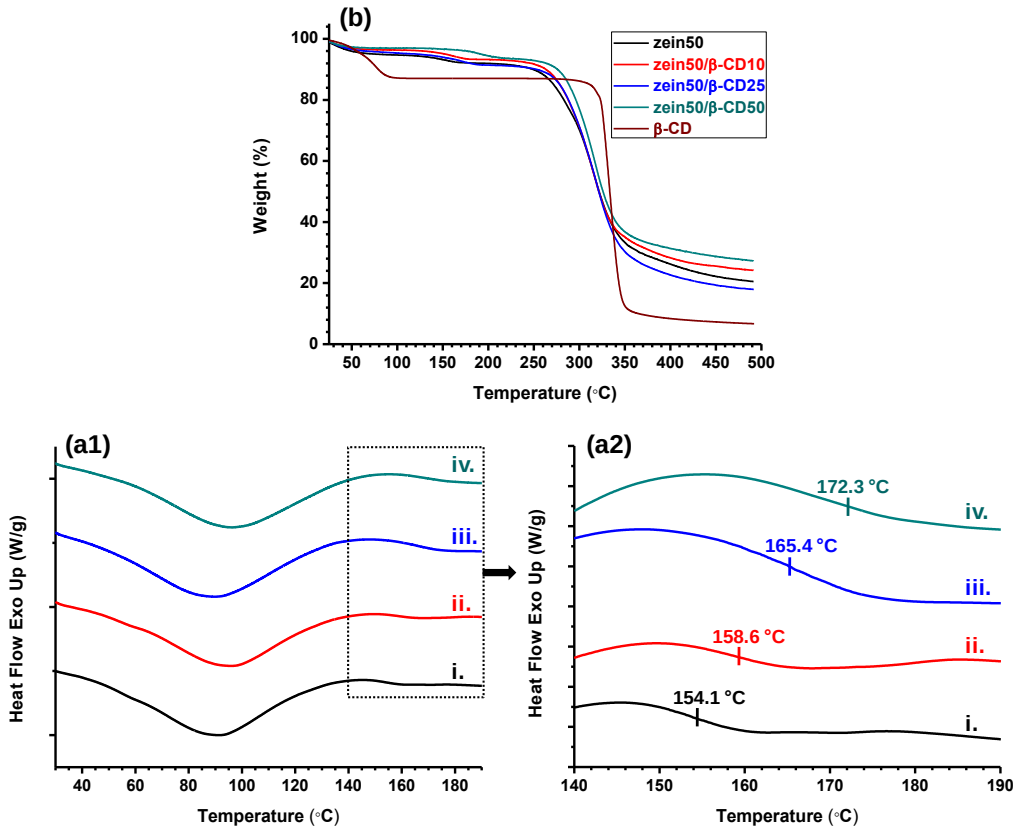

Figure 46. (a1) DSC thermograms of electrospun nanofibers, and (a2) Magnified views of Tg values of (i) zein50, (ii) zein50/β-CD10, (iii) zein50/β-CD25 and (iv) zein50/β-CD50; (b) TGA thermograms of zein50, zein50/β-CD nanofibers and β-CD. (Copyright © 2012, Elsevier. Reprinted with permission from Ref.[287])

3.2.3. Conclusions

Zein/CD nanofibers were obtained from electrospinning of zein/CD solutions in DMF. Three tpes of CD (α-CD, β-CD and γ-CD) using different weight loadings (10%, 25% and 50% w/w) were incorporated in zein solutions having various concentrations (40%, 50% and 60% w/v), and these zein/CD solutions were successfully electrospun. We found that the addition of CD in the zein solutions caused an increase in solution viscosity and therefore resulted in improvement of the electrospinnability, and less beaded structures and/or bead-free zein/CD nanofibers were obtained at lower zein concentrations when compared to pristine zein solutions. Depending on the zein concentration, CD weight percentage and CD type, bead-free zein/CD nanofibers having fiber diameters in the range of ~100 nm thru ~400 nm were obtained. The morphological, structural, surface and thermal characterizations of zein/CD nanofibers were studied by SEM, XRD, ATR-FTIR, XPS, DSC and TGA. SEM imaging revealed that the morphologies of the electrospun zein/CD nanofibers were significantly affected by the CD weight percentage and CD type added in zein/CD solutions. XRD study suggested structural changes for zein chain packing where the spacing of the inter-helix packing of zein chains was disturbed with the addition of CD, in addition, it was found that CD were mostly distributed in the fiber matrix without forming crystalline aggregates when lower weight percentages of CD were used (10% and 25% of β-CD and γ-CD and 10% of α-CD), however, incorporation of 50% of all three types of CD and 25% of α-CD yielded crystalline aggregates in the zein fiber matrix. The thermal analyses carried out by DSC and TGA indicated the improvement of thermal properties for zein/β-CD nanofibers, that is, zein/β-CD nanofibers have shown higher glass transition temperature and higher degradation temperature with increasing β-CD content when compared to pristine zein nanofibers. The surface analyses by ATR-FTIR and XPS elucidated that some amount of CD molecules were present on the surface of zein/β-CD nanofibers. These electrospun zein/CD nanofibers may have the potential to be used as active food packaging materials owing to very high surface area of zein nanofibers and surface associated CD molecules since CD molecules have inclusion

complexation capability with various molecules and therefore removal of unpleasant odors from the surroundings can be achieved by CD.

3.3. Electrospun Nylon 6,6 Nanofibers Functionalized with Cyclodextrins for Removal of Toluene Vapor

3.3.1. Experimental

Materials: Three types of native CD (α-CD, β-CD and γ-CD) were purchased from Wacker Chemie AG. Nylon 6,6 pellets (relative viscosity: 230.000-280.000),formic acid (98-100%), toluene (puriss., ≥99.5%), and acetonitrile chromasolv (ACN, 99.9%)were purchased from Sigma-Aldrich. All chemicals were used as-received without any further purification.

Preparation of the solutions for electrospinning: First, nylon 6,6 solution without CD was prepared by dissolving 10% (w/v) nylon 6,6 in formic acid. In the case of nylon 6,6/CD solutions, α-CD, β-CD and γ-CD in different ratio (25% and 50%, w/w, with respect to nylon 6,6) were dissolved in formic acid and then, nylon 6,6 (10%, w/v) was added to each CD solution individually and stirred for 3 h at room temperature to obtain homogeneous and clear solutions. Table 10 summarizes the compositions of the resulting nylon 6,6 and nylon 6,6/CD solutions used for electrospinning.

Electrospinning: The individual nylon 6,6 and nylon 6,6/CD solutions were loaded into 10 mL syringes fitted with metallic needles (~0.7 mm inner diameter). The syringes were placed horizontally on the syringe pump (KDS 101, KD Scientific). The feed rate of the solutions was set to 1 mL/h during electrospinning. The high voltage power supply (Matsusada, AU Series) was used to apply a voltage of +15 kV for the electrospinning. Randomly oriented nanofibers were deposited on a grounded stationary cylindrical metal collector (height: 15 cm, diameter: 9 cm) covered by a piece of aluminum foil and located at 10 cm from the end of the tip. The

electrospinning process was performed at ~23 °C and 29% relative humidity in an enclosed Plexiglas chamber.

Measurements and characterizations: Anton Paar Physica MCR 301 Rheometer equipped with cone/plate accessory (spindle type CP40-2) was used to measure the viscosity of the each solution used for electrospinning at 22 oC and a constant shear rate of 100 s-1. Scanning electron microscope (SEM, FEI-Quanta 200 FEG) was employed to investigate the morphology and dimensions of nylon 6,6and nylon 6,6/CD nanofibers. A nominal 5 nm Au/Pd was sputtered on the samples prior to SEM analysis. The average fiber diameters (AFD) of the samples were determined taking about 100 measurements from the SEM images of each sample. X-ray diffraction (XRD) patterns of the nanofibers were recorded in the range of 2θ=5˚-30˚ using PANalytical X'Pert Pro Multi Purpose X-ray diffractometer with Cu Kα radiation (λ=1.5418 Å). Thermogravimetric analyzer (TGA, TA Q500) was used to investigate the thermal properties of the nanofibers. TGA measurements were performed from room temperature to 600 °C at a constant heating rate of 20 °C/min under the nitrogen atmosphere. The surface chemical characterizations of the nanofibers were performed by attenuated total reflectance Fourier transform infrared spectroscopy (ATR-FTIR, Bruker, VERTEX 70) and X-ray photoelectron spectroscopy (XPS, Thermo Scientific K-Alpha, monochromated Al Kα X-ray source, hν=1486.6 eV) with flood gun charge neutralizer. The ATR-FTIR spectra were recorded with FTIR spectrometer equipped with ATR set up containing a germanium crystal and a liquid nitrogen-cooled mercury cadminium telluride detector. Each spectrum over a range 900-3700 cm−1was obtained with a resolution of 4 cm−1 by taking 64 scans.XPS wide energy survey scans (0–1360 eV) and the O 1s core-level spectra were obtained from the surface of the samples (400 μm spot size) at pass energy of 150 and 50 eV with energy step size of 1 and 0.1 eV, respectively. Peak deconvolutions for the core-level spectra were performed with Avantage software.

Entrapment of toluene vapor by the nanofibrous membranes: Toluene was used as a model VOC in order to investigate the molecular entrapment capability of the

nylon 6,6, nylon 6,6/25α-CD, nylon 6,6/25β-CD, nylon 6,6/25γ-CD, nylon 6,6/50α-CD, nylon 6,6/50β-CD and nylon 6,6/50γ-CD nanofibers. The nanofibrous membranes were exposed to the toluene vapor in a sealed glass desiccator (30 cm (diameter) and30cm (height)). In this experiment, a glass Petri dish including 20 mL of toluene (as-received, without any dilution) was located at the bottom of desiccator while three pieces of each sample (about 22 mg, 4x4 cm2) were placed on the supporting layer positioned at 7 cm high from the bottom of desiccator. After the electrospun nanofibrous membranes were kept in this sealed desiccator for 12 hours to expose to excess toluene vapor, they were taken out of the desiccator and kept in the suction hood for 5 hours in order to remove the uncomplexed toluene molecules that were only adsorbed on the membranes. Finally, high performance liquid chromatography (HPLC, Agilent 1200 series) equipped with VWD UV detector was used in order to determine the amount of toluene entrapped by the membranes. For this, each membrane was immersed in 4 mL ACN and kept in it for 2 hours to extract toluene from the membranes. Then 0.5 mL of these solutions wasput into HPLC vials, individually to measure toluene concentration in them. Injection volume was set to 5 µL and toluene was detected at 254 nm, in 4 min using the Agilent C18 column (150 mm x 4.6 mm, 5 µm pores) and ACN (100%) as a mobile phase with the 0.5 mL/min of flow rate. The toluene peak areas in the resulting HPLC chromatograms were converted to toluene concentration using the calibration curve (R2=0.999) that was prepared using toluene solutions having different concentrations (58, 29, 14.5, 7.2, 3.6, 1.8 and 0.9 ppm).

Computational Method: The structures of toluene, α- [258-259], β- [260], and γ-CD [261], and their IC were optimized by using ab initio methods based on density functional theory (DFT) [251-252] implemented in the Vienna ab initio simulation package [253-254]. The initial geometries were obtained from Cambridge Structural Database [262]. The exchange-correlation was treated within Perdew-Burke-Ernzerh of parametrization of the generalized gradient approximation (GGA-PBE) [255] with inclusion of Van der Waals correction [256]. The element potentials were described by projector augmented-wave method [257] using a plane-wave basis set with a kinetic energy cutoff of 400 eV. The Brillouin zone integration was performed at the

gamma-point. All structures were considered as isolated molecules in a vacuum and were relaxed using the Kosugi algorithm with simultaneous minimization of the total energy and interatomic forces. The convergence on the total energy and force was set to 10-5eV and 10-2eV/Å, respectively.

3.3.2. Results and Discussion

The representative SEM images of nylon 6,6 and nylon 6,6/CD nanofibers are given in Figure 47. Bead-free nanofibers were yielded from the nylon 6,6 (10%, w/v) solutions both without and with CD.

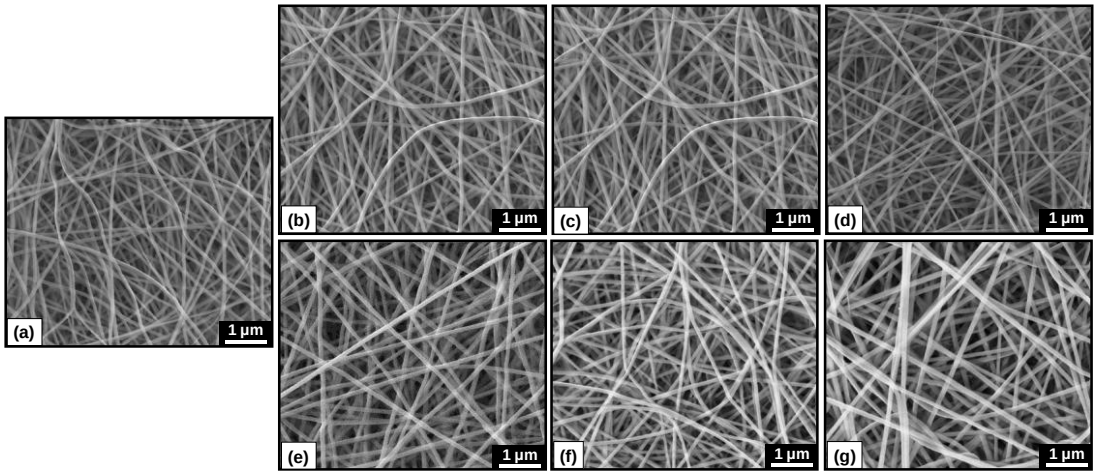

Figure 47. Representative SEM images of electrospun nanofibers from the solutions of (a) nylon 6,6, (b) nylon 6,6/α-CD25, (c) nylon 6,6/β-CD25, (d) nylon 6,6/γ-CD25, (e) nylon 6,6/α-CD50, (f) nylon 6,6/β-CD50, (g) nylon 6,6/γ-CD50.

The properties of the solutions (composition and viscosity) and AFD of resulting electrospun nanofibers are summarized in Table 10. It was observed that the AFD of nylon 6,6/CD nanofibers was slightly increased when compared to pristine nylon 6,6 nanofibers. This is possibly due to greater resistance to stretching and elongation of the electrified jet of nylon 6,6/CD solutions having higher solution viscosity, and that is comparable with the general observation in the literature [7, 10, 242]. Moreover, as the content of the CD increased from 25% to 50% (w/w, with respect to nylon 6,6) viscosity of the solutions increased too, and larger AFD was yielded for the nylon 6,6/CD. A possible reason for the viscosity increase may be some interaction (H

bonds) between the CD molecules and nylon 6,6 polymer chains, which is given in ATR-FTIR discussion later on [313].

Table 10. Properties of nylon 6,6 and nylon 6,6/CD solutions and the resulting nylon and nylon/CD nanofibers.

samples	% nylon (w/v)[a]	type of CD, % (w/w)[b]	viscosity (Pa·s)	AFD (nm)
nylon 6,6	10	-	0.063	95 ± 15
nylon 6,6/α-CD25	10	α-CD, 25	0.078	105 ± 20
nylon 6,6/β-CD25	10	β-CD, 25	0.072	110 ± 25
nylon 6,6/γ-CD25	10	γ-CD, 25	0.084	110 ± 20
nylon 6,6/α-CD50	10	α-CD, 50	0.113	140 ± 35
nylon 6,6/β-CD50	10	β-CD, 50	0.097	130 ± 25
nylon 6,6/γ-CD50	10	γ-CD, 50	0.106	130 ± 20

[a] with respect to solvent (formic acid).

[b] with respect to polymer (nylon).

In order to investigate whether any crystalline CD aggregates were present in the fiber matrix or not, XRD patterns of the as-received CD and nanofibers were obtained (Figure 48). The as-received α-CD, β-CD and γ-CD have 'cage type' crystalline structures in which cavity of each CD molecule is blocked by the adjacent CD molecules [230, 242], and so their XRD patterns have distinct diffraction peaks that are annotated in Figure 48a: 2θ≅12.0°, 14.4°, 21.7° for α-CD, 2θ≅10.8°, 12.6°, 19.7°, 21.3° for β-CD and 2θ≅12.3°, 16.5°, 21.8° for γ-CD. However, the broad halo XRD patterns of pristine nylon 6,6 and nylon 6,6/CD electrospun nanofibrous membranes (Figure 48b) did not show any crystalline peaks of α-CD, β-CD and γ-CD, indicating that all three types of CD were distributed in the nylon 6,6 fiber matrix without forming crystal aggregates.

In Figure 48b, the XRD pattern of pure nylon 6,6 nanofibers exhibited the reflection of (100) and (010, 110) planes at about 20.3° and 23.7° indicating α-type crystals structure of nylon 6,6 (triclinic phase) [321-324]. The α1 peak (2θ≅20.3°) arises from the distance between hydrogen bonded chains, while the separation of hydrogen-bonded planar sheets results in the occurrence of α2 peak (2θ≅23.7°) [322-323, 325-326]. As stated in the literature, besides α phase, γ phase showing peaks at about

13.33° and 22.2° can also exist in nylon 6,6. However, γ phase illustrating pleated sheets of methylene units with hydrogen bonding between sheets rather than within sheets, is more thermodynamically unstable than α phase, and so it not often appears in nylon 6,6 at room temperature [326-327]. The XRD patterns of all nylon 6,6/CD nanofibers are very similar to the XRD pattern of pure nylon 6,6 nanofibers as displayed Figure 48b, indicating the crystalline structure of nylon 6,6 (only α phase/triclinic) have remained unchanged with the presence of CD.

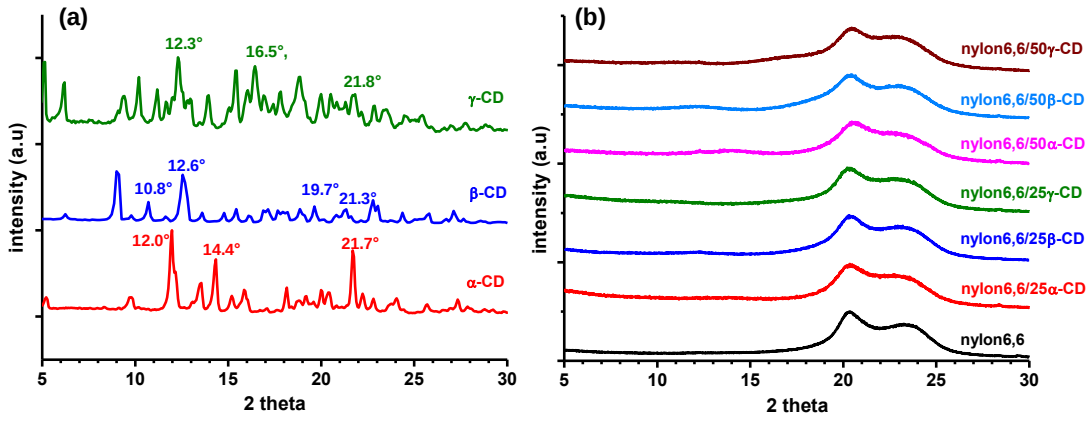

Figure 48. XRD patterns of (a) as-received CD and (b) the electrospun nanofibers.

On the other hand, the inclusion complexation possibility between nylon chains and CD has been reported in the literature under specific conditions (heating technique) and certain solution preparation procedure [328-330]. In those studies, the precipitation of the IC occurred in the prepared solutions and the characteristic XRD peaks of 'channel-type' CD crystal structure in which CD molecules are aligned and stacked on top of each other [228, 230, 313], were confirmed the inclusion complexation between CD and nylon [328-330]. However, we did not observe neither precipitation nor 'channel-type' CD crystal structure in our XRD results suggested that CD and nylon 6,6 chains did not form inclusion complexes (IC) in our experimental conditions. It is know that the IC formation between host molecules and guest CD is affected by process temperature, solvent type, and host/guest ratio [59].

TGA was used to investigate thermal characteristics of the samples and to determine the weight percentage of CD in the resulting electrospun nylon 6,6/CD nanofibers. We found out that TGA data of nylon 6,6/CD nanofibers obtained from α-CD, β-CD and γ-CD were almost same. So as a representative data, TGA and derivative of TGA thermograms of nylon 6,6/α-CD nanofibers (nylon 6,6/25α-CD, nylon 6,6/50α-CD) compared with pristine nylon 6,6 nanofibers and α-CD are only given in Figure 49.

The TGA of pure α-CD has an initial weight loss (~10%) below 100 °C and major weight loss between 275-365 °C owing to water loss and main degradation of CD, respectively [70, 312].The degradation of nylon 6,6 nanofibers occurs between 345-490 °C as it is seen in the TGA thermogram of pristine nylon 6,6 nanofibers. The observation of CD degradations in the TGA thermograms of nylon 6,6/CD nanofibers confirmed the incorporation of CD molecules in the nylon 6,6 fiber matrix. It is obvious from these thermograms that the thermal stability of CD within nanofibers is higher than that of as-received CD. Therefore, the degradation of α-CD was observed in the range of 290-390 °C and 290-400 °C for nylon 6,6/25α-CD and nylon 6,6/50α-CD nanofibers, respectively. The degradations of β-CD and γ-CD in the nanofibers also started at ~290 °C, however they carried out until approximately 385 and 375 °C for nylon 6,6/25β-CD and nylon 6,6/25γ-CD, respectively; 395 and 390 °C for nylon 6,6/50β-CD and nylon 6,6/50γ-CD, respectively (data not shown). The increase of degradation temperature of CD in the nanofibers occurred depending on CD type and amount in the nanofibers. Moreover, we also observed that the thermal degradation of nylon 6,6 in the nylon 6,6/CD nanofibers was also shifted to slightly higher temperature with increasing CD content. The improved thermal stability of the resulting nylon 6,6/CD nanofibers are attributed to the interaction between the polymeric matrix and the CD which is verified by the ATR-FTIR data.

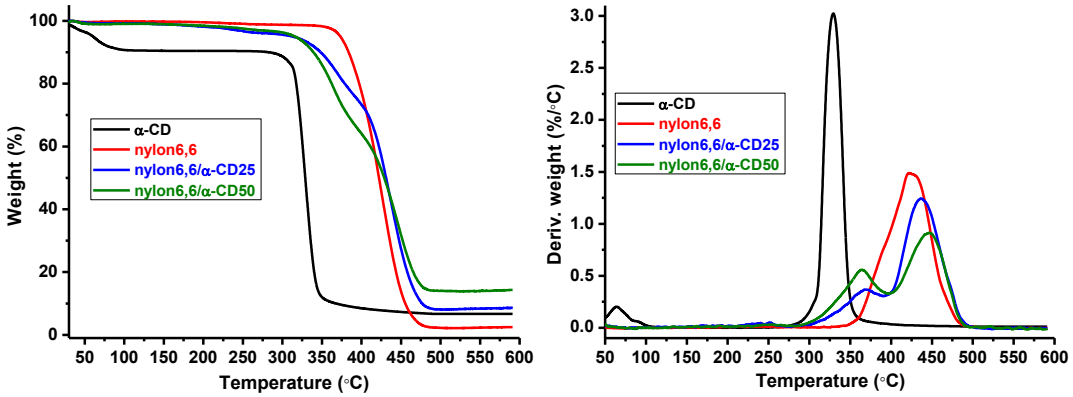

Figure 49. TGA and derivative TGA thermograms of as-received α-CD and the electrospun nanofibers.

The amount of CD present in the nylon 6,6/CD nanofibers was calculated from TGA thermograms as approximately 18% and 33% weight in nylon 6,6/25α-CD and nylon 6,6/50α-CD nanofibers, respectively. About 17% and 33% weight β-CD were determined in nylon 6,6/25β-CD and nylon 6,6/50β-CD nanofibers, respectively. In the case of nylon 6,6/25γ-CD and nylon 6,6/50γ-CD nanofibers, γ-CD was calculated as nearly 19% and 35%, respectively. In order to prepare nylon 6,6/25CD and nylon 6,6/50CD solutions 20% and 40% (w/w, with respect to sample) CD hydrates including about 10% water were used, respectively. The actual initial content of CD in nylon 6,6/CD solutions were calculated as ~18% and ~36% (w/w, with respect to sample) by subtracting the water amount. As a result, the calculation for nylon 6,6/25CD nanofibers almost matched with the initial amount of CD added in nylon 6,6/25CD solutions. In addition, the γ-CD content in nylon 6,6/50γ-CD nanofibers was also coherent with the initial amount in that solution. However, the CD amount was calculated slightly less amount for nylon 6,6/50α-CD and nylon 6,6/25β-CD nanofibers possibly because of overlapping of degradation temperatures of nylon 6,6 and CD. On the other hand, we did not observe any weight loss up to100 °C in the TGA thermograms of nylon 6,6/CD nanofibers despite of 10% water in pure CD, indicating the cavities of CD in the nanofibers are free of water, similar to our previous study [271, 312].

Phase separation of CD from polymer matrix is quite possible during solvent evaporation in the electrospinning process due to their different hydrophilic/hydrophobic nature, and certain amount of CD molecules may reside on the polymeric fiber surface [266-267, 271, 312]. To confirm the presence of CD on the surface of the nylon 6,6/CD nanofibers that is quite important for entrapment efficiency of VOC [54, 271], surface chemical characterization of the nanofibers were performed by using ATR-FTIR and XPS techniques.

The ATR-FTIR spectra in the region from 3700 and 900 cm-1 obtained for the as-received CD, electrospun nylon 6,6 and nylon 6,6/CD nanofibers are shown in Figure 50a. The spectrum of pristine nylon 6,6 nanofibers exhibited main characteristic peaks at 3301 cm−1 (N–H stretching vibration), 2934 cm−1 (–CH2 stretching vibration), 2860 cm−1 (–CH– symmetric stretching vibration), 1637 cm−1 (–C=O stretching vibration) and 1536 cm−1 (N–H bending vibration) [324, 331]. These peaks were also observed in the spectra of nylon 6,6/CD nanofibers. On the other hand, the ATR-FTIR spectra of the semi-crystalline nylon 6,6 and nylon 6,6/CD nanofibers have α-type crystalline phase located at 934, 1199 and 1475 cm−1 and amorphous components indicated at 1141 and 1180 cm−1 [321, 331]. The absence of the FTIR peak at 977 cm−1 assigned to the γ-type crystalline phase [327, 332] in the spectra of the nanofibers confirmed that the CD did not change the crystalline structure of nylon 6,6, which is coherent with the XRD data. In the FTIR spectra of α-CD, β-CD and γ-CD, the very broad band between 3000 and 3700 cm-1 assigned to the symmetric and antisymmetric O–H stretching vibrations and the absorption peak at about 2924 cm-1 corresponding to C-H bond of CD was observed [333-334].

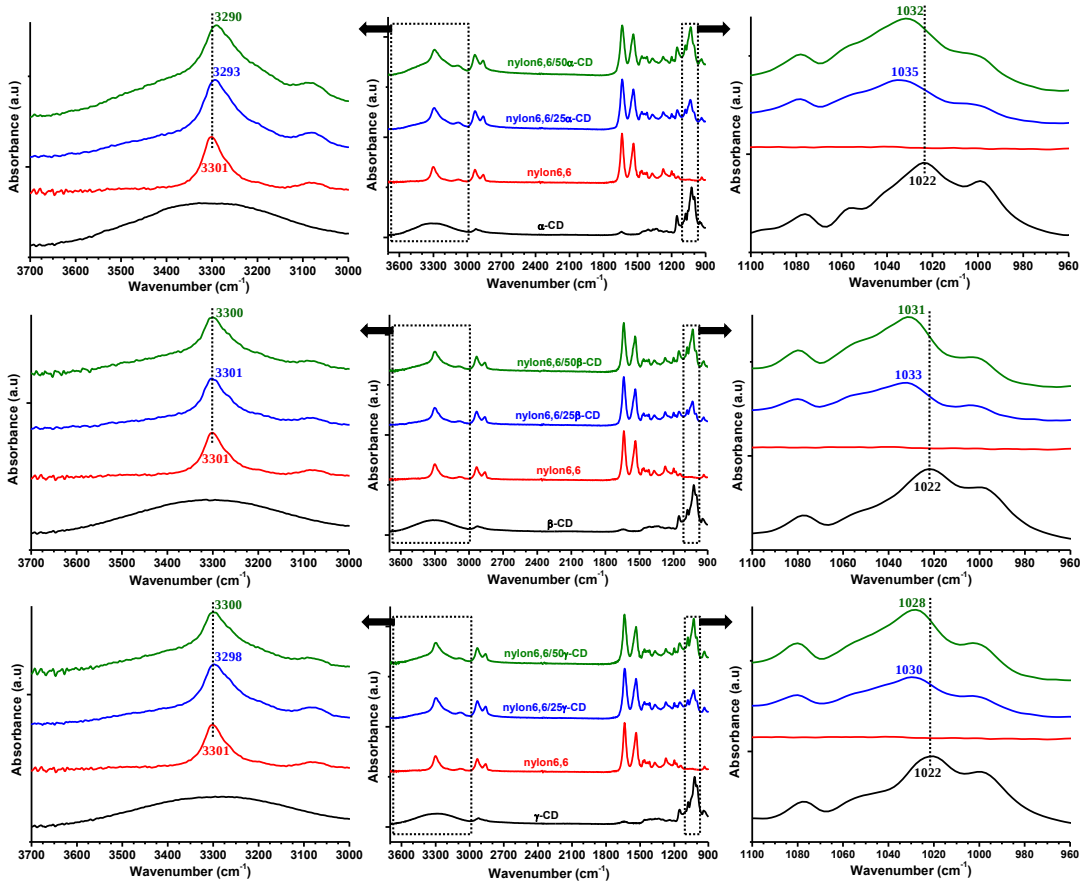

Figure 50. ATR-FTIR spectra of the as received CD, electrospun nylon 6,6 and nylon 6,6/CD nanofibers. Enlarged region of these spectra are given at left side (between 3700 and 3000 cm-1) and right side (between 1100 and 960 cm-1).

The obvious characteristic CD peaks at between 1000 and 1100 cm-1 attributed to coupled C–C/C–O stretching vibrations, and the peak at 1152 cm-1 assigned to the antisymmetric stretching vibration of the C–O–C glycosidic bridge [271, 287, 312-314] were identified in all ATR-FTIR spectra of nylon 6,6/CD nanofibers, but not in the spectrum of pristine nylon 6,6 nanofibers. The enhanced intensity of these CD related peaks was also clearly observed as the CD content increased from 25% thru 50% (w/w) in the nylon 6,6/CD nanofibers. This result indicated the existence of CD on the surface of the nylon 6,6/CD nanofibers, and the inclusion complexation capability of these CD could be used for the removal of VOC from the environment.

Moreover, it was observed in the enlarged region of ATR-FTIR spectra between 3700 and 3000 cm-1 (Figure 50a, left side) that the N–H stretching peak of

nylon 6,6 was generally shifted to lower wavenumber for nylon 6,6/CD nanofibers when compared to pure nylon 6,6 nanofibers. On the other hand, the enlarged region of FTIR spectra between 1100 and 960 cm-1 in Figure 50a, right side indicated the obvious CD peak shift to higher wavenumber for nylon 6,6/CD nanofibers compared to pure CD. The shifts of these two peaks for nylon 6,6/CD nanofibers suggested that the interaction (hydrogen bonds mainly) exists between nylon 6,6 and CD. More distinctive peak shifts were observed for nylon 6,6/α-CD nanofibers possibly due to smaller size of α-CD which can more interact with the nylon 6,6 chains. The higher thermal degradation temperature of α-CD in the nanofibers compared to other CD types, which discussed in TGA discussion is possibly because of higher interaction between α-CD and nylon 6,6 chains. Similar FTIR peak shifts were also observed in our previous study for zein/CD and PET/CD nanofibers due to interaction between zein and CD [271, 287], PET and CD [271, 287].

In order to determine the CD amount on the surface of nylon 6,6/CD nanofibers, XPS technique was used providing more surface sensitivity compared to ATR-FTIR (i.e. about 10 nm depth for XPS and650 nm depth for ATR-FTIR having germanium crystal, respectively) [312]. The atomic concentrations of as-received CD and the electrospun nanofibers obtained from wide energy XPS survey spectra are indicated in Table 11. The appearance of a higher oxygen content outer surface of the nylon 6,6/CD nanofibers compared to pristine nanofibers provides evidence of the presence of CD on the fiber surfaces. Moreover, an increase in the surface oxygen content was also observed with the increasing amount of CD (from 25% to 50% (w/w)).

Furthermore, high energy resolution O 1s spectra of the nanofibers were also recorded to get more detailed information about the surface components and confirm the existence of CD onto surface of nylon 6,6/CD nanofibers. O 1s XPS spectra of pristine nylon 6,6, nylon 6,6/25α-CD and nylon 6,6/50α-CD nanofibers are given in Figure 51. Similar XPS spectra were also recorded for samples of nylon 6,6nanofibers incorporating β-CD and γ-CD.

Table 11. Atomic concentrations generated from XPS wide energy survey scans.

samples	C (%)	O (%)	N (%)
α-CD	58.45	41.55	-
β-CD	57.69	42.31	-
γ-CD	58.47	41.53	-
nylon 6,6	75.45	12.67	11.88
nylon 6,6/α-CD25	74.25	14.87	10.88
nylon 6,6/β-CD25	75.86	14.43	9.71
nylon 6,6/γ-CD25	74.65	14.13	11.22
nylon 6,6/α-CD50	74.28	17.05	8.67
nylon 6,6/β-CD50	69.35	20.25	10.4
nylon 6,6/γ-CD50	74.58	18.37	7.05

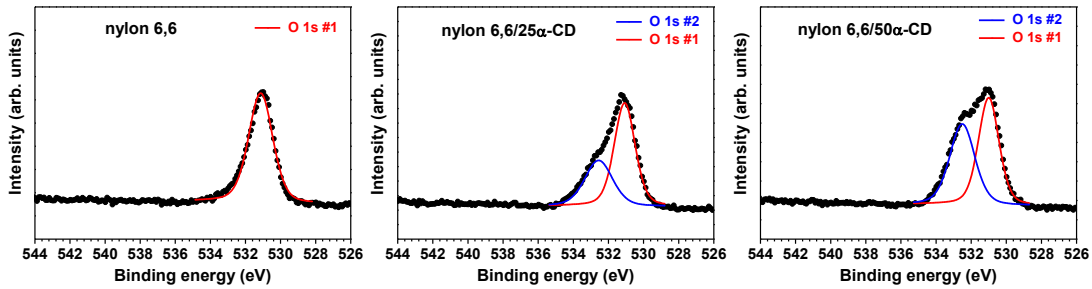

Figure 51. Core-level XPS spectra of O 1s from the nanofibers.

The spectrum of nylon 6,6 nanofibers has only π-bonded oxygen (C=O*) at peak binding energy of 531.13 eV [335]. On the other hand, beside this carbonyl group (O 1s #1) assigned to nylon 6,6 matrix, one more fitting peak (O 1s #2) is also represented at peak binding energy of about 532.53 in the nylon 6,6/CD spectra due to σ-bonded oxygen (C-O*C) and hydroxyl groups (C-O*H) of CD [271, 335].The higher ratio of O 1s #2 peak corresponding CD components was also observed in nylon 6,6/50α-CD nanofibers compared to nylon 6,6/25α-CD sample. These results indicated that enhanced oxygen content on the surface of the nylon 6,6/CD nanofibers originated from the ether and alcohol groups of CD. Using the atomic concentrations obtained from XPS survey spectra (Table 11), it was calculated that 8%, 6%, 5 %, 15%, 26% and 20% CD were present in the probed volume of nylon 6,6/25α-CD, nylon 6,6/25β-CD, nylon 6,6/25γ-CD, nylon 6,6/50α-CD, nylon 6,6/50β-CD and nylon 6,6/50γ-CD nanofibers, respectively. It is known that the component having lower molecular weight in such blend systems generally migrate

to the surface due to energetic and entropic effects [271, 336-339]. Here, the lower concentrations of CD on the surface of the nylon 6,6/CD nanofibers compared to the compositions of the electrospun solutions indicated that some of the CD molecules situated on the fiber surface whereas some CD molecules hidden in the bulk of the fiber matrix.

In order to test the entrapment efficiency of nanofibrous membranes, toluene vapor is selected as a model VOC since CD can form IC with toluene that is commonly used in industry for certain purposes [85, 340-342].The toluene vapor entrapment performance of the nylon 6,6 and nylon 6,6/CD nanofibers was compared. The amount of toluene entrapped by nanofibers was calculated by performing HPLC analyses and the data is given in Figure 52. Quite low amount of toluene (~1.3 ppm) was adsorbed by pristine nylon 6,6 nanofibers most probably due to a very weak interaction between toluene and nylon 6,6 nanofibers. This suggest that nylon 6,6 nanofibrous membrane without CD has minimal capability of trapping toluene vapor [54]. In the case of nylon 6,6/CD nanofibers, the amount of entrapped toluene was considerable higher (at least two times) possible due to the complexation capability of the CD present on the nanofiber surface (Figure 53).

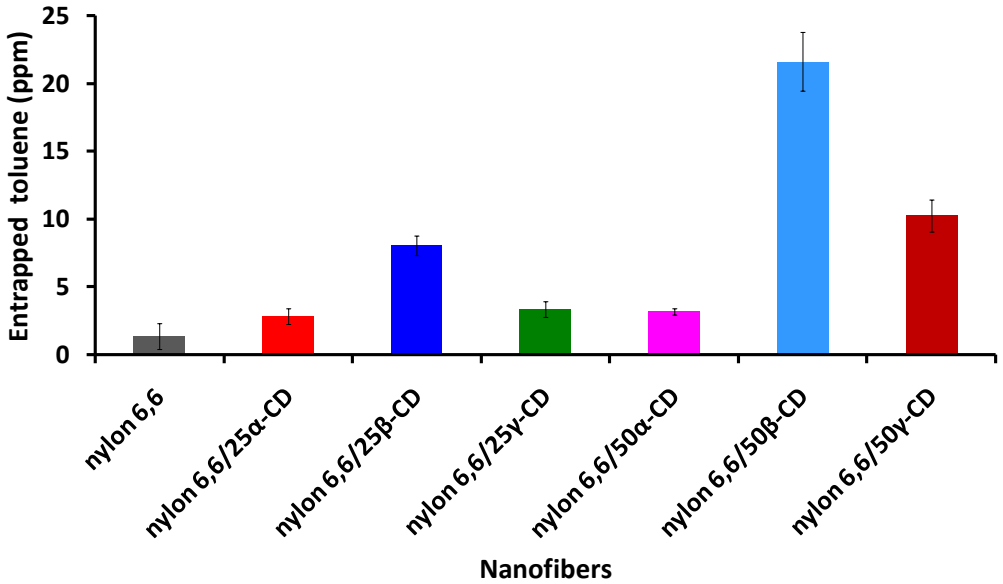

Figure 52. The amount of entrapped toluene (ppm) by the electrospun nanofibers.

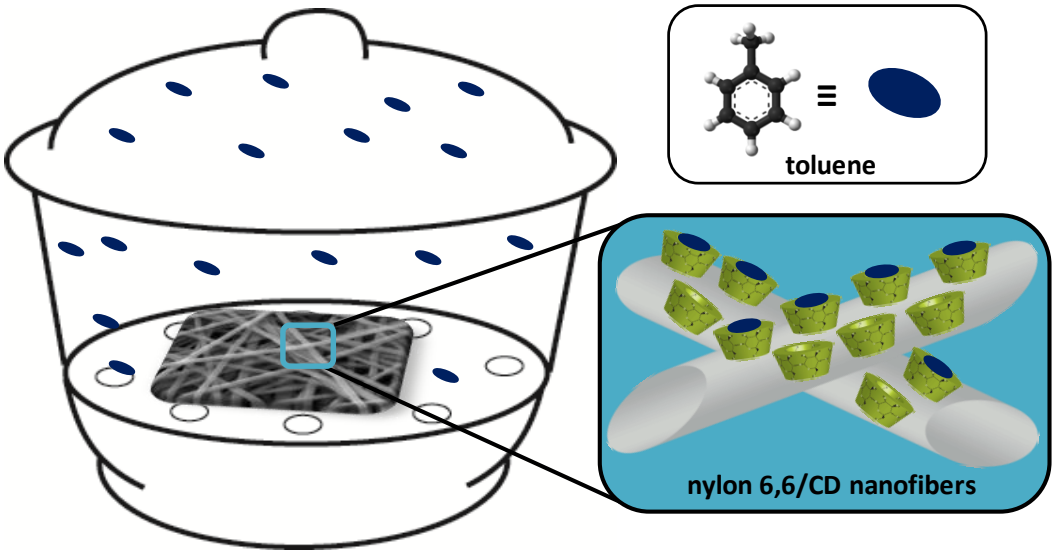

Figure 53. Schematic representation of entrapment of toluene through complexation with fiber surface associated CD.

Nylon 6,6/25α-CD, nylon 6,6/25β-CD and nylon 6,6/25γ-CD nanofibers captured ~2.8, 8.1 and 3.4 ppm toluene, while the amount of toluene entrapped by nylon 6,6/50α-CD, nylon 6,6/50β-CD and nylon 6,6/50γ-CD nanofibers was ~3.2, 21.6, 10.2 ppm. For each CD type, we observed that the amount of toluene entrapped was increased as the loading of CD in the nanofibers was increased from 25% to 50%.This is because the amount of CD present on the fiber surface was also increased as confirmed by XPS data. When the CD types were compared, the amount of entrapped toluene vapor was on the order of nylon 6,6/β-CD > nylon 6,6/γ-CD > nylon 6,6/α-CD, indicating that the used CD type was quite important for the inclusion complexation owing to different size/shape match between the host CD and toluene. The inclusion comlex formation depends on the relative size of the CD cavity to the size of the guest molecule [70, 199, 201-202, 266]. Based on the different CD dimensions (Figure 6), generally, α-CD can form complex for compounds with aliphatic side chains or low molecular weight molecules, β-CD can form complex with heterocycles and aromatics, and γ-CD can accommodate larger molecules such as steroids and macrocycles [58, 343]. Therefore each CD type can have different capability for the inclusion complexation with the same guest molecule. Our result indicated that β-CD cavity is more suitable host for toluene

molecule possibly due to a better fit and size match between cavity size of β-CD and toluene molecule [340]. Moreover, nylon 6,6/50β-CD presented the highest toluene entrapment efficiency among the other samples, since the XPS survey scans shows that surface of this sample has highest amount of CD which could complex with more amount of toluene. It can be concluded that the toluene entrapping efficiency of the nanofibers depends on both the amount of surface associated CD molecules and the type of CD. In brief, the findings suggested that CD functionalized electrospun nylon 6,6 nanofibers would be very effective for the removal of VOC from the environment due to their very large surface area along with inclusion complexation capability of surface associated CD on the nanofibers.

The stability of IC-CD when one (1:1) and two (2:1) toluene molecules included in CD is examined by using first-principles modeling techniques. Firstly, the initial geometries of α-, β-, and γ-CD and toluene molecule(s) are fully optimized separately in vacuum. In order to form a complex, firstly single toluene molecule is introduced into each CD at various positions and with different orientations. For each case the whole system is optimized without imposing any constraints. For the lowest energy configurations (Figure 54), the complexation energy ($E_{complex}$), which determines the stability of different complexes, is calculated as

$$E_{complex} = E_{CD} + n * E_{toluene} - E_{toluene+CD}$$

where E_{CD}, $E_{toluene}$ and $E_{toluene+CD}$ is the total energy (including van der Waals interaction) of CD (α, β, and γ), toluene, and toluene-CD complex, respectively and n is the number of toluene molecules. $E_{complex}$ is calculated as 16.14, 18.45, and 11.53 kcal/mol for α-, β-, and γ-CD, respectively. According to our analysis all CD can make IC with single toluene but the most stable one (with largest $E_{complex}$) is obtained for β-CD.

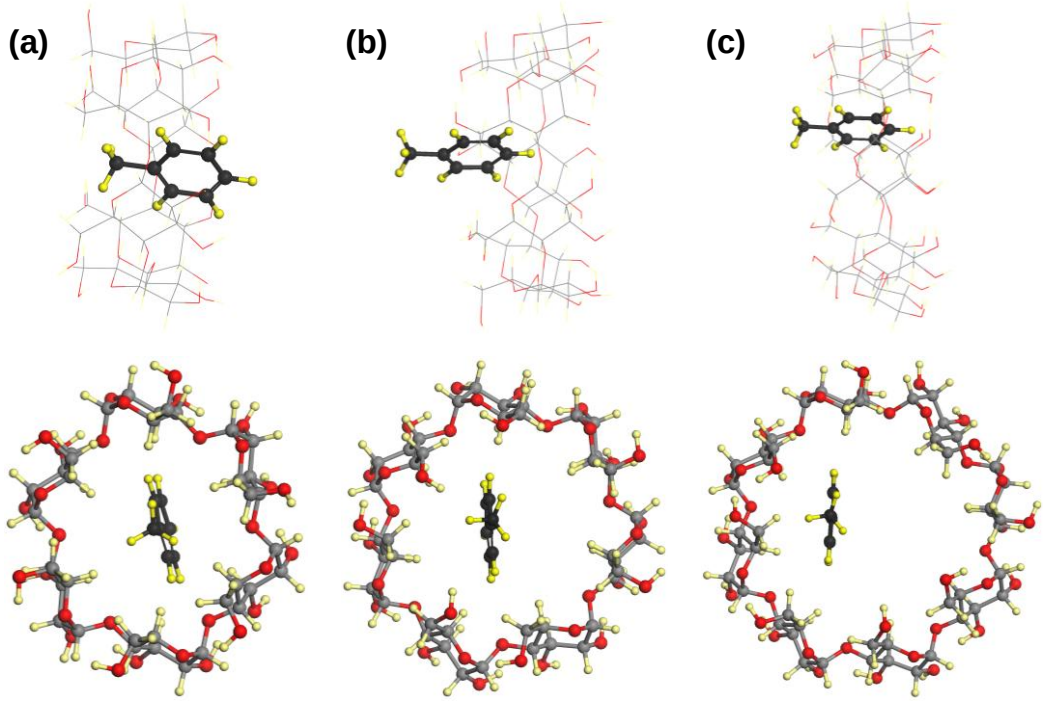

Figure 54. Side and top view of optimized structures of single toluene and (a) α- (b) β- (c) γ- CD-IC (1:1). Gray, red, and yellow spheres represent carbon, oxygen, and hydrogen atoms, respectively.

In a similar manner we examine the possibility of two toluene molecules entering the host CD (2:1). Initially, two toluene molecules are optimized in vacuum and the equilibrium distance between them is calculated as 3.6 A with the interaction energy (Etol-tol) 2.02 kcal/mol which indicates an intermolecular π-π interaction. When toluene pair enters α-CD, it deforms the host and second toluene is expelled as shown in Figure 55(a). Accordingly Ecomp reduces and becomes 14.90 kcal/mol upon introducing a second toluene when Etol-tol is taken account indicating that 2:1 complex formation is not favored for α-CD. On the other hand, for β-, and γ-CD, toluene pair can fit in the cavity (Figure 55b-c) and this further reduces the total energy of the system with increasing Ecomp to 27.86 and 25.46 kcal/mol, respectively. Finally, our ab initio modeling results confirmed 2:1 toluene:β-CD stoichiometry and suggests that β-CD cavity is the most suitable host for toluene pair yielding the highest complexation energy.

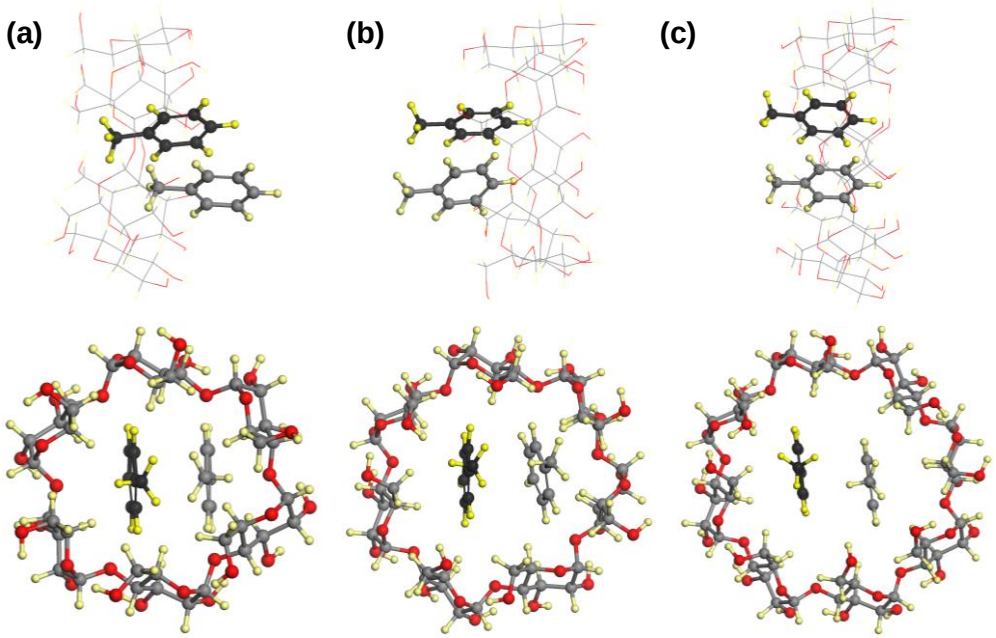

Figure 55. Side and top view of optimized structures of two toluene molecules and (a) α- (b) β- (c) γ- CD-IC (2:1). Gray, red, and yellow spheres represent carbon, oxygen, and hydrogen atoms, respectively.

3.3.3. Conclusions

In this study, we combined the very high surface area of electrospun nanofibers with the inclusion complexation capability of CD molecules for the efficiently removal of toluene vapor from the surrounding. For this purpose, CD functionalized electrospun nylon 6,6 nanofibrous membranes were produced via electrospinning, using three different types of native CD(α-CD, β-CD and γ-CD) having 25% and 50% (w/w) weight loading in the nanofiber matrix. SEM images indicated that bead-free nanofibers were obtained by electrospinning of nylon 6,6 and nylon 6,6/CD solutions. The distribution of CD into fiber matrix without forming any crystalline aggregates was confirmed via XRD study. The % weight of CD within resulting nanofibers calculated from TGA thermograms was consistent with the initial CD loading in the solutions used forelectrospinning.TGA thermograms of resulting nylon 6,6/CD nanofibers also indicated enhanced thermal stability of both CD and nylon 6,6 owing to the interaction between the polymeric matrix and the CD. ATR-FTIR and XPS analyses indicated that some of CD were located on the surface

of nylon 6,6/CD nanofibers. The existence of CD amounts on the fiber surface increased as the CD content increased from 25% thru 50% (w/w, with respect to polymer) in the nylon 6,6/CD nanofibers. Moreover, ATR-FTIR peak shift was observed due to interaction (possibly H bonding) between CD and nylon 6,6. Toluene vapor was used as a model VOC for entrapment experiments. We observed that nylon 6,6/CD nanofibrous membranes entrapped higher amount of toluene when compared to pristine nylon 6,6 nanofibers due to the IC formation capability of the surface associated CD molecules. The entrapment efficiency of toluene vapor was found to be better for nylon 6,6/β-CD nanofibers when compared to nylon 6,6/α-CD and nylon 6,6/γ-CD nanofibers possibly due to better fit and size match between β-CD cavity and toluene. Moreover, our computational modeling results based on first-principles calculations show that, the complexation energy of toluene-CD is higher for β-CD compared to α-CD and γ-CD. Both experimentally and theoretically, β-CD cavity is found the most suitable host for toluene molecule. Our results suggested a very promising and interesting potential application of electrospun nylon 6,6 nanofibers functionalized with CD as molecular filters for VOC in air filtration.

3.4. Electrospun Polyester/Cyclodextrin Nanofibers for Entrapment of Volatile Organic Compounds

3.4.1. Experimental

Materials: Three types of native cyclodextrins (CD); α-CD, β-CD and γ-CD were purchased from Wacker Chemie AG. Polyester (polyethylene terephthalate, PET) chips were gift from the company of Korteks (Bursa, Turkey). Dichloromethane (DCM, Sigma Aldrich, extra pure), trifluoroacetic acid (TFA, Sigma Aldrich, 99%), acetonitrile chromasolv (Sigma Aldrich, 99.9%) and aniline (Sigma Aldrich, %99) were purchased. All materials were used as-received without any further purification.

Preparation of the solutions for electrospinning: PET/CD solutions were prepared by dissolving PET and CD (α-CD, β-CD and γ-CD) in TFA/DCM (1/1, v/v) solvent

system. The polymer concentration was 20% (w/v, with respect to the solvent), and the CD concentration was 25% (w/w, with respect to the polymer) in these solutions. Moreover 20% and 22.5% (w/v, with respect to the solvent) PET solutions without CD were also prepared. Table 12 summarizes the compositions of all solutions used for electrospinning.

Electrospinning: The PET and PET/CD solutions were loaded into 5 mL syringes fitted with a metallic needles (0.7 mm outer diameter), individually. The syringes were placed horizontally on the syringe pump (KDS 101, KD Scientific). A grounded stationary cylindrical metal collector (height: 15 cm, diameter: 9 cm) covered by a piece of aluminum foil was used for the fiber deposition. The feed rates of the solutions were 1 mL/h during electrospinning, and needle tips-to-collector distances were set to 10 cm. The high voltage power supply (Matsusada, AU Series) was used to apply a voltage of 15 kV. The electrospinning processes were performed at 22 °C and 46% relative humidity in an enclosed Plexiglas box.

Measurements and characterizations: The viscosity measurement of the each solution used for electrospinning was performed by using the Brookfield DV-II+Pro viscometer equipped with cone/plate accessory of spindle type CP42 with 20 rpm at 22 ^{o}C. The conductivity of the solutions was measured by using Mettler Toledo conductivity meter (LE705, Five Easy^{TM} FE 30) at 24 ^{o}C. Scanning electron microscope (SEM, FEI-Quanta 200 FEG) was used to investigate the morphology of PET and PET/CD nanofibers. The samples were coated with 5 nm Au/Pd prior to SEM analysis. Around 100 fiber diameters of each sample were measured from the SEM images to determine the average fiber diameter (AFD) of the samples. X-ray diffraction (XRD) data of the nanofibers were collected by using PANalytical X'Pert Powder diffractometer with Cu Kα radiation in a range 2θ = 5°-30°. The infrared spectra of the electrospun nanofibers were recorded from 600 to 2000 cm^{-1} with a resolution of 4 cm^{-1} and 64 scans by using FTIR spectroscopy (Bruker-VERTEX 70). A small amount of each sample was mixed with potassium bromide (FTIR grade) in a mortar and then pellet was obtained by applying high pressure for FTIR analyses. The thermal properties of the samples were investigated by using

thermogravimetric analyzer (TGA, TA Q500). In TGA measurements, the nanofibers were heated from room temperature to 600 °C at a constant heating rate of 20 °C/min under the nitrogen atmosphere. The surface chemical characterization of the PET and PET/CD nanofibers were performed by X-ray photoelectron spectroscopy (XPS, Thermo Scientific). XPS data were taken by a flood gun charge neutralizer system equipped with a monochromated Al K-α X-ray source (hv= 1486.6 eV) from 400 μm diameter circular spot on the nanofibers. Wide energy survey scans of the nanofibers were recorded over the 0-1360 eV binding energy range, at detector pass energy of 200 eV and with energy step size of 1 eV. The O 1s high resolution spectra of the nanofibers were also obtained at pass energy of 50 eV and with energy steps of 0.1 eV. The static water contact angles on the nanofibrous webs were evaluated using contact angle analyzing instrument (OCA30, Dataphysics Instrument Company) at room temperature. Deionized water (0.4 μL) was automatically dropped on the webs and Laplace-Young fitting was applied on contact angle measurements. The measurement was repeated ten times at different places of the PET nanofibrous web to get average contact angle value. The stress–strain curves for the nanofibrous webs were obtained using a dynamic mechanical analyzer (DMA, TA Q800) in tension film clamp at a constant stress rate of 2 N/min. The samples having size of 10 mm (gap) × ~2.75 mm (width) × ~0.35 mm (thickness) was measured. Ultimate stress and elongation at break of electrospun nanofibers were determined from the obtained stress-strain curves and young modulus was calculated from the linear region of these curves. The average and standart deviation of these values were calculated by testing 3 specimens for each sample.

Entrapment of organic vapor waste by the nanofibrous webs: The molecular entrapment capability of PET, PET/α-CD, PET/β-CD and PET/γ-CD nanofibrous webs was tested by evaluating the amount of entrapped aniline (a model volatile organic compound (VOC)) in vapor phase. This experiment was carried out in a sealed glass desiccator (30 cm (diameter) and 30cm (height)). First, 10 mL of aniline (as-received, without any dilution) was put into glass Petri dish, and it was placed at the bottom of desiccator. Then, three piece of PET, PET/α-CD, PET/β-CD and PET/γ-CD rectangular shaped nanofibrous webs (50 mg, about 3x4 cm^2) were placed

on the supporting layer which positioned at 7 cm high from the bottom of desiccator. The webs were left in this sealed desiccator for 12 hours and exposed to aniline vapor. Afterwards, the webs were removed from desiccator and kept in the suction hood for 3 hours in order to remove the excess aniline molecules that were absorbed by the electrospun webs. In order to investigate the amount of aniline entrapped by the webs, high performance liquid chromatography (HPLC, Agilent 1200 series) equipped with VWD UV detector was used. First, each of the web was immersed in 2 mL acetonitrile (ACN), individually, and kept in it for 3 hours to extract aniline entrapped by the nanofibers. 0.5 mL of each solution was withdrawn and put into HPLC vial to measure aniline concentration in these solutions. Aniline was detected by using the Agilent C18 column (150 mm x 4.6 mm, 5 µm pores) at 254 nm. ACN (100%) was used as a mobile phase. Flow rate, injection volume and total run time were 0.5 mL/min, 5 µL and 4 min, respectively. After the calibration curve (R^2=0.996) was prepared by using aniline solutions having different concentrations (500 ppm, 1000 ppm, 2000 ppm, 4000 ppm), the filtrated aniline amount was determined by converting the aniline peak area to concentration (ppm) from the curves in HPLC chromatograms. The results were reported as the average±standard deviation of aniline concentration entrapped by the nanofibrous webs since three different samples were used for each web.

3.4.2. Results and Discussion

The characteristics (composition, viscosity and conductivity) of the PET and PET/CD solutions, average fiber diameters (AFD) and morphological characteristics of the resulting electrospun nanofibers are summarized in Table 12. Figure 56 shows the representative SEM images of PET and PET/CD nanofibers. PET (20%, w/v) solution without CD yielded beaded nanofibers (Figure 56a). The beaded structures were eliminated and bead-free nanofibers were produced by increasing the PET concentration to 22.5% (w/v) (Figure 56b), since the electrified polymer jet could be stretched fully due to higher solution viscosity [7, 10, 242]. Moreover, thicker fibers were yielded from the 22.5% (w/v) PET solution having higher viscosity and lower conductivity compared to 20% (w/v) PET solution, which is compatible with general

observation in the literature [7, 10, 242]. Bead-free PET nanofibers obtained from 22.5% PET solution were used for the rest of the study. High enough concentration/viscosity was required to produce uniform bead-free PET nanofibers. However, bead-free PET/CD nanofibers were obtained by adding 25% (w/w) α-CD, β-CD and γ-CD to 20% (w/v) PET solution, individually (Figure 56c-e). This is possibly due to the higher solution viscosity and conductivity of PET/CD solutions when compared to 20% (w/v) PET solution. A possible reason for the viscosity increase may be some interaction between the CD molecules and PET polymer chains, which indicating in FTIR discussion [313]. Having required viscosity of PET/CD solutions may be one of the reasons why bead-free PET/CD nanofibers were obtained from lower polymer concentrations. Since the CD causes an increase in the solution conductivity, the possibility of the presence of salt impurity in the CD was considered, and indeed sodium ion was detected in our previous study [312]. The increase in conductivity of the solution resulted in higher stretching of polymer solution under the high electrical field, which is another reason that bead-free fibers could be obtained from lower polymer concentrations. It was concluded that the addition of CD into polymer solutions improved the electrospinnability and bead-free nanofibers could be obtained at lower polymer concentrations when compared to the polymer solution without CD. Similar findings were also observed for the electrospinning of other types of polymer systems incorporating CD in our previous studies [287, 312-314]. As mentioned above, generally thicker fibers are yielded from the polymer solutions having higher viscosity and lower conductivity due to the less stretching of the electrified jet [7, 10, 242]. The addition of CD into the PET solutions increased not only viscosity but also conductivity of the solutions. The AFD of the PET/CD nanofibers were larger compared to pristine PET nanofibers obtained from 20% (w/v) PET solution. This is possibly because of the higher solution viscosity of PET/CD solutions although the solution conductivities were slight higher than that of PET solution. On the other hand, the AFD of PET (22.5 %w/v) and PET/CD nanofibers are more or less close to each other without showing any considerable differences. The slight variations in AFD (~800 thru 900 nm) among the PET (22.5 %w/v) and PET/CD nanofibers are summarized in Table 12.

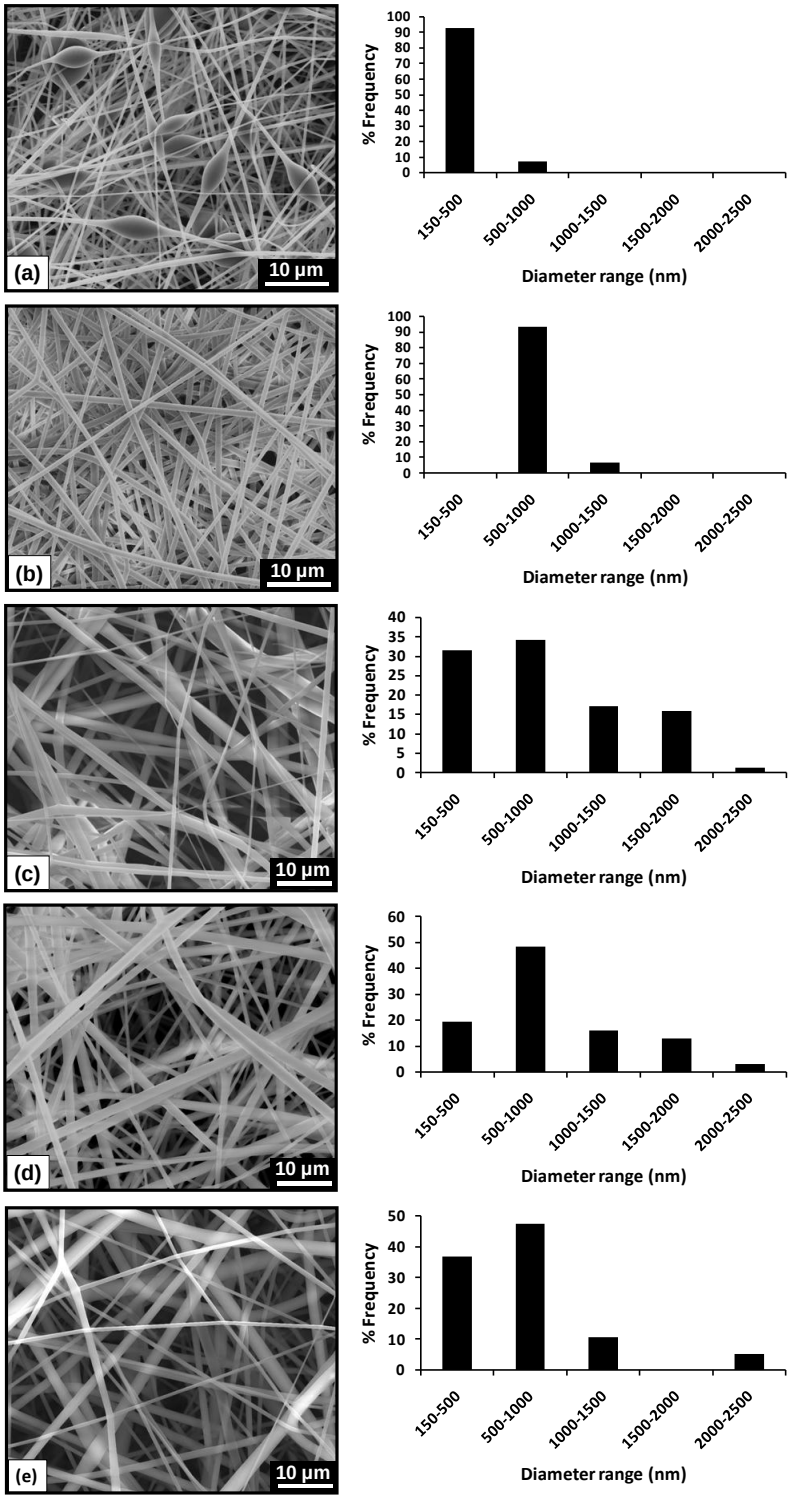

Figure 56. Representative SEM images and fiber diameter distributions of electrospun nanowebs from the solutions of (a and b) PET at concentrations of 20% and 22.5% (w/v), (c) PET/α-CD, (d) PET/β-CD, (e) PET/γ-CD. (Copyright © 2014 Society of Plastics Engineers. Reprinted with permission from Ref.[271])

Table 12. Properties of PET and PET/CD solutions and the average fiber diameters and morphological characteristics of the resulting electrospun nanofibers.

samples	% PET (w/v)[a]	CD type, % (w/w)[b]	viscosity (cP)	conductivity (μs/cm)	AFD (nm)	fiber diameter range (nm)
PET	20	-	112.8	0.87	360±100	150-660
PET	22.5	-	139.8	0.76	820±150	620-1040
PET/α-CD	20	α-CD, 25%	170.9	1.84	900±560	160-2330
PET/β-CD	20	β-CD, 25%	134.6	1.90	830±510	300-2200
PET/γ-CD	20	γ-CD, 25%	123.9	1.69	790±490	310-2500

[a] with respect to solvent (TFA/DCM, v/v, 1/1).
[b] with respect to polymer (PET).

The crystalline structures of the nanofibers were investigated by XRD to investigate whether any crystalline CD aggregates were present in the fiber matrix or not. The XRD patterns of as-received CD (α-CD, β-CD and γ-CD) having distinct diffraction peaks in the range of 2θ=5°-30° are depicted in Figure 57a. The diffraction peaks at 2θ≅12.0°, 14.4°, 21.7° in the XRD pattern of as-received α-CD, 2θ≅10.8°, 12.6°, 19.7°, 21.3° in the XRD pattern of as-received β-CD, and 2θ≅12.3°, 16.5°, 21.8° in the XRD pattern of as-received γ-CD are associated with their cage type crystal structures in which cavity of each CD molecule is blocked by the adjacent CD molecules [230, 313]. Another CD crystal structure, 'channel-type' in which CD molecules are aligned and stacked on top of each other, is generally observed in inclusion complexation of CD [228, 230, 313]. The broad halo XRD patterns of pristine PET and PET/CD electrospun nanofibrous webs without any strong diffraction peaks are observed in Figure 57b. The absence of any crystalline peaks of α-CD, β-CD and γ-CD elucidated that all three types of CD were distributed in the PET fiber matrix without forming any phase separated crystal aggregates. Although inclusion complexation between PET chains and γ-CD was possible under specific conditions and certain solution preparation procedure as reported in literature [329, 344], Our results suggested that CD and PET chains did not form inclusion complexes. Therefore used solvent, temperature and host/guest ratio could be effected the inclusion complex (IC) formation [59]. As a result, the cavity of CD

molecules present onto fiber surface would be available for inclusion complexation with organic waste molecules.

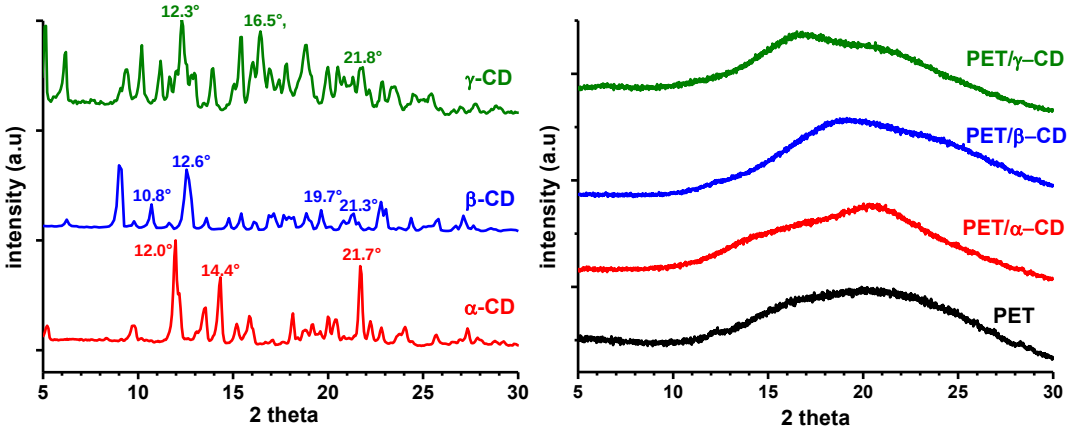

Figure 57. XRD patterns of as-received CD and the electrospun nanofibers. (Copyright © 2014 Society of Plastics Engineers. Reprinted with permission from Ref.[271])

The FTIR spectra of the electrospun PET nanofibers and PET/CD nanofibers are shown in Figure 58. The characteristic peaks in the FTIR spectrum of the pristine PET nanofibers appeared at 1721 (C=O stretching), 1413 (C–C stretching and C–H in plane deformation in aromatic ring), 1339 (CH_2 wagging) and 1246 (O=C–C stretching of ester), 1102 (O–CH_2 stretching) and 1027 (Ring C–H in-plane bending), 871(Parasubstituted benzen ring) and 729 cm-1 (C–C bending and C–H out of plane in aromatic ring) [345]. The characteristic peak of coupled C–C/C–O stretching vibrations and the antisymmetric stretching vibration of the C–O–C glycosidic bridge of CD could not identified in the FTIR spectra of PET/CD nanofibers because of the overlapping of absorption peaks of CD and PET. Yet, in the enlarged region of FTIR spectra (Figure 58, left side), it was observed that the O–CH_2 stretching and ring C–H in-plane bending peaks were shifted to lower wavenumber for PET/CD nanofibers when compared to pure PET nanofibers. The O–CH_2 stretching peak was observed at 1100 cm^{-1} for PET/CD nanofibers. More distinctive shift to lower wavenumber was observed for ring C–H in-plane bending peak. That is, absorption peak of ring C–H in-plane bending was observed at 1022 (PET/α-CD) or 1020 cm^{-1} (PET/β-CD and PET/γ-CD). The peak shift of these two peaks to lower wavenumbers for PET/CD nanofibers suggested the presence of

interaction between PET and CD. FTIR peak shifts were also observed in our previous study fror zein/CD nanofibers due to interaction between zein and CD [287].

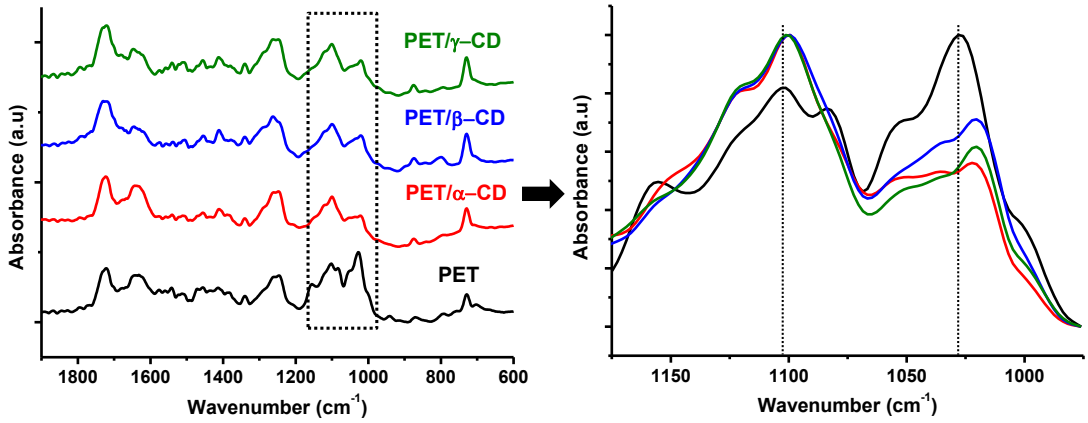

Figure 58. FTIR spectra of the electrospun nanofibers, and overlay of these spectra in the enlarged region (right side). (Copyright © 2014 Society of Plastics Engineers. Reprinted with permission from Ref.[271])

Thermogravimetric analyzer (TGA) was used to investigate the thermal characteristics of the nanofibers. The weight percentage of CD in the resulting electrospun PET/CD nanofibers were determined by TGA. Figure 59 indicates the TGA thermograms of pristine PET and PET/CD nanofibers. The initial weight losses below 100 °C in the TGA thermograms of PET and PET/CD nanofibers were almost same (~5%) that were possibly correspond to absorbed water or the residual solvent in the nanofibers. The main degradation of PET nanofibers occurred between 370-480 °C as it was seen in the TGA thermogram of pristine PET nanofibers. The degradation of CD was observed in the range of 280-370 °C [287, 313] for PET/CD nanofibers. The observation of CD degradations in the TGA thermograms of PET/CD nanofibers confirmed the incorporation of CD molecules in the PET fiber matrix. The amount of CD present in the PET/CD nanofibers was calculated as about 18% weight in the all PET/CD nanofibers, and this calculation accurately matched with the initial amount of CD added in PET/CD solution. Although 20% (w/w, with respect to polymer) CD hydrates were used for the preparation of PET/CD solution, actual initial content of CD in PET/CD solutions were calculated as ~18% (w/w, with respect to polymer); since as-received CD contains about 10% water [287, 313].

Hence, TGA data indicated that the initial CD content in the PET/CD solutions was preserved, and CD molecules were incorporated into the PET nanofibers without any loss during electrospinning process. On the other hand, as it mentioned previously, we did not observe higher weight loss up to 100 °C for PET/CD nanofiber compared to pure PET nanofibers despite of 10% water in as-received. The reason of this result indicated that the cavities of the CD molecules are free of water, similar to our previous study [313].

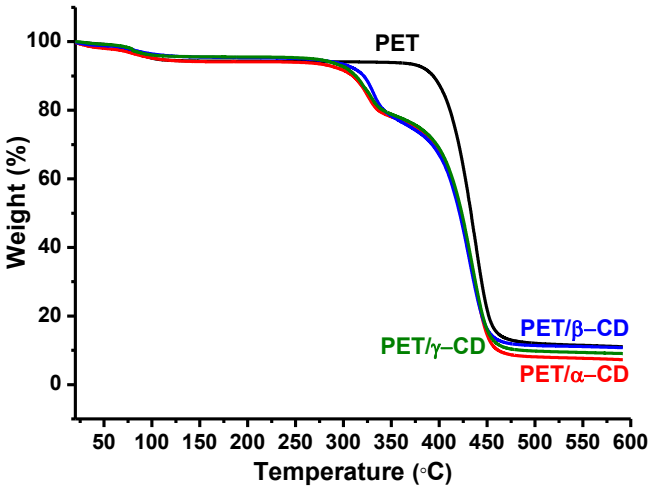

Figure 59. TGA thermograms of the electrospun nanofibers. (Copyright © 2014 Society of Plastics Engineers. Reprinted with permission from Ref.[271])

The existence of CD on the fiber surface is quite important in order to improve the entrapment efficiency of volatile organic compounds (VOCs) by nanofibrous webs [54]. The surface chemical characterization of PET/CD nanofibers was performed by using X-ray photoelectron spectroscopy (XPS). Table 2 shows elementary compositions based on wide energy survey spectra of CD and the electrospun nanofibers. The molecular structures of PET and CD are composed of C and O elements, so the XPS survey spectra of CD and nanofibers indicated two peaks: C 1s and O 1s. The percentages of C 1s and O 1s onto pristine PET nanofibers were determined as 75.15 and 24.85, respectively, which was coherent with the literature [346]. We observed that the percentage of O 1s onto PET/CD nanofibers was increased compared to pristine PET nanofibers. The increasing oxygen ratio on the surface of the PET/CD nanofibers indicated the presence of CD

onto PET/CD nanofibers. From the atomic concentrations in probed volume (Table 2), it is calculated that approximately 52%, 49% and 43% of oxygen on the surface of PET/CD nanofibers originated from α-CD, β-CD and γ-CD, respectively. This indicates that the most of CD molecules located on the fiber surface possibly due to phase separation from the PET matrix during the electrospinning. In fact, higher amount of surface associated CD is desired since CD molecules that are present on the fiber surface have capability of complex formation with VOCs.

Table 13. Atomic concentrations generated from XPS wide energy survey scans.

samples	C (%)	O (%)
α-CD	58.45	41.55
β-CD	57.69	42.31
γ-CD	58.47	41.53
PET	75.14	24.86
PET/α-CD	66.39	33.61
PET/β-CD	66.57	33.43
PET/γ-CD	67.89	32.11

In order to verify the existence of CD onto surface of PET/CD nanofibers, high energy resolution O 1s spectra of pristine PET and PET/CD nanofibers were also recorded. Since the O 1s XPS spectra of PET/α-CD, PET/β-CD and PET/γ-CD nanofibers were almost same, only one of them (PET/γ-CD) was given in Figure 60 to compare with the O 1s spectrum of pristine PET nanofibers. Distinctive two fitting peaks (O 1s #1 and O 1s #2) are represented within the O 1s spectra of pristine PET nanofibers (Figure 60) at peak binding energies of 531.8 and 533.39 eV due to π-bonded oxygen ($C=O^{*}$) and σ-bonded oxygen ($C-O^{*}C$) in PET structure, respectively [347-349]. Theoretical ratio of these two components is 50:50 in PET structure, and therefore the ratio of these peaks (50.76:48.22) was determined coherently. There is also one additional peak (O 1s #3) having very low ratio (~1.02% of the total O 1s ratio) at peak binding energy of 535.2 eV because of absorbed water [348]. Besides of the peaks assigned to PET components ($C-O^{*}C$, $C=O^{*}$) and adsorbed H_2O, the additional fitting peak (O 1s #4) was also observed in the O 1s spectrum of PET/CD nanofibers (Figure 60b) at peak binding energy of 533.15 eV owing to hydroxyl

groups of CD (C-O*H). This finding confirmed the presence of the CD on the surface of the PET/CD.

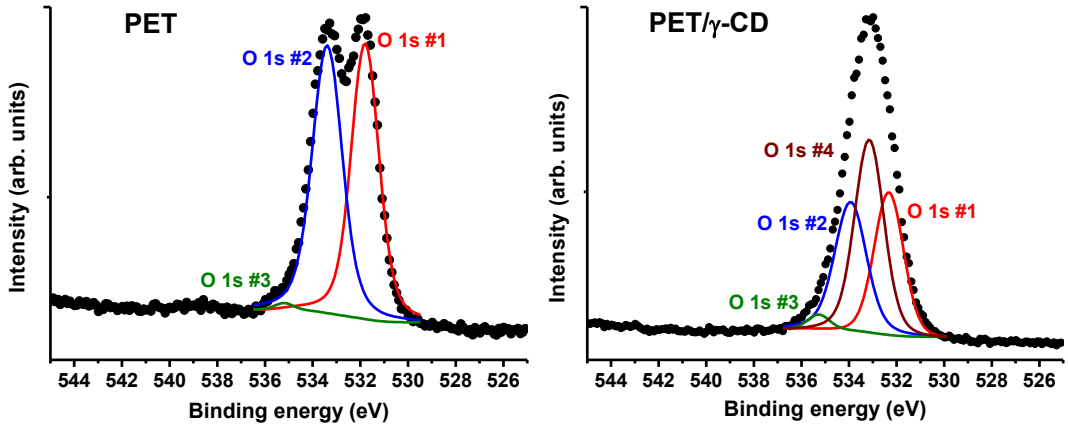

Figure 60. O 1s high resolution XPS scans of electrospun nanofibers of PET and PET/γ-CD. (Copyright © 2014 Society of Plastics Engineers. Reprinted with permission from Ref.[271])

The surface properties of electrospun nanofibers were also characterized by water contact angle measurement. Water contact angle on the pure PET nanofibers was determined as 145.7±3.9° indicating generally known hydrophobic feature of PET fibers [350-351]. On the other hand, the contact angles of the PET/CD webs could not be measured, since droplets were absorbed on the surface of the fibers where oxygen-containing polar groups resulted in the significant enhancement of hydrophilicity [352]. This increased hydrophilicity of the webs is another evidence of the existence of CD on the fiber surface. Videos in supporting info are showing the hydrophobicity of PET nanofibers and hydrophilicity of PET/CD nanofibers during water contact angle measurement.

As discussed previously, hydrophilic nature CD molecules could phase separate from the hydrophobic PET matrix during the solvent evaporation in the electrospinning process, and heterogeneously mixed throughout the fiber matrix [266]. Moreover, in such blend systems, it is proposed that the lower molecular weight component generally migrate to the surface due to energetic and entropy effects [336-339]. It is likely because of those; the surface analysis results by XPS

and contact angle measurement clearly indicated that there is a surface enrichment or segregation of CD molecules on the fibers.

We used DMA to investigate the effect of CD on the mechanical properties of the nanofibers. The mechanical properties of electrospun nanofibers determined from the stress-strain curves for the nanofibers were summarized in Table 14. We observed that ultimate stress was nearly two times higher for PET/CD nanofibers than pristine PET nanofibers, while elongation at break of PET and PET/CD nanofibers was found almost same. Specifically, the young modulus of the PET/CD nanofibers was three times as strong compared to PET nanofibers. These results were possibly due to interaction between PET and CD that was mentioned in the FTIR discussion. Likely, the interaction gave the stiffening effect to the fibers.

Table 14. Summary of the mechanical properties of electrospun nanofibers.

samples	Ultimate stress (MPa)	Elongation at break (%)	Young modulus (MPa)
PET	9 ± 4	73 ± 11	59 ± 12
PET/α-CD	18 ± 4	74 ± 10	183 ± 32
PET/β-CD	12 ± 7	62 ± 26	126 ± 64
PET/γ-CD	14 ± 5	78 ± 18	142 ± 43

The entrapment performance of the PET and PET/CD nanofibrous webs was investigated by using aniline vapor as a model VOC. Aniline is commonly used in industry for certain purposes and it is one of the common VOCs present in the environment. CD can form IC with aniline [54, 85], and therefore we have chosen aniline as a model VOC as proof of concept study. The amount of aniline entrapped by PET, PET/α-CD, PET/β-CD and PET/γ-CD nanofibrous webs were calculated by high performance liquid chromatography (HPLC) and the data is given in Figure 61. The absorption of ~1300 ppm aniline by pristine PET nanofibers was observed. On the other hand, the amount of entrapped aniline was considerable higher for PET/CD nanofibrous webs when compared to pristine PET web. This is simply because the surface associated CD molecules increased the entrapment efficiency of PET nanofibers by facilitating complex formation with aniline. Moreover, the absorption of higher amount of aniline could be supplied by PET/CD nanofibers possibly due to

having higher hydrophilicity compared to PET nanofibers. So, our findings suggested that better entrapment efficiency of aniline by PET/CD was both due to the absorption of aniline by high surface area of nanofibers and also by inclusion complexation of aniline with CD. The complex formation of aniline with CD cavity is illustrated in Figure 62, schematically. Here, we observed that PET/α-CD and PET/β-CD nanofibrous webs captured ~2600 ppm of aniline, while the amount of aniline entrapped by PET/γ-CD nanofibrous web was ~3400 ppm at the end of entrapment test. PET/γ-CD presented the highest entrapment efficiency among the other samples, although the surface of this sample has less amount of CD. This is possibly due to bigger size of γ-CD cavity which could complex with more amount of aniline [85]. In brief, our results showed that all three PET/CD nanofibers can effectively entrap aniline vapor from the surrounding due to their very large surface area along with inclusion complexation capability of surface associated CD on the nanofibers.

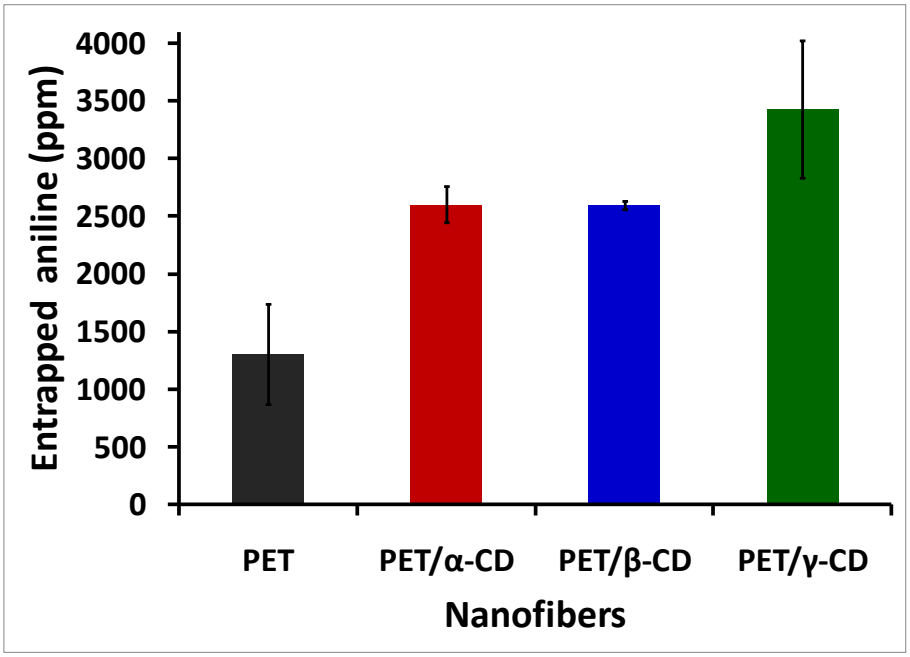

Figure 61. The amount of entrapped aniline (ppm) by the electrospun nanofibers.

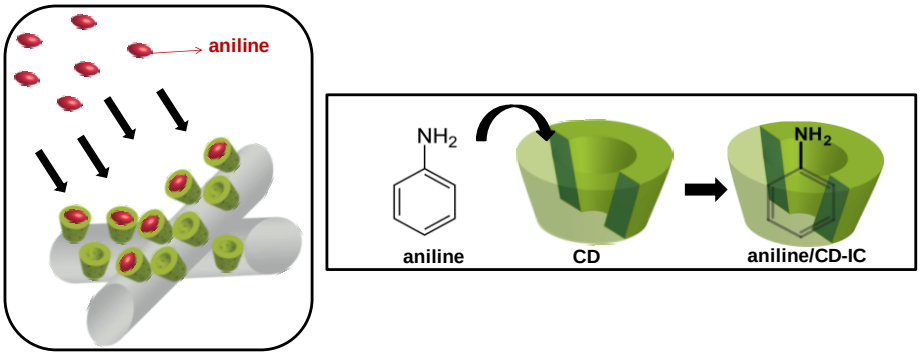

Figure 62. Schematic representations of formation of aniline/CD-IC on the surface of the nanofibers. (Copyright © 2014 Society of Plastics Engineers. Reprinted with permission from Ref.[271])

3.4.3. Conclusions

Here, we produced CD functionalized electrospun PET nanofibers by using three different types of native CD (α-CD, β-CD and γ-CD) having 25% (w/w) loading. XRD studies of PET/CD nanofibers suggested that CD molecules were distributed in the nanofiber matrix without any crystalline CD aggregation. The interaction between CD could carry out, since FTIR peak shift was observed. TGA data indicated that the initial weight percentage of CD in polymer solution was preserved in the fiber matrix after the electrospinning of PET/CD nanofibers. XPS studies and contact angle measurements of PET/CD nanofibers confirmed that most of CD molecules were located on the surface of PET nanofibers. Higher mechanical properties were observed for PET/CD nanofibers compared to pristine PET nanofibers. The entrapment performance of the resulting PET/CD nanofibers was tested by removal of aniline in vapor phase. Higher amount of aniline was entrapped by PET/CD nanofibrous webs when compared to pristine PET web since the surface associated CD molecules increased the entrapment efficiency of the nanofibers by IC formation with aniline. The amount of aniline entrapped by PET/γ-CD web was higher than that of PET/α-CD and PET/β-CD webs possibly due to bigger cavity size of γ-CD. Our results suggest that CD functionalized electrospun PET nanofibers can be promising filtering materials for air filtration and the removal of VOCs due to very high surface area of nanofibrous web and surface associated CD molecules having inclusion complexation capability with VOCs.

3.5. Surface Modification of Electrospun Polyester Nanofibers with Cyclodextrin Polymer for the Removal of Phenanthrene from Aqueous Solution

3.5.1. Experimental

Materials: Polyethylene terephthalate (PET) chips were gift from Korteks (Bursa, Turkey). Dichloromethane (DCM, Sigma Aldrich, extra pure), trifluoroacetic acid (TFA, Alfa Aesar, 99%), acetonitrile chromasol V (Sigma Aldrich, 99.9%), citric acid monohydrate-gritty puriss (CTR, Sigma Aldrich, 99.5-100.5%), sodium hypophosphite hydrate (SHPI, Sigma Aldrich), phenanthrene (Sigma Aldrich, 98%), and cyclodextrins (α-CD, β-CD and γ-CD, Wacker Chemie AG) were purchased and used as-received without any purification. Distilled water was from Millipore Milli-Q ultrapure water system.

Preparation of polymer solution and electrospinning of nanofibers: First, different polymer concentrations were used for the electrospinning of PET solution in order to obtain uniform and bead-free PET nanofibers, and 22.5% (w/v) polymer concentration was found to be the optimal. Therefore, 22.5% (w/v) PET was dissolved in TFA/DCM (50/50, v/v), and the resulting solution was loaded into 5 mL syringe fitted with a metallic needle having an inner diameter of 0.8 mm. Then, the syringe was placed horizontally on the syringe pump (KD Scientific, KDS 101). The polymer solution was pumped with 1 mL/h flow rate during the electrospinning, and the distance was set to 12 cm between needle tip and grounded stationary cylindrical metal collector (height: 15 cm, diameter: 9 cm) covered with a piece of aluminum foil. A voltage of 15 kV was applied for the electrospinning by using high voltage power supply (Matsusada, AU Series). The electrospinning process was carried out at 24.5 °C and at 17% relative humidity in an enclosed Plexiglas box.

Formation of cyclodextrin polymer (CDP) onto PET nanofibers: 10% (w/v) of α-CD, β-CD and γ-CD was mixed individually in 150 mL aqueous solution at 50 °C, and then, 10% (w/v) CTR as a crosslinking agent and 1.2% (w/v) SHPI as a catalyst

were added to each CD solution separately, and stirred for 30 min at 50 °C. After all reactants were dissolved in aqueous solution, three rectangular shaped (about 12x11 cm^2, 0.4 g) electrospun PET nanofibrous mats were immersed into the each resulting solution and kept for 3 h at 50 °C. Then these nanofibrous mats were dried at 105 °C for 10 min, and then cured at 180 °C for 7 min for the CDP formation onto PET nanofibers. Finally the resulting nanofibrous mats were washed two times with warm water (40 °C) for the removal of unreacted CD and CTR if any present, and then dried at 105 °C for 7 min. In order to make clear identification, CDP modified PET nanofibers are named as PET/α-CDP, PET/β-CDP and PET/γ-CDP according the type of CD used (α-CD, β-CD and γ-CD).

Characterizations and measurements: The morphology and the diameter of the PET and PET/CDP nanofibers were examined by using scanning electron microscope (SEM, FEI-Quanta 200 FEG). The nanofibers were coated with 5 nm Au/Pd prior to SEM analysis. To report the average fiber diameter (AFD) of the nanofibers, around 100 fibers of each sample were measured.

The chemical surface analyses of the PET and PET/CDP nanofibers were carried out by means of K-Alpha-monochromated high-performance X-ray photoelectron spectroscopy (XPS,Thermo Scientific). XPS data were taken by a flood gun charge neutralizer system equipped with a monochromated Al K-α X-ray source (hv= 1486.6 eV). In order to determine the surface elemental compositions wide energy survey scans of the nanofibers were acquired over the 0–1360 eV binding energy range, at pass energy of 150 eV with energy step size of 1 eV from 400 μm diameter circular spot in nanofibers. The high resolution spectra were recorded for O 1s region at pass energy of 30 eV and with energy steps of 0.1 eV in order to analyze the bonding states.

The thermal analyses of the samples were investigated by using thermogravimetric analyzer (TGA, TA Q500). TGA measurements were carried out under the nitrogen atmosphere, and the samples were heated from room temperature to 600 °C (nanofibers) or 500 °C (CTR and CD) at a constant heating rate of 20 °C/min.

The dynamic thermo mechanical performance of the nanofibrous mats was carried out using a dynamic mechanical analyzer (DMA, TA Q800) in tension film clamp at a constant frequency of 1 Hz. The samples having size of 10 mm (gap) × ~3 mm (width) × ~0.12 mm (thickness) was measured. The amplitude was 20 μm with the fiber aligning direction in the samples parallel to the stretching direction. The storage modulus and loss tangent (tan δ) of the nanofibrous mats were recorded in the range of 50-150 °C at a heating rate of 3 °C/min.

The surface area, pore (mesopore) sizes and volumes of the resulting PET and PET/CDP nanofibers were examined using Brunauer– Emmett–Teller (BET) surface area analyzer (Quantachrome, IQ-C model) with low-temperature (77.35 K) nitrogen adsorption isotherms measured over a wide range of relative pressures from 0.00 to 1.00. Prior to measurement, the each sample was placed in a 9 mm cell and degassed at 323.15 K for 12 h in the degas pot of the adsorption analyzer. The surface area of the samples was determined with multipoint BET method. On the other hand, density functional theory (DFT) was used to determine pore cumulative pore volume.

The molecular filtration performance of the resulting nanofibrous mats for water purification was tested by using phenanthrene as a model polycyclic aromatic hydrocarbon (PAH). First, phenanthrene was dissolved in acetonitrile, and then 10 μL of this solution was dropped in 50 mL pure water in order to obtain 1.8 ppm phenanthrene aqueous solution. Square shaped of PET, PET/α-CDP, PET/β-CDP and PET/γ-CDP nanofibrous mats (6x6 cm^2) were immersed individually in the 1.8 ppm phenanthrene aqueous solution (50 mL). We kept the size of the mats identical; however, the weight of each PET/CDP mat was about 0.38 g, while that of PET nanofiber was about 0.63 g due to difference in the thickness of the mats, since the nanofibers were collected in different times for each sample. It is quite difficult to keep the thickness of the electrospun mats even identical time. For filtration measurements, 0.5 mL of each solution was withdrawn to measure phenanthrene concentration in the solution and replenished with same amount of water at pre-determined time intervals. The phenanthrene filtration performance from aqueous solution by PET and PET/CDP nanofibrous mats was investigated by high

performance liquid chromatography (HPLC, Agilient 1200 series) equipped with VWD UV detector. The column was Agilient C18, 150 mm x 4.6 mm (5 µm pores) and the detection was accomplished at 254 nm. Mobile phase, flow rate, injection volume and total run time were acetonitrile (100%), 0.6 mL/min, 10 µl and 5 min, respectively. As a result, the amount of phenanthrene remaining in the solution was determined from the area of phenanthrene peak observed in HPLC chromatograms. Then the calibration curve was prepared by using phenanthrene solutions (1.8 ppm, 0.9 ppm, 0.45 ppm, 0.23 ppm, 0.12 ppm) and R^2 was calculated as 0.985. The peak area under curves was converted to concentration (ppm) according to the calibration curve. This experiment was repeated three times for each sample. The results were reported as the average±standard deviation of phenanthrene concentration remaining in the solution.

3.5.2. Results and Discussion

In this study, PET nanofibers were obtained by electrospinning of 22.5 % (w/v) PET solution in TFA/DCM (50/50, v/v), as it is schematically given in Figure 63a. The chemical reaction cannot occur between CD/CTR and PET nanofibers directly, since PET, a polymer based on terephtalic acid and ethylene-glycol, does not contain free reactive groups. Therefore, we modified the surface of the electrospun PET nanofibers through the polymerization reaction between CTR and CD [308, 311, 353]. Water-insoluble CDP network was formed by the crosslinking reaction between CD and CTR [354]. Three different types of native CD (α-CD, β-CD and γ-CD) were used to form α-CDP, β-CDP and γ-CDP. Initially, electrospun PET nanofibrous mats were impregnated in a solution of CD, CTR, and sodium hypophosphite (SHPI, catalyst), and then dried, followed by curing at 180 °C for 7 min. CTR turn into a cyclic anhydride intermediate by thermal dehydration at elevated temperature, and then hydroxyl groups of CD reacted with the carboxyl groups of citric acid [353]. The mechanism of the CDP formation is schematically described in Figure 63b. CDP was formed as a three-dimensional network structure onto PET nanofibers. Due to crosslinked structure, the CDP is stable and water-insoluble [355-356]. Thereby, surface modification of CDP onto PET nanofibers is

permanent and can resist to leaching or washing process [308, 311, 353, 357]. The resulting CDP having the essential structural characteristics of CD was not covalently fixed to the PET nanofibers, but it was physically adhered or was entangled onto PET fiber matrix [308, 311]. CDP modified PET nanofibers are called as PET/CDP. The representative photograph of the easily handled free-standing PET/CDP nanofibrous mat and the schematic representation of PET/CDP nanofibers are given in Figure 63c.

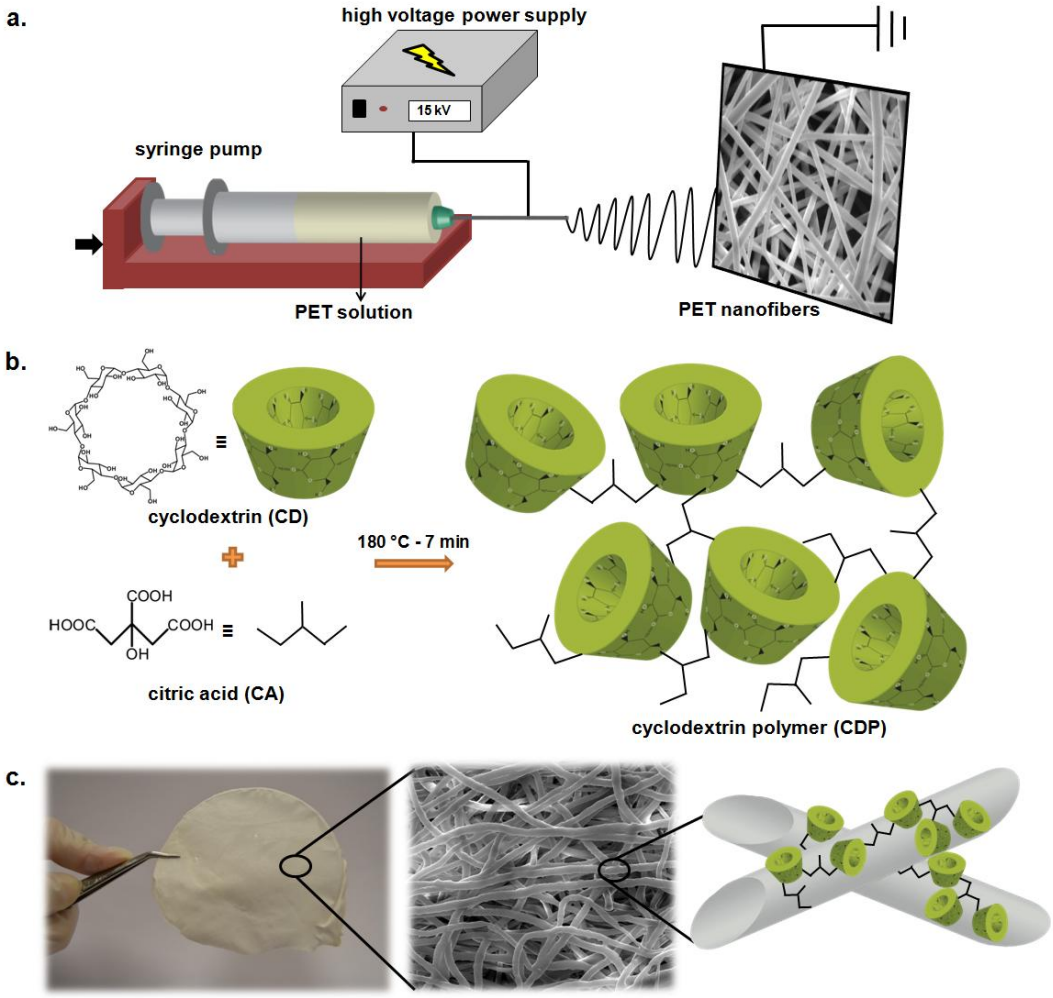

Figure 63. Schematic representations of (a) electrospinning of PET nanofibers, (b) formation mechanism of CDP and; (c) the representative photograph of PET/CDP nanofibrous mat and its SEM image and schematic representation of PET/CDP nanofibers. (Copyright © 2013, Elsevier. Reprinted with permission from Ref.[299])

SEM analysis was performed to investigate any morphological changes after the surface modification PET nanofibers with CDP. Figure 64 shows the representative SEM images and AFD of unmodified PET, PET/α-CDP, PET/β-CDP and PET/γ-CDP nanofibers. As clearly seen from SEM images, the surface morphologies of all three PET/CDP nanofibers were obviously different from the unmodified PET nanofibers. The surface of the unmodified PET nanofibers was smooth and uniform, whereas the surfaces of the PET/CDP nanofibers appear rough possibly due to CDP layer onto nanofibers.

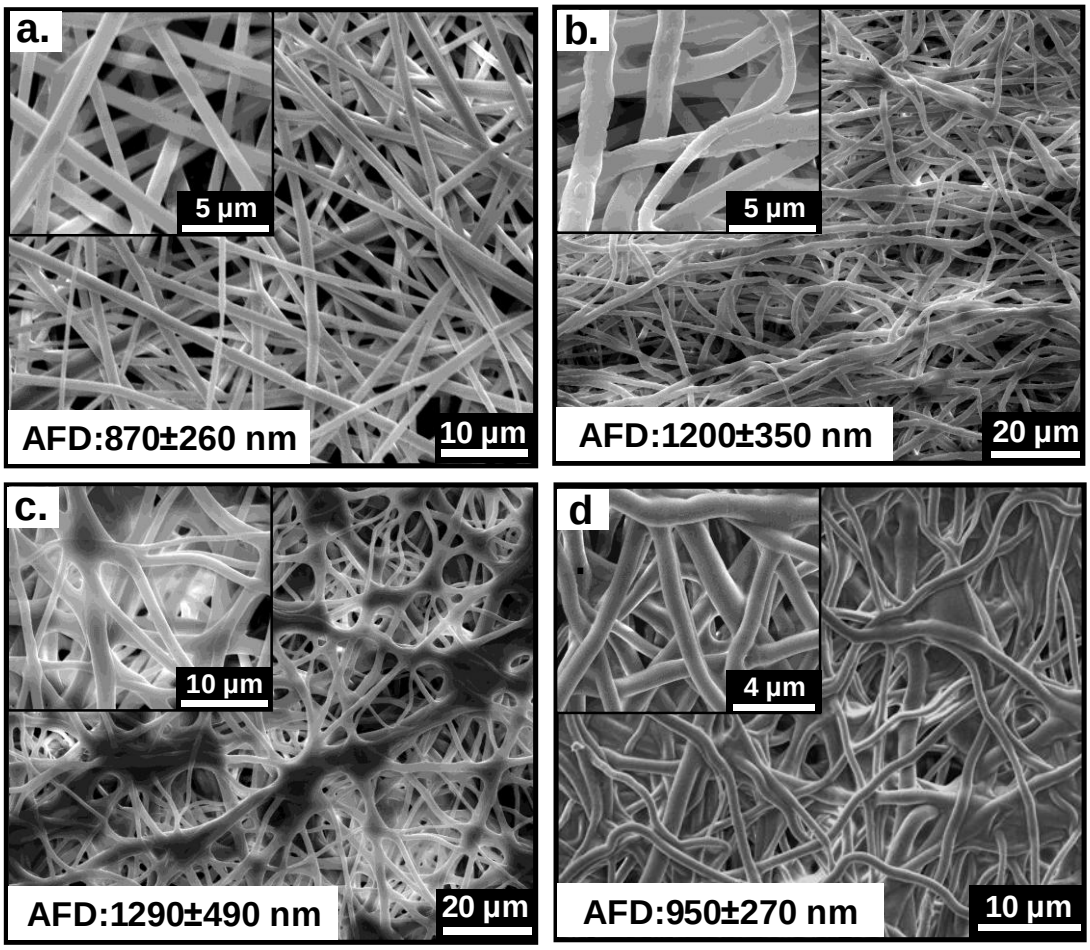

Figure 64. Representative SEM images and AFD of (a) PET, (b) PET/α-CDP, (c) PET/β-CDP, (d) PET/γ-CDP nanofibers. The insets show higher magnification images. (Copyright © 2013, Elsevier. Reprinted with permission from Ref.[299])

The rough surface has also been reported for cotton fabrics grafted with glycidyl methacrylate/β-CD [305] and hydroxypropyl-CD grafted woven PET vascular prosthesis [308-309]. Moreover, surface irregularities at certain points were also observed in the SEM images of PET/CDP nanofibers. Similar morphological observations were also reported for cotton fabric grafted with monochlorotriazinyl-β-CD/butylacrylate [358]. In brief, the rough and irregular surface of modified PET nanofibers suggested the successful attachment of CDP onto PET nanofibers. More importantly, CDP surface modification process did not deform the fibrous structure of PET as clearly seen from the SEM images. The unmodified PET nanofibers have 870±260 nm of AFD, while the AFD of PET/α-CDP, PET/β-CDP and PET/γ-CDP were measured as 1200±350, 1290±490 and 950±270 nm, respectively. The increase in the AFD of PET/CDP nanofibers compared to unmodified PET nanofibers could be due to the coating of the CDP onto PET nanofibers. Additionally, slight swelling of nanofibers during the modification process might also have resulted in fiber diameter increase.

The surface chemical characterization of PET/CDP nanofibers was performed by using X-ray photoelectron spectroscopy (XPS) in order to further demonstrate the coating of CDP onto PET nanofibers. Table 15 shows elementary compositions based on wide energy survey spectra of the unmodified PET nanofibers and PET/CDP nanofibers. The survey spectra comprising two peaks: C 1s and O 1s are consistent with the molecular structure of PET and CDP. The XPS data showed that the unmodified PET nanofibers have C 1s:O 1s = 72.21:27.79 (%) which is in full agreement with the literature [346]. Oxygen content on the surface of the samples was increased with the modification of CDP onto PET nanofibers. Thus, the appearance of higher oxygen content provides an evidence of the presence of CDP on the PET fiber surfaces.

Table 15. Atomic concentrations generated from XPS wide energy survey scans.

Samples	C (%)	O (%)
PET	72.21	27.79
PET/α-CDP	64.92	35.08
PET/β-CDP	61.29	38.71
PET/γ-CDP	67.89	34.31

High energy resolution O 1s XPS spectra were also recorded to get more detailed chemical state information about surface chemistry of the PET/CDP nanofibers. Figure 65 shows the normalized O 1s spectra of PET and PET/γ-CDP nanofibers. The assigned different components within these spectra and their individualized fitting parameters (peak binding energy and % area ratio) are also given in Table 16. Since the O 1s spectra of all PET/CDP nanofibers (PET/α-CDP, PET/β-CDP and PET/γ-CDP) are similar to each others, those XPS data acquired for PET/α-CDP and PET/β-CDP nanofibers were not given. The O 1s spectrum of unmodified PET nanofibers clearly represent the two types of oxygen atoms within the ester groups; π-bonded oxygen ($C=O^*$) and σ-bonded oxygen ($C–O^*$) at binding energies of 531.54 and 533.12 eV, respectively [347-349, 359]. The ratio of these peaks is 56.18:42.13, which is in reasonable agreement with the theoretical ratio of 50:50 [360]. In addition to these expected O 1s peaks, PET nanofibers have a very small peak situated at 534.52 eV assigned to adsorbed water [348]. After the CDP modification on the surface of PET nanofibers, the contribution of additional O 1s fitting peak at 532.35 related to aliphatic $C–O^*H$ came into view. The appearance of $C–O^*H$ component belongs to hydroxyl groups and carboxyl groups of CDP elucidated the successful surface modification of PET nanofibers with CDP. Moreover, as it was expected, CDP modification onto PET nanofibers resulted in significant increase of relative XPS signal intensity in the O 1s peak situated at 533.06 eV assigned to σ-bonded oxygen ($C–O^*$) compared with π-bonded oxygen ($C=O^*$) located at 532.35 eV. In brief, there are three different components ($C–O^*$, $C=O^*$ and $C–O^*H$) for O 1s high-resolution spectra of the PET/CDP nanofibers. The

increase in oxygen content of PET/CDP nanofibers compared to unmodified PET nanofibers was especially due to the appearance of C–O*H for the samples. The presence of CDP on the fiber surface is quite important in terms of the filtration application of PET/CDP nanofibrous mats [54, 266-267].

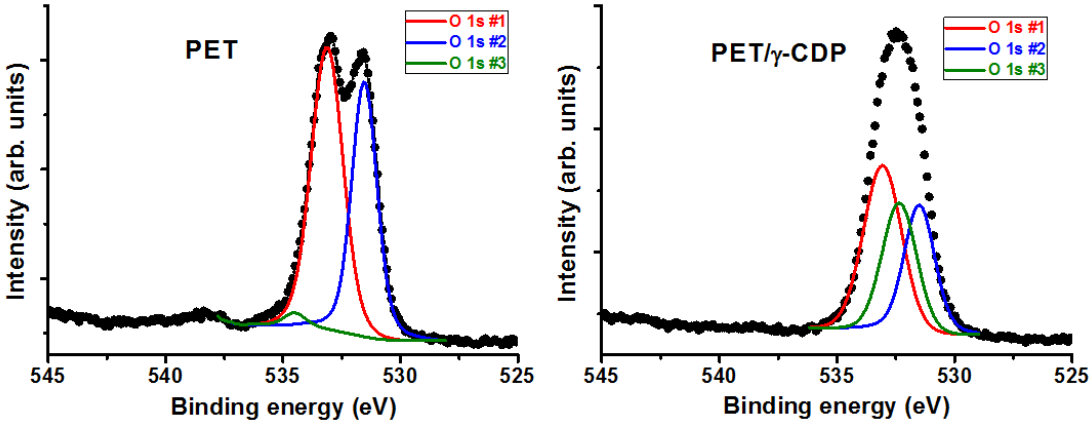

Figure 65. High resolution O 1s XPS spectra of PET and PET/γ-CDP nanofibers. (Copyright © 2013, Elsevier. Reprinted with permission from Ref.[299])

Table 16. Fitting parameters of the O 1s XPS spectra of PET and PET/γ-CDP nanofibers. (Copyright © 2013, Elsevier. Reprinted with permission from Ref.[299])

samples	fitting peaks	bonds	peak binding energy	area ratio (%)
PET	O 1s #1	C-O*	533.12	56.2
	O 1s #2	C=O*	531.54	42.1
	O 1s #3	adsorbed H_2O	534.52	1.7
PET/γ-CDP	O 1s #1	C-O*	533.06	42.5
	O 1s #2	C=O*	531.5	27.7
	O 1s #3	C-O*H	532.35	29.8

The thermal characteristics of the PET/CDP samples were investigated by using thermogravimetric analyzer (TGA). In Figure 66, the TGA thermograms of CTR and CD (α-CD, β-CD and γ-CD) (Figure 66a), and unmodified PET and PET/CDP nanofibers (Figure 66b) are given. Moreover, the derivative TGA

thermograms of nanofibers are also shown as inset in Figure 66b. The weight loss for CTR started at around 130 °C, and CTR completely degraded before 250 °C. TGA thermograms of CD (α-CD, β-CD and γ-CD) presented an initial weight loss below 100 °C and a major weight loss between 300-350 °C which correspond to the water loss and main degradation of CD, respectively [287]. The main degradation of PET nanofibers occurred between 375-475 °C. For the PET/CDP nanofibers two major weight losses were recorded between 200-350 °C and 375-475 °C which correspond to main thermal degradation of CDP and PET, respectively. The % weight loss between 200-350 °C corresponding to CDP in the PET/CDP nanofibers was 23%, 44% and 32% for PET/α-CDP, PET/β-CDP and PET/γ-CDP nanofibers, respectively, suggesting that the amount of CDP coating onto PET nanofibers was on the order of β-CDP>γ-CDP>α-CDP. When the derivative weight % loss were analyzed (Figure 66b), it was observed that the peak point for the unmodified PET (~437 °C) shifted slightly to higher temperature (~445 °C) for the PET/CDP nanofibers. This indicated that the modification of PET nanofibers with CDP resulted in slightly higher thermal stability due to more energy requirement for decomposition of these samples having crosslinked structure. The increased thermal stability has been also observed for CD grafted polyamide 6 fabrics [361]. Moreover, the char yield was higher for PET/CDP nanofibers when compared to unmodified PET nanofibers possibly owing to the crosslinked CDP structure providing higher carbon residue upon burning.

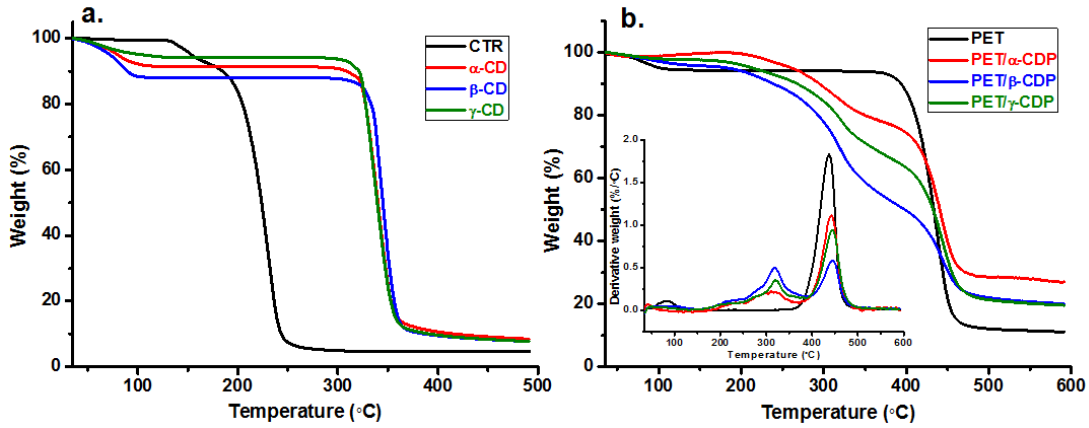

Figure 66. (a) TGA thermograms of CTR and three CD types (α-CD, β-CD and γ-CD), (b) TGA and derivative (inset) TGA thermograms of nanofibers. (Copyright © 2013, Elsevier. Reprinted with permission from Ref.[299])

Dynamic mechanical analyzer (DMA) was used to investigate the effect of CDP modification on the thermomechanical properties of the PET nanofibers. The storage modulus and tan δ of the unmodified PET and PET/CDP nanofibrous mats were recorded up to 150 °C (Figure 67). The storage modulus of the samples decreased with increasing temperature due to the transition from glassy state to rubbery state. It was observed that storage modulus of the PET/CDP nanofibrous mats was much higher than the unmodified PET nanofibers possibly due to stiffening effect of crosslinked CDP coating. Since the transferred stress for PET nanofibers was shared by CDP coating, the storage modulus of PET nanofibers enhanced with CDP modification. Moreover, for CDP modified nanofibers, tan δ peak shifted to the higher temperature region indicating that the glass transition temperature (Tg) for these nanofibers was higher when compared to unmodified PET nanofibers. The Tg value of PET nanofibers was 92 °C, while the T_g values of PET/CDP nanofibers were recorded as 109, 112 and 113 °C for PET/α-CDP, PET/β-CDP and PET/γ-CDP nanofibers, respectively. This result suggested that the mobilization of PET macromolecular chains were affected and the segmental motion of PET chains were hindered by CDP modification. Furthermore, broader tan δ peaks observed for PET/CDP nanofibers which can be originated from two Tg values correspond to not only PET, but also CDP [362].

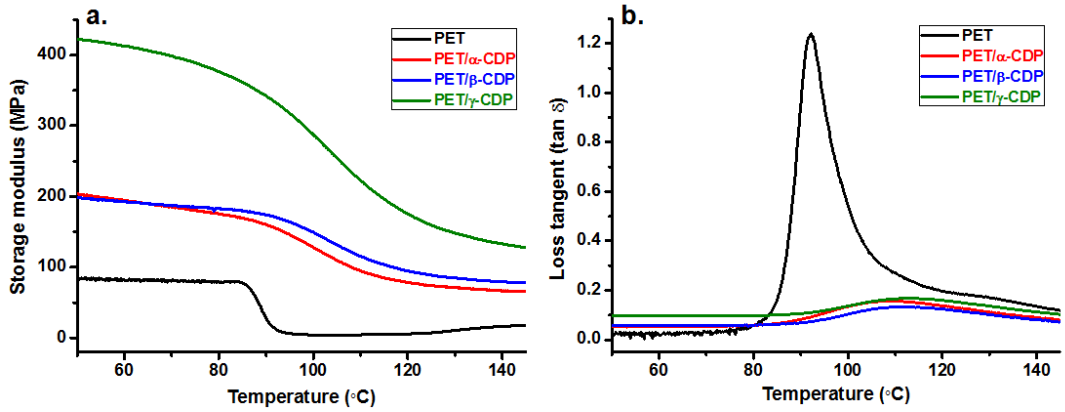

Figure 67. DMA thermograms of nanofibrous mats (a) storage modulus, (b) tan δ.

The surface areas, pore (mesopore) sizes and volumes of the PET and PET/CDP nanofibers investigated by Brunauer–Emmett–Teller (BET) with nitrogen adsorption measurements at 77.35 K are summarized in Table 17. The results indicate that the multipoint BET surface area of electrospun PET nanofibers is 6.03m^2/g. The surface area decreases to 1.56, 0.57 and 0.72 m^2/g for PET/α-CDP, PET/β-CDP and PET/γ-CDP nanofibers, respectively. As mentioned in SEM characterization, the surface modification of the PET nanofibers with CDP resulted in the irregularities on the fiber surfaces and increase in the AFD, which are the reasons of the decrease in surface area of nanofibers. The surface irregularities of nanofibers like crosslinking are clearly observed especially in the SEM images of the PET/β-CDP and PET/γ-CDP nanofibers (Figure 64c,d). Hence, the surface areas of PET/β-CDP and PET/γ-CDP nanofibers were less than PET/α-CDP. Moreover, since PET/β-CDP has the largest AFD among the samples (Figure 64c), the surface area of PET/β-CDP nanofibers was determined slightly less than PET/γ-CDP nanofibers. It is well known that the AFD have great effect on the surface area of fibers [363].

Table 17. Surface area, pore size and volume data of the nanofibers. (Copyright © 2013, Elsevier. Reprinted with permission from Ref.[299])

Samples	**Multipoint BET surface area (m^2/g)**	**Average pore diameter (nm)**	**DFT cumulative pore volume (cc/g)**
PET	6.03	15.3	$1.03e^{-2}$
PET/α-CDP	1.56	12.4	$3.22e^{-3}$
PET/β-CDP	0.57	13.6	$1.28e^{-3}$
PET/γ-CDP	0.72	14.0	$1.05e^{-3}$

We investigated the mesopore structure (diameter and volume) of the nanofibers to determine the effect of molecular capturing. It was observed that, the average pore diameter and cumulative pore volume determined by DFT also decreased after surface modification of the PET nanofibers with CDP possibly due to surface irregularities of nanofibers like crosslinking.

The molecular filtration capability of PET and PET/CDP nanofibrous mats has been tested using a phenanthrene as a model polycyclic aromatic hydrocarbon (PAH). phenanthrene is a common pollutant and can form inclusion complexes (IC) with CD [81, 341, 364]. Figure 68 summarizes the cumulative % decrease of phenanthrene concentration over time when PET and PET/CDP mats have been kept in aqueous solution of phenanthrene.

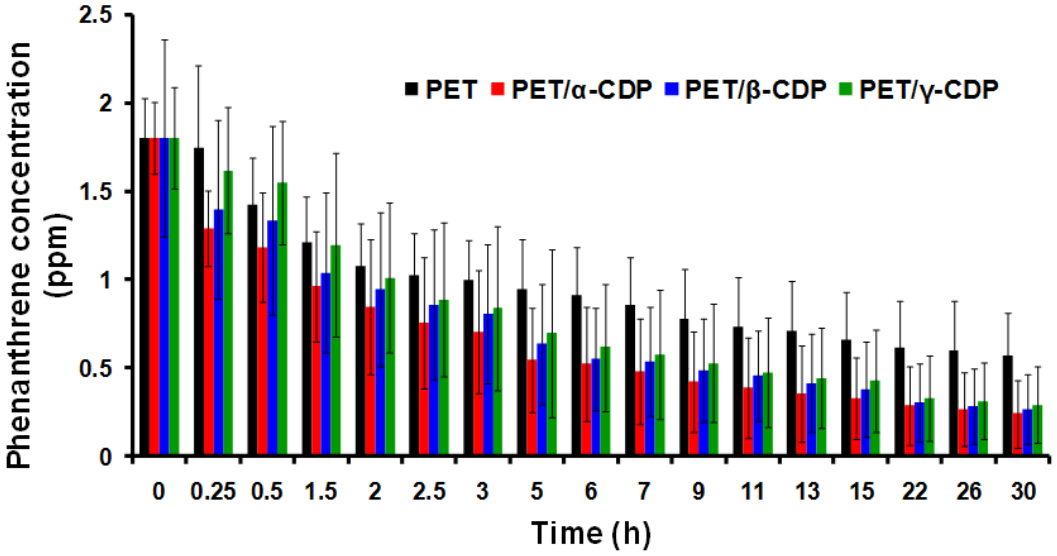

Figure 68. Time-dependent decrease of phenanthrene concentration in the aqueous solution containing nanofibrous mats. (Copyright © 2013, Elsevier. Reprinted with permission from Ref.[299])

As seen from Figure 68, the concentration of phenanthrene in the aqueous solution decreased within the contact time. The adsorption of phenanthrene by PET nanofibers for the first 2 h was observed, and then the concentration of phenanthrene slightly decreased over time. On the other hand, the decrease of phenanthrene concentration for PET/CDP mats was more significant. Although less amount of PET/CDP nanofibers were used compared to PET nanofiber for filtration test, the removal efficiency of the phenanthrene from its aqueous solution was better when PET/CDP nanofibers were used. Water-insoluble CDP can be very effective in removal of many organic pollutants from aqueous media, since CD cavity is capable

of forming IC with a wide variety of organic molecules [58-59, 87, 266, 305, 356]. Therefore, the surface modification of electrospun PET nanofibers with CDP increased the efficiency of filtration by facilitating complex formation with phenanthrene compounds. Here, all three PET/CDP nanofibers demonstrated the ability to function as a molecular filter for water purification through complexation of the phenanthrene with CDP.

As it mentioned in the previous section it is notable that the average pore size (or surface area) of nanofibers appeared to decrease after CDP modification. However the filtration efficiency is still further improved for PET/CDP nanofibers compared to PET nanofibers due to the CDP structure onto nanofibers, which plays a crucial role in capturing phenanthrene.

When the CD types were compared, all three PET/CDP samples showed approximately same filtration efficiency for the removal of phenanthrene at the end of filtration test. Although TGA suggested that the amount of CDP coating onto PET nanofibers was on the order of β-CDP>γ-CDP>α-CDP, it is likely that not all the CD molecules are available for complexation. So, the three PET/CDP samples may have comparable amount of CD cavity available for complexation. Even so, the average percentage removal of phenanthrene with respect to initial time was slightly better for PET/α-CDP and this is possibly because of the higher surface area of PET/α-CDP nanoweb compared to PET/β-CDP and PET/γ-CDP nanowebs.

We have also inspected the dimension stability of the PET and PET/CDP nanofibers, and we observed that the mats kept their nanofibrous structure after the filtration test (Figure 69). In short, the surface modification of electrospun PET nanofibers with CDP enhanced the efficiency of its filtration performance by facilitating complex formation with organic compounds such as phenanthrene.

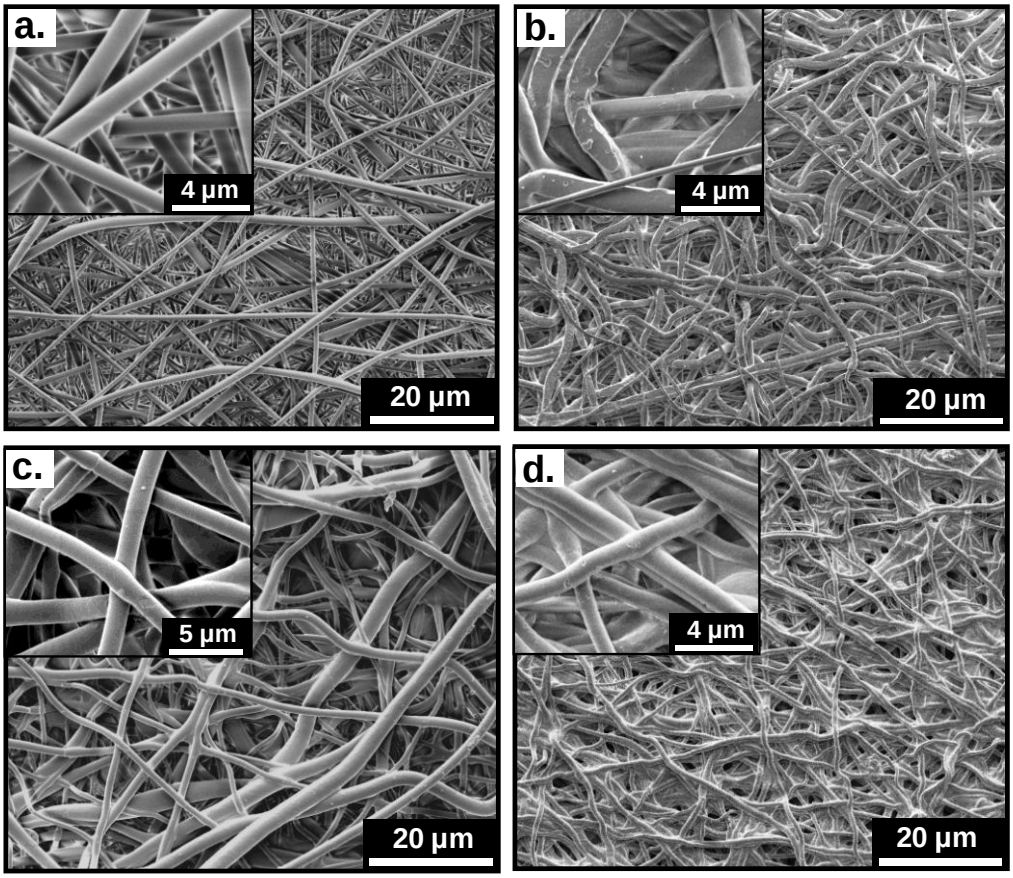

Figure 69. Representative SEM images of (a) PET, (b) PET/α-CDP, (c) PET/β-CDP and (d) PET/γ-CDP nanofibers after the filtration test. The insets show higher magnification images. (Copyright © 2013, Elsevier. Reprinted with permission from Ref.[299])

3.5.3. Conclusions

In this study, we have achieved the surface modification of electrospun PET nanofibers with CDP. First, PET nanofibers were obtained via electrospinning, then, water-insoluble crosslinked CDP coating was formed onto PET nanofibers by polymerization reaction between CD and crosslinking agent (citric acid). For a comparative study, three different types of CD; α-CD, β-CD and γ-CD were used to form CDP onto electrospun PET nanofibers. The imaging analysis by SEM revealed that nanofibrous structure of the PET nanofibers was preserved after surface modification with CDP. Yet, the surface of the PET/CDP nanofibers was

rough/irregular, whereas that of unmodified PET nanofibers was smooth. Moreover the diameter of the PET nanofibers increased after CDP modification possibly due to the presence of CDP layer onto nanofibers and/or swelling of the nanofibers during modification process. The presence of CDP coating on the surface of PET nanofibers was supported by XPS analyses. The thermal analysis of PET/CDP nanofibers carried out by TGA showed two main thermal degradation steps corresponding to CDP and PET degradation. The modification of PET nanofibers with CDP resulted in slightly higher thermal stability, and the char yield was higher for PET/CDP nanofibers compared to unmodified PET nanofibers. The TGA data also indicated that the amount of CDP coating onto PET nanofibers was on the order of β-CDP>γ-CDP>α-CDP. DMA results elucidated the improvement of mechanical properties for PET/CDP nanofibers, that is, PET/CDP nanofibers have shown higher storage modulus and higher glass transition temperature compared to unmodified PET nanofibers. The filtration performance of the CDP surface modified PET nanofibers was tested by removal of the polycyclic aromatic hydrocarbon waste molecule (phenanthrene) from its aqueous solution. We observed that PET/CDP nanofibers have shown better filtration efficiency when compared to the unmodified PET nanofibers due to the inclusion complexation capability of CDP onto PET nanofibers. Initially, the average percentage removal of phenanthrene with respect to time was slightly better for PET/α-CDP, but, at the end of filtration test the all PET/CDP samples showed more or less same filtration efficiency for the removal of phenanthrene from the aqueous solution. It was also observed that PET/CDP mats have kept their nanofibrous structure after the filtration test. In brief, our results indicated that PET/CDP nanofibers have shown the potentials to be used as a filter/membrane for water purification owing to very high surface area of electrospun nanofibers and surface associated CDP, since CD molecules have inclusion complexation capability with polycyclic aromatic hydrocarbons and other types of organic waste molecules.

CHAPTER 4

4. FUNCTIONAL NANOFIBERS VIA ELECTROSPINNING AND ATOMIC LAYER DEPOSITION

The work described in this chapter was published in part as:

(1**) Kayaci, F.**; Ozgit-Akgun, C.; Donmez, I.; Biyikli, N.; Uyar, T., Polymer–inorganic core–shell nanofibers by electrospinning and atomic layer deposition: Flexible nylon–ZnO core–shell nanofiber mats and their photocatalytic activity. *ACS Applied Materials & Interfaces* 2012, *4* (11), 6185-6194. *DOI: 10.1021/am3017976.*

(2) **Kayaci, F.**; Ozgit-Akgun, C.; Biyikli, N.; Uyar, T., Surface-decorated ZnO nanoparticles and ZnO nanocoating on electrospun polymeric nanofibers by atomic layer deposition for flexible photocatalytic nanofibrous membranes. *RSC Advances* 2013, *3* (19), 6817-6820. *DOI: 10.1039/C3RA40359A.*

(3) **Kayaci, F.**; Vempati, S.; Ozgit-Akgun, C.; Biyikli, N.; Uyar, T., Enhanced photocatalytic activity of homoassembled ZnO nanostructures on electrospun polymeric nanofibers: A combination of atomic layer deposition and hydrothermal growth. *Applied Catalysis B: Environmental* 2014, *156-157*, 173-183. *DOI: 10.1016/j.apcatb.2014.03.004*.

(4) **Kayaci, F.**; Vempati, S.; Donmez, I.; Biyikli, N.; Uyar, T., Role of zinc interstitials and oxygen vacancies of ZnO in photocatalysis: A bottom-up approach to control the defect density. *Nanoscale* 2014. *DOI: 10.1039/c4nr01887g.*

(5) **Kayaci, F.**; Vempati, S.; Ozgit-Akgun, C.; Donmez, I.; Biyikli, N.; Uyar, T., Selective isolation of the electron or hole in photocatalysis: ZnO-TiO_2 and TiO_2-ZnO core-shell structured heterojunction nanofibers via electrospinning and atomic layer deposition. *Nanoscale* 2014, *6* (11), 5735-5745. *DOI: 10.1039/C3NR06665G*.

4.1. Summary

Functional materials showing photocatalytic properties which facilitate the degradation of organic contaminants in water under visible or UV light has attracted significant interest in recent years [144-145, 149, 174-176], as it mentioned in third part of Chapter 1 (1.3). In this Chapter, there is an overview of the researches [11, 130, 153, 157, 365] in which we obtained functional nanofibrous membranes showing remarkable photocatalytic properties by combining of electrospinning and atomic layer deposition (ALD) processes (see Figure 70). In the third part of Chapter 1 (1.3), ALD process was explained in depth.

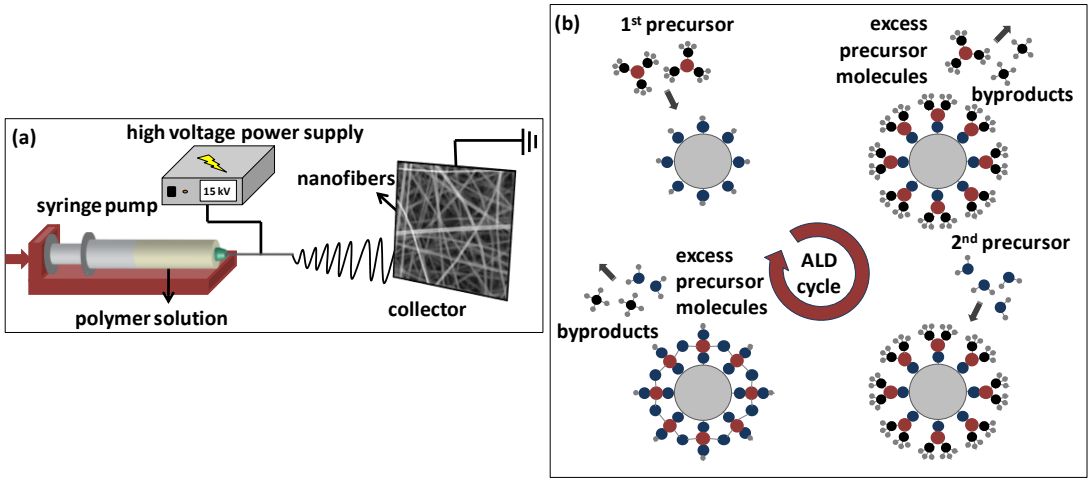

Figure 70. Schematic representations of the processing steps for the production of polymer-inorganic nanofibers: (a) electrospinning, (b) ALD.(Copyright © 2013, Royal Society of Chemistry. Reproduced with permission from Ref.[130])

ZnO has unique properties due to its high photosensitivity, high catalytic activity [144-145, 175], suitable bandgap (3.36 eV), low cost, and environmental compatibility [176, 366], as well as antibacterial property [175]. The morphology of ZnO is quite crucial for photocatalytic efficiency, and therefore ZnO nanoparticles and nanofibers have shown excellent photocatalytic properties due to their very high surface area and more porous nature [144]. In order to cope with the usage difficulty of ZnO materials having brittle nature, we obtained polymer-ZnO nanofibrous membranes having structural flexibility [11, 130, 157, 365]. These studies are reported in the initial four parts of this chapter (4.1, 4.2, 4.3, 4.4)

In our research study mentioned in the next part (4.2), we have successfully achieved polymer-inorganic core-shell nanofibers; nylon 6,6 (polymeric core) nanofibers were obtained by electrospinning, and then, ZnO (inorganic shell) were precisely deposited onto electrospun nylon 6,6 nanofibers by ALD technique. Electrospun nylon 6,6 nanofibers having three different average diameters (~80, ~240 and ~650 nm) were coated with 90 nm of ZnO layer by ALD. Nylon 6,6 is a synthetic polymer type which is suitable for filtration application due to its distinctive properties such as high strength, toughness, elasticity, abrasion resistance and good chemical resistance. Photocatalytic activity (PCA) of the core-shell nylon 6,6-ZnO nanofiber mats were tested by following the photocatalytic decomposition of rhodamine-B (Rh-B) dye.

In the next study mentioned third part of this chapter (4.3), polymeric nanofibers surface-decorated with ZnO nanoparticles (NP) and ZnO nanocoating were fabricated. Initially, polymeric (nylon 6,6) nanofibers having an average fiber diameter of ~80 nm were produced via electrospinning technique. In the next step, ZnO was grown onto smooth surfaces of polymeric nanofibers via ALD [110-111] by altering deposition parameters. Altering the ALD parameters resulted in various ZnO morphologies on polymeric nanofibers; surface-decorated ZnO NP and highly dense ZnO NP, and a continuous ZnO nanocoating having uniform thickness (~27 nm). PCA of the resulting nanostructures were compared using Rh-B as a model organic dye.

The importance of lattice defects in semiconductors in PCA efficiency was mentioned in the fourth part of Chapter 1 (1.4). We should agree with the fact that ideally defect-free-ZnO can use only UV region (3-4 %) of the solar spectrum because of its wider band gap and therefore 44-47 % of visible light is left unused. Hence, it obviously is a wise choice to harness the visible as well as UV region of solar energy to achieve significantly higher PCA. In order to initiate or improve the light absorption in the visible region one can engage the native defects of ZnO [161, 166], which form sub-band gap states [151]. For example, oxygen vacancies (V_O's) are induced in ZnO and recently shown to improve PCA [128, 133, 367], alongside

of other similar studies [161, 166, 368]. On the other hand, V_O's not only create intermediate bands, but also shown to act as self-dopants and induced bandgap reduction [367]. Therefore, by considering the various properties of nanostructured-ZnO, it is convincing and logical to design a smart and efficient ZnO catalyst depicting high PCA is of fundamental as well as technological importance. In another two studies of this chapter (4.4 and 4.5), we employed photoluminescence (PL) spectra to identify and quantify the density of defect for the samples, and related with these, PCA studies were interpreted.

In the fourt part of this chapter (4.4), we reported a novel hybrid approach, in which we combine chemical vapor deposition and liquid phase deposition techniques. Namely ALD and hydrothermal growth are combined to fabricate a hierarchy of nanostructured-ZnO on electrospun poly(acrylonitrile) (PAN) nanofibers. The resulting ZnO nanostructures depicted synergy effect and shown enhanced PCA. PAN nanofibers are well adoptable in water filtration where their unique properties such as high surface area, nanoporous structure, low basis weight, easy permeability, good stability and chemical resistance are worth mentioning [369-372]. In our previous study mentioned in the third part of this chapter (4.3), electrospun polymeric nanofibers were subjected to varying ALD parameters where we have studied how the PCA is influenced when nanoparticles transform into continuous film [130]. We have inferred that highly dense nanoparticles have shown relatively higher PCA due to the increased surface area, and polycrystalline film alone is not adequate to yield high PCA. Thereby in this study (4.4), we have grown single crystalline ZnO nanoneedles (with an average diameter and length of ~25 nm and ~600 nm, respectively) on the ALD-seed coating. Note that the single cyrstalline ZnO nanoneedles can depict the lowest possible defect density. Furthermore, previous studies [128, 133, 161, 166, 367-368] have introduced V_O's throughout the catalyst, however, in contrast we have combined two materials one of which is dominant in oxygen related defects, while the other is virtually defect-free single crystal. Then PCA was tested within the present combination using methylene blue (MB) as a model organic dye.

V_Os in ZnO are well known to enhance the PCA, despite of various other intrinsic crystal defects [144, 153, 157-159, 161]. In next study we aim to elucidate the effect of Zn_i and V_Os on the PCA, which has applied as well as fundamental interest. In order to achieve this one needs to overcome the major hurdle of fabricating ZnO with controlled defect density, where it is acknowledged that the defect level control in ZnO significantly hard [163]. As shown in literature, Zn_is are very instable when compared to V_Os which are found to be stable even at 400 ˚C [373]. Theoretical support for this instability is given by Janotti et al.[374] where the authors suggest that Zn_is diffuse faster through a migration barrier as low as 0.57 eV, *cf* for V_Os it is from 1.7 to 2.4 eV. Since the ionization energies are in the range of 0.05 to 2.8 eV,[373] the formation temperature is detrimental for the relative concentrations of the various defects. One has to choose non-equilibrium processes to induce Zn_is [375-376] in which the samples were subjected to thermal annealing to control the density of the defects. Under oxygen deficient conditions at high temperatures V_Os are typical,[377] while Zn vapor-rich environments produce Zn_is [378-379]. As an example, when ZnO crystals are annealed in zinc vapor at 1100 ˚C, Zn_is are introduced into the lattice [380-381]. More recently Zeng et al.[163] followed an earlier reported method [375-376] in which zinc target is laser ablated in aqueous solution. The resultant colloids were subjected to thermal annealing in various atmospheres [163].

In our study mentioned in the fifth part of this chapter (4.5), we showed that ALD, a powerful bottom-up approach can be employed to produce ZnO on polymeric fibers consisting of Zn_is along with or without V_Os [365]. In order to control defects, we have chosen polysulfone (PSU) electrospun nanofibers as a substrate on which non-uniform adsorption of ALD precursors is inevitable due to the differences in the hydrophilic nature of the functional groups. The variation of ALD cycle numbers (*viz* 100, 200, 300 and 400) has yielded structures of ZnO with a clear transformation from quantum dots (QDs) to nanocoating (NC) on PSU fibers, during which the predominance transfers from Zn_is to V_Os while the density of the former is sustained for all cases. Notably, the earlier methods [163, 375-376] require post thermal treatments to control the defect density; in contrast we have noticed

predominantly Zn_i or Zn_i and V_Os in as-fabricated samples depending on the cycle numbers. After thorough characterization (structural, optical and surface), the PCA is tested and juxtaposed against defect density. We believe that this study deepens the understanding of least studied crystal defect of ZnO, Zn_is in connection to their PCA.

Both the charge carriers (*electron* and *hole*) are involved in catalysis for the semiconductor heterostructures cases in literature [178-180], which makes it rather hard to determine unambiguously the individual role of each, apart from the intrinsic surface chemistry [138] of the materials. It is notable that charge exchange process and hence the mechanism of PCA at heterojunction is still unclear even after the decades of research [382]. If one of the charge carriers can be effectively isolated from the catalysis then it would be very insightful for future studies on the design of new catalytic materials. To address this issue we have fabricated core-shell heterojunction (CSHJ) nanofibers from ZnO and TiO_2 in two combinations where only the 'shell' part of the heterojunction is exposed to the environment to participate in the photocatalysis. It is notable that similar structures were studied, however, for their O_2 [124-125] and NO_2 [125] sensing characteristics. In an earlier article by Agrawal et al. [383] spherical core-shell structures were studied only in one combination (ZnO-TiO_2) for their PCA. Pd@CeO_2 hollow core-shell catalysts were studied for photo as well as thermal catalysis [154]. In both the cases, [154, 383] however, charge carrier separation and their individual roles were not addressed. Recently, an interesting study appeared in literature in which photo-generated *e/h* pairs from $[Ru(bpy(CO_2CH_3)_2)_3]^{2+}$ based visible-light-sensitizer were separated *via* Co_3O_4-SiO_2 core-shell nanoparticles [177]. The separated *holes* are migrated through SiO_2 shell into Co_3O_4 core and *electrons* directly participate in the catalysis. Other investigations on core-shell structures include $PbTiO_3$–TiO_2, [384] (Ba,Sr)TiO_3-TiO_2 [385] etc. These studies emphasize the need for a better understanding of the roles of *electron* and *hole* in the catalysis. In our study mentioned in the last part of this chapter (4.6), ZnO-TiO_2 and ZnO-TiO_2 CSHJ nanofibers were fabricated *via* electrospinning and ALD, respectively which were then subjected to calcination. These CSHJ were characterized and studied for the PCA. These two combinations expose *electrons* or *holes* selectively to the environment.

4.2. Polymer-Inorganic Core-Shell Nanofibers by Electrospinning and Atomic Layer Deposition: Flexible Nylon-ZnO Core-Shell Nanofiber Mats and Their Photocatalytic Activity

4.2.1. Experimental

Materials: Nylon 6,6 pellets (relative viscosity: 230.000-280.000) were purchased from Sigma-Aldrich. Formic acid (FA, Sigma-Aldrich, 98-100 %), 1,1,1,3,3,3-hexafluoro-2-propanol (HFIP, Sigma-Aldrich, ≥ 99%) and rhodamine-B (Rh-B, Sigma-Aldrich, dye content ~95 %) were used in this study. In addition, Diethylzinc ($(C_2H_5)_2Zn$ or DEZn, Sigma-Aldrich) and HPLC grade water (H_2O) were used as the zinc precursor and oxidant for the ALD of ZnO, respectively. All materials were used without any purification.

Electrospinning of Nylon 6,6 Nanofibers: Electrospinning of nylon 6,6 nanofibers having different average fiber diameters were obtained by varying the solvent type. Accordingly, 8 wt. % nylon 6,6 was dissolved in the as-received two different solvents; HFIP and FA, separately; and 5 wt. % nylon 6,6 was dissolved in HFIP as well. These solutions were stirred for 3 h at room temperature. The homogeneous clear solutions were placed in 3 ml syringes fitted with metallic needles of 0.8 mm of inner diameter. Then the syringes were fixed horizontally on the syringe pump (Model: SP 101IZ, WPI). The polymer solutions were pumped with feed rate of 1 ml/h during electrospinning. The applied voltage to the metal needle tip by using high voltage power supply (Matsusada, AU Series) was 15 kV and the tip-to-collector distance was set at 10 cm for the electrospinning of the prepared solutions. On the way to the grounded stationary cylindrical metal collector (height: 15cm, diameter: 9 cm), the solvents evaporated and the electrospun nylon 6,6 nanofibers were deposited on the aluminum foil covering on the collector. The electrospinning processes were carried out at 23 ^{o}C and 36 % relative humidity in an enclosed Plexiglas box.

Preparation of ZnO Shell Structure by ALD: ZnO deposition on the electrospun nylon 6,6 nanofibers was carried out at 200°C in a Savannah S100 atomic layer deposition (ALD) reactor (Cambridge Nanotech). Deposition rate of ZnO on the nylon 6,6 nanofibers at this temperature was ~1.13 Å/cycle. N_2 was used as the carrier gas with a flow rate of 20 sccm. 800 cycles were deposited, where one cycle consisted of DEZn pulse (0.015 s)/ N_2 purge (10 s)/ H_2O pulse (0.015 s) / N_2 purge (10 s).

Characterization Techniques: The viscosity of the nylon 6,6 solutions was measured by using Anton Paar Physica MCR-301 Rheometer equipped with a cone/plate accessory using the spindle type CP40-2 at 22 ^{o}C and a constant shear rate of 100 s^{-1}. The morphology, uniformity and dimensions of the pristine nylon 6,6 nanofibers and core-shell nylon 6,6-ZnO nanofibrous membranes were studied by using scanning electron microscope (SEM) (FEI – Quanta 200 FEG). The samples were coated with 5 nm Au/Pd prior to SEM imaging. In order to determine the average fiber diameter (AFD) from SEM images, around 100 fibers were analyzed. The elemental analyses of the core-shell nylon 6,6-ZnO nanofibers without coating of Au/Pd were performed by using SEM equipped with an energy dispersive X-ray (EDX) system operating at an accelerating voltage of 15 kV. Additionally, transmission electron microscope (TEM) (FEI – Tecnai G2F30) was used for the detailed morphological investigation of the core-shell nylon 6,6-ZnO nanofibers, as well as measurement of core and shell thicknesses. For TEM image, the samples were prepared by sonicating core-shell nylon 6,6-ZnO nanofibers in ethanol for 5 minutes and dropping the suspensions onto the HC200 TEM grids, and allowing them to dry under IR lamp for few minutes. Selected area electron diffraction (SAED) patterns of the core-shell nylon 6,6-ZnO nanofibers were also obtained by using TEM in order to investigate the crystal structure of ZnO shell. The surface compositions of pristine nylon 6,6 nanofibers and the core-shell nylon 6,6-ZnO nanofibers were determined by using X-ray photoelectron spectroscopy (XPS, Thermo Scientific) by means of a flood gun charge neutralizer system equipped with a monochromated Al K_α X-ray source ($h\nu$ = 1486.6 eV). XPS data were taken from 400 μm diameter circular spot on the surface of the samples. Wide energy survey scans were obtained over a 0–1360 eV binding

energy range, at pass energy of 150 eV, and with an energy step of 1 eV. The high resolution spectra were recorded for Zn 2p regions at pass energy of 30 eV, and with energy steps of 0.1 eV in order to analyze the bonding states. The thermal analysis of the nanofibers by thermal gravimetric analyzer (TGA) (TA Q500) was performed from room tem-perature to 550 °C with a heating rate of 20 °C/min under the nitrogen atmosphere. Moreover, XRD data of the pristine nylon 6,6 nanofibers and core-shell nylon 6,6-ZnO nanofibrous membranes were collected within the range of 2θ = 10^{o}- 100^{o} by using PANalytical X'Pert Multi Purposer X-ray Diffractometer with Cu Kα radiation, operating at a voltage of 45 kV and a current of 40 mA. The structures of the nanofibers were investigaetd by attenuated total reflectance Fourier transform infrared spectroscopy (ATR-FTIR) (Bruker, VERTEX 70) The ATR-FTIR spectra were recorded from 700 to 4000 cm^{-1} with a resolution of 4 cm^{-1} by taking 64 scans for each sample, and these spectra were obtained with FTIR spectrometer equipped with a liquid nitrogen cooled mercury cadmium telluride detector by using ATR set up contain-ing a germanium crystal.

Photocatalytic Activity (PCA) of the Core-Shell Nylon 6,6-ZnO Nanofibrous Membranes: The PCA of the samples was analyzed by the photodegradation of rhodamine-B (Rh-B) (1.04×10−5 M) in aqueous medium. 8%-nylon 6,6/FA-ZnO and 8%-nylon 6,6/HFIP-ZnO were used in this experiment in order to investigate the effect of fiber diameter on the photocatalytic activity. The core-shell nylon 6,6 - ZnO nanofibrous membranes (weight of nanofiber mat: 9.3 mg, dimension of the nanofiber mat: 2.0 cm×1.5 cm and 2.0 cm×2.0 cm) was put into quartz cuvettes (width: 1 cm, length: 1 cm, and height: 5 cm, Hellma) filled with Rh-B solution. The cuvettes were placed with a distance of 10 cm from the UV source (8 W, UVLMS-38 EL) and kept under UV irradiation at 365 nm wavelength. Dye concentration in the cuvettes was measured by using UV-Vis-NIR spectrophotometer (Varian Cary 5000) at certain time intervals. The core-shell nylon 6,6-ZnO nanofibrous membranes stayed at the bottom of the dye solution during the experiment, and therefore the membranes did not interfere with the UV-Vis measurement.

4.2.2. Results and Discussion

First, several nylon 6,6 concentrations were used for different solvent systems; formic acid (FA) and 1,1,1,3,3,3-hexafluoro-2-propanol (HFIP), in order to optimize the morphology of electrospun nylon 6,6 nanofibers and the optimal concentrations were chosen as follow to obtain uniform bead-free nylon 6,6 nanofibers having different average fiber diameters (AFD) for each solvent system. Schematic representation of the formation process of core-shell polymer-inorganic nanofibers *via* combination of electrospinning and ALD is illustrated in Figure 71. In the first step, nylon 6,6 nanofibers having three different average fiber diameters (AFD) were produced by electrospinning technique.

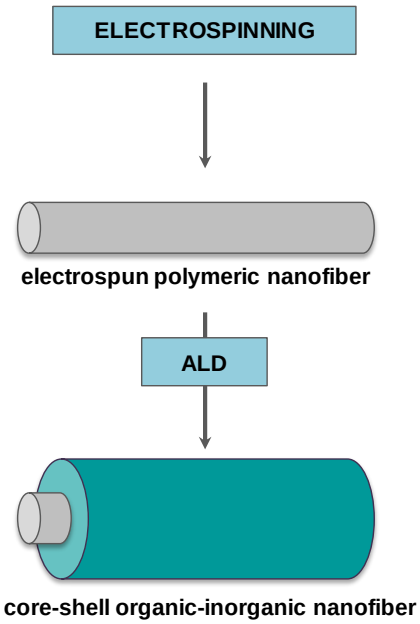

Figure 71. Schematic representation of the formation process of core-shell polymer-inorganic nanofibers: preparation of the polymeric nanofiber by electrospinning and conformal inorganic shell deposition on the electrospun nanofiber *via* ALD. (Copyright © 2012, American Chemical Society. Reproduced with permission from Ref.[11])

The representative SEM images of the electrospun nylon 6,6 nanofibers obtained from 8% (w/v) formic acid (FA) and 5% and 8% (w/v) 1,1,1,3,3,3-hexafluoro-2-propanol (HFIP) solutions are given in Figure 72(a1-3). It is apparent

that uniform bead-free nanofibers having smooth surface were obtained in all three cases.

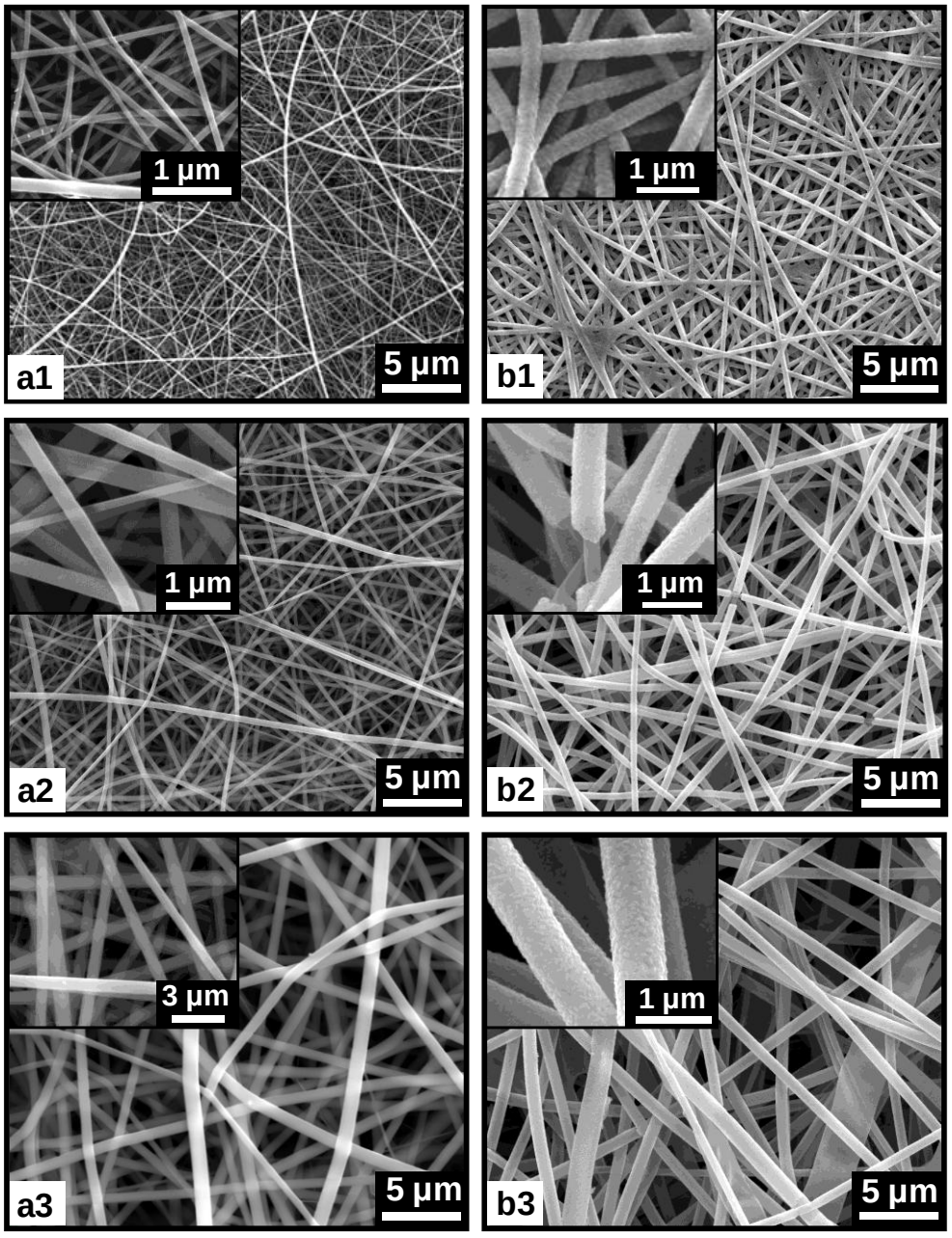

Figure 72. Representative SEM images of (a1) 8%-nylon 6,6/FA, (a2) 5%-nylon 6,6/HFIP, (a3) 8%-nylon 6,6/HFIP nanofibers; and (b1) 8%-nylon 6,6/FA-ZnO, (b2) 5%-nylon 6,6/HFIP-ZnO, (b3) 8%-nylon 6,6/HFIP-ZnO core-shell nanofibers. The insets show higher magnification images. (Copyright © 2012, American Chemical Society. Reprinted with permission from Ref.[11])

The characteristics (composition and viscosity) of the nylon 6,6 solutions and AFD of the electrospun nylon 6,6 nanofibers are summarized in Table 18. In electrospinning, fiber diameters strongly depend on the polymer solution viscosity, hence, type of the solvent used and concentration of the polymer solution are quite important to control the diameter of the electrospun fibers [7, 242]. Here, two different solvent systems were used; formic acid (FA) and hexafluoro-2-propanol (HFIP). 8% (w/v) nylon 6,6 was used for FA system while two different nylon 6,6 concentrations (5% and 8%, w/v) were used for HFIP system in order to produce nanofibers with different AFD. The viscosity of each nylon 6,6 solution was different; therefore, electrospinning of these solutions yielded nylon 6,6 nanofibers with different fiber diameter. It is anticipated that higher solution viscosity resulted in less stretching of the electrified jet and therefore thicker nanofibers were obtained in electrospinning [7, 242]. AFD of the nylon 6,6 nanofibers was found as 80±15, 240±45 and 650±140 nm for 8%-nylon 6,6/FA, 5%-nylon 6,6/HFIP and 8%-nylon 6,6/HFIP systems, respectively. Although the polymer concentration of 8%-nylon 6,6/FA is higher than 5%-nylon 6,6/HFIP and same with 8%-nylon 6,6/HFIP, much thinner nanofibers (AFD = 80±15 nm) were obtained owing to the much less solution viscosity of 8%-nylon 6,6/FA when compared to nylon 6,6/HFIP systems. These randomly oriented nylon 6,6 nanofibers having different AFD were used as the core structures for fabrication of the core-shell nylon 6,6-ZnO nanofibers.

Table 18. Properties of nylon 6,6 solutions and the resulting electrospun nanofibers. (Copyright © 2012, American Chemical Society. Reproduced with permission from Ref.[11])

Name	**Solvent system**	**% nylon 6,6 (w/v) [a]**	**Viscosity (Pa·s)**	**AFD (nm) before ALD**	**AFD (nm) after ALD**
8%-nylon 6,6/FA	FA	8	0.0228	80 ± 15	305 ± 50
5%-nylon 6,6/HFIP	HFIP	5	0.115	240 ± 45	470 ± 70
8%-nylon 6,6/HFIP	HFIP	8	0.24	650 ± 140	835 ± 320

[a] with respect to the solvent.

The next processing step is the deposition of ZnO shell on the electrospun nylon 6,6 nanofibers by ALD. ZnO shell was grown layer-by-layer onto the smooth and round surfaces of individual nylon 6,6 nanofibers by applying 800 ALD cycles at 200 °C. Figure 72 (b1-3) displays the representative SEM images of the core-shell nylon 6,6-ZnO nanofibers having three different AFD. From these SEM images, it was clearly observed that ALD process did not destroy the fibrous structure of the electrospun nylon 6,6 samples, and uniform thickness of ZnO deposition onto nylon 6,6 nanofibers was achieved successfully in all three cases.

As seen in Figure 72 (a1-3), nylon 6,6 nanofibers have smooth and uniform surface, however, the surface of the core-shell nylon 6,6-ZnO nanofibers was increased roughness (Figure 72 (b1-3)) due to the grainy structure of the outer ZnO layer [386]. Since the deposited film is polycrystalline with a hexagonal wurtzite structure, ALD growth starts with the nucleation of ZnO islands. With the increasing number of ALD cycles, these islands coalesce to form a continuous film. The resulting film, therefore, consists of ZnO grains and this increase the surface roughness. Amorphous films deposited by ALD, on the other hand, generally result in smoother films with lower surface roughness values [387]. The SEM images also showed that the ALD process yielded uniform thickness of ZnO shell layer over a relatively large surface area of the electrospun nanofibers. In addition, no significant difference was observed for nylon 6,6 nanofibers having different AFD indicating that ZnO shell layer with uniform thickness can be deposited regardless of the fiber diameter variation. These results clearly confirmed that ALD technique provided conformal ZnO deposition onto electrospun nanofibers which is quite unique when compared to other less-conformal deposition methods such as sputtering [118]. The AFD of the core-shell nylon 6,6-ZnO nanofibers were measured as 305±50, 470±70 and 835±320 nm for 8%-nylon 6,6/FA, 5%-nylon 6,6/HFIP and 8%-nylon 6,6/HFIP systems, respectively (Table 1). The AFD of nylon 6,6-ZnO nanofibers were more or less same with the expected values when total of ~180 nm thickness (~90 nm layer in both sides of the fiber) of ZnO layer was added to the fiber diameter of the nylon 6,6 core.

EDX analyses were also performed for the core-shell nylon 6,6-ZnO nanofibers. Zinc (Zn), oxygen (O) and carbon (C) elements were detected in the EDX spectrum (Figure 73); Zn and O are originated from ZnO shell layer and C is coming from the polymeric core structure of nylon 6,6. Elemental mapping results shown in Figure 73 further confirmed the successful deposition of ZnO shell layer onto nylon 6,6 nanofibers.

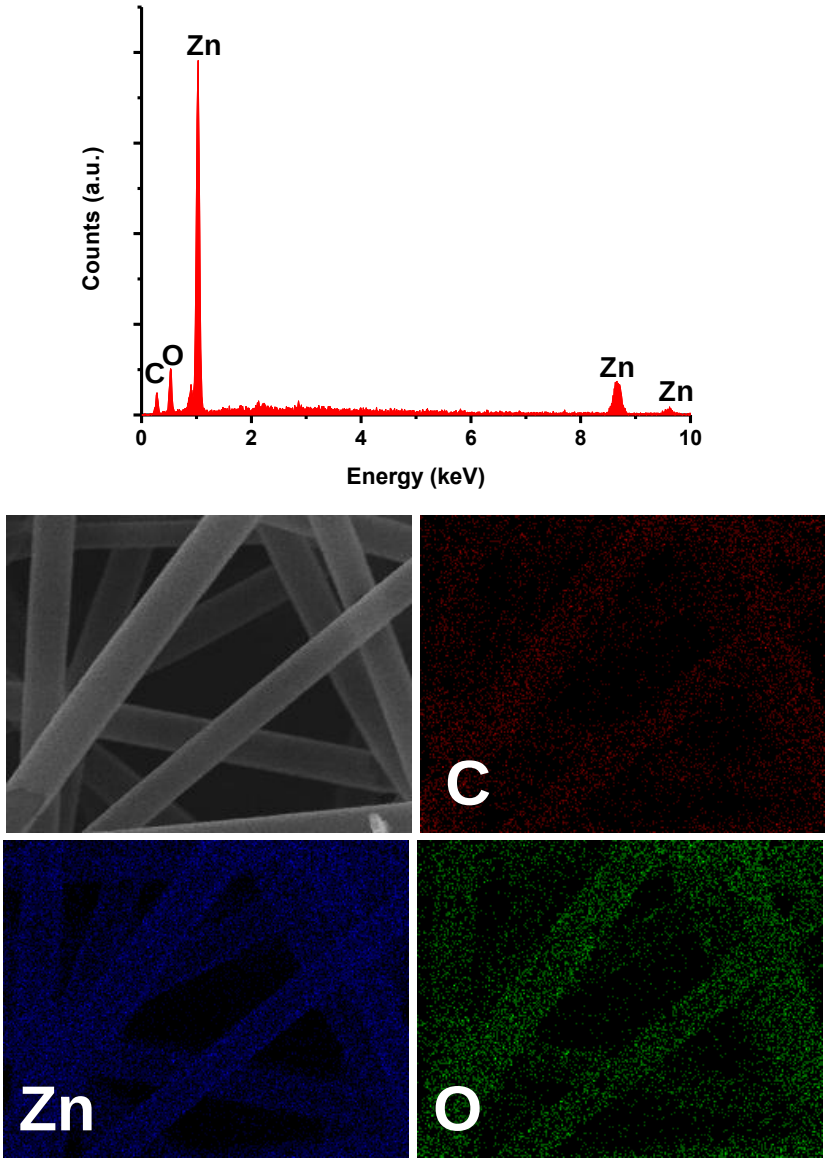

Figure 73. EDX spectrum of nylon 6,6-ZnO core-shell nanofibers (8%-nylon 6,6/HFIP-ZnO NF) and chemical maps of C, Zn and O. (Copyright © 2012, American Chemical Society. Reprinted with permission from Ref.[11])

The morphologies of the core-shell nylon 6,6-ZnO nanofibers were further investigated by TEM. The representative TEM images given in Figure 74 clearly showed that nylon 6,6-ZnO nanofibers have core-shell structure. It is evident that ZnO shell layer with uniform thickness was deposited onto individual nylon 6,6 nanofibers. The surface of nylon 6,6-ZnO nanofibers was rougher due to the nanosize grains of ZnO having an average grain size of ~25 nm.

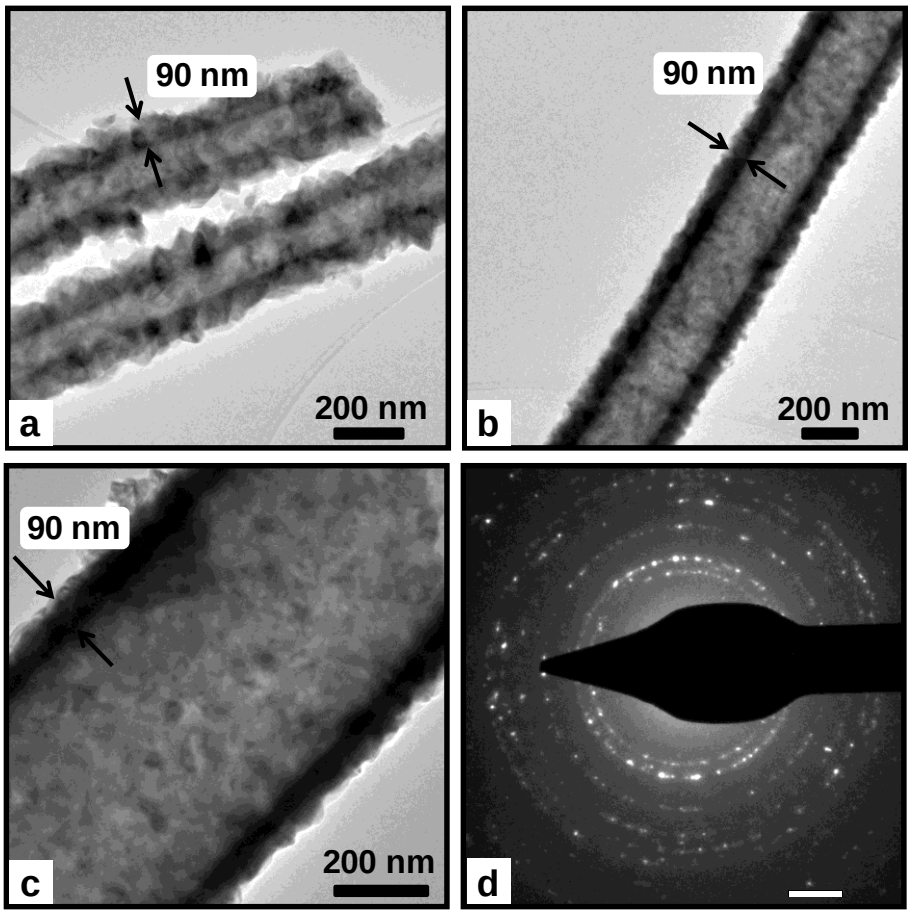

Figure 74. Representative TEM images of (a) 8%-nylon 6,6/FA-ZnO, (b) 5%-nylon 6,6/HFIP-ZnO, (c) 8%-nylon 6,6/HFIP-ZnO core-shell nanofibers; (d) represantative SAED pattern of the core-shell nylon6,6-ZnO nanofibers (8%-nylon 6,6/HFIP-ZnO NF). (Copyright © 2012, American Chemical Society. Reprinted with permission from Ref.[11])

The TEM images also revealed that the thickness of the ZnO shell layer was about 90 nm for each core-shell nylon 6,6-ZnO nanofiber sample having different

AFD (Figure 74). The conformal, layer-by-layer deposition of ZnO onto the round surfaces of individual electrospun nanofibers is unique to ALD process, which resulted in uniform thickness of the ZnO shell layer even the nylon 6,6 nanofibers were randomly distributed in the form of nonwoven, and the fiber diameters were very different from each other. The representative SAED pattern of the core-shell nylon 6,6-ZnO nanofibers presented in Figure 74d indicates polycrystalline nature of the ZnO shell which correlates well with the XRD patterns of the nanofibers which will be discussed in the following sections.

Surface chemical composition and bonding states of the pristine nylon 6,6 nanofibers and core-shell nylon 6,6-ZnO nanofibers were investigated by using XPS. Table 19 summarizes the compositional data of pristine nylon 6,6 nanofibers and core-shell nylon 6,6-ZnO nanofibers in atomic concentrations. As anticipated, C 1s, O 1s and N 1s peaks were detected in the XPS survey scan of pristine nylon 6,6 nanofibers since the nylon 6,6 polymer consists of carbon, oxygen and nitrogen atoms only. In the case of core-shell nylon 6,6-ZnO nanofibers, only Zn 2p3, O 1s and C 1s peaks were detected from survey scans. Zn and O contents were assigned to ZnO shell layers, which were found to be almost stoichiometric as expected. On the other hand, the absence of nitrogen peak in the XPS survey scans for core-shell nylon 6,6-ZnO nanofibers indicated that the surface of the nylon 6,6 nanofibers were coated successfully by ZnO layer using ALD. However, C was observed for the core-shell nylon 6,6-ZnO nanofibers that was most probably due to surface contamination; because if the carbon content was from the polymer core, we would have also detected N for these nanofibers in the XPS scans. In order to prove this claim, we etched the ZnO shell by Ar ion sputtering for 30 s, and observed considerable decrease in the amount of C. Formation of ZnO on the surface of the nylon 6,6 nanofibers was also confirmed by Zn 2p high resolution XPS scan (Figure 75). Zn 2p3/2 and Zn 2p1/2 subpeaks of the Zn 2p doublet located at 1021.73 and 1044.76 eV, respectively, were found to be related to Zn-O bonding in ZnO [388].

Table 19. Atomic concentrations generated from XPS wide energy survey scans. (Copyright © 2012, American Chemical Society. Reprinted with permission from Ref.[11])

Samples	**C (%)**	**O (%)**	**Zn (%)**	**N (%)**
pristine nylon 6,6 NF	76.52	12.5	-	10.93
8%-nylon 6,6/FA-ZnO NF	20	41.19	38.81	-
5%- nylon 6,6/HFIP-ZnO NF	18.45	44.36	37.19	-
8%-nylon 6,6/HFIP-ZnO NF	20.67	41.44	37.89	-
8%-nylon 6,6/FA-ZnO NF (after 1st cycle of UV treatment)	27.05	41.07	31.88	-
8%-nylon 6,6/HFIP-ZnO NF (after 1st cycle of UV treatment)	23.39	43.38	32.63	-

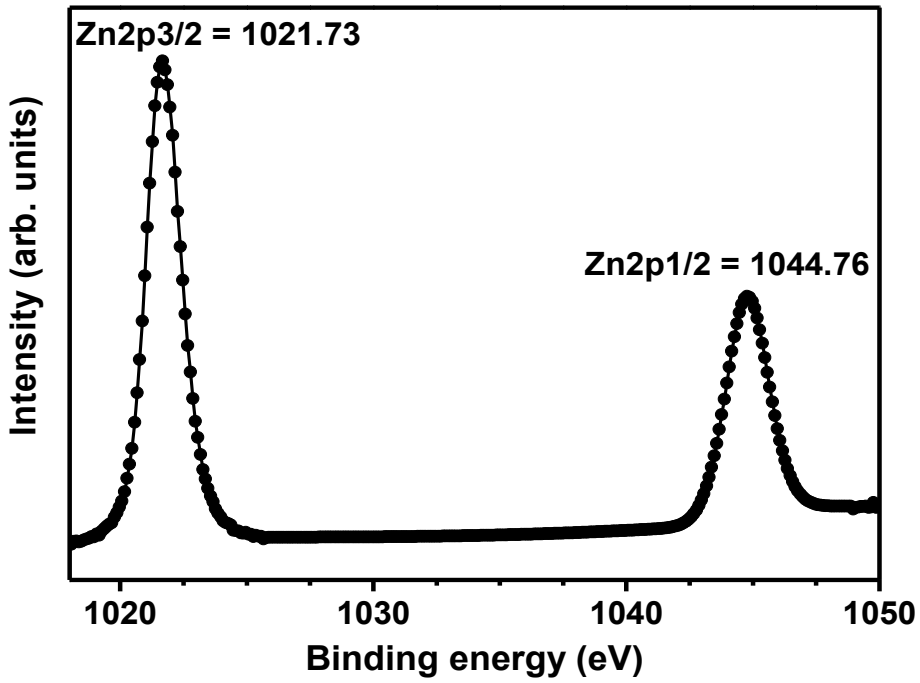

Figure 75. Zn 2p high resolution XPS scan of core-shell nylon 6,6-ZnO nanofibers (8%-nylon 6,6/FA-ZnO NF). (Copyright © 2012, American Chemical Society. Reprinted with permission from Ref.[11])

We have also calculated the compositional weight percentage of the core-shell nylon 6,6-ZnO nanofibers by TGA. The TGA thermograms (Figure 76) indicated that 8%-nylon 6,6/FA-ZnO, 5%-nylon 6,6/HFIP-ZnO and 8%-nylon 6,6/HFIP-ZnO contain 85, 81 and 80 weight% of ZnO, respectively and this approximately correlates with calculated theoretical weight% of ZnO in the core-shell fibers.

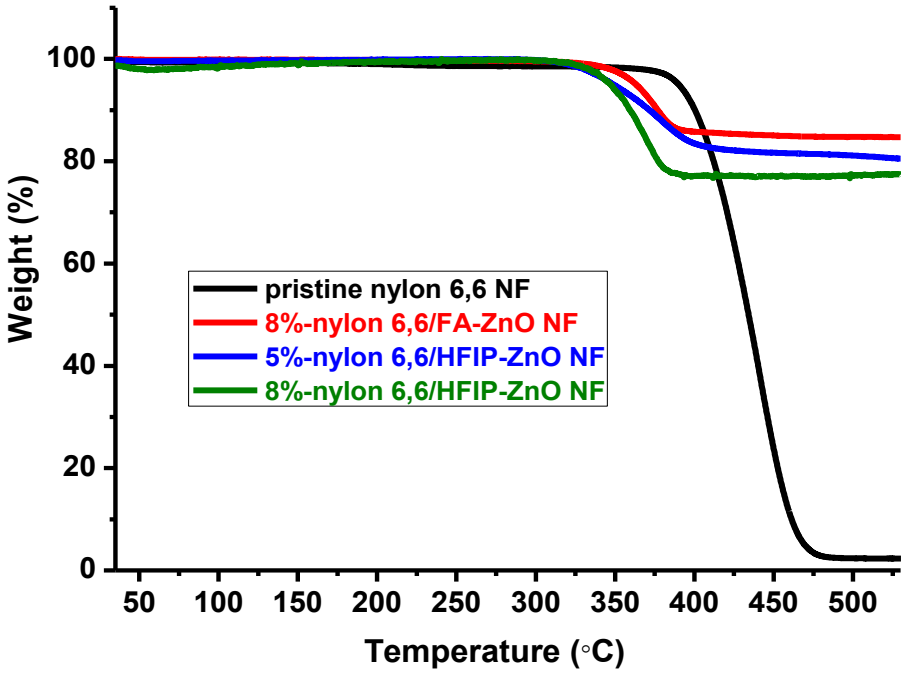

Figure 76. TGA thermograms of pristine nylon 6,6 nanofibers (NF) and core-shell nylon 6,6-ZnO NF. (Copyright © 2012, American Chemical Society. Reprinted with permission from Ref.[11])

It was also noted that the main decomposition temperature of nylon 6,6 in core-shell nanofibers (decomposition onset at about 270, 295 and 300 °C for 8%-nylon 6,6/FA-ZnO, 5%-nylon 6,6/HFIP-ZnO and 8%-nylon 6,6/HFIP-ZnO, respectively) was lower than that of pristine nylon 66 nanofibers (decomposition onset at 350 °C) which is possibly due to the catalytic activity of ZnO resulting in oxidative and earlier decomposition of nylon 6,6. Similar result was reported where the thermal degradation temperature of polymer was decreased with the presence of TiO_2 as inorganic filler [389].

We also performed ATR-FTIR analysis (data not given) to see if there is any degradation of nylon 6,6 during the ALD process. Amide I and amide II peaks of pristine nylon 6,6 nanofibers were observed at around 1635 cm^{-1} (C = O stretch) [390] and 1539 cm^{-1} (in-plane N-H deformation) [390], respectively. We did not see any significant change in these characteristic FTIR peaks for core-shell nylon 6,6-ZnO nanofibers when compared to pristine nylon 6,6 nanofibers, suggesting that there was no degradation of nylon 6,6 nanofibers during or after the ALD process.

The XRD patterns of pristine nylon 6,6 and core-shell nylon 6,6-ZnO nanofibers are given in Figure 77. Nylon 6,6 has various crystalline forms called α phase, β phase and γ phase [391]. The XRD pattern of the pristine nylon 6,6 nanofibers exhibited two distinct diffraction peaks at about 20.4° (100) and 23.0°(010, 110) confirming the presence of the α phase in the sample [322, 391]. The α1 peak (2θ = 20.4°) corresponds to the distance between hydrogen bonded chains whereas the α2 peak (2θ = 23°) corresponds to the separation of hydrogen-bonded sheets [391]. The absence of the reflections of β phase at 2θ values of ~12 and 19° or γ1 peak (2θ = 13°) and γ2 peak (2θ = 22°) [391] in the XRD pattern of pristine nylon 6,6 nanofibers indicating that the nylon 6,6 nanofibers have a pure triclinic α phase comprising hydrogen-bonded sheets [392]. The XRD patterns of nylon 6,6 nanofibers obtained from FA and HFIP solvent systems were also same, indicating that α crystalline phase was obtained from both solvent systems.

In the case of core-shell nylon 6,6-ZnO nanofibers, the XRD patterns of all three samples have shown the diffraction peaks of the hexagonal wurtzite crystal structure of ZnO (ICDD 01-074-0040) elucidating the successful deposition of ZnO onto electrospun nylon 6,6 nanofibers by ALD. Although the nylon 6,6 diffraction peak intensities were substantially decreased due to the presence of ZnO layer, the peaks of nylon 6,6 of α1 and α2 phase were also observed in the XRD patterns of core-shell nylon 6,6-ZnO nanofibers. This also suggested that the crystalline structure of nylon 6,6 nanofibers was not affected during the ALD process.

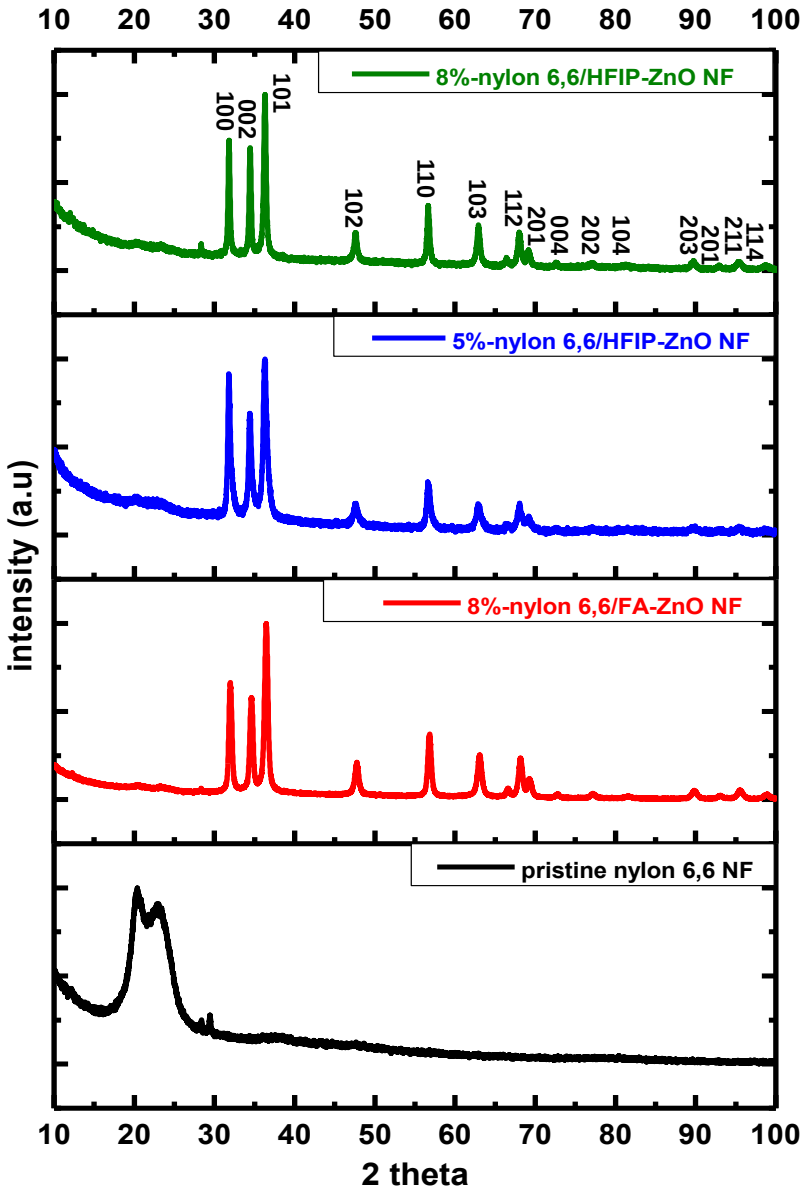

Figure 77. XRD patterns of pristine nylon 6,6 nanofibers (NF) and core-shell nylon 6,6-ZnO NF. (Copyright © 2012, American Chemical Society. Reprinted with permission from Ref.[11])

We have tested the PCA of the core-shell nylon 6,6-ZnO nanofiber mat by following the photocatalytic decomposition of rhodamine-B (Rh-B) which was used as a model azo-reactive dye under the irradiation of UV-light at 365 nm wavelength. The core-shell nylon 6,6-ZnO nanofibers having two different AFD (8%-nylon 6,6/FA, AFD ~80 nm and 8%-nylon 6,6/HFIP, AFD ~650 nm) were used in order to investigate the effect of fiber diameter on the efficiency of photocatalytic activity.

The PCA of these core-shell nylon 6,6-ZnO nanofiber mats were studied by spectroscopic UV–Vis measurement, by recording the change in the absorbance of the Rh-B solutions as a function of the UV irradiation time. As a control experiment, the Rh-B solution without containing any nanofibers was subjected to the same UV treatment in order to investigate whether any direct photolysis occurred or not. The change in the absorption peak of Rh-B at 554 nm in the UV–Vis spectra was monitored as a function of UV irradiation time (Figure 78a). Moreover, the absorption peak points were used for calculating the degradation rate of Rh-B defined as C/C_0 where C_0 and C represent the initial concentration of Rh-B before UV irradiation and after UV irradiation at time t, respectively (Figure 78b). As given in Figure 78a, direct photolysis was not observed for the blank Rh-B solution without containing core-shell nylon 6,6-ZnO nanofiber mat and therefore pink color of the Rh-B solution was not changed after the UV irradiation over a period of 16 h. On the other hand, the reduction of the absorbance of the Rh-B solutions containing core-shell nylon 6,6-ZnO nanofiber mat with respect to UV irradiation time clearly showed effective photocatalytic degradation of Rh-B. Furthermore, the photocatalytic degradation rate of Rh-B was higher for 8%-nylon 6,6/FA (AFD ~80 nm) nanofiber mat compared to 8%-nylon 6,6/HFIP (AFD ~650 nm) nanofiber mat, which was possibly due to the much thinner fiber diameter and resulting higher surface area of this sample. For 8%-nylon 6,6/FA nanofiber mat, 59% of Rh-B decomposed in 4 h and total of 93% of Rh-B was decomposed in 16 h. In the case of 8%-nylon 6,6/HFIP nanofiber mat, the decomposition of Rh-B was 47% and 88% in 4 h and 16 h, respectively. The Rh-B solutions containing nylon 6,6-ZnO nanofiber mat were decolorized during the UV irradiation and pink color of these solutions was almost disappeared after 16 h of UV irradiation elucidating the successful photocatalytic decomposition of Rh-B by the core-shell nylon 6,6-ZnO nanofiber mat (Figure 78a).

Here, we demonstrate that the core-shell nylon 6,6-ZnO nanofiber mat can be a very good candidate as filtering material because of the flexible polymeric core and the PCA of the ZnO shell layer. These nanofiber mats can be easily handled and folded as a free standing material (Figure 78c).

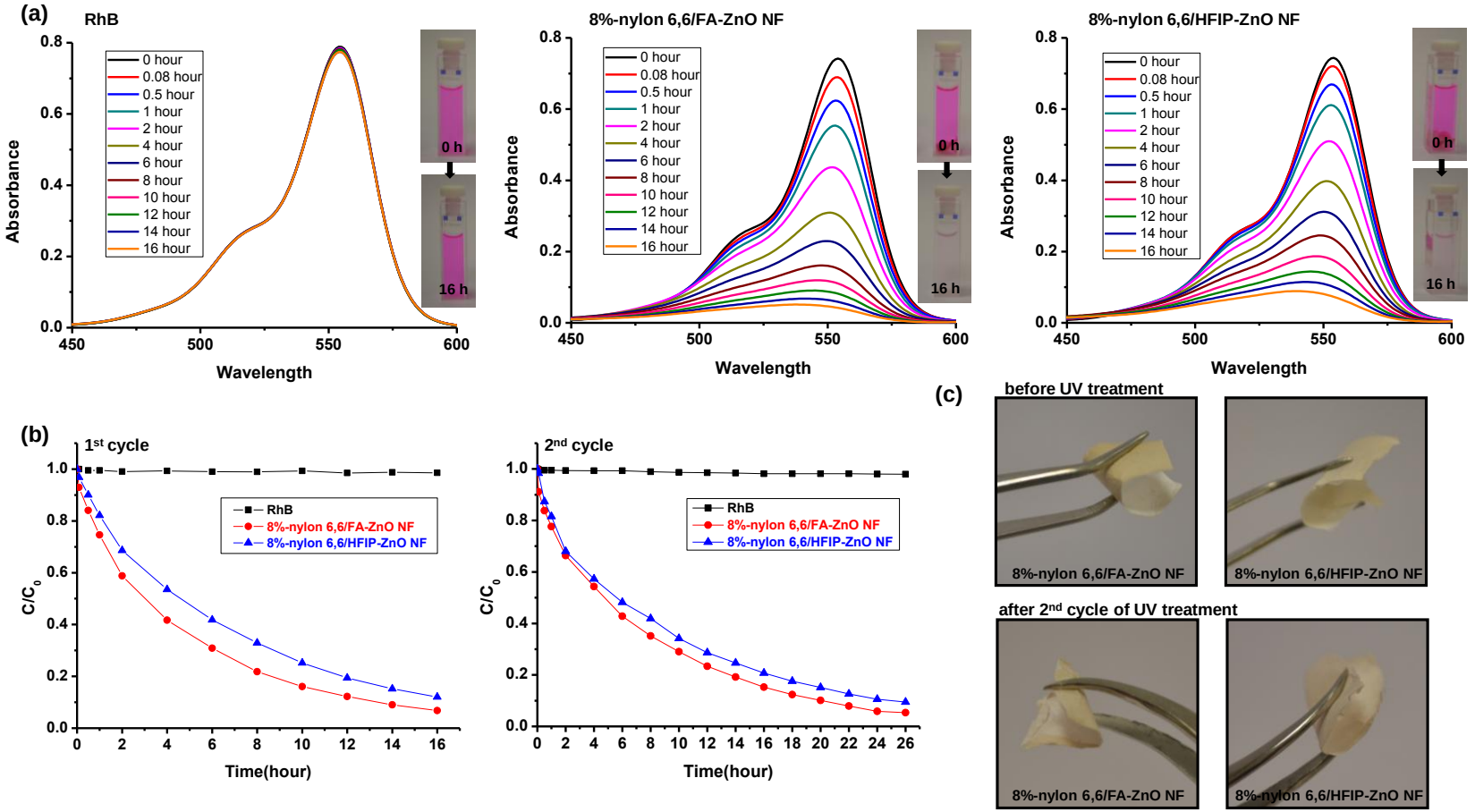

Figure 78**.** (a) UV–Vis spectra of the Rh-B solution with and without core-shell nylon 6,6-ZnO nanofibers (NF) as a function of the UV irradiation time for 1st cycle experiment, (b) the rate (C/C_0) of Rh-B degradation of the Rh-B solution with and without core-shell nylon 6,6-ZnO NF by exposing UV light with 365 nm wavelength for 1st and 2nd cycle experiments; (c) representative photographs of the flexible nylon 6,6-ZnO core-shell NF before UV treatment and after 2nd cycle of UV treatment.

The structural stability of these core-shell nylon 6,6-ZnO nanofiber mat are quite important since the potential application of these nanofibrous membranes would be in water purification where continuous and long lasting PCA is required for the treatment of organic pollutants present in the water supply. Accordingly, we have also examined the stability of these core-shell nylon 6,6-ZnO nanofiber mat. The structural and chemical stabilities of these nylon 6,6-ZnO nanofiber mats were investigated by SEM imaging and XPS measurement after the UV irradiation experiment. Figure 79 shows the representative SEM images of the 8%-nylon 6,6/FA and 8%-nylon 6,6/HFIP nanofiber mat after 16 h of UV irradiation in Rh-B solution. It was observed that the samples maintained their nanofibrous structure without any deformation; yet, in few spots, destruction of ZnO layer was detected. This is possible because of the mechanical deformation of the nanofiber mat during the UV-Vis measurements where the nanofiber mats were pressed in the bottom of the UV cuvettes. Therefore the ZnO shell layer was damaged to some extent but not significantly. The XPS study of these samples after the UV irradiation experiment also revealed the loss of a small amount of ZnO layer from the samples (Table 19).

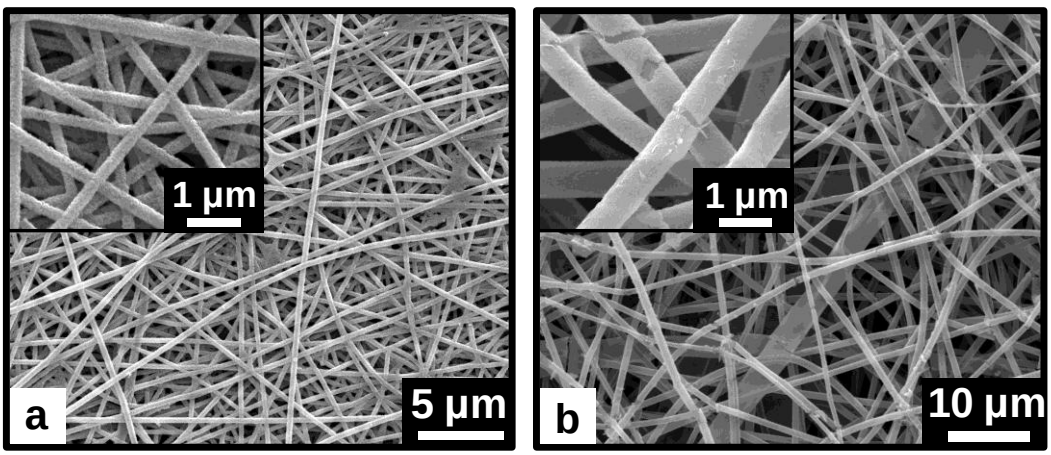

Figure 79. Representative SEM images of (a) 8%-nylon 6,6/FA-ZnO and (b) 8%-nylon 6,6/HFIP-ZnO core-shell nanofibers after 16 h of UV irradiation in Rh-B solution (1st cycle). (Copyright © 2012, American Chemical Society. Reprinted with permission from Ref.[11])

We repeated the PCA experiment for these nylon 6,6-ZnO nanofiber mats in order to investigate the potential reusability of these materials for the photocatalytic decomposition of Rh-B solution. The photocatalytic efficiency of these nanofiber mats for the 2nd cycle was slightly lower than the 1st cycle. Therefore, in the 2nd cycle, 85 and 80 % of the Rh-B was decomposed in 16 h for 8%-nylon 6,6/FA and 8%-nylon 6,6/HFIP nanofiber mat, respectively. This slight decrease is possibly due to the loss of some ZnO layer after the 1st cycle; in addition, in the 2nd cycle less amount of material was used for the PCA experiment (9.3 mg of nanofiber mat was used in the 1st cycle and 8.7 mg of nanofiber mat was used in the 2nd cycle, since some amount of nanofiber mat was used in SEM and XPS analyses after the 1st cycle). Furthermore, we observed that the nanofibers maintained their flexibility after 2nd cycle of UV treatment as shown in Figure 78b. From the ATR-FTIR analysis (data not shown) of these samples after 2nd cycle of UV treatment, we did not detect any notable change in the characteristic IR peaks of nylon 6,6 nanofibers (amide I and amide II peaks) when compared to pristine nylon 6,6 nanofibers, and this suggested that the PCA of ZnO layer did not cause any significant degradation of polymeric core.

4.2.3. Conclusions

In this study we have fabricated of core-shell nylon 6,6-ZnO nanofibers by combining electrospinning and ALD techniques. In the first step, nylon 6,6 nanofibers having different average fiber diameters were electrospun by using different solvent systems. In the second step, ZnO shell layer with precise thickness was deposited on the round surface of the nylon 6,6 nanofibers by ALD. The imaging analyses by SEM and TEM revealed the core-shell structure of nylon 6,6-ZnO nanofibers, and the thickness of the ZnO shell layer was measured ~ 90 nm for each sample having different core fiber diameters. ALD provided growth of ZnO layer having uniform thickness regardless of the differences in core fiber diameter. In

addition, it was observed that the nylon 6,6 fibrous structure was not deformed during the ALD of ZnO shell layer. This confirms that ALD has significant advantages over other deposition techniques such as less-conformal sputtering and high-temperature conventional CVD, since ALD is a relatively low temperature process where the thermal damage can be avoided when temperature sensitive substrates such as polymers are used. The core-shell nylon 6,6-ZnO nanofibers have shown unique properties such as structural flexibility due to the polymeric core and PCA due to the ZnO shell layer. The photocatalytic properties of the core-shell nylon 6,6-ZnO nanofiber mats were tested by monitoring the photocatalytic decomposition of rhodamine-B organic dye molecule which was used as a model organic waste compound. We observed that nylon 6,6-ZnO nanofiber mat having thinner average fiber diameter (AFD ~80 nm) has shown better photocatalytic efficiency when compared to the nanofiber mat having AFD of ~650 nm, possibly due to the higher surface area of this sample. We have also shown that these nylon 6,6-ZnO nanofiber mats are chemically and structurally stable after the 2^{nd} cycle of the photocatalytic experiments carried out under UV irradiation.

In brief, our results indicate that core-shell nylon 6,6-ZnO nanofiber mats can be quite applicable as a filtering/membrane material for treatment of organic pollutants for water purification due to their efficient photocatalytic properties, structural flexibility and stability. Nevertheless, the combination of electrospinning and ALD techniques offers a promising alternative approach for the fabrication of functional core-shell nanofiber structures. ALD is a relatively low-temperature process providing ultimate conformality, therefore, three-dimensional, polymeric nanofiber templates can easily be coated by ALD of inorganic materials for producing flexible nanofiber mats. Consequently, depending on the type of the polymeric core and the type of the shell layer, various polymer-inorganic core-shell nanofibers can be fabricated for many applications including filters/membranes, catalysis, sensors, photonics, electronics, energy, biotechnology, *etc.*

4.3. Surface-Decorated ZnO Nanoparticles and ZnO Nanocoating on Electrospun Polymeric Nanofibers by Atomic Layer Deposition for Flexible Photocatalytic Nanofibrous Membranes

4.3.1. Experimental

Materials: Nylon 6,6 pellets (relative viscosity: 230.000-280.000), formic acid (98-100 %) and rhodamine-B (Rh-B, dye content ~95 %) were purchased from Sigma-Aldrich and used without any purification. For ZnO deposition by ALD, diethylzinc ($(C_2H_5)_2Zn$ or DEZn, Sigma-Aldrich) and HPLC-grade water (H_2O) were used as the zinc and oxygen precursors, respectively.

Electrospinning of Polymeric Nanofibers: 8 wt % nylon 6,6 was dissolved in formic acid by stirring for 3 h at room temperature, for each sample. The resulting homogeneous clear solutions were located in 10 ml syringes fitted with metallic needles having inner diameter of 0.8 mm. The syringes were fixed horizontally on the syringe pump (Model: SP 101IZ, WPI). The polymer solutions were pumped with feed rate of 1 ml/h during electrospinning and the tip-to-collector distance was set to 10 cm. Voltage of 15 kV was applied to the metal needle tip by using high voltage power supply (Matsusada, AU Series) for the electrospinning of the prepared solutions. The solvent evaporated on the way to the grounded stationary cylindrical metal collector (height: 15 cm, diameter: 9 cm) covered with a piece of aluminum foil, on which the electrospun nylon 6,6 nanofibers were deposited. The electrospinning setup was enclosed in Plexiglas box and the electrospinning was carried out at 23 ^{o}C and 36 % relative humidity.

Preparation of ZnO Structures by ALD: ZnO depositions were carried out at 200 °C in a Savannah S100 atomic layer deposition (ALD) reactor (Cambridge Nanotech

Inc.) using diethylzinc (DEZn, or $(C_2H_5)_2Zn$) as the zinc precursor and HPLC-grade water (H_2O) as the oxidant. N_2 was used as both carrier and purge gas with flow rates of 20 and 10 sccm under dynamic and static vacuum conditions, respectively. 144 cycles were deposited using different deposition parameters. For the first set of samples, one ALD cycle consisted of H_2O pulse (0.015 s) / N_2 purge (10 s) / DEZn pulse (0.015 s) / N_2 purge (10 s). Increased doses of DEZn and H_2O (i.e. 0.09 s) were used for the second set, again with a 10 s N_2 purge between the precursor pulses. Another set was prepared by using the *exposure mode* (a trademark of Cambridge Nanotech Inc.). In this mode, dynamic vacuum was switched to static vacuum before each precursor pulse by closing the valve between the reaction chamber and the pump. After a certain period of time (i.e. exposure time) it was switched back to dynamic vacuum for purging excess precursor molecules and gaseous by-products. For this process, one ALD cycle was as follows: valve OFF / H_2O pulse (0.015 s) / exposure (10 s) / valve ON / N_2 purge (10 s) / valve OFF / DEZn pulse (0.015 s) / exposure (10 s) / valve ON / N_2 purge (10 s).

Characterization Techniques: The morphology of the pristine nylon nanofibers and nylon/ZnO nanofibers were investigated by using scanning electron microscope (SEM, FEI–Quanta 200 FEG). The nanofibers were coated with 5 nm Au/Pd for SEM imaging. Around 100 fiber diameters were measured from the SEM image of pristine nylon nanofibers in order to calculate the average fiber diameter (AFD). Detailed morphological investigation of the nylon/ZnO nanofibers was performed by using transmission electron microscope (TEM, FEI–Tecnai G2F30, Hillsboro, OR). Small pieces of nylon/ZnO nanofibrous membranes sonicated in ethanol for 5 minutes to obtain individual nanofibers dispersed through the solvent, followed by dropping the suspensions onto the copper TEM grids (HC200), and allowed them to dry under IR lamp for a few minutes prior to TEM imaging. Crystal structure of ZnO on nanofibers was investigated from selected area electron diffraction (SAED) patterns of nylon/ZnO nanofibers obtained by TEM. PANalytical X'Pert Multi

Purpose X-ray Diffractometer with Cu Kα radiation was used to collect X-ray diffraction (XRD) data of the pristine nylon and nylon/ZnO nanofibers in a range of $2\theta = 10^{o}$-100^{o}. X-ray photoelectron spectroscopy (XPS, Thermo Scientific) was used to detect the surface elemental composition of pristine nylon and nylon/ZnO nanofibers. XPS data were taken from 400 μm diameter circular spot on the sample surface by means of a flood gun charge neutralizer system equipped with a monochromated Al K_{α} X-ray source (hv = 1486.6 eV). Wide energy survey scans were obtained over a 0-1360 eV binding energy range, at pass energy of 150 eV, and with an energy step of 1 eV. Zn 2p high resolution XPS scan was also taken at pass energy of 30 eV, and with energy steps of 0.1 eV in order to analyze the bonding states. Thermal analysis of the nanofibers was performed by using thermogravimetric analyzer (TGA, TA Instruments–Q500) from room temperature to 600 ^{o}C at a heating rate of 20 ^{o}C/min under nitrogen atmosphere.

Photocatalytic Activity (PCA) of the Nylon/ZnO Nanofibrous Membranes: Photodegradation of rhodamine-B (Rh-B) (1.04×10^{-5} M) in aqueous medium with nylon/ZnO nanofibers were investigated to determine the efficiency of PCA of the samples. 10 mg nylon/ZnO nanofibrous membranes with three different ZnO morphologies (about 3.0 cm×2.5 cm) were put into quartz cuvettes (width: 1 cm, length: 1 cm, and height: 5 cm, Hellma) filled with Rh-B solution, separately. Then these cuvettes were kept under the irradiation of UV-light with a wavelength of 365 nm by placing them at a distance of 10 cm from the UV source (8 W, UVLMS-38 EL). UV-Vis-NIR spectrophotometer (Varian Cary 5000) was used to measure dye concentrations in the cuvettes at certain time intervals. The nanofibrous membranes which stayed at the bottom of the dye solution during UV-Vis measurement did not interfere with the UV-light; hence they did not contribute to the measurement results.

4.3.2. Results and Discussion

In this work, polymeric nanofibers surface-decorated with ZnO nanoparticles (NP) and ZnO nanocoating were fabricated by using a two-step approach; electrospinning and ALD (Figure 70). Initially, polymeric (nylon 6,6) nanofibers having an AFD of ~80 nm were produced via electrospinning technique. In the next step, ZnO was grown onto smooth surfaces of polymeric nanofibers via ALD [110-111] by altering deposition parameters. Altering the ALD parameters resulted in various ZnO morphologies on polymeric nanofibers; surface-decorated ZnO NP and highly dense ZnO NP, and a continuous ZnO nanocoating having uniform thickness (~27 nm). The resulting ZnO nanostructures onto nanofibers are illustrated schematically in Figure 80.

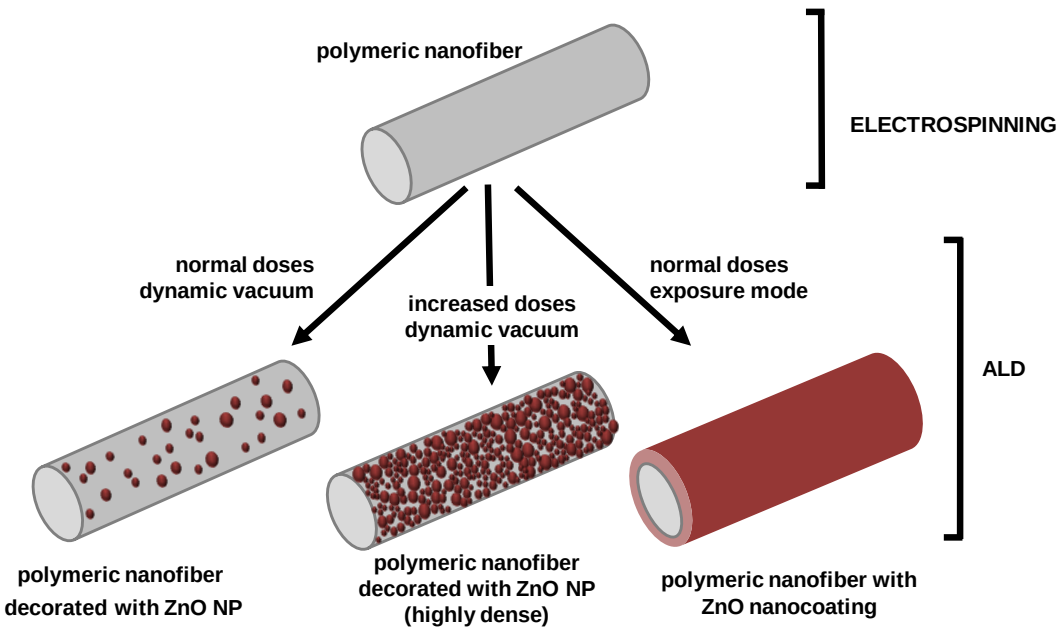

Figure 80. Schematic representation of the formation process of polymer/ZnO nanofibers: electrospinning of the polymeric nanofiber and ZnO deposition with different morphologies on the electrospun nanofiber by using various ALD parameters. (Copyright © 2013, Royal Society of Chemistry. Reprinted with permission from Ref.[130])

The SEM images clearly elucidated that ALD process did not destroy the fibrous structure of the polymer; in addition, when compared to pristine polymeric nanofiber, nylon/ZnO nanofibers had rougher surfaces due to the deposition of ZnO NP and nanocoating (Figure 81). Overall, the sample decorated with highly dense ZnO NP exhibited the highest surface roughness due to the presence of greater number of individual ZnO NP (Figure 81c and 82b).

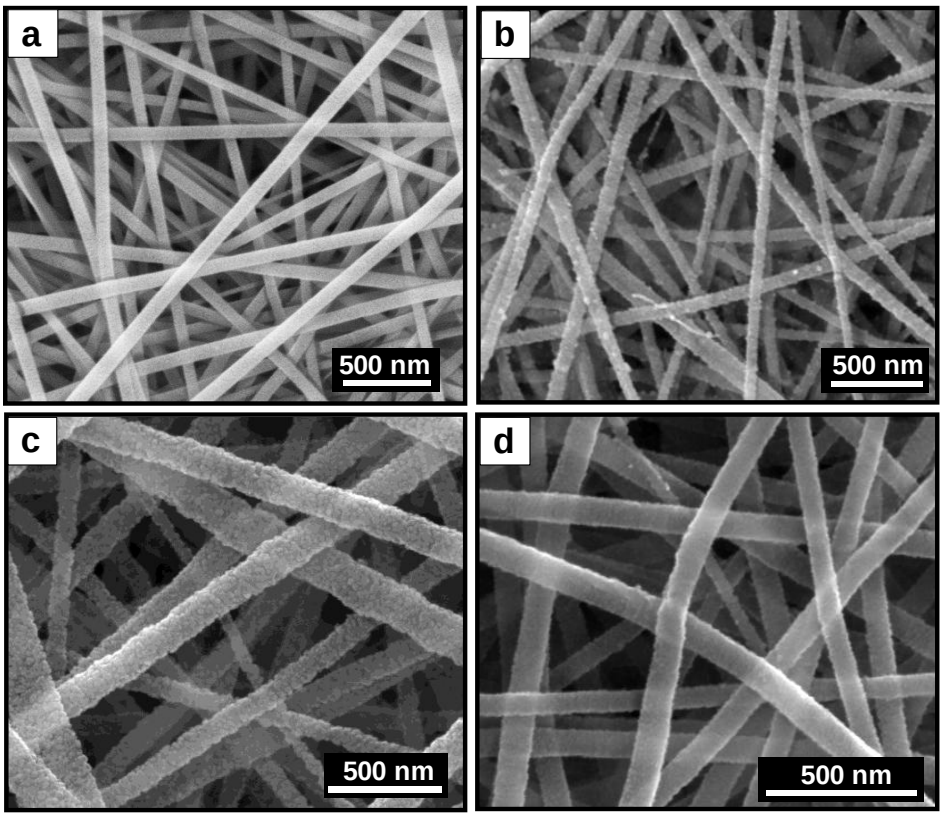

Figure 81. SEM images of nanofibers; (a) pristine nylon, (b) nylon/ZnO NP, (c) nylon/ZnO NP (highly dense), and (d) nylon/ZnO nanocoating. (Copyright © 2013, Royal Society of Chemistry. Reprinted with permission from Ref.[130])

The TEM images clearly revealed the morphologies of ZnO deposited on polymeric nanofibers (Figure 82). For the sample shown in Figure 82a, ALD was performed under the dynamic vacuum condition with 0.015 s pulses and 10 s purges.

The resulting morphology was in the form of randomly distributed individual ZnO NP with an average size of 20±15 nm. When ran for 800 cycles, this recipe resulted in ~90 nm thick uniform ZnO coating on electrospun nylon nanofibers [11]. Deposition of highly dense ZnO NP was obtained when pulse times of DEZn and H_2O were both increased to 0.09 s (Figure 3b). TEM image shown in Figure 82c belongs to a sample which was prepared by using the exposure mode (a trademark of Cambridge Nanotech Inc.) with 0.015 s pulses, 10 s exposures, and 10 s purges. Exposure mode aims at keeping the precursor molecules inside the reaction chamber for a certain period of time by switching dynamic vacuum to static vacuum just before the precursor pulses. After the exposure, static vacuum is switched back to dynamic vacuum for purging. The resulting morphology was a ~27 nm thin ZnO coating around the polymeric nanofibers. This process, therefore, yielded a ZnO nanocoating with a uniform thickness over the relatively large surface area of electrospun nanofibers.

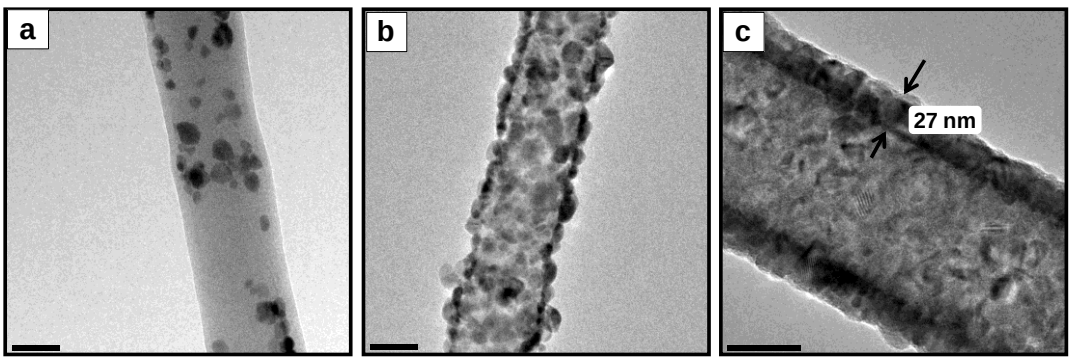

Figure 82. Representative TEM images of nanofibers; (a) nylon/ZnO NP, (b) nylon/ZnO NP (highly dense), and (c) nylon/ZnO nanocoating. (Copyright © 2013, Royal Society of Chemistry. Reprinted with permission from Ref.[130])

All three samples were decorated with ZnO NP or coated with a uniform ZnO thin film. The formation of NP instead of a continuous film for the samples prepared under the dynamic vacuum conditions is not due to the limitation in diffusion, since we observed that the precursor molecules can reach every point on the nanofibrous

membranes and produce either randomly distributed NP or continuous thin film. As the number of precursor molecules increases, the probability for these molecules to coincide with one of the reactive sites on the substrate also increases. Therefore, the increased number of ZnO NP with the increased DEZn and H_2O doses was an expected outcome. Our results indicate that the nucleation and growth of ZnO on polymeric nanofibers proceeds through the formation of islands and coalescence of these islands to form a continuous film, i.e. Volmer-Weber (3D) growth. ALD technique has been used to produce conformal and very thin inorganic coatings onto polymeric fibrous materials [11, 103, 105, 108]. On the other hand, ZnO NP were grown on single-walled carbon nanotubes by ALD [393-394]. In another study, Libera et al. [395] reported that the ALD of ZnO on amorphous silica forms NP in the early stages of growth instead of uniform thin coating. In our study, by taking advantage of the slow nucleation and/or growth kinetics of ZnO, ZnO NP were decorated onto polymeric nanofibers under the dynamic vacuum conditions. Although it has been shown that the number of particles can be increased by increasing the precursor doses, parameters controlling the size of these NP are unknown at the moment. Research is currently being conducted to investigate the very initial stages of growth, as well as fully control the morphology of resulting NP.

Polycrystalline nature of the deposited ZnO was revealed from the selected SAED patterns of the nylon/ZnO nanofibers (Figure 83), which correlate well with the XRD results (Figure 84). Moreover, bright spots on the polycrystalline diffraction rings were observed for all the three samples, which pointed out the existence of large crystal grains. Intensities of the SAED patterns were different for different morphologies due to the relative amounts of ZnO present on nanofibers. In XRD, the semi-crystalline nature of the pristine nylon nanofibers was confirmed with two distinct diffraction peaks at 20.4° (100) and 23.0° (010, 110) [391]. These peaks, yet they are suppressed due to the deposition of ZnO, were also observed in the XRD patterns of nylon/ZnO samples suggesting that the crystalline structure of the

polymer was not affected during the ALD process. The crystal structure of ZnO deposited onto nanofibers by ALD was determined as hexagonal wurtzite from the XRD patterns of the samples, in which diffraction peaks were indexed according to The International Centre for Diffraction Data (ICDD) (Reference Code: 01-074-0040). Similar to SAED patterns, the intensities of ZnO diffraction peaks in the XRD patterns were amplified as the relative amount of ZnO on the sample increased.

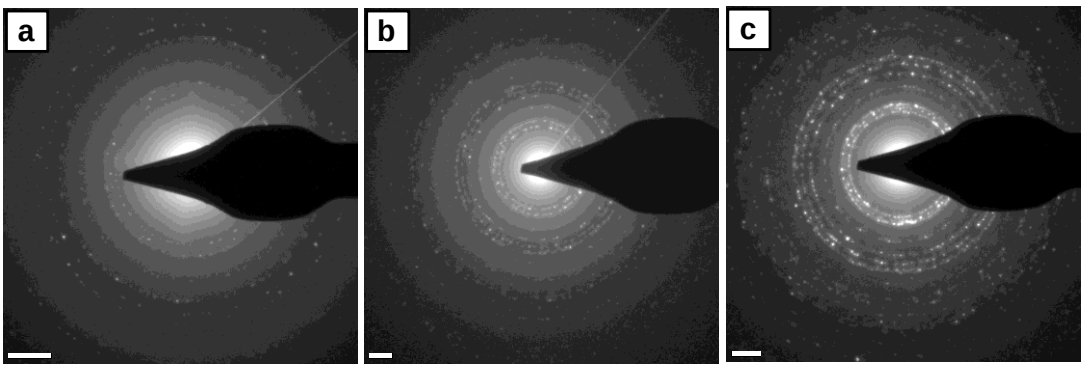

Figure 83. SAED patterns of nanofibers; (a) nylon/ZnO NP, (b) nylon/ZnO NP (highly dense), and (c) nylon/ZnO nanocoating. (Copyright © 2013, Royal Society of Chemistry. Reprinted with permission from Ref.[130])

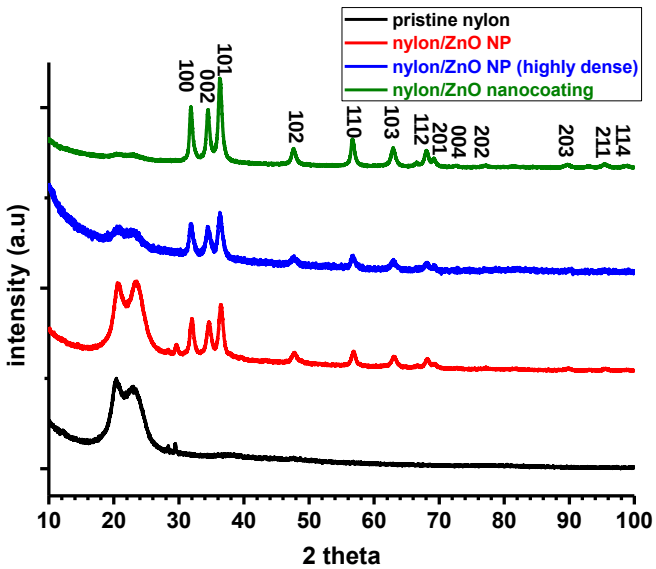

Figure 84. XRD patterns of pristine nylon and nylon/ZnO nanofibers. (Copyright © 2013, Royal Society of Chemistry. Reprinted with permission from Ref.[130])

Surface chemical composition of the nylon/ZnO nanofibers was investigated by using XPS (Table 20). As expected, C 1s, O 1s, and N 1s peaks from polymer (nylon 6,6) were observed in the XPS survey scans of both of the nylon/ZnO NP samples. In the case of nylon/ZnO nanocoating, N 1s peak could not be detected due to the continuous layer of ZnO as also proven by TEM analysis (Figure 82c). In addition, contamination could increase the amount of C observed in survey scans for all samples. Presence of Zn 2p3 and increased intensity of O 1s peaks in the XPS survey scans of samples were assigned to the ZnO structures on the nanofibers (Table 20). High resolution XPS scan was also taken to confirm the formation of ZnO on the surface of nylon nanofibers. Zn 2p doublet consisting of Zn 2p3/2 and Zn 2p1/2 subpeaks located at 1022.88 and 1045.86 eV, respectively, was observed confirming the Zn-O bonding state (Figure 85) [388].

Table 20. Atomic concentrations generated from XPS wide energy survey scans.

samples	**C (%)**	**O (%)**	**Zn (%)**	**N (%)**
pristine nylon	77.06	11.61	-	11.33
nylon/ZnO NP	68.13	15.95	5.53	10.38
nylon/ZnO NP (highly dense)	31.23	36.19	29.76	2.81
nylon/ZnO nanocoating	30.74	38.53	30.73	-

The compositional wt % of the samples was calculated from the TGA thermograms (Figure 86); 17, 54, and 82 wt % ZnO were determined in nylon/ZnO NP, nylon/ZnO NP (highly dense), and nylon/ZnO nanocoating, respectively. It was also observed that the main decomposition temperature of nylon for nylon/ZnO samples was lower (~280 °C) compared to that of pristine nylon nanofibers, which was ~350 °C. The lower degradation temperature observed for nylon/ZnO nanofibers was possibly because of the catalytic activity of ZnO, which resulted in early

polymer decomposition [11, 389].

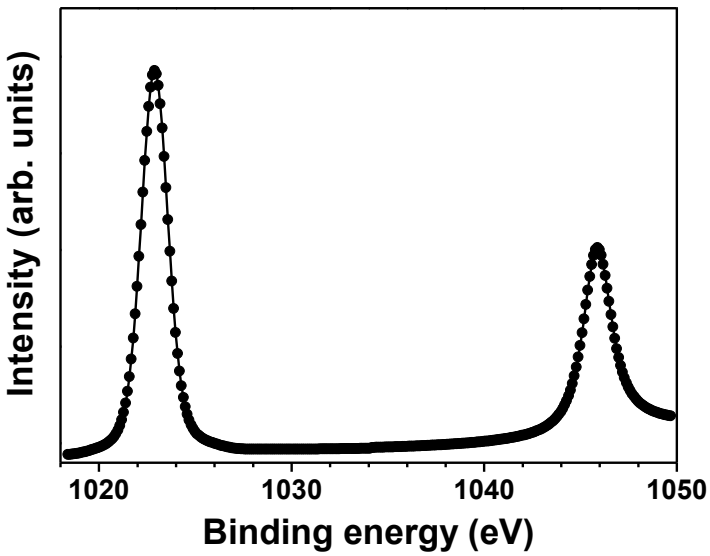

Figure 85. Zn 2p high resolution XPS scan of nanofibers of nylon/ZnO nanocoating. (Copyright © 2013, Royal Society of Chemistry. Reprinted with permission from Ref.[130])

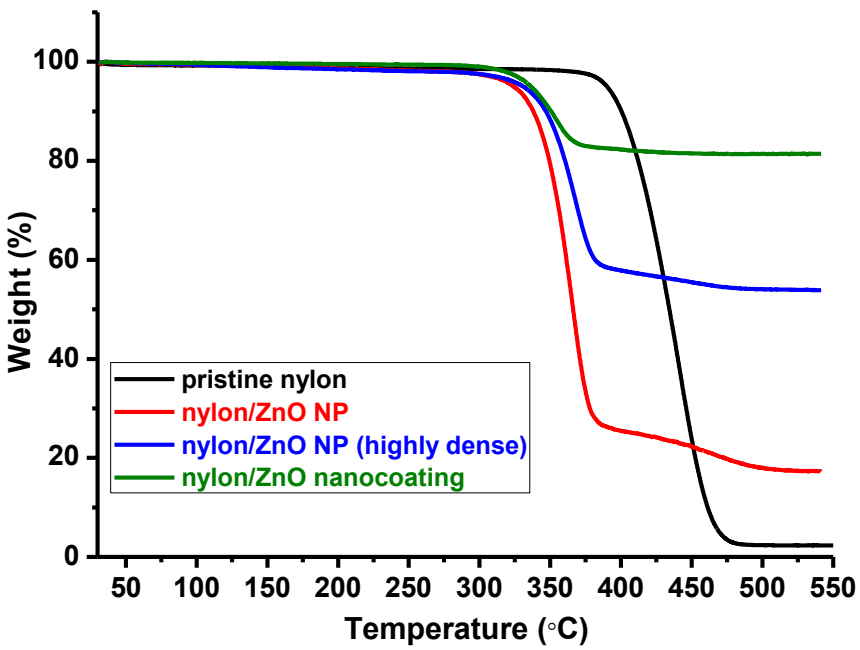

Figure 86. TGA thermograms of nylon and nylon/ZnO nanofibers. (Copyright © 2013, Royal Society of Chemistry. Reprinted with permission from Ref.[130])

The resulting nylon/ZnO nanofibrous membranes were easily handled and folded as a free standing material due to the flexible polymeric component (Figure 87). In order to investigate the effect of ZnO morphology on the efficiency of photocatalytic activity, nylon/ZnO nanofibers with three different ZnO morphologies were tested. The photocatalytic activities of these flexible nylon/ZnO nanofibrous membranes were tested by following the photocatalytic decomposition of a model azo-reactive dye (Rh-B) under the irradiation of UV-light. The degradation rates of Rh-B were calculated by using the absorption peak points and defined as C/C_0 where C_0 and C represent the initial concentration of Rh-B before UV irradiation and certain time of UV irradiation, respectively (Figure 87). No significant direct photolysis was observed for the blank Rh-B solution, and therefore the pink color of the dye solution did not change after the UV irradiation over a period of 24 h. On the other hand, the effective photocatalytic degradation of Rh-B was clearly observed for all Rh-B solutions containing nylon/ZnO nanofiber samples. The absorbencies of these solutions were reduced distinctly with respect to UV irradiation owing to the PCA of ZnO nanostructures onto nanofibers (Figure 87). The Rh-B solutions containing nylon/ZnO nanofiber membranes were decolorized during the UV irradiation, and pink color of the solution was almost disappeared after 24 h of UV irradiation due to the successful photocatalytic decomposition of Rh-B by the nylon/ZnO nanofibers (Figure 87). For nylon/ZnO NP, 53% of Rh-B decomposed in 4 h and total of 93% of Rh-B was decomposed in 24 h. Similar result was obtained for nylon/ZnO nanocoating; 49% of Rh-B decomposed in 4 h and total of 94% of Rh-B was decomposed in 24 h. In the case of nylon/ZnO NP (highly dense) sample, the decomposition of Rh-B was 63% and 99% in 4 and 24 h, respectively. Therefore, the highest photocatalytic degradation rate of Rh-B was observed for nylon/ZnO NP (highly dense), which is possibly because of the presence of large number of individual ZnO NP resulting in a higher surface area. This result clearly indicated that there is no need for a continuous ZnO nanocoating on the polymeric nanofibers,

since surface-decorated ZnO NP depending on its concentration exhibited same or better efficiency for the photocatalytic decomposition of model organic dye.

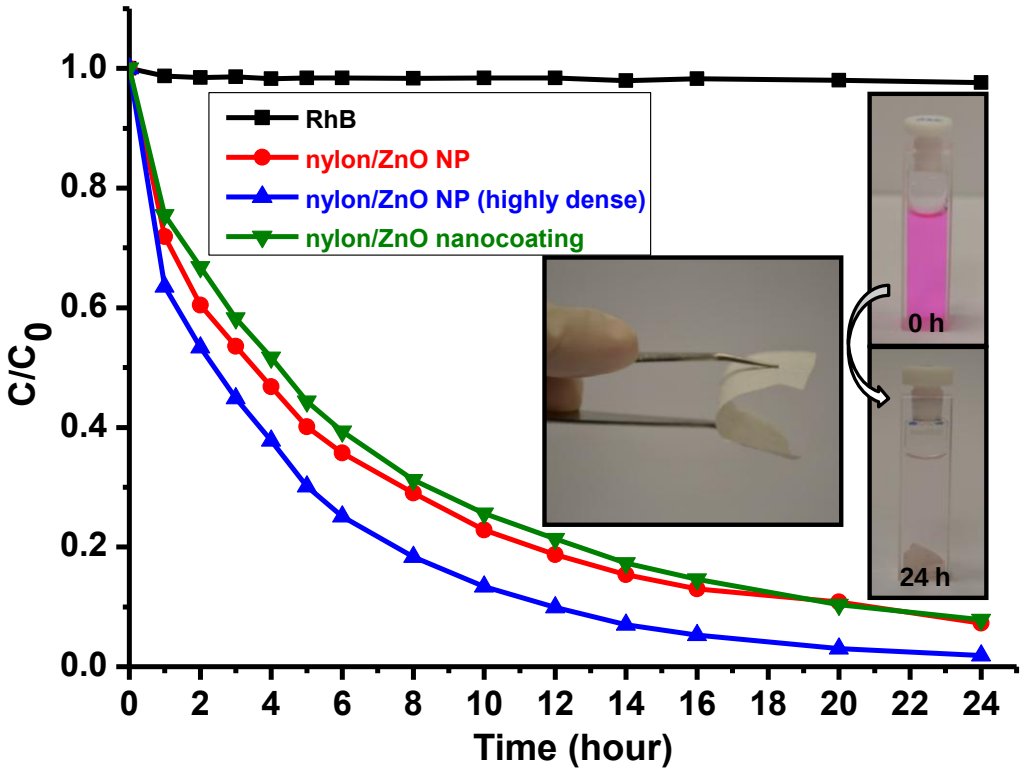

Figure 87. The rate (C/C_0) of Rh-B degradation with and without nylon/ZnO nanofibers by exposing UV light with 365 nm wavelength; representative photographs of flexible nylon/ZnO NP (highly dense) nanofibrous membrane and change of color of the Rh-B solution with this membrane as a function of the UV irradiation time. (Copyright © 2013, Royal Society of Chemistry. Reprinted with permission from Ref.[130])

4.3.3. Conclusions

In summary, we have fabricated flexible photocatalytic nanofibrous membranes by combining electrospinning and ALD techniques. By altering the ALD parameters various ZnO morphologies onto polymeric nanofibers such as ZnO NP or a continuous ZnO nanocoating were obtained. Nanofibrous membrane surface-decorated with the highly dense ZnO NP exhibited the highest efficiency for the photocatalytic decomposition of Rh-B dye due to its high surface area. These functional nanofibrous membranes may find applications as filtering materials for water purification and organic waste treatment.

We showed that ALD can provide not only uniform and conformal coatings with precise thickness control, but it can also be used to surface-decorate polymeric nanofiber templates with inorganic NP and the distribution density of the NP can easily be adjusted by altering the deposition parameters.

This approach can be used to produce functional flexible nanofibrous membranes for filtration, catalysis, sensors, photonics, electronics, energy, and biotechnology, depending on the selection of polymer type and inorganic components.

4.4. Enhanced Photocatalytic Activity of Homoassembled ZnO Nanostructures on Electrospun Polymeric Nanofibers: A Combination of Atomic Layer Deposition and Hydrothermal Growth

4.4.1. Experimental

Materials: PAN (Mw: ~150,000) was purchased from Scientific Polymer Products, Inc. N,N-dimethylformamide (DMF, Pestanal, Riedel) was used as a solvent. ALD of ZnO was performed using diethylzinc (DEZn, Sigma-Aldrich) and HPLC grade water (H_2O) as the zinc precursor and oxidant, respectively. For hydrothermal process zinc acetate dihydrate (ZAD, ≥ 98%, Sigma-Aldrich) and hexamethylene tetramine (HMTA, ≥ 99%, Alfa Aesar) were used. Methylene blue (MB, Sigma-Aldrich, certified by the Biological Stain Commission) was used as a model organic dye to test PCA of the PAN nanofibers and PAN/ZnO nanofibrous mats. All materials were used without any purification. De-ionised (DI) water is obtained from Millipore Milli-Q system.

Electrospinning of PAN nanofibers: In brief, we have optimized the PAN concentration (12% (w/v) in DMF) to yield uniform and bead-free nanofibers. Prior to electrospinning, PAN solution was stirred for 3 h at room temperature to obtain homogeneous and clear solution. Well-stirred solution was taken in a 5 mL syringe fitted with a metallic needle of ~0.8 mm of inner diameter. The syringe was fixed horizontally on the syringe pump (KD Scientific, KDS 101) with a feed rate set to 1 mL/h. A high voltage of 15 kV is applied (Matsusada, AU Series) between the syringe needle and a stationary cylindrical metal collector (wrapped with a clean aluminum foil) located at 12 cm from the end of the tip. The electrospinning process was carried out at ~25 oC and 22 % relative humidity in an enclosed chamber.

Preparation of ZnO seed structure by ALD: ZnO deposition on electrospun PAN nanofibers was carried out at ~200 °C in a Savannah S100 atomic layer deposition (ALD) reactor (Cambridge Nanotech Inc.). N_2 was used as a carrier gas at a flow rate of ~20 sccm. 400 cycles were applied via exposure mode (a trademark of Ultratech/Cambridge Nanotech Inc.) in which dynamic vacuum was switched to static vacuum before each precursor pulse. This is achieved by closing the valve between the reaction chamber and the pump. After a predetermined exposure time the vacuum was switched back to dynamic mode for purging excess precursor molecules and gaseous byproducts. One ALD cycle consists of the following steps: valve OFF/N_2 flow set to 10 sccm / H_2O pulse (0.015 s) / exposure (10 s) / valve ON / N_2 purge (20 sccm, 10 s) / valve OFF / N_2 flow set to 10 sccm / DEZn pulse (0.015 s) / exposure (10 s) / valve ON / N_2 purge (20 sccm, 10 s).

Growth of ZnO nanoneedles by hydrothermal method: ZnO coated PAN nanofibers (PAN/ZnO seed) were used as a seed substrate for the growth of ZnO nanoneedles. ~3.6 mg of PAN/ZnO seed nanofibrous mat was immersed into ~33 mL aqueous solution of equimolar ZAD, HMTA (0.02 M) and mildly stirred overnight at RT. This solution is then heated to 90 °C and kept for 5 h. When the crucible cools down to RT, the nanofibrous mat was thoroughly rinsed with DI water to remove any residual salts and dried in vacuum oven at ~40 °C for 12 h.

Characterization techniques: The morphology of the samples was studied using a scanning electron microscope (SEM, FEI – Quanta 200 FEG) with a nominal 5 nm of Au/Pd sputter coating. These images are used to estimate the average fiber diameter (AFD). For transmission electron microscopy (TEM) imaging, samples were sonicated in ethanol for 5 minutes and the dispersion is collected on holey carbon coated TEM grid. TEM (FEI–Tecnai G2F30) and elemental analysis (energy dispersive X-ray spectroscopy, EDX) was performed on the PAN/ZnO seed nanofibers. Selected area electron diffraction (SAED) patterns of the PAN/ZnO seed

nanofibers were also obtained. High resolution TEM (HRTEM) image was obtained for needle. X-ray diffraction (XRD) pattern from the pristine PAN, PAN/ZnO seed and PAN/ZnO needle samples were collected ($2\theta = 10^{o}$-100^{o}) using PANalytical X'Pert Pro MPD X-ray Diffractometer using Cu Kα radiation (λ = 1.5418 Å). For surface analysis, samples were subjected to X-ray photoelectron spectroscopy (Thermoscientific, k-Alpha) under Al K_{α} (hv = 1486.6 eV) line with a charge neutralizer. Pass energy, step size, and spot size were 30 eV, 0.1 eV, and 400 μm, respectively. Peak deconvolution was performed with Avantage software where the number of peaks was chosen based on the physics of the material while the spectral location and full width at half maximum (FWHM) were allowed to vary. Photoluminescence (PL) measurements were performed using Horiba Scientific FL-1057 TCSPC at an excitation wavelength of 360 nm.

Photocatalytic activity (PCA) of the nanofibers: The PCA's of the PAN nanofibers, PAN/ZnO seed and PAN/ZnO needle samples were analyzed through photo induced degradation of MB in aqueous medium (18.8 μM). The nanofibrous mats (weight: 3.6 mg) were immersed in quartz cuvettes containing the MB solution. The cuvettes were exposed to UV light (300 W, Osram, Ultra-Vitalux, sunlight simulation) placed at a distance of ~15 cm. Dye concentrations in the cuvettes were measured using a UV-Vis-NIR spectrophotometer (Varian Cary 5000) at regular time intervals. The nanofibrous mats were pushed to the bottom of the cuvettes during the UV-Vis spectroscopy. The weight of PAN/ZnO seed sample before and after the needle growth is ~3.6 mg and ~3.9 mg respectively which is equivalent to an increase of ~8 wt%. Then the weight of PAN/ZnO needle sample is corrected to equate PAN/ZnO seed sample (3.6 mg). Hence the 3.6 mg of PAN/ZnO needle contains 3.32 mg of seed and 0.28 mg of needles. The rate of dye degradation is quantified via first order exponential fit ($y = y_0 + Ae^{-x/t}$) for each data set. This fit is performed under automated routine with Origin 6.1, where all the parameters are set as free until convergence. We have also repeated the PCA experiment twice (i.e. 2^{nd} and 3^{rd}

cycles) for PAN/ZnO needle sample (~3.3 mg) to determine the reusability versus performance.

4.4.2. Results and Discussion

ZnO nanoneedles were hydrothermally grown on the ZnO seed-coated polymeric nanofibers which were fabricated through combining electrospinning and ALD. The process for fabricating the hierarchical polymer/ZnO nanofiber is illustrated in Figure 88.

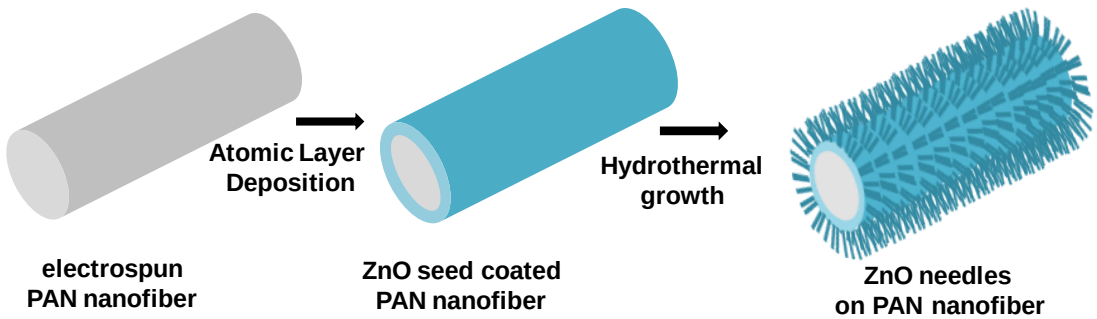

Figure 88. Schematic representations of the fabrication process of hierarchical PAN/ZnO needle nanofiber. (Copyright © 2014, Elsevier. Reproduced with permission from Ref.[157])

The representative SEM images of PAN nanofibers are given in Figure 89(a1-2). The nanofibers morphology is optimized against several PAN concentrations (results not shown here). About 12% (w/v) is found to be the optimum for the chosen parameters yielding bead-free morphology with an AFD of ~655 ± 135 nm. In electrospinning, it is very typical to obtain fibers in a range of diameters as reported by us [312, 396] and many others [7, 10]. A close inspection of the morphology reveals a texture like structure, which is sometimes observed for certain electrospun polymeric nanofibers due to the type of solvent used [7, 10, 397]. These nanofibers were employed for the second step of seeding with ALD [109-111] by applying 400 cycles at 200 °C using exposure mode (see experimental section). After the ALD

process, we have recorded the SEM images which are shown in Figure 89(b1-2) where the AFD is ~715 ± 125 nm. This measurement suggested an increase in AFD because of ALD coating. The fiber structure was not destroyed during the ALD process where a well defined and stable fiber structure suggests the suitability of the chosen parameters. It is important to point out the need of compatibility between the precursor and polymer as the former can degrade the latter by chemically reacting with it; see the case with ALD processing of Al_2O_3 [123]. On the other hand in the case of poly (propylene) fibers Al_2O_3 base layer is employed to deposit ZnO, where the former protects the diffusion of DEZn into the polymer [398]. Despite of these limitations, ALD coating can yield coral [122], core-shell [116] like complex nanostructures. Such structures are potential for photocatalytic applications [399]. In the present case the morphological changes are similar to our earlier observation [11, 130]. It is clear from the image (Figure 89(b2)) that the surface roughness is increased after ALD process, which is most probably due to the grainy structure of ZnO [11, 130]. In our earlier investigation [130], we have shown the grain formation under ALD for different stages of processing cycles. The closely and uniformly packed grains act as the seed layer for the subsequent growth of nanoneedles of ZnO in hydrothermal process. Note that this grainy structure is not undesired, on the other hand it helps to enhance the PCA, where we can expect the formation of depletion layer within the grain boundaries [150, 173]. Such depletion layers are extremely helpful and we will address them in the context of PCA latter in this article. Subsequently, the hydrothermal method was employed to grow ZnO nanoneedles on the ZnO seed-coated polymeric nanofibers. Figure 89(c1-2) shows the representative SEM image of the resulting nanoneedle assemblies (PAN/ZnO needle). It can be seen that grown ZnO nanoneedles cover the surface of the ZnO seed-coated PAN nanofibers. The nanoneedles were straight and no branching is observed. Branching generally occurs because of the irregularity in the seed where it can promote the growth of more than one needle. Notably, in the present context the seeds grown through ALD-process are uniform and do not initiate or support multi-needle growth.

By analyzing the SEM images we have estimated the average diameter and length of the nanoneedles to be ~25 nm and ~600 nm, respectively (Figure 89(c2)). Detailed discussion on the mechanism of the growth of ZnO nanoneedles can be found in the literature [166]. Seeding of ZnO with ALD process and subsequent hydrothermally grown nanorods of ~50 nm diameter with a length of ~0.5-1μm can be seen in the literature [145, 186].

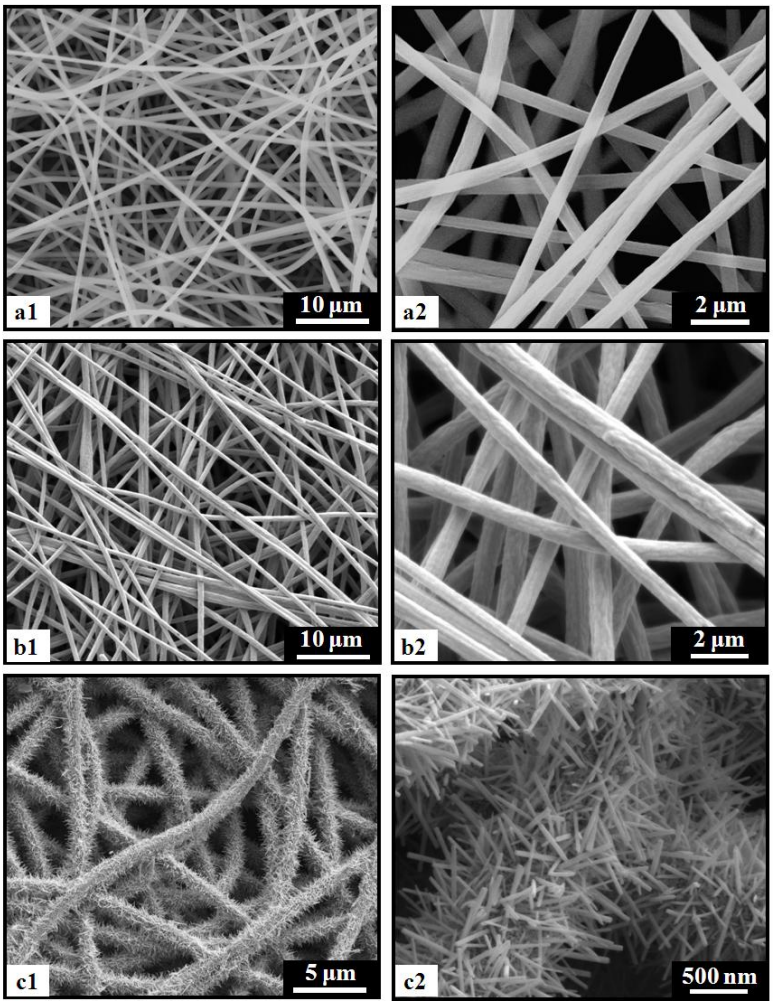

Figure 89. Representative SEM images of (a1-2) pristine PAN, (b1-2) PAN/ZnO seed, and (c1-2) PAN/ZnO needle nanofibers at different magnifications. (Copyright © 2014, Elsevier. Reprinted with permission from Ref.[157])

The morphologies of the PAN/ZnO seed nanofibers were further investigated by TEM and shown in Figure 90(a1). The conformal coating of ZnO can be evidenced from the image with a uniform thickness (~50 nm) in spite of the relatively large surface area of the nanofibers. Notably this supports the earlier argument on uniformity of the grains which are not favourable for multi-needle growth. ALD is well suitable for the high surface area substrates such as a non-woven nanofibers mat as shown by us earlier [11, 130]. Growth per cycle for ZnO on the PAN nanofibers was calculated to be ~1.25 Å in the present ALD conditions. In our previous study [11] we observed that ALD of ZnO with 0.015 s pulses and 10 s purges under the dynamic vacuum conditions results in uniform coatings only after a certain number of ALD cycles. In contrast, here we have employed exposure mode (see experimental section) which also resulted in a continuous and uniform ZnO coating without the need of high number of ALD cycles. Exposure mode keeps the precursor molecules inside the reaction chamber for a certain period of time which allows them to diffuse into the substrate. The local crystal structure of the ALD-ZnO is investigated through SAED pattern, and shown in Figure 90(a2). The pattern reveals the polycrystalline nature of ZnO seed. Moreover, the bright spots on the polycrystalline diffraction rings indicate the presence of well crystalline grains [130]. Various diffracted planes are annotated on the image and are consistent with the literature [151, 168]. EDX analysis (Figure 91, left panel) on the PAN/ZnO seed nanofibers has shown zinc, oxygen, carbon, nitrogen and copper (from TEM grid) elements. Zn and O are originated from ZnO seed, whereas C and N are due to the polymeric core structure of PAN.

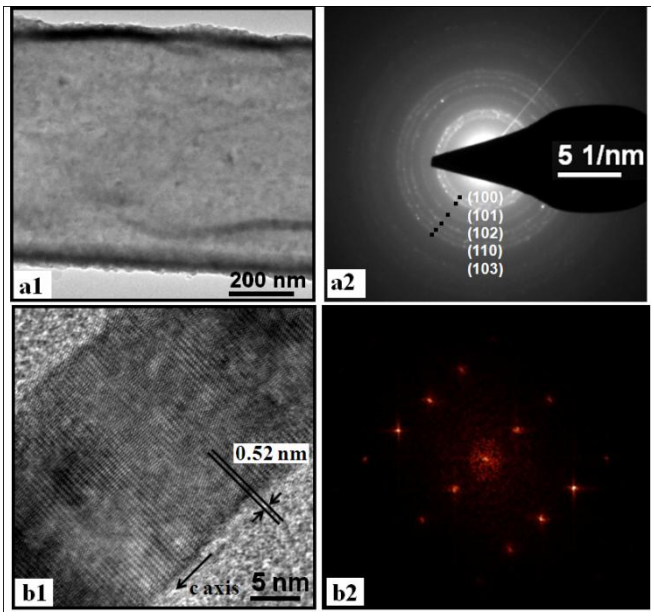

Figure 90. Representative (a1) TEM image and (a2) SAED pattern of PAN/ZnO seed nanofibers; (b1) HRTEM image and (b2) FFT image of ZnO needle. (Copyright © 2014, Elsevier. Reprinted with permission from Ref.[157])

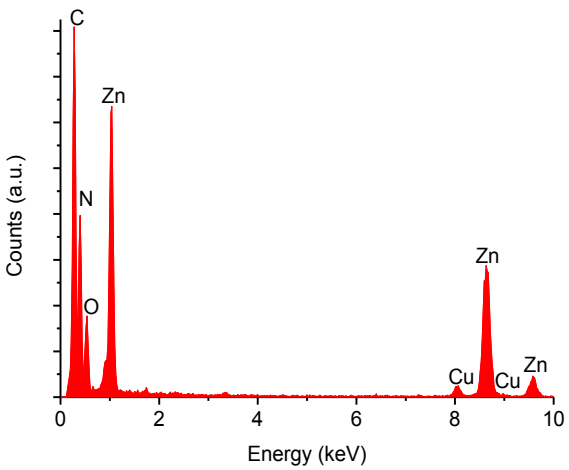

Element	At%	Error%
C	67.38	0.71
N	22.96	0.49
O	4.94	0.17
Cu	0.28	0.06
Zn	4.42	0.25

Figure 91. (Left panel) EDX spectrum of PAN/ZnO seed nanofibers, (right panel) quantification of the spectrum shown in the left panel. (Copyright © 2014, Elsevier. Reprinted with permission from Ref.[157])

Also the quantification (Figure 91, right panel) of Zn and O atomic percentages suggests that the material is nominally oxygen rich, within the detection limit of EDX. This is because of the very high surface area yielding defective sites (oxygen vacancies) where molecular oxygen can be adsorbed. It is notable that oxygen vacancies are typical for ZnO in other processing techniques as well, which were determined through an indirect method [150-151, 167-168]. We will see that the oxygen deficiency is consistent with the PL of ZnO. Furthermore, HRTEM image demonstrated a single crystalline nature of ZnO nanoneedles (Figure 90(b1)). The lattice spacing is measured to be ~0.525 nm corresponding to the c-axis of ZnO, which is the preferential growth direction of the nanoneedles. It is important to determine the growth direction where the polar planes of ZnO have shown to depict relatively higher PCA [161]. The fast Fourier transform (FFT) image is shown in Figure 90(b2) also demonstrates the single phase [178] structure.

The XRD patterns of pristine PAN, PAN/ZnO seed and PAN/ZnO needle nanofibers are shown in Figure 92. The XRD pattern of pure PAN nanofibers shows a peak at ~16.93° corresponding to orthorhombic PAN (110) reflection [400] with a FWHM of ~2.282°. Also a broad and less intense peak like structure can be seen in the range of 20°-30° which corresponds to the (002) reflection of PAN [401]. After the ALD process the (110) plane has shown a significant reduction in the FWHM (to ~0.761°) and the broad peak (2θ = 20°-30° indicated with * on the image) has stabilized at ~29.69° and became more sharp (FWHM ~0.776°). This is because of the reorganization of the polymeric chains at ~200 °C (ALD processing temperature) equivalent to typical annealing. Furthermore, since the nanoneedles are grown at slightly elevated temperature (~90 °C) for substantial period of time, there is a nominal increase in the FWHM of the PAN diffraction peaks ((110) and (002))

because of the incompatible processing temperature. However the relative intensity of this peak was considerably subdued because of the ZnO nanoneedles.

Moving onto the peaks corresponding to the ZnO, we have annotated the reflections on the image for the samples PAN/ZnO seed, and PAN/ZnO needle (Figure 92a). PAN/ZnO seed and needle samples exhibited diffraction peaks of hexagonal wurtzite structure of ZnO (ICDD 01-074-9940) revealing the successful deposition of ZnO seed as well as nanoneedles on electrospun PAN nanofibers by ALD and hydrothermal technique, respectively. The XRD patterns from PAN/ZnO seed and PAN/ZnO needle match in terms of peak positions with the reference pattern. Also these peak positions match with the literature, when ZnO is prepared through different methods [150-151, 167-168]. However, a close observation of (100), (002) and (101) reflections (Figure 92b) reveal vital information. If we compare the FWHM of these peaks across seed and needle samples, we can see that the former is less crystalline than the latter. There is also a shift in the position of the peaks towards higher 2θ value upon needle formation. For the diffraction pattern of PAN/ZnO needle, we can see a shoulder like structure (denoted with s on Figure 92b) corresponds to the PAN/ZnO seed, while a more intense peak corresponding to the highly crystalline ZnO nanoneedle. Peak shift is generally associated with the residual stress (induced defect) in the material. The stress might be originated from the oxygen vacancies in the lattice [367] or the substrate (PAN nanofibers) [402]. Since the peak shift is noticed for (100), (002) and (101) reflections we can expect that the sample is under compressive strain in the said crystal directions [402]. Notably, the XRD pattern of PAN/ZnO seed is consistent with SAED pattern. Furthermore, the intensity ratios of (002) polar plane to (100) nonpolar plane is estimated and it turns out to be the case that seed (~0.78) sample has large fraction of polar planes than needle (~0.65) sample, where larger fraction indicates possibly higher PCA [166].

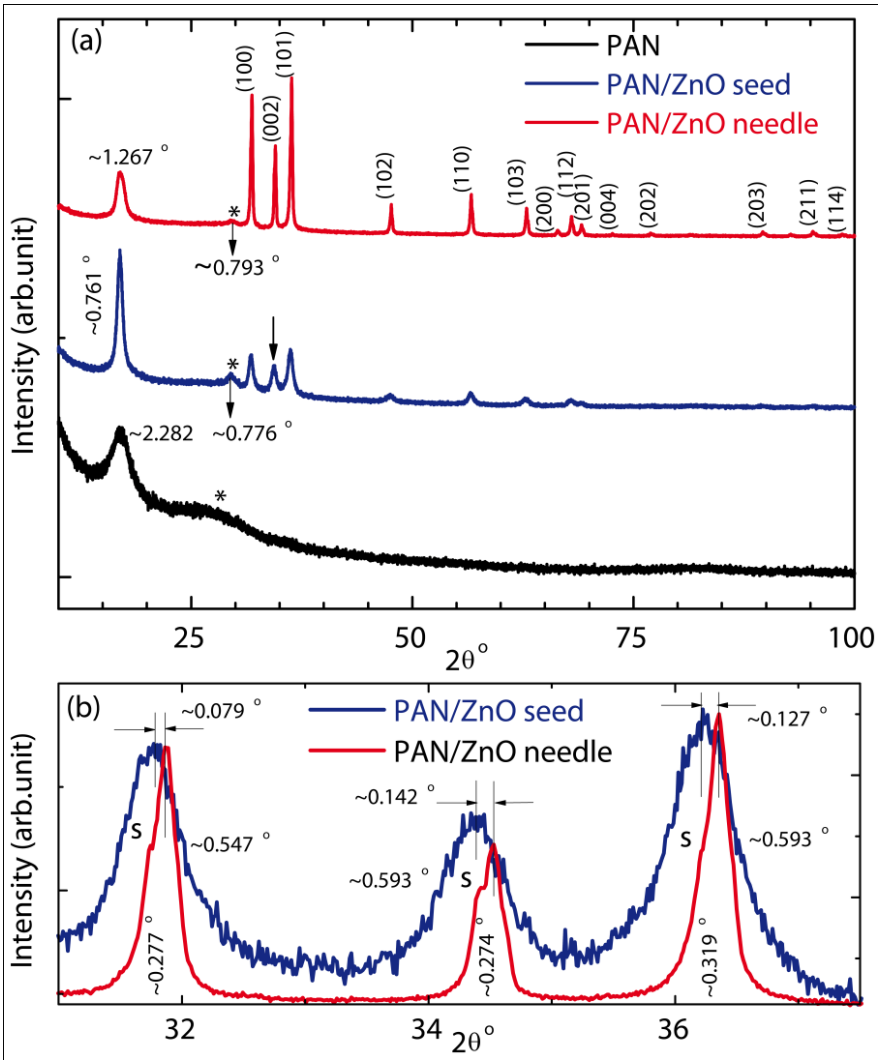

Figure 92. (a) XRD patterns of nanofibers of PAN, PAN/ZnO seed and PAN/ZnO needle, and (b) magnified XRD patterns in the range of 31-37.5°. (Copyright © 2014, Elsevier. Reprinted with permission from Ref.[157])

The ionic state of oxygen generally determines the optical emission properties in visible region [151, 167-168] (associated with oxygen related defects) and hence the photocatalytic properties [128, 133, 161, 166, 368]. The O1s XPS spectrum can be deconvoluted into two peaks as shown in Figure 93, with the peak positions annotated on the image. The peak at ~530.5 eV corresponds to the oxygen in ZnO, which is nominally at the same spectral position for both the samples. The other peak

seen at ~531.8 and ~532.2 eV for seed and needle sample respectively corresponds to the chemisorbed oxygen of two different chemical origins. The peaks at 531 eV and 531.5 eV are attributed to O^{-x} ions (O^{-} and O^{-2} ions) in the oxygen deficient regions, while peaks at 532.3 eV and 532.7 eV are generally ascribed to the presence of oxygen related species such as –OH, –CO, adsorbed H_2O or O_2 on the surface of ZnO [367, 403-404]. During the hydrothermal growth of the needles, grain boundaries and oxygen deficient regions are exposed to hydroxyl ions. These ions perhaps occupy some of the oxygen deficient regions as reflected with a peak at ~532.2 eV. Apart from the difference in the spectral location, the number density of such occupancies is seen in the area of the peak where for PAN/ZnO seed the area ratio is (~49 %) significantly higher than needle case (~22 %). It is notable that the signal from PAN/ZnO seed sample can be attributed to the sample directly without any ambiguity, however, for the PAN/ZnO needle case, it can be an integral spectrum of seed as well as needle. Despite of the latter ambiguity, the above given interpretation still well applicable and we will see that it is in line with optical and PCA measurements. Finally, a large oxygen-deficient state of the surface layer [367, 403] can be seen for PAN/ZnO seed, while in contrast, PAN/ZnO needle sample has shown significantly less oxygen vacancies. Needles resulted in a more stable ZnO enrichment on PAN nanofibers when compared to PAN/ZnO seed [403].

The valence band spectra for PAN/ZnO seed as well needle is shown in Figure 94 where the intensity axis is normalized against the maximum counts and plotted with reference to the binding energy in eV. In zinc oxide, the conduction band (CB) and the valance band (VB) are formed from O1s and Zn2p orbitals, respectively. As a whole, both the samples have shown the density of states which are typical to zinc oxide [367]. Also the features and their spectral location for both the samples is exactly retraced (Figure 94). This is in contrast to an earlier observation [367] in which VO's has shown to induce a band gap narrowing by expanding the minimum of CB. However, here the V_O's did not induce any such

tailing of CB though evidenced in O1s XPS analysis. The energetic location of oxygen vacancy (V_O) defects within the band gap will be discussed in the context of PL.

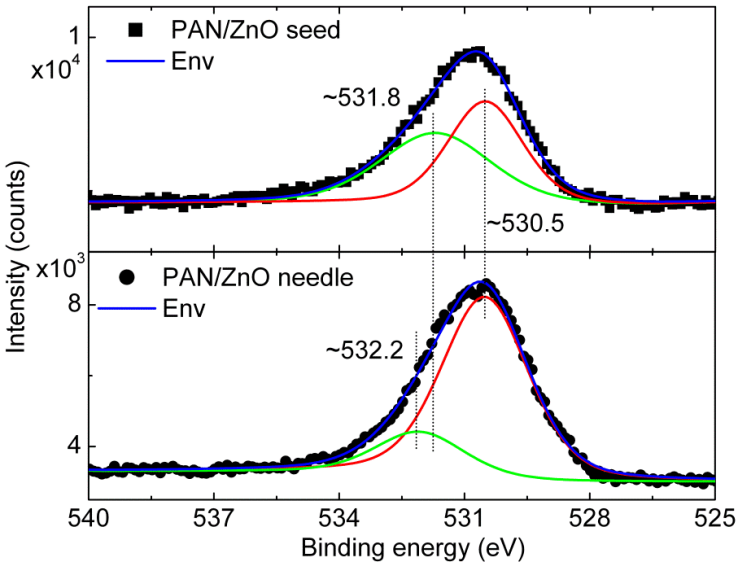

Figure 93. Peak deconvolution of core-level XPS spectra of O1s from PAN/ZnO seed and PAN/ZnO needle samples. The spectral location of the peaks are annotated on the image. (Copyright © 2014, Elsevier. Reprinted with permission from Ref.[157])

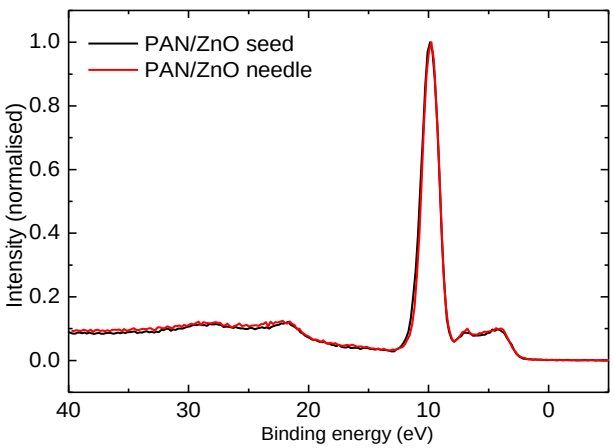

Figure 94. Valence band XPS spectra for PAN/ZnO seed and PAN/ZnO needle nanofibers. (Copyright © 2014, Elsevier. Reprinted with permission from Ref.[157])

As mentioned earlier, the surface defects play a crucial role in determining the PCA; we can infer the information about such defects through PL spectroscopy. The PL spectra of PAN/ZnO seed and PAN/ZnO needle nanofibers shown in Figure 95a were obtained at RT. As shown in earlier investigations [150-151, 167], the visible emission from ZnO can be decomposed (fittings not shown) into various plausible transitions which will be discussed as we go along. It is known that the typical excition emission band lies in the UV region for ZnO, while the defect related emission in visible region [150-151, 167-168, 173, 405]. Based on the literature the possible transitions and the corresponding emission wavelengths are schematized in Figure 95b, which are cross-annotated on Figure 95a with arrows on the wavelength axis.

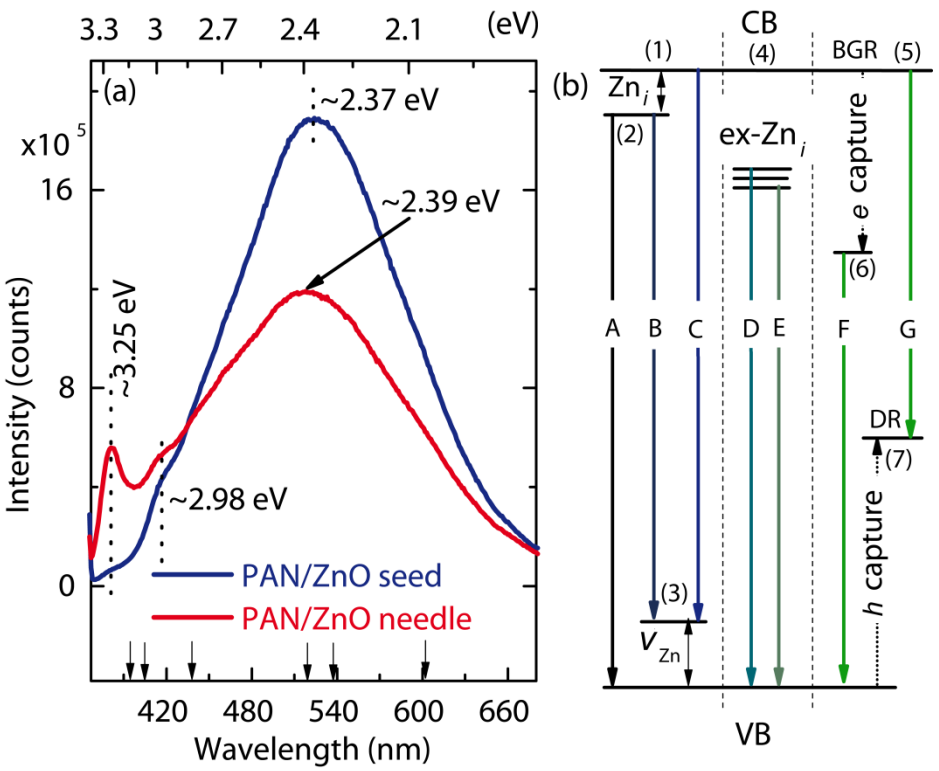

Figure 95. (a) PL spectra of PAN/ZnO seed and needle counterpart and (b) depicts various crystal defects and possible transitions. (Copyright © 2014, Elsevier. Reprinted with permission from Ref.[157])

We start with the peaks corresponding to the interband transition (excitonic recombination) which is the least controversial emission. As expected, relatively better crystalline PAN/ZnO needle has shown a clear peak at ~3.25 eV, while in contrast, only a signature of such emission is noticed for PAN/ZnO seed sample. This emission peak is consistent with the literature in terms of spectral location [151], yielding a bandgap of 3.31 eV [151] when an excition binding energy of 60 meV is assumed. The relative intensity of this interband transition is enhanced upon needle formation on ALD seed layer, which suggests an improvement in the overall optical quality of the material. In the literature [165, 184-185], we can see needle/rod like structure, however, the samples depicted broad near UV emission and almost negligible visible emission. However, in contrast, we have comparatively sharp UV emission and significant visible emission, where we are aimed to harness the defect related PCA. Note that the emission from PAN/ZnO needle is the integral response of two components, one of which is from the needle itself, while the other is from PAN/ZnO seed. As PAN/ZnO seed did not show any clear excition emission, the peak seen in needle sample arises from the ZnO-nanoneedle. In the case of PAN/ZnO seed because of the large grain boundaries from the film like structure on the cylindrical peripheral a significant amount of surface recombination takes place giving the predominant visible emission. Various plausible emissions are schematized in Figure 95b and shown with numerals (1) though (7) where the energetic locations of the defects have been obtained from the corresponding references; (1) [43], (2) [406], (3) [407-408], (4) [163], (5) [150, 173], (6) [409-410] and (7) [410]. Violet emissions centered at about 410 nm are broader, and not as prominent as green emission centered around 520 nm, which were intepreted to be related to the defects such as zinc interstitials (Zni) and VO's, respectively. Violet emission can result from an integral response of three transitions [172, 406-408] as denoted on Figure 95b with A through E. The alphabets stand for emission wavelengths in nanometer, where A = 395, B = 437, C = 405, D = 440, E = 455, F =

~500, and G = 564. VZn is located 0.30 eV above the VB, while Zni is at 0.22 eV below the CB.

In the visible region of the spectrum, both the samples have exhibited a broad emission which is again an integral response of the defects of two different origins. Also, a slight though noticeable blue shift can be noticed in the center of the peak (peak positions are annotated on the image) for PAN/ZnO needle from its seed counterpart. Although the variation is nominal (~0.02 eV), when it comes to the density of the defects, it plays a crucial role in determining the PCA of the material. The optical quality of the semiconductor can be estimated by taking the intensity ratios of UV to visible emission [151, 167-168]. It is worth noting that the ratio of the intensity of band to band transition (~381 nm) to the intensity of the defect level emission (~520 nm) is ten times higher for the PAN/ZnO needle than PAN/ZnO seed. This high ratio indicates higher optical quality of the PAN/ZnO needle sample. Unlike the violet emission, green emission is slightly complex [150, 173]. In the bulk grain region (BGR) singly positively charged V_O captures an electron from CB and forms a neutral V_O (i.e. $V_O^{+} \rightarrow V_O^{*}$). In the depletion region (DR) if the singly positively charged V_O captures a hole from the VB, it forms doubly positive V_O (i.e. $V_O^{+} \rightarrow V_O^{++}$). Hence, the green emission is a combination of transitions from V_O^{*} to the VB and CB to V_O^{++} emitting F and G wavelengths, respectively (Figure 95b) [150, 173]. Also, relatively lower intense interband emission suggests that the photo-generated electrons and holes are captured by V_O^{+} emitting photons in the visible region of the spectrum. This interpretation will be employed to explain the PCA of the samples.

We have comparatively investigated the PCA of PAN nanofibers, PAN/ZnO seed and PAN/ZnO needle by analyzing the time dependent decomposition of MB in aqueous medium under illumination. To evaluate the degradation rate of MB, its characteristic absorption peak (~665 nm) is monitored against UV-exposure time.

The rate of degradation is defined as C/C_o where C_o and C represent the initial concentration of MB before and after irradiation at a given time respectively. The pristine PAN nanofibers are porous to adsorb (not degrade) the dye up to a noticeable level (results not shown) until equilibrium between adsorption and desorption is attained. Hence we have taken the surface adsorption as reference and analyzed the PAN nanofibers effect on dye degradation, where no effect is seen (Figure 96a). This is consistent with the literature [411].

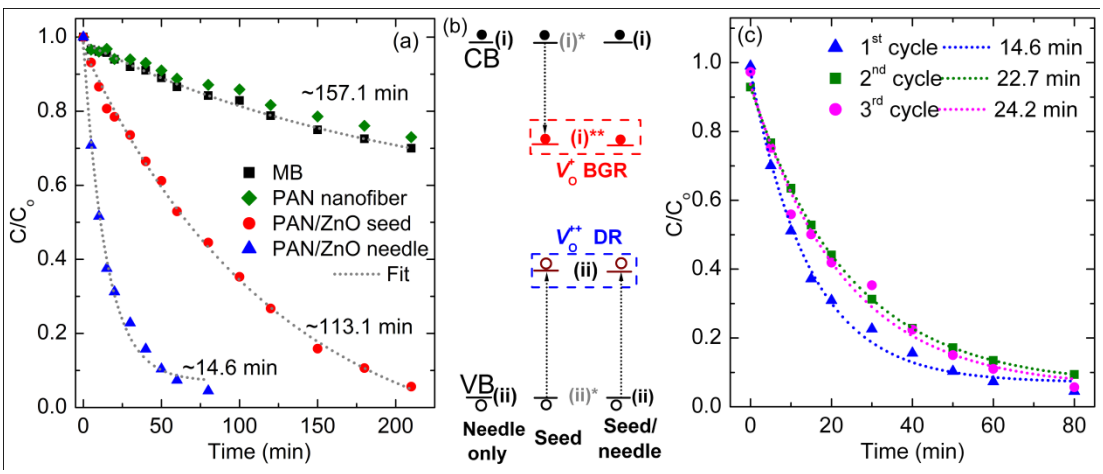

Figure 96. (a) Degradation rate of MB in aqueous environment tested for pristine, in the presence of PAN nanofibers, PAN/ZnO seed and PAN/ZnO needle (1st cycle) cases, (b) plausible mechanism of photocatalysis involving oxygen vacancies, where (i) and (ii) stand for processes acceptor → acceptor$^-$ and donor → donor$^+$ respectively, and (c) PCA of PAN/ZnO needle nanofibers for 1st, 2nd and 3rd cycles. (Copyright © 2014, Elsevier. Reprinted with permission from Ref.[157])

On the other hand it is notable that ALD unveils conformal coating on electrospun nanofibers and hence the exposure of PAN nanofibers directly to the dye can be very unlikely.In the case of PAN/ZnO seed and needle cases we have observed a nonlinear behavior, and the electron transfer between donor states and the dye governs the degradation ratio [412-413]. Hence we have addressed the nature of

degradation in the context of each sample independently. When the catalysts are immersed in the MB solution, the PCA with respect to UV irradiation time is depicted in Figure 96a along with the pristine MB solution which was subjected to the same UV treatment. According to the Langmuir–Hinshelwood model the exponential relationship of (C/C_o) against time indicates that MB degradation follows pseudo-first-order kinetics. We have performed exponential fit to the each data set and the decay constants are given on the figure.

In the case of UV exposure to pristine solution the data has shown decay constant of ~157 min. Notably though to the naked eye, the degradation of the MB (without nanofibers) is not clearly observed upon exposure to UV radiation for 210 min (see Figure 97 for digital photographs). For PAN/ZnO seed, ~47% of MB decomposed in nominal 60 min yielding a degradation rate of ~113 min. An improvement of ~28% is noticed when compared to the degradation rate in the case of no catalyst. Eventually, the blue solution was almost decolorized after ~210 min of UV irradiation (Figure 97). In the case of PAN/ZnO needle, the decomposition of MB was ~93% in ~60 min. Interestingly, in the case of PAN/ZnO needles, at a degradation rate of ~15 min has shown improvement of ~91% and ~87% for no catalyst and PAN/ZnO seed samples, respectively. PCA was relatively higher for the PAN/ZnO needle than PAN/ZnO seed, which is because of not only relatively higher surface area but also its higher crystal quality of the needle-morphology. As pointed in section 2.6, ZnO-seed content in PAN/ZnO needle sample is less than PAN/ZnO seed, where the needles compensate the remainder of the weight. Although the needles are about 0.02 mg in PAN/ZnO needle they shown significant effect on PCA. As an aside the improvement in the surface area is about 30 times, where ~1200-1500 needles are approximated on fiber (~800 nm and 715 nm of length and diameter respectively). In our previous study [130] high density nanoparticles have shown ~1.2 times higher PCA than nanocoating case. It needs to be emphasized that within this study we have achieved an improvement of dye degradation rate of nearly 8

times for needle case when compared to seed case. In the following, we establish the argument for PCA and latter correlate with each of the samples. Under suitable illumination electrons can be excited from the VB to reach the CB, leaving behind holes in the VB [150-151]. If these separated charges can migrate to the surface of the semiconductor before they recombine, then they have a chance to participate in the redox reactions [152]. Formation of hydroxyl radical ($^{\cdot}OH$) is the key for the PCA, in which holes [140] as well as electrons (which may be captured by molecular oxygen forming superoxide anions [139], $^{\cdot}O_2^-$) are involved at VB and CB, respectively. Because of the presence of highly oxidative hole as well as $^{\cdot}OH$ radicals the organic dye can be decomposed either partially or completely. We have already shown the possible mechanism [136, 139-140] in the last part of Introdution (1.4). In the literature [136, 414], it is discussed that PCA takes place at the VB and the defect state (formed either by doping [414] or intrinsic [136] e.g. V_O's), where the latter captures a free electron from the CB. However, under illumination, O_2 can capture an electron from CB promoting the PCA. The basis for this argument is the interband transition seen in the PL spectrum from PAN/ZnO needle sample which suggests a possibility of photo-electrons recombining with holes in CB, bypassing the defect state. Hence, at a given time, under illumination electrons are populated in CB to be captured by O_2. On the other hand, the photo-electrons can also be captured by O_2 at V_O's producing superoxide radical anions. It is also shown earlier that the V_O's can act as active sites for PCA in ZnO nanostructures [161, 367, 415]. Since the V_O's are located on the surface (interfaces of the grains and depletion regions) [150, 173] they directly involve in PCA [156]. Notably, V_O is treated as electron acceptors [156] by capturing an electron from CB [150-151, 173] and hence the recombination process is delayed [136]. In the PCA at heterojunction (e.g. ZnO/ZnSe [178], ZnO/Cu_2O [179]) (i) acceptor → acceptor$^-$ and (ii) donor → donor$^+$ processes occur at CB of ZnO and VB of ZnSe (or Cu_2O) respectively, where the charge migration across the heterojunction delays the recombination process. In the context of Pt-ZnO

nanocomposite [156], a well defined emission from interband transition in PL is not seen because of the low recombination rate of e/h pairs which is induced by Pt.

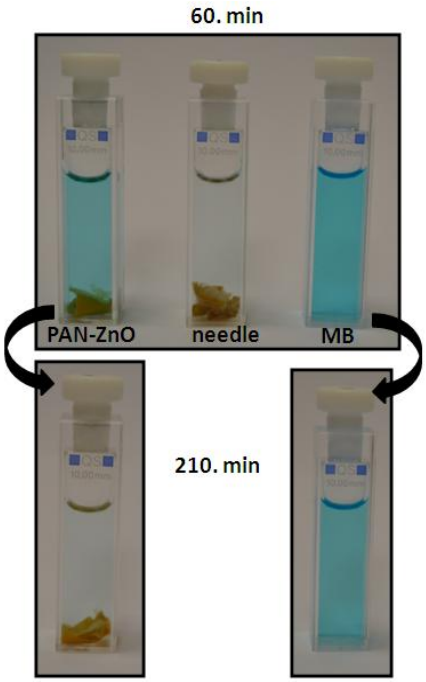

Figure 97. The photographs of the MB solutions with/without nanofibrous web in certain UV irradiation time (1st cycle). (Copyright © 2014, Elsevier. Reprinted with permission from Ref.[157])

In the background of the above discussion, for a hypothetical case of virtually defect free nanoneedle (i.e. high optical quality, Figure 96b, Needle only), PCA is because of (i) and (ii) processes taking place at CB and VB of ZnO nanoneedle respectively. In the case of PAN/ZnO seed, there is just a signature of interband transition in PL, hence the PCA that takes place at CB and VB is not dominant, which is denoted with (i)* and (ii)*, respectively (Figure 96b, Seed). The defect site V_O^+ is located in the bulk of the grain [150-151, 167, 173] (Figure 95b) and hence it is not accessible for PCA, unless the captured electron migrates to the surface. This may a very unlikely case as these states are highly localized. Furthermore, the PCA associated with V_O^+ is relatively weak and is denoted with (i)**. In contrast, the

defect site V_O^{++}, which is located in the depletion region (e.g. grain boundaries [150-151, 167, 173], Figure 95b) is well accessible for PCA and is denoted with (ii). In principle, the present ALD grown ZnO film is evidenced to be grainy with large portions of grain boundaries. For PAN/ZnO needle case, the PCA is an integral effect of V_O's ((ii), from PAN/ZnO seed sample) as well as the catalysis taking place at CB (i) and VB (ii) of needle (Figure 96b, Seed/needle). The combined effect of all these processes yielded significantly higher PCA. We have also seen that the seed sample has large fraction of polar planes than needle sample (analysis from XRD), hence it is expected [166] that seed sample should have shown better PCA. Although it appears to be not the case here, a careful understanding of the both the materials reveal that the present results are in line with the Ref.[166]. It is well agreed that the sample with larger fraction of polar planes yield higher PCA (owing to their V_O's) what we see is a synergy effect of the needle and the seed, hence these results are not in contrast to an earlier observation [166].

The structural durability of the PAN/ZnO seed and PAN/ZnO needle nanofibers was also examined through SEM after the photocatalysis (Figure 98). We note that the stability as well as durability plays a vital role because of their potential application in water purification of the organic pollutants. As outlined in the introduction, we characterize the material in terms of their catalytic efficiency and durability with reference to recycling. We have repeated the PCA experiment twice for the PAN/ZnO needle (Figure 96c). There is a slight decrease in the efficiency of PCA from 1st cycle to the following cycles, where the 1st cycle has shown ~93% in ~60 min of UV irradiation (Figure 96c). The deterioration could have occurred from various factors. Firstly, a small quantity (~0.3 mg) of nanofibrous mat was used for SEM analysis after the 1st cycle, leaving behind less amount of catalytic material for the 2nd and 3rd cycles. Secondly, by considering the SEM images of the latter cycles (after 1st cycle, Figure 98b; after 3rd cycle Figure 98c), it is clear that the density of nanoneedles is decreased to a certain degree. This is because of the mechanical

fatigue while inserting the nanofibrous mat through a tiny hole of the cuvette and UV-Vis spectroscopy. If the nanofibrous mat has been handled carefully then we believe that the performance of catalyst after the 2nd cycle will be as good as or at least comparable with that of a fresh sample.

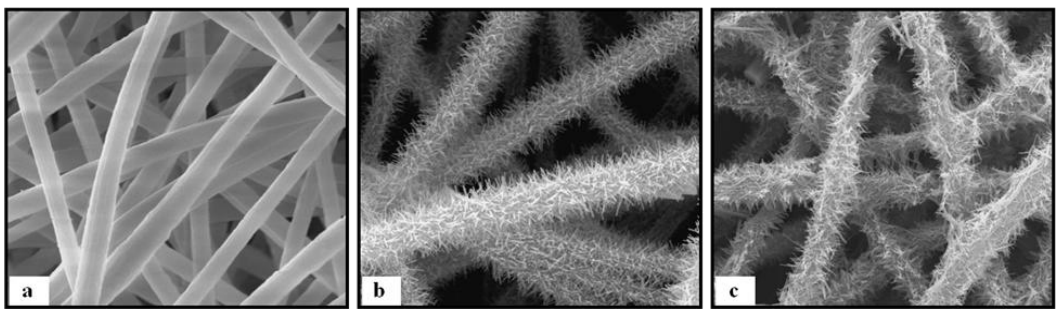

Figure 98. Representative SEM images of (a) PAN/ZnO seed and (b) PAN/ZnO needle nanofibers after the 1st cycle of UV irradiation in MB solutions; (c) PAN/ZnO needle nanofibers after the 3rd cycle of UV irradiation in MB solution. (Copyright © 2014, Elsevier. Reprinted with permission from Ref.[157])

4.4.3. Conclusions

Here we have reported the results of an investigation on ZnO based photocatalyst synthesized on electrospun PAN nanofibers. This catalyst harnesses PCA at three different energetic locations within the band gap of ZnO, namely, oxygen vacancy sites, VB and CB. In order to achieve this, morphologically well defined PAN nanofibers are produced via electronspinning, followed by ALD to deposit ZnO in a well controlled manner yielding a thin and conformal coating on the nanofibers. The last step consists of hydrothermal growth of ZnO single crystal needle like structures on the ALD seed coating. The present investigation also re-iterates the flexibility of various techniques and a combination of ALD and hydrothermal growth. The ALD parameters are optimized in such a way that the seeds do not initiate multi-needle growth which in turn improves the subsequent processing of hydrothermal growth as in the present case or other methods such as

sol-gel. The structural investigation (XRD) revealed the stress related information of the wurtzite structured PAN/ZnO seed as well as PAN/ZnO needle. The stress in the material might have been originated due to the polymeric nanofibrous substrate and the associated high surface area. Investigation on local crystal structure (TEM) also supported the wurtzite structure and hinted oxygen deficiency in ALD -ZnO. However, as expected hydrothermally grown ZnO happened to be in single crystalline state and no multiple phases were observed in the FFT image. The origin of the defect and the oxygen deficiency can be identified with XPS rather precisely, where we have noticed that PAN/ZnO seed sample consists of O^{-x} type ions, while PAN/ZnO needle sample consists of –OH, –CO, H_2O or O_2 adsorbed at the defect site. The former further supports the grain boundaries of PAN/ZnO seed and less defective PAN/ZnO needle. Being very crucial for PCA, the results from PL suggested an oxygen deficient PAN/ZnO seed while the PAN/ZnO needles of relatively better optical quality. We note the consistency between the PL and XPS measurements. Based on the literature, various emission bands have been ascribed to their plausible origin. We have suggested a mechanism for the improved PCA of PAN/ZnO needle sample, when compared with PAN/ZnO seed. We have interpreted the PCA in conjunction with PL, where we point out the fact that oxygen vacancy captures a hole from the CB and hence the recombination process is delayed. Also this captured hole can take part in PCA as it is located within the grain boundary region. The improvement is attributed to the collective effect which enabled the active participation of defect state and the catalysis taking place at CB as well as VB. If photocatalysis consists of only defect related activity, or that takes place at CB and VB is not suffice to achieve higher PCA. On the other hand, the discussion on PCA assumes that the surface defects on nanoneedles are negligible at an acceptable level by given its crystallinity, and the relative intensity of visible emission has in fact subdued when compared to the UV emission. Furthermore, the samples are subjected to recycling and nominally the PAN/ZnO needle depicted a comparable performance with the fresh sample. Since the catalyst is synthesized on flexible polymeric

nanofibers, the membrane can be handled rather easily. (Figure 99). Finally it is convincing that these ZnO nanostructures are well suited and potential candidates for waste water treatment with solar energy where their performance, structural stability and reusability are worth mentioning.

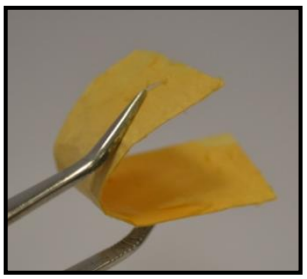

Figure 99. Representative photograph of the PAN-ZnO needle nanofibers showing the easiness in handling. (Copyright © 2014, Elsevier. Reprinted with permission from Ref.[157])

4.5. Role of Zinc Interstitials and Oxygen Vacancies of ZnO in Photocatalysis: A Bottom-up Approach to Control the Defect Density

4.5.1. Experimental

Materials: Polysulfone (PSU, M_w ~60,000) was purchased from Sp^2, Scientific Polymer Products, Inc. N, N-dimethylacetamide (DMAc, Sigma Aldrich, 99 %) was used as solvent. Methylene blue (MB, Sigma Aldrich, certified by the Biological Stain Commission) was employed in the catalysis study. In the ALD process, diethylzinc (DEZn, Sigma Aldrich) and HPLC grade water were used as zinc precursor and oxidant respectively. All materials were used as received.

Electrospinning of PSU fibers: PSU (35 wt %) in DMAc was rigorously stirred for 4 h at 60 ^{o}C to yield a homogeneous, clear yellowish solution. This solution when reached room temperature was taken into a syringe fitted with a metallic needle of 0.8 mm inner diameter. This syringe was fixed horizontally on a syringe pump (SP 101IZ, WPI) which was set to a feed rate of 0.75 mL/h. 15 kV bias was applied (Matsusada, AU Series) across the metal needle and the collector which were placed about 15 cm apart. The electrospun PSU fibers were collected onto an aluminum foil which was wrapped around a grounded metal electrode. The electrospinning process was performed in an enclosed chamber at 26 ˚C and 29 % relative humidity.

Atomic layer deposition (ALD) of ZnO on electrospun fibers: PSU fibers were subjected to ALD reactor (Savannah S100 ALD reactor, Cambridge Nanotech Inc.) at 200 ˚C. Exposure mode (a trademark of Cambridge Nanotech Inc.) is employed to deposit ZnO, in which the pump valve was closed during the pulse steps and opened during the purge steps of the ALD cycle. Pulse times of the Zn-precursor and oxygen source were both 0.015 s, which were waited in the chamber for 10 s. Then, pump valve was opened for purging using N2 at a flow rate of 20 sccm for 10 s. Using this procedure 100, 200, 300 and 400 ALD cycles were deposited. For the thickness estimation, same recipe and cycles were applied to a clean Si wafer.

Characterization: Scanning electron microscopy (SEM, FEI – Quanta 200 FEG) is performed on pristine PSU and ZnO coated PSU (PSU-ZnO) fibers after 5 nm thick Au-Pd sputter coating. Average fiber diameter (AFD) was calculated by measuring nearly 100 fibers from the SEM images. Spectroscopic ellipsometry (SE, Variable Angle Spectroscopic Ellipsometer, VASE© J.A. Woollam Co.) was employed to determine the thicknesses of the ZnO films on Si/SiOx wafer. SE spectra from ZnO films on Si/SiOx substrate were recorded at three angles of incidence (65˚, 70˚ and 75˚) within the wavelength range of 450-1200 nm. Cauchy dispersion function was employed to estimate the thickness of the ZnO film via Si/SiO_2/ZnO model where

the native oxide thicknesses of the Si substrates were measured through SE spectra. XRD patterns from pristine PSU and PSU-ZnO samples were obtained within the range of 2θ = 10^{o}-90^{o} by using PANalytical X'Pert Multi Purpose X-ray Diffractometer with Cu Kα radiation. Transmission electron microscopy (TEM, FEI – Tecnai G2F30) is also performed on the PSU-ZnO fibers, for which the fibers were dispersed in ethanol and a tiny droplet is dried on a holey carbon coated TEM grid. Selected area electron diffraction (SAED) patterns were also recorded. The surface composition of pristine PSU and PSU-ZnO fibers were determined via X-ray photoelectron spectroscope (XPS, Thermoscientific, K-alpha) equipped with a monochromated Al K_{α} X-ray source ($h\nu$ = 1486.6 eV) and flood gun charge neutralizer system. Avantage software is employed for the deconvolution of various peaks. Horiba Scientific FL-1057 TCSPC was used for the PL measurements performed at an excitation wavelengths of ~320, 330 or 350 nm. The interband transition is taken as reference and each of the spectra was normalized individually. Then these spectra were subjected to the deconvolution using Origin 6.1. The thermal properties of the PSU and PSU-ZnO fibers were investigated via thermogravimetric analyzer (TGA, Q500, TA Instruments) from RT to 700 ˚C at a heating rate of 20 ˚C/min under N_2 flow.

Photocatalytic activity (PCA) of the PSU-ZnO fibers: MB aqueous solution (18.8 μM) is the subject for the investigation of PCA of the PSU-ZnO fibers, and compared with the pristine and no catalyst cases. The samples (~11 mg) were immersed into MB solution in quartz cuvettes and exposed to UV irradiation (8 W, UVLMS-38 EL, 365 nm) from a distance of ~10 cm. The PSU and PSU-ZnO fiber were at the bottom of the cuvette during the experiment, and therefore did not interfere with the measurement. As a control experiment, the MB solution without any catalyst was subjected to the same UV treatment in order to compare with the catalyst case. The changes in the absorption peak of MB at 665 nm as a function of UV-irradiation time (t) were analyzed via UV-Vis-NIR spectrophotometer (Varian

Cary 5000). The concentrations of MB before and after UV irradiation are defined as C_0 and C respectively. The rate of dye degradation (C/C_0) is quantified with first order exponential fit ($y = y_0 + \alpha\ e^{-x/\tau}$) for each sample with an automated routine in Origin 6.1, where α-pre exponential factor, x- time axis, y- C/C_0 at different 't' and τ-decay constant. All the parameters are set as free (unless otherwise stated) until convergence.

4.5.2. Results and Discussion

PSU-ZnO fibers were fabricated via two-step process in which electrospinning is followed by ALD with varying cycle numbers (Figure 100). In the first step (Figure 100a), bead free PSU fibers were produced and then transferred to an ALD chamber (Figure 100b) to deposit ZnO for 100, 200, 300 or 400 ALD cycles. By varying the number of cycles, we have achieved QDs or NC on PSU fibers (Figure 100c). The PSU-ZnO samples obtained using various cycle numbers *viz* 100, 200, 300 and 400 ALD cycles will be referred as PZ1 QD, PZ2 NC, PZ3 NC and PZ4 NC respectively. As we go along we will see that this nomenclature is quite appropriate for each sample.

Polymeric structure can be easily deformed or degraded under the deposition of other materials via conventional chemical vapor deposition,[96] which require elevated temperatures. In contrast, ALD uses relatively lower temperature in which the substrate is exposed to two or more precursors separated by purging/evacuation periods (Figure 100b). Notably, ALD is a powerful tool to deposit ZnO and/or other inorganic layers on polymeric films [101] and fiber mats [101, 103, 105]. In this process the substrate is exposed to gaseous precursor molecules which do not react with themselves, and new surface sites are formed for the following precursor pulse [416]. The morphology of the pristine PSU and PSU-ZnO fibers was investigated via SEM. The optimized electrospinning parameters yielded bead-free fibers although

the surface of the fiber is noticeably rough (Figure 101a). After the ALD processing we have recorded SEM images for all cycle numbers and shown in Figure 101b-e. The fibers retained their structure after the ALD process in all cases, where it is notable that compatibility between the precursor and the substrate is vital [101, 123]. The initial stage of transformation of QDs into NC can be seen from the inset of Figure 101c, where the grains of ZnO are explicit. The AFDs of the PSU and PSU-ZnO fibers are summarized in Figure 101f and an obvious increase in the fiber diameter is noticed for higher ALD cycles, as expected. However, by given the standard deviation in the diameter measurement, we have estimated the thickness of the ZnO coating by other methods which will be discussed later.

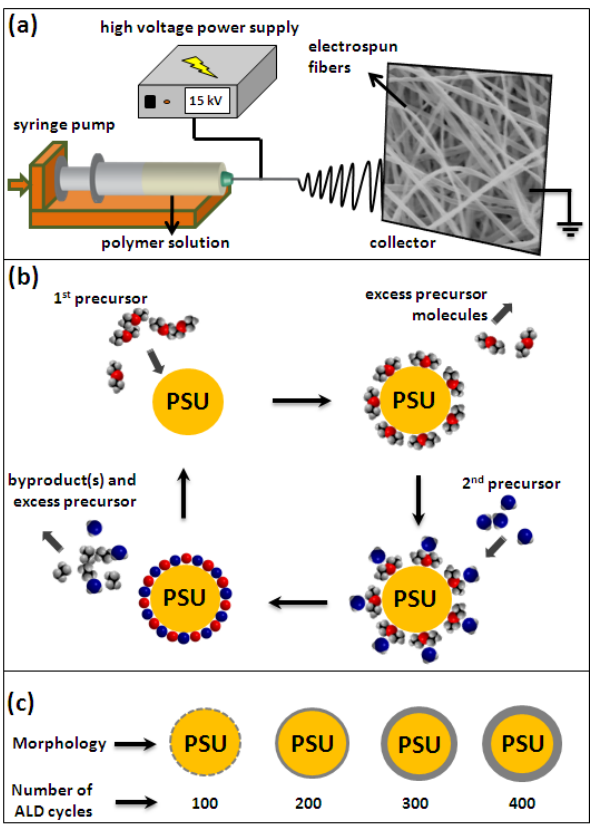

Figure 100. Schematic of (a) electrospinnig, (b) ALD and (c) the resultant morphology of the samples obtained applying different ALD cycle numbers. (Copyright © 2014, Royal Society of Chemistry. Reprinted with permission from Ref.[365])

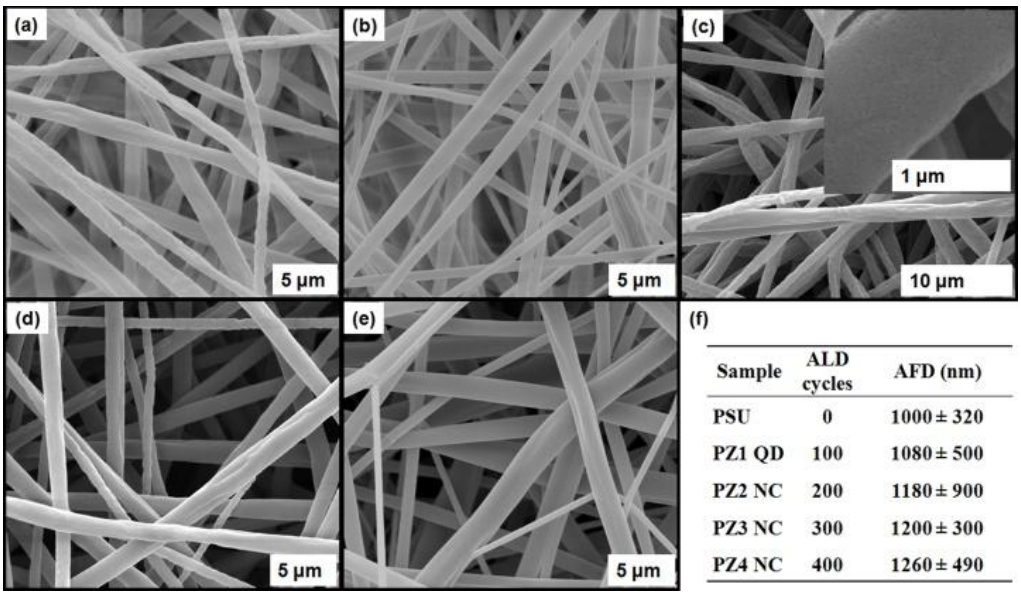

Sample	ALD cycles	AFD (nm)
PSU	0	1000 ± 320
PZ1 QD	100	1080 ± 500
PZ2 NC	200	1180 ± 900
PZ3 NC	300	1200 ± 300
PZ4 NC	400	1260 ± 490

Figure 101. SEM images of electrospun fibers of (a) pristine PSU, (b) PZ1 QD, (c) PZ2 NC, (d) PZ3 NC, (e) PZ4 NC and (f) average fiber diameters. (Copyright © 2014, Royal Society of Chemistry. Reprinted with permission from Ref.[365])

The morphologies of the PSU-ZnO fibers were further investigated by TEM (Figure 102). Figure 102a shows the QD formation on the surface of PSU fibers for 100 ALD cycles. In this sample, highly-dense ZnO QDs with an average diameter ~10 nm were homogenously distributed on the fiber surface (Figure 103). When the number of cycles was increased, the process yielded a continuous ZnO coating on PSU fibers of uniform thickness, *viz* for 200, 300 and 400 cycles see Figure 102b, c and d, respectively. Note the dark region at the edge of the fiber which represents the ZnO coating gets thicker with increasing ALD cycles. Therefore, ALD process with sufficient cycle numbers yielded conformal and layer-by-layer deposition of ZnO on PSU fibers [11, 123, 130, 153]. For cycle numbers ≥ 200, a continuous film is formed due to the coalescence of grains/islands. Figure 102e shows high resolution TEM image of PZ4 NC, where we can see the lattice fringes as well as grains grown in different lattice directions (see double arrows on figure). This grainy structure is consistent with the earlier observation for less number of ALD cycles. Left inset of

Figure 102e shows the lattice resolved image with a lattice spacing of ~2.23 nm, which represents the *c*-axis of ZnO. Furthermore SAED pattern from PZ4 NC is shown as right inset of Figure 102e, which indicates a polycrystalline sample. The diffraction planes are annotated on the image and found to be consistent with the literature [151, 168]. Furthermore, we have measured the thickness of ZnO coating from TEM images and determined to be ~43, 56 and 75 nm for PZ2 NC, 3 NC and 4 NC, respectively.

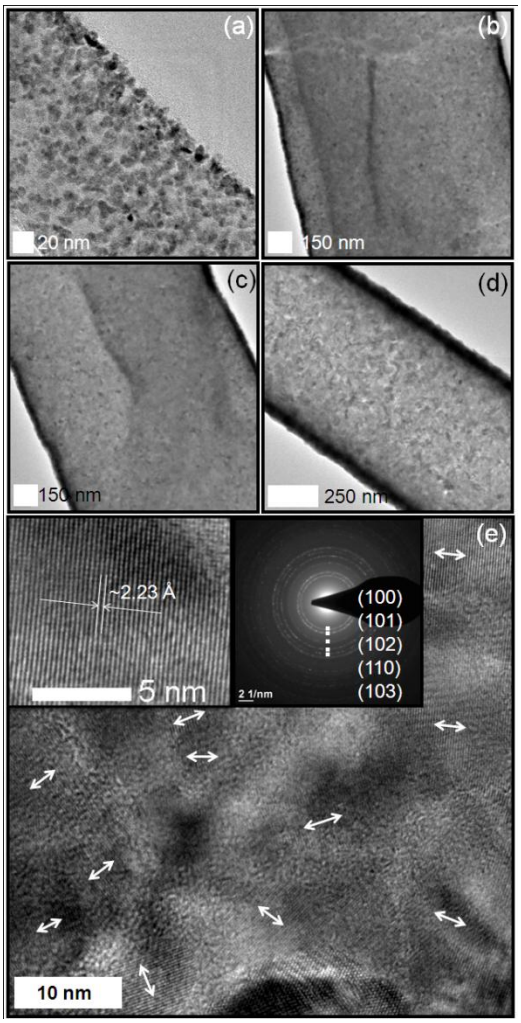

Figure 102. TEM images of (a) PZ1 QD, (b) PZ2 NC, (c) PZ3 NC and (d) PZ4 NC; (e) high resolution images and electron diffraction pattern from PZ4 NC. (Copyright © 2014, Royal Society of Chemistry. Reprinted with permission from Ref.[365])

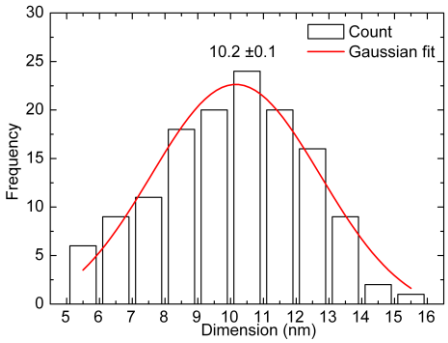

Figure 103. Particle size analysis from TEM image for PZ1 QD. (Copyright © 2014, Royal Society of Chemistry. Reprinted with permission from Ref.[365])

The ZnO shell thicknesses as a function of ALD cycle numbers are shown in Figure 104 for two contexts, namely, PSU-ZnO fibers and ZnO coating on silicon wafer. The former case is from TEM image analysis, while the latter from SE. We can see the consistency in both the methods, meaning the conformal coating of ZnO on the surface of the polymer fibers. Note that the thickness of the ZnO-shell on the fibers for 100 ALD cycles is not shown as it forms island like structure than a continuous film. A linear fit for the data points from TEM analysis yielded a growth rate of 0.20 nm/cycle where ALD should be acknowledged for the excellent control on the film thickness against deposition cycles [4, 130, 266]. On the other hand, SE from Si yielded 0.18 nm/cycle which is closely comparable with the results from TEM.

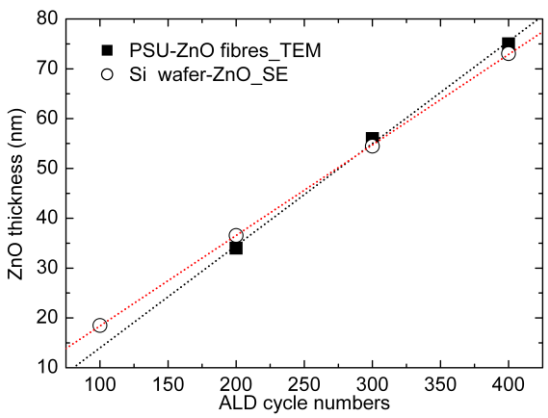

Figure 104. The thickness of ZnO as a function of ALD cycle numbers for two contexts, namely, PSU-ZnO fibers and ZnO coating on silicon wafer. (Copyright © 2014, Royal Society of Chemistry. Reprinted with permission from Ref.[365])

Figure 105 shows the XRD patterns from PSU-ZnO fibers of varying cycle numbers. Broadly, the diffraction peaks of ZnO were found to be wurtzite structure for all cases. Reflections corresponding to ZnO, *viz* (100), (002) and (101) planes (30-38°) are annotated as (i), (ii) and (iii) respectively and shown on Figure 105a. We observed that as the cycle number increases the peaks became sharper (see full width at half maximum, *fwhm* in Table 21) and more well defined. As we can see from Figure 105a (also see Table 21) a significant shift (δ°) is observed for all the three peaks (ICDD 01-074-0040) [151, 168]. In an earlier report [163] the authors have observed similar shift for (100) peak from the normal, where the shift is attributed to lattice defects. As outlined in the introduction we are interested in creating defects related to Zn_is, on the other hand, we note that lattice has gone through a 'strain' induced by defects. Hence it is important to establish if we can expect defects of Zn_i origin in the present samples. In the earlier study,[163] the defects are induced by non equilibrium process, which are sensitive to temperature and can only withstand low temperature annealing [417]. Vlasenko et al. suggested that Zn_is are not stable unlike V_Os which are stable up to ~400°C [373]. In line with this, results from a simulation study also suggested that Zn_is diffuse faster than V_Os where the migration barriers are 0.57 eV and 1.7 to 2.4 eV, respectively [374]. While keeping this in the background, we can see that the other reflections, (002) and (101) have also shown some nonlinear deviation. These features indicate that the as-prepared samples (PSU-ZnO) are rich in some kind of defects induced during the ALD process. Since the present deposition temperature is about 200°C, the defects such as Zn_is are stable as shown by other researchers [373-374]. As we go along we will see that these defects are actually interstitial zinc. Various other diffraction planes within 45-90° are annotated on Figure 105b and found to be consistent with the literature [151, 167-168]. As the cycle number increases (300 and 400) we can see that the peaks (200), (112) and (201) have been evolved to be clearer and well-defined when compared to PZ1 QD and PZ2 NC samples. Furthermore, we have also observed a single peak for pristine PSU at 17.9° due to the semi-crystalline nature of the PSU fibers (Figure

106). As the cycle number increases, this peak is relatively extinguished (not shown here) as it is screened by the inorganic (ZnO) coating. However, it is notable that ALD did not significantly influence the crystalline nature of PSU, where we note the deposition has taken place at 200˚C.

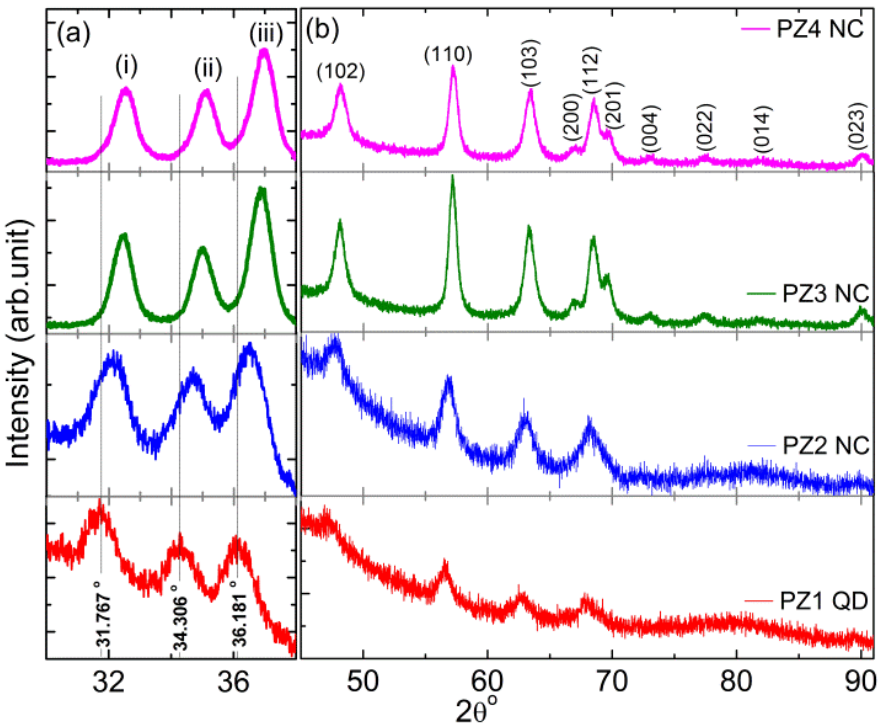

Figure 105. XRD patterns from PZ1 QD, PZ2 NC, PZ3 NC, and PZ4 NC within (a) 30-38˚and (b) 45-90˚regions. (Copyright © 2014, Royal Society of Chemistry. Reprinted with permission from Ref.[365])

Table 21. XRD characteristics of three selected peaks (Copyright © 2014, Royal Society of Chemistry. Reprinted with permission from Ref.[365])

Sample	(i)˚ **(100)**		(ii)˚ **(002)**		(iii)˚ **(101)**	
	FWHM	δ	FWHM	δ	FWHM	δ
PZ1 QD	1.239	-	1.055	-	1.135	-
PZ2 NC	1.150	**0.330**	0.983	**0.379**	0.957	**0.270**
PZ3 NC	0.680	**0.679**	0.646	**0.709**	0.713	**0.737**
PZ4 NC	0.759	**0.740**	0.667	**0.804**	0.751	**0.802**

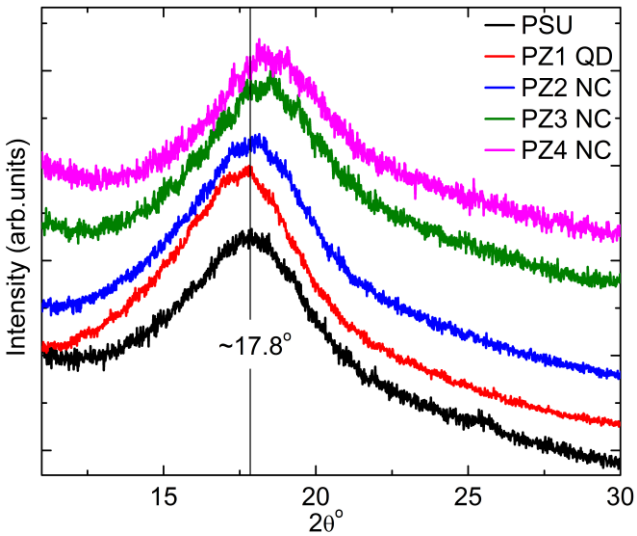

Figure 106. XRD patterns for pristine and ZnO coated samples within the region of ~10-30˚. (Copyright © 2014, Royal Society of Chemistry. Reprinted with permission from Ref.[365])

The core-level XPS spectra of O 1*s* and Zn 2*p* are shown in Figure 107 and Figure 108 respectively. O 1*s* spectra have been deconvoluted for all the cases depending on the chemistry of the surface. The spectral location of the deconvoluted peaks match with the literature [418]. Pristine PSU has shown two principle peaks corresponding to two oxygen molecules in different chemical environment (O/S and O/C) where O/S and O/C represent the oxygen bonded to sulfur or carbon respectively (Figure 107a) [418]. In PZ1 QD sample we can observe oxygen from ZnO (O/Zn) and PSU owing to the absence of continuous ZnO layer on the PSU fibers as evidenced from TEM images. All the deconvoluted spectra suggested the presence of chemisorbed oxygen (O_{Ch}, shaded area on the figure). This O_{Ch} can be from any of the species such as –OH, –CO, adsorbed H_2O and/or O_2 (ref. [100, 153, 157, 404]) or O^- and O^{-2} ions [153, 157]. The area under the peak corresponding to O_{Ch} is annotated on the image. If we keep aside the O_{Ch} of PSU, the origin of such species for the PZ1 QD is at higher binding energy than the other PSU-ZnO cases. This is not surprising because ZnO has not completely covered the surface of PSU

which means that the peak in the spectrum is the sum of two contributions. O_{Ch} from PZ1 QD has shown an area of 0.28 eV·cps, while the other PSU-ZnO samples have shown an average value ~0.42 eV·cps. In the case of ZnO, the quantity of O_{Ch} is a measure of V_Os,[153, 157, 168] as the former occupies the place of the latter in the lattice. Hence the density of V_Os is increased with the thickness of ZnO or with the ALD cycle numbers (≥ 200). We will refer to the density of V_Os and their effect on emission properties in the context of PL.

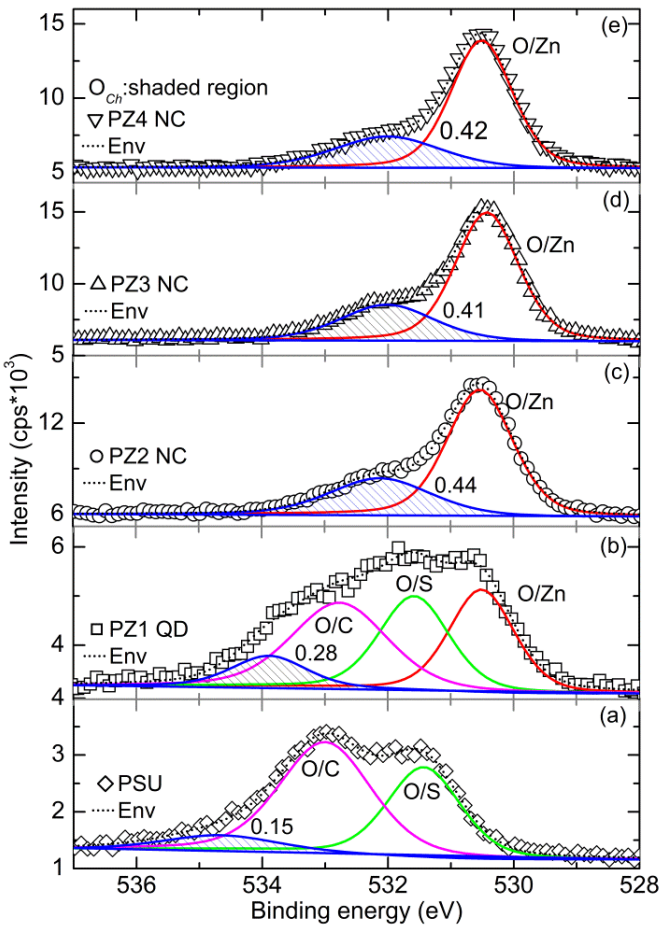

Figure 107. Core-level XPS analysis for O 1*s* from PSU, PZ1 QD, PZ2 NC, PZ3 NC and PZ4 NC samples. The area under the shaded peak corresponding to chemisorbed oxygen (O_{Ch}) is annotated on the image in the units of eV·cps. (Copyright © 2014, Royal Society of Chemistry. Reprinted with permission from Ref.[365])

Zn 2*p* core level spectrum is important to study, especially when we suspect the interstitial defects related to zinc. The spectra in Figure 108 are broadly similar across all samples and the spectral position of each peak is consistent with literature conforming the formation of ZnO [418]. However, a closure inspection of spectrum from PZ1 QD sample has shown shoulder like feature at higher energy side of Zn $2p_{3/2}$ and Zn $2p_{1/2}$ peaks (see the shaded area in Figure 108a). The energetic location of these shoulders (1024.19 and 1047.11 eV) suggests that the zinc is in its more oxidized form than ZnO. Note that this does not correspond to Zn $(OH)_2$, in which case $2p_{3/2}$ peak should occur in between 1022.70-1021.80 eV [418]. This is an important observation, where the Zn atom has taken an interstitial site and surrounded by more than one oxygen atoms at the same time. This can be treated as a direct evidence for the presence of Zn_is and on the other hand, we may also expect some V_{Zn} defects about which we will discuss in the context of PL in detail [163]. We did not see any shoulder or like features in the spectra of Zn 2*p* from PZ2 through PZ4 NC samples (Figure 108b, c and d). We believe that the surface adsorption during the ALD process has taken its toll and shown a significant effect. Initially, DEZn is adsorbed on the surface of PSU and then H_2O vapor arrives to react. However, the adsorption of H_2O on the surface of PSU is not uniform, as it has two functional groups one of which is more hydrophilic (O=S=O) than the other (C-O-C). Hence the molecular adsorption of H_2O varies from place to place on the surface. As the cycle number increases, the surface is coated with ZnO which leads to the change in the surface chemistry and we can expect more uniform adsorption of precursor molecules. In the initial cycles, the uneven distribution of molecules on the surface of PSU would have caused the growth of ZnO with dominating Zn_i related defects. Nevertheless, it does not necessarily mean that Zn_is are not present for the higher cycle numbers, as we will see in the context of PL. However the lack of signal from Zn_is might be due to increased Zn signal contribution from ZnO.

In the discussion of O_{Ch} (or V_Os), it is noted that PZ1 QD possesses the least amount of V_Os while Zn 2*p* analysis suggests that it has higher amount of Zn_i related defects. As the thickness of ZnO coating increased (≥ 200 ALD cycles) Zn_i related defects were not detected, while simultaneously O_{Ch} signal was increased. Finally, for the first 100 ALD cycles Zn_is are seen with limited V_Os; as the thickness of ZnO increases, although the presence of Zn_is is not explicit, the density of V_Os is definitely increased. In other words, V_Os and Zn_is are predominant in thicker and thinner coatings, respectively.

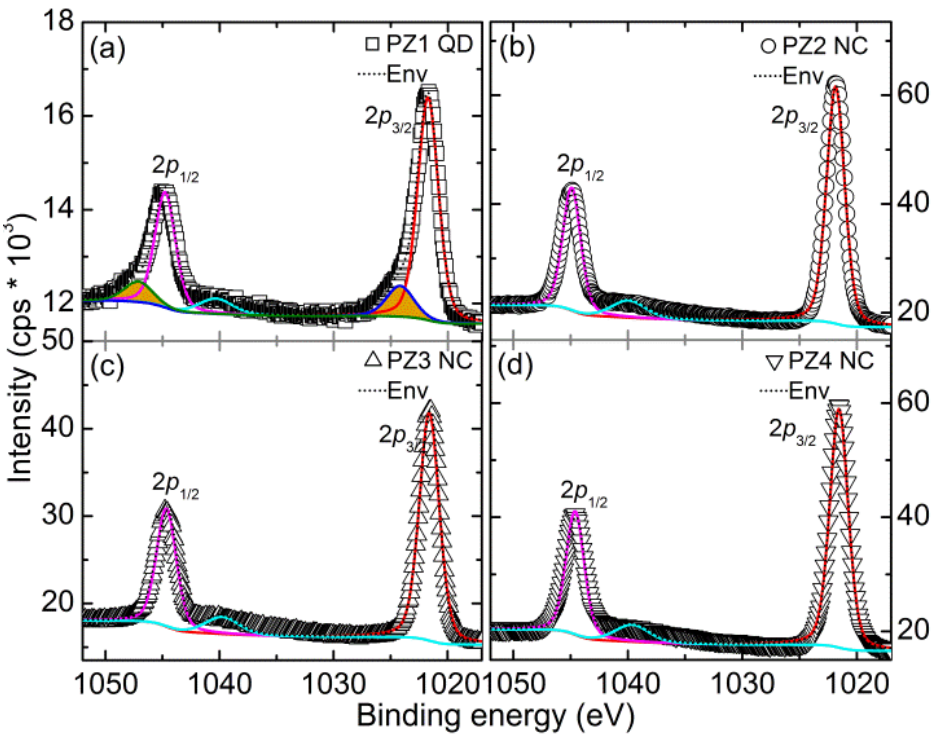

Figure 108. Core-level XPS analysis for Zn 2*p* from PZ1 QD, PZ2 NC, PZ3 NC and PZ4 NC samples. (Copyright © 2014, Royal Society of Chemistry. Reprinted with permission from Ref.[365])

The PCA of any semiconductor can be understood by carefully analyzing the optical properties [153, 157] where the information about the radiative recombination

centers (other than CB) associated with crystal defects would be revealed. As it mentioned in Introduction Chapter (1.4), which defect (Zn_i or V_O) dominates in native, undoped ZnO is still under debate [163]. To emphasize, in the present case, the density of Zn_i is controlled by simply altering the ALD cycle numbers for which researchers have used non-equilibrium processes [163, 375-376] followed by thermal annealing to control the defect density, in contrast we will see that as prepared samples possesses defects such as Zn_is. Zn_is come from Frenkel reaction, Eq (1), and further ionization reactions, Eq (2) and (3).

$$Zn_{Zn} \Leftrightarrow Zn_i^* + V_{Zn}^* \quad (1)$$

$$Zn_i^* \Leftrightarrow Zn_i^+ + e^- \quad (2)$$

$$Zn_i^+ \Leftrightarrow Zn_i^{++} + e^- \quad (3)$$

Blue emission from ZnO nanoparticles has been explained earlier by H. Zeng et al.[163] in which Zn_i are at the core of the emission. Furthermore, extended states of Zn_i (ex-Zn_is) can be formed according to the defect ionization reaction, equations (2) and (3), and can result in defect localization coupled with a disordered lattice. It is notable that blue emissions are quite infrequent [163] for the as-prepared samples when compared with the literature [150-151, 167-168, 406, 419-420]. To note, Zn_i is 0.22 eV below the CB,[172] V_{Zn} is 0.30 eV above the VB [407-408, 421] and ex-Zn_is are 0.54 to 0.635 eV below the CB [163] in ZnO for a typical band gap of 3.36 eV [151]. As mentioned earlier, the other set of major defects are V_Os, which have been addressed in the literature extensively, see the discussion and cross-references in Ref [151]. Despite of various interpretations, previous studies [150, 173] are found to be rather useful in which the energetic location of V_Os has been confirmed through an indirect method. Based on this, V_O^+ state captures an *electron* from CB and forms a neutral state (V_O^*), from which a transition to VB takes place emitting green light of ~500 nm wavelength, Eq (4) [150-151, 173]. On the other hand, V_O^+ captures a *hole*

from VB and forms a V_O^{++} state into which an *electron* recombines from CB and emits green light of ~565 nm wavelength, Eq (5).

$$V_O^* \Leftrightarrow V_O^+ + e^- \qquad (4)$$

$$V_O^{++} \Leftrightarrow V_O^+ + h^+ \qquad (5)$$

To note, V_O^* is ~0.86 eV below the CB and V_O^{++} is 1.16 eV above the VB,[173] for a typical band gap of 3.36 eV with an exciton binding energy of 60 meV [151]. The processes described in Eq (4) and (5) take place in bulk grain region (BGR) and depletion region (DR) respectively.

Based on the above discussed defects and their energetic location within the band gap, the present PL spectra were deconvoluted and shown in Figure 109a and the possible emission mechanism is schematized in Figure 109b. Numerals (1) through (5) represent PCA that can take place at different places. Emissions from ZnO, $a_{1\text{-}4}$, $b_{1\text{-}4}$, $c_{1\text{-}4}$, $d_{1\text{-}4}$ and $e_{1\text{-}4}$ in Figure 109a correspond to the transitions *a*, *b*, *c*, *d*, and *e* in Figure 109b. The spectral location of each peak (in eV and nm) is tabulated in Table 22, along with the emission mechanism. Before we discuss about the various emission lines, it would be appropriate to mention about the fluorescence peak of PSU, from PZ1 QD sample on which the ZnO coating is not continuous. We have employed 350 nm excitation (λ_{Ex}) for analyzing the emission from ZnO for which PSU has shown a shoulder like structure; see the normalized emission spectra for three different excitations in Figure 110. By considering the shape of the emission, Lorentzian fit is employed for PSU, and we can see a perfect retrace of the data points on Figure 109a (top left panel), which peaked at ~363 nm (*P'*) for 320 nm excitation. Keeping this in the background, in the case of PZ1 QD, during the deconvolution the spectral location of this peak is fixed (*P''*) and the other parameters are allowed vary, where the excitation wavelength is 350 nm. As mentioned earlier, in the case of ZnO, the peak attributions and their wavelengths are still under severe

discussion,[163] however, the present assignments were performed based the available evidence in the literature while placing a logical approach for the cases where more than one transition is feasible. Also refer to the schematic diagram Figure 109b, for each transition that is described below.

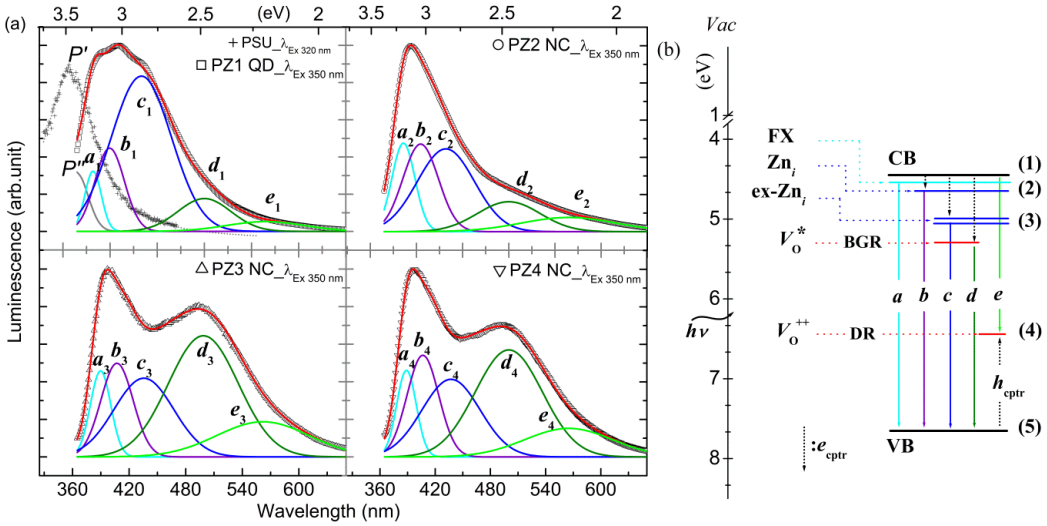

Figure 109. (a) Luminescence spectra from electrospun fibers of PSU and PZ1 QD, PZ2 NC, PZ3 NC, and PZ4 NC. (b) Schematic diagram depicting the various defects and the ascribed transition. (Copyright © 2014, Royal Society of Chemistry. Reprinted with permission from Ref.[365])

The least controversial emission from interband transition occurred in the range of 382-390 nm ($a_{1\text{-}4}$) for all samples, where an *electron* from free exciton (FX) level recombines with a *hole* in VB. FX and Zn_i are 0.06 eV and 0.22 eV below the CB respectively,[172] while ex-Zn_is are 0.54 to 0.635 eV below the CB [163]. V_O^* is ~0.86 eV below the CB and V_O^{++} is 1.16 eV above the VB,[173] for a typical band gap of 3.36 eV (ref.[151]) The CB and VB locations are taken from Ref [422]. The blue region of the emission contains two probable transitions related to V_{Zn} and Zn_i, i.e. *electron* from CB recombines with the *hole* at V_{Zn} or an *electron* is captured by Zn_i then recombines with *hole* in VB. Either or both of these transitions take place emitting $b_{1\text{-}4}$ [151, 172, 421]. After a careful inspection it appears to be the case that

the observed emission ($b_{1\text{-}4}$) should be ascribed to $Zn_i \rightarrow$VB transition, as we have noted interstitial zinc in the XPS, at least for PZ1 QD case. In 2010 a study by Zeng et al.[163] introduces probable transitions from Zn_i or ex-Zn_is to the VB, while an earlier investigation in 2009 by Ahn et al. which suggests transitions form Zn_i to V_{Zn} states [172]. Further complicating the attribution, in our case both the arguments have a reasonable over lap within blue wavelength region, $c_{1\text{-}4}$ (Table 22). In the discussion given by Zeng et al,[163] *electrons* from CB are relaxed to Zn_i (in line with Ahn et al.[172]) and/or ex-Zn_i via non-radiative process and then to VB via emitting violet and/or blue emissions respectively. On the other hand, Ahn et al.[172] suggest two transitions from Zn_i to VB and/or V_{Zn}, nevertheless, in the present context this description might not be feasible, because as we have evidenced Zn_is through XPS. Hence the peaks, $c_{1\text{-}4,}$ are attributed to ex-Zn_i to VB transition, as the dominant Zn_is can form extended states. Finally, the green emission occurs due to V_Os constituting two transitions [150, 168, 173] as shown in Table 22. These transitions are annotated with $d_{1\text{-}4}$ and $e_{1\text{-}4}$ in the Table 22 fall within 498-501 nm and 562-566 nm, respectively. The spectral locations of all of the above mentioned peaks are quite consistent with the literature [150-151, 153, 163, 167-168]. It is clear that the present samples possess defects such as Zn_is and V_Os, however, in the following we will consider the relative densities (integrated area of the peak) of each transition that is ascribed in Table 22. Such comparison is found to be very useful by us in explaining the PCA earlier [153, 157].

To start with, $a_{1\text{-}4}$ are supposed to be sharp and intense for defect free ZnO,[151] also see cross-references therein. However in the present case the *fwhm* does not vary significantly across all samples. While the area under the peak (A) seemed to improve from PZ1 QD to the rest of the samples indicating slightly improved optical quality [151, 167-168]. The next region to consider is violet emission, $b_{1\text{-}4}$, where the *fwhm* is almost same for all samples. Further, PZ1 QD has shown lowest A, which nominally increased with the ALD cycle numbers. The blue

emission, $c_{1\text{-}4}$, has shown interesting features, where the *fwhm* is almost similar for all sample, in contrast *A* is almost twice for PZ1 QD when compared to other PSU-ZnO samples. It will be more contextual to discuss the reason for this difference after addressing the rest of the emissions. We can see that *fwhm* of $d_{1\text{-}4}$ increased with the ALD cycle numbers while, *A* is comparable among the samples set wise, PZ1 QD and PZ2 NC; PZ3 and PZ4 NC. In the case of PZ1 QD and PZ2 NC the thickness of the ZnO is not more than ~40 nm, while the transitions d_1 and d_2 take place in the BGR. Since the grains are not completely formed for such thicknesses, the intensity of the transition is comparatively low. In the context of d_3 and d_4, there is a significant increase in the thickness which has led to the formation of high density BGRs emitting relatively higher intensity green light, thereby higher *A*. Peak *e* occurs from the DR, in which case the argument given for $d_{1\text{-}4}$ is still valid (Figure 109b). At lower thickness values, the density of V_Os is relatively less, especially with PZ1 QD. Thereby it is clear that the capture of electrons by V_O^+ state is almost negligible; hence a predominant emission is noticed for c_1 with *A* value of ~67 nm·counts which is almost the double intensity of $c_{2\text{-}4}$.

Table 22. Spectral locations of deconvoluted peaks and ascribed emission mechanism. The wavelength of the emission is given in nm, and eV for convenience.

Sample	Interband (nm, eV)	V_{Zn} or Zn_i related (nm, eV)		V_O related (nm, eV)	
PZ1 QD	382, 3.25 **(a_1)**	400, 3.10 **(b_1)**	433, 2.86 **(c_1)**	501, 2.47 **(d_1)**	564, 2.20 **(e_1)**
PZ2 NC	386, 3.21 **(a_2)**	404, 3.06 **(b_2)**	432, 2.87 **(c_2)**	498, 2.49 **(d_2)**	565, 2.20 **(e_2)**
PZ3 NC	390, 3.18 **(a_3)**	407, 3.04 **(b_3)**	436, 2.85 **(c_3)**	499, 2.49 **(d_3)**	562, 2.21 **(e_3)**
PZ4 NC	389, 3.19 **(a_4)**	407, 3.04 **(b_4)**	437, 2.83 **(c_4)**	500, 2.48 **(d_4)**	566, 2.19 **(e_4)**
Mechanism	$\mathbf{FX} \xrightarrow{395\ nm} \mathbf{VE}$	$\mathbf{Zn}_i \xrightarrow{395\ nm} \mathbf{VB}$ $\mathrm{CB} \xrightarrow{405\ nm} V_{Zn}$	$\mathbf{ex\text{-}Zn}_i \xrightarrow{440-455\ nm} \mathbf{VB}$ $\mathrm{Zn}_i \xrightarrow{437\ nm} V_{Zn}$	$V_O^* \xrightarrow{500\ nm} \mathbf{VB}$	$\mathbf{CB} \xrightarrow{564\ nm} V_O^{++}$

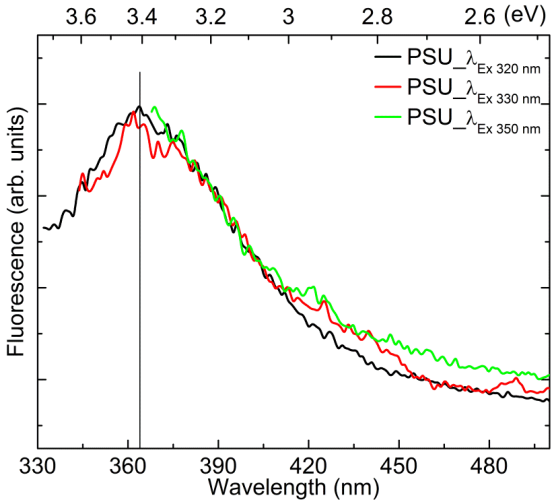

Figure 110. Emission spectra from pure polysulfone electrospun nanofibers for three different excitations. (Copyright © 2014, Royal Society of Chemistry. Reprinted with permission from Ref.[365])

Finally, to comment on the overall defect density and their predominance, the emission due to V_Os is gradually increasing where the intensity due to Zn_i is almost stable. This is very significant finding [163] where it is believed that the obtaining a balance between V_Os and Zn_is is rather hard task, i.e. if the density of Zn_i increases than that of V_Os decreases.

To further justify the existence Zn_is, their origin and their balance against V_Os needs to be considered. The relative concentration of these defects is strongly dependent on formation temperature as their ionization energies lie in the range of ~0.05 to 2.8 eV [373]. In the case of vapor phase deposition, the partial pressure and their relative pressures of zinc and oxygen are also found to be vital [377, 423] and as expected under highly reducing environment together with high temperatures causes V_Os to dominate [377] or under zinc rich environments Zn_is are the predominant defects. Under high temperature (~1100˚C) annealing of ZnO crystals depicted Zn_is [381]. Therefore, the chosen parameters of ALD has yielded high densities of Zn_is, where the duration of the precursor pulse, substrate and its temperature are believed to be detrimental.

Since we have employed different cycle numbers to manipulate the morphology, the amount of ZnO is quantified from TGA thermograms (see Figure 111). The weight percentages of ZnO in the PSU-ZnO fibers were calculated by subtracting the char yield (%) of the pristine PSU fibers at 700˚C yielding 10, 14, 19 and 25 % in PZ1 QD, PZ 2 NC, PZ 3 NC and PZ4 NC respectively.

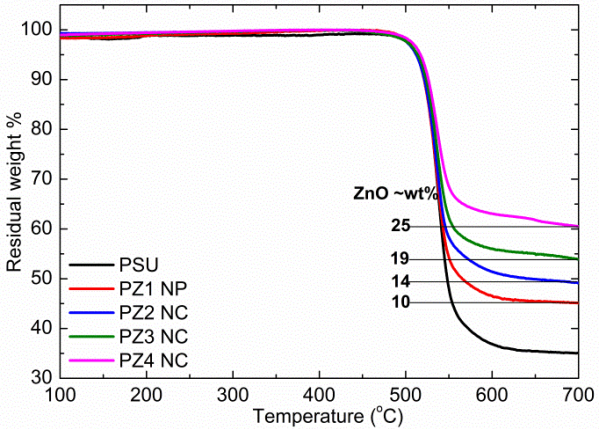

Figure 111. TGA of PSU-ZnO samples compared with pristine case. (Copyright © 2014, Royal Society of Chemistry. Reprinted with permission from Ref.[365])

PCA on MB in the presence of PSU-ZnO samples was tested under UV-illumination of 365 nm wavelength; as a result, *electrons* are excited to CB rather any defect sites. The degradation of MB (C/C_0) as a function of 't' is plotted in Figure 112a. We have observed exponential decay behavior which falls into pseudo-first-order kinetics as explained by Langmuir-Hinshelwood model. Note that the degradation follows [138] Langmuir sorption isotherms,[424] in which organic molecules are adsorbed on the surface as a monolayer at a distance of 1 Å.

In the no catalyst and PSU cases no degradation is observed within the UV exposure, in contrast, PSU-ZnO samples have shown a finite decay time of varying spans (Figure 112a). The ·OH radical formation at VB, CB and defect sites have already mentioned in Chapter 1 (1.4). In PCA on the surface of ZnO, the defect sites play a crucial role in trapping the charge carriers. Please refer to Figure 7b for the energetic location of each defect with reference to CB and VB of ZnO, where the active sites for PCA are indicated with numerals, (1) through (5). Zn_i, and ex-Zn_i can capture *electrons* from CB and can take part in PCA. Although V_O^* exists in the bulk

of the grain, however, it depicts indirect effect by capturing an *electron* from CB there by delaying the recombination process. Hence due to V_O^*, PCA takes place at VB via *hole*. On the other hand V_O^{++} exists in the DR, which may be available for PCA, showing enhanced effect when compared to V_O^*. This is because V_O^{++} can be on the surface or at grain boundaries where the captured *hole* and the delayed *electron* at CB can participate in PCA.

As mentioned in the introduction, we aim to elucidate the effect of Zn_is and V_Os on the PCA. In order to achieve this we have compared the activities and the percentage increase for each defect density (area under the peaks of $a_{1\text{-}4}$ through $e_{1\text{-}4}$ corresponding to each defect type) is calculated (please refer to the description in the Table S2 legend of ESI) with reference to PZ1 QD which were correspondingly annotated as primed alphabets (Figure 112b). Also note that if *electron* is captured by a defect, the associated *hole* at VB takes part in catalysis. Conversely, if *hole* is captured by a defect then, *electron* in CB can take part in catalysis. The percentage decrease in τ is also calculated with reference to that of PZ1 QD ($[\tau_{PZ1\ QD}\text{-}\tau_{PZ2,\ 3\ or\ 4\ NC}]*100/\tau_{PZ1\ QD}$) and shown on Figure 112c. By taking into account of the discussion on relative densities of various defects, in the following we will attribute the difference in τ for PSU-ZnO samples referring to Figure 112b and c. Notably, PZ1 QD has shown longer τ than the others (Figure 112a). However, the percentage decrement of τ suggests an improvement in performance of ~77 % for PZ2 NC. This increment is cumulative from various defects as expected. PZ1 QD is predominant with ex-Zn_is hence the PCA takes place at (2) and (3) in addition to (1) and (5) (Figure 112b). In the case of PZ2 NC, Zn_is are as dense as PZ1 QD sample while ex-Zn_i states are subdued. On the other hand *a'* and *e'* are almost doubled, which enhance the PCA at (1), (5) and (1), (4) respectively. b_2 emission is slightly improved while ignoring that of d_2. Hence, majorly the ~77 % improvement is a sum effect of contribution from *a'* [(1), (5)], *e'* [(1), (4)] and *b'* [(2), (5)] in that order. If similarly argued, the following conclusions can be drawn for the rest of the samples. PZ1 QD to PZ3 NC an improvement of ~80 % is noticed. This is a sum effect of contribution from *e'* [(1), (4)], *d'* [(5)], *a'* [(1), (5)] and *b'* [(2), (5)] in that order. Finally, PZ1 QD to PZ4 NC an improvement of ~88 % is noticed which is a sum effect of contribution

from *e'* [(1), (4)], *d'* [(5)], *a'* [(1), (5)] and *b'* [(2), (5)] in that order. As discussed earlier, the physical location of V_Os suggests that for the same defect levels of *e'* and *d'*, the former shows higher PCA than the latter. By given the overall scenario, the important thing to note is that the PCA is not severely affected by defect density above a certain degree. For example, PZ1 QD to PZ3 NC, the net increase in the defect density is nearly 770 %; however, the PCA has shown an improvement from 77 to 80 %. On the other hand, PZ1 QD to PZ2 NC, the net increase in the defect density is 200 % which has shown 77% improvement in PCA. Although the ex-Zn_is have subdued, the increased optical quality and V_O^{++} states have shown an improvement of 77 % in PCA, which is a significant finding. Despite of such great contribution from V_Os it is notable that further increase in their density did not help to enhance the PCA. However, it is convincing that V_Os enhance the PCA, [144, 153, 157-159, 161] which can probably dominate the contribution from Zn_is and/or ex-Zn_is. This is because of the differences in the intrinsic nature of the defects. From equations (1) through and (5) it appears that both the Zn_i and V_Os can form ionized levels, however in the earlier explanation by Zeng et al.[163] there is no discussion on charged zinc interstitials forming defect bands within the band gap. In clear contrast to this, V_Os form two defect levels [150, 173, 409-410] within the band gap by following the equations (4) and (5). Among these two bands although one is not directly accessible for PCA, it shows an indirect effect by capturing an *electron* from CB. Furthermore, equation (5) is feasible [150, 173] in the DR of the semiconductor, where the obvious places on the surface are the grain boundaries. As the thickness increases, initially grains take shape along with grain boundaries where the latter are very favorable places for the dye to adsorb. As evidenced in XPS, V_Os are occupied by oxygen related functional groups, which can be, for example, –OH, H_2O and/or O_2. These species can participate and/or mediate the PCA directly. Although the point of zero charge for ZnO is 9.0 ± 0.3, due to the predominance of V_Os the surface of ZnO can be negatively charged in the presence of –OH groups, which are more favorable for the cationic dye like MB. In the present context we did not consider the pH of the solution and its effects. Also note that the PCA involving H_2O is associated with h_{VB}^+ forming the most reactive hydroxyl radical (E^0 = +3.06 V) where the *holes* can be captured by V_O^+. In our earlier study [153] we have given further explanation

why *holes* are more reactive than *electrons*. Hence by given the above reasons, it is concluded that Zn_is are less reactive than V_Os.

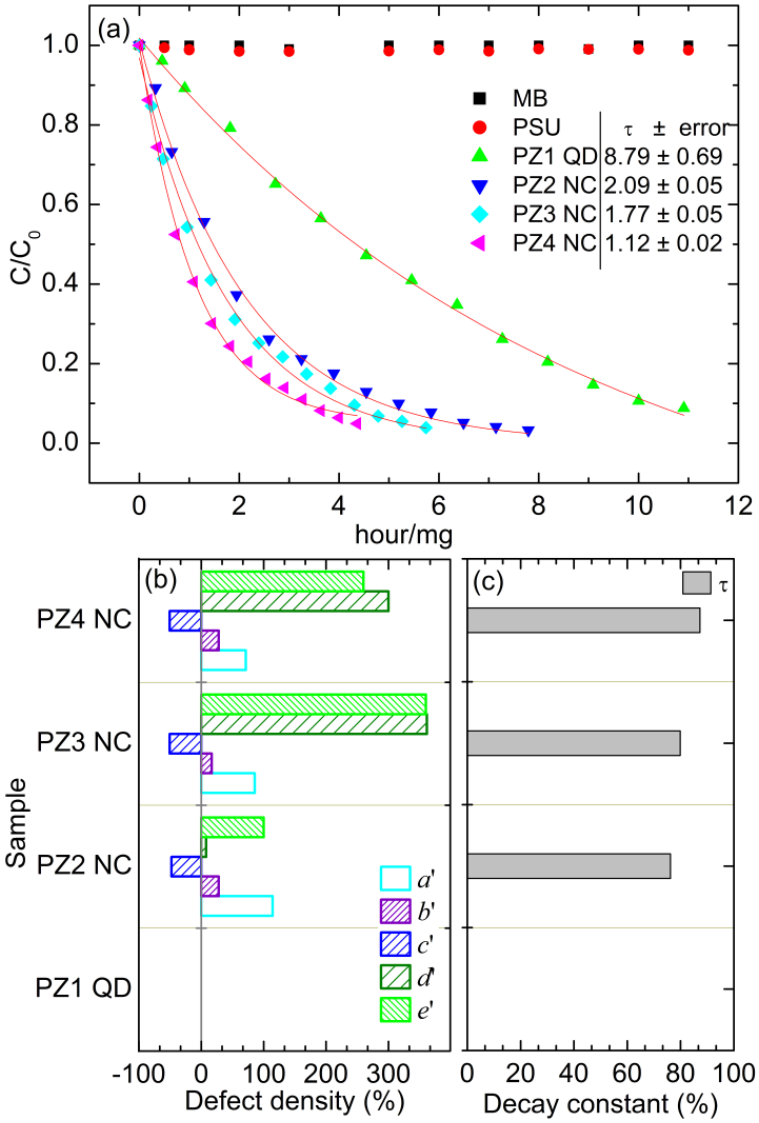

Figure 112. (a) PCA of various samples compared with pristine PSU and no catalyst cases, (b) densities of various defects and (c) improvement in decay constant are referenced with PZ1 QD case and shown in percentage. (Copyright © 2014, Royal Society of Chemistry. Reprinted with permission from Ref.[365])

4.5.3. Conclusions

We have fabricated ZnO QDs on the surface of electrospun PSU fibers and carefully investigated the changes in the properties when QDs transform into NC when ALD cycles are increased. Since polymers are known for their flexibility, PSU-ZnO fibers were no exception in ease handling, as shown in Figure 113.

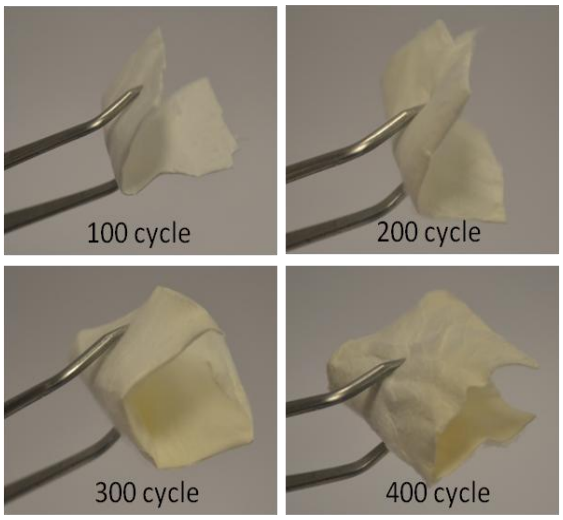

Figure 113. Digital photographs showing the convenience in handling the ZnO coated fiber mats. (Copyright © 2014, Royal Society of Chemistry. Reprinted with permission from Ref.[365])

The morphological characterization suggested that the ALD precursors and PSU are well compatible. The growth rate of ZnO film is determined to be ~0.2 nm/cycle. The morphological transformation has shown significant variance in the crystal and optical properties of the samples. The average size of the ZnO QDs is determined to be around 10 nm from TEM micrograms. SAED patterns were recorded and a representative pattern to be identified as polycrystalline ZnO. Apart from the confirmation of wurtzite structure, the XRD data suggested that the samples have suffered from severe strain, which might be due to the intrinsic lattice defects. XPS has evidenced Zn_i related defects quite explicitly for PZ1 QD sample. This is because of non-uniform molecular adsorption of H_2O vapor on surface of PSU to react with DEZn. The PL spectra are recorded for all the samples, and the probable transitions are recognized based on the available evidence in line with literature.

Interestingly, PZ1 QD has shown nominal signature of V_Os from XPS which is consistent with PL data. Significantly, the increase in the density of V_Os occurred for higher ALD cycle numbers, *viz* ≥ 300 for almost the same density of Zn_is. The PCA experiment is performed on the samples which depicted pseudo first order kinetics. The decay constant is estimated for all PSU-ZnO samples via first order exponential fit. The fitting outputs of PL spectra are employed to estimate the relative densities of Zn_is and V_Os by considering the area under each peak corresponding to the defect related transitions. The percent improvement in PCA is juxtaposed against the defect densities. The results suggest that Zn_is and related defects are less efficient than V_Os in the context of photocatalysis. This is mainly because of the accessibility of these defects for the PCA. Both of Zn_i and V_O capture charge carriers thereby delaying the recombination process, however, the intrinsic nature of V_O allow them to exist in the grain boundaries (V_O^{++}) where the region is depleted with charge carriers and in the bulk of the grain (V_O^{*}). Trapped *hole* at V_O^{++} consequently an *electron* is delayed at CB can participate in the PCA in addition to delayed hole at VB due to V_O^{*}. This double effect is not seen in the case of Zn_is which makes them less efficient when compared to V_Os. Figure 114 summarizes our findings.

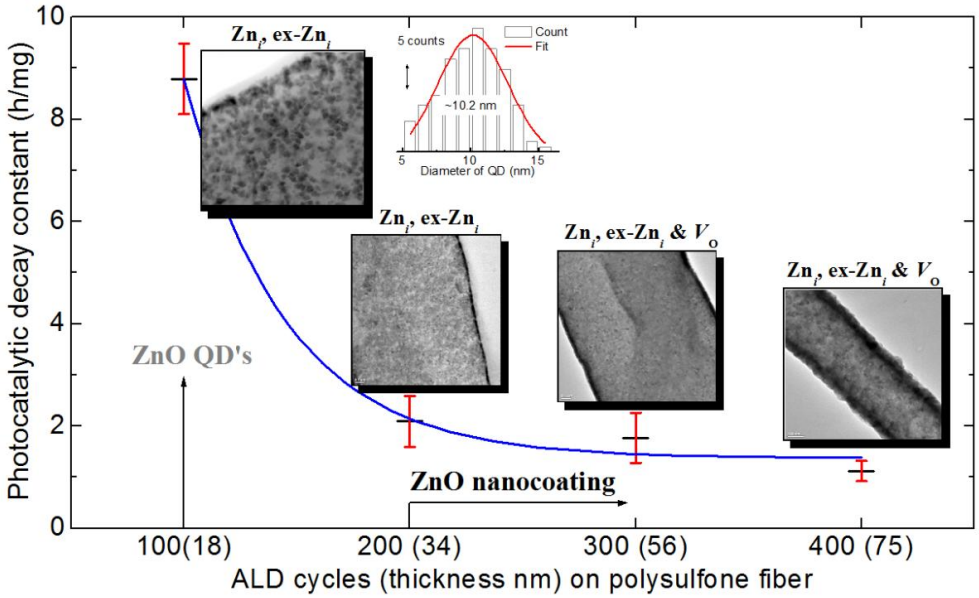

Figure 114. PCA of the resulting nanofibers depend on their morphology and defect type. (Copyright © 2014, Royal Society of Chemistry. Reprinted with permission from Ref.[365])

4.6. Selective Isolation of *Electron* or *Hole* in Photocatalysis: $ZnO-TiO_2$ and TiO_2-ZnO Core-Shell Structured Heterojunction Nanofibers *via* Electrospinning and Atomic Layer Deposition

4.6.1. Experimental

Materials: Poly (vinylpyrrolidone) (PVP, M_w~$1.3x10^6$, Sigma-Aldrich), titanium (IV) isopropoxide (TTIP, 97%, Sigma-Aldrich), zinc acetate dihydrate (ZnAc, reagent grade, Sigma-Aldrich), ethanol (≥ 99.8%, Sigma-Aldrich), glacial acetic acid (100%, Merck) and N, N-dimethylformamide (DMF, Pestanal, Riedel) were used in electrospinning. Tetrakis (dimethylamido) titanium (TDMAT, Sigma-Aldrich), diethylzinc (DEZn, Sigma-Aldrich), and HPLC grade water (H_2O) were used in the ALD process. Methylene blue (MB, Sigma-Aldrich, certified by the Biological Stain Commission) was used as a model organic dye to evaluate the PCA of the $ZnO-TiO_2$ and TiO_2-ZnO CSHJ nanofibers. De-ionized (DI) water is obtained from Millipore Milli-Q system. All the chemicals were used as received.

Electrospinning of PVP-ZnAc and PVP-TTIP nanofibers: *PVP-ZnAc solution*: PVP (0.4 g) was dissolved in ethanol (2 mL)/DMF (2 mL) solvent mixture for 1 h. Then 1.4 g ZnAc was added to this PVP solution and stirred for 2 h to yield homogeneous PVP-ZnAc solution.

PVP-TTIP solution: TTIP (2.88 mL) was stirred in glacial acetic acid (2 mL)/ethanol (2 mL) solvent system for 15 min, and PVP (0.6 g) solution in ethanol (3 mL) was added to the above. The resulting mixture was constantly stirred for 2 h, and the yellowish PVP-TTIP solution was obtained.

The above two precursor solutions were taken into two separate syringes fitted with metallic needle (~0.6 mm of inner diameter). The syringes were then placed on the syringe pump (KD Scientific, KDS 101) horizontally. Electric field of ~15 kV (Spellman, SL Series) was applied across the syringe needle and stationary metal

collector (covered with a clean aluminum foil). Tip to collector distance was between 10 to 12 cm. Electrospinning was carried out in an enclosed chamber at ~25 ˚C and 10 % relative humidity. Then ALD process was implemented on these electrospun PVP-ZnAc and PVP-TTIP nanofibers to yield TiO_2 and ZnO shell structures, respectively.

Atomic layer deposition (ALD) of TiO_2 and ZnO: TiO_2 and ZnO depositions on electrospun PVP-ZnAc and PVP-TTIP nanofibers, respectively, were carried out at ~200 °C in a Savannah S100 ALD reactor (Cambridge Nanotech Inc.). N_2 was used as a carrier gas at a flow rate of ~20 sccm. 500 cycles TiO_2 and 144 cycles ZnO were applied using the exposure mode (a trademark of Ultratech/Cambridge Nanotech Inc.) where dynamic vacuum was switched to static vacuum before each precursor pulse by closing the valve between the reaction chamber and the pump, and switched back to dynamic vacuum for purging excess precursor molecules and gaseous byproducts. This allows the substrate to be exposed to precursor molecules for a certain amount of time (i.e. exposure time). For the TiO_2 deposition, one ALD cycle was as follows: valve OFF/N_2 flow set to 10 sccm/TDMAT pulse (0.1s, TDMAT heated to ~75 °C)/exposure (10 s)/valve ON/N_2 purge (20 sccm, 10 s)/valve OFF/N_2 flow set to 10 sccm/H_2O pulse (0.015 s)/exposure (10 s)/valve ON/N_2 purge (20 sccm, 10 s). For the ZnO deposition, one ALD cycle consists of the following steps: valve OFF/N_2 flow set to 10 sccm/H_2O pulse (0.015 s)/exposure (10 s)/valve ON/N_2 purge (20 sccm, 10 s)/valve OFF/N_2 flow set to 10 sccm/DEZn pulse (0.015 s)/exposure (10 s)/valve ON/N_2 purge (20 sccm, 10 s).

ZnO-TiO_2 and TiO_2-ZnO core-shell heterojunction nanofibers: TiO_2 coated PVP-ZnAc (PVP-ZnAc-TiO_2) and ZnO coated PVP-TTIP (PVP-TTIP-ZnO) nanofibers were calcined at ~500 °C for 3 h in order to remove polymeric precursors. This process enabled the formation of inorganic cores in both cases, yielding the final CSHJ structures to be ZnO-TiO_2 and TiO_2-ZnO.

Characterization techniques: Scanning electron microscope (SEM, FEI – Quanta 200 FEG) was employed to investigate the morphology and dimensions of the nanofibers before and after the calcination. A nominal 5 nm Au/Pd was sputtered on

the samples prior to the observation under SEM. About 100 measurements were considered to determine the average fiber diameter (AFD) from SEM images. CSHJ nanofibers were subjected to transmission electron microscopy (TEM, FEI–Tecnai G2 F30) where the sample was dispersed in ethanol and a tiny droplet was analyzed from holey carbon coated TEM grid. TEM-EDX spectra were also recorded for both of the samples. X-ray diffraction (XRD) patterns were recorded in the range of 2θ =10˚-100˚ using PANalytical X'Pert Pro Multi Purpose X-ray diffractometer with Cu K_α radiation (λ = 1.5418 Å). The bonding states of the constituent elements at the surface of the samples (400 µm spot size) were investigated by X-ray photoelectron spectroscopy (XPS, Thermoscientific K-Alpha, Al K_α radiation, hv = 1486.6 eV) with flood gun charge neutralizer. For the core-level spectra, pass energy and step size were set to 30 eV and 0.1 eV, respectively. VB spectra were also recorded with a pass energy of 30 eV in energy steps of 0.2 eV. Spectral deconvolutions of the XPS data were performed through Avantage software. Horiba Scientific FL-1057 TCSPC was used for the photoluminescence (PL) measurements performed at an excitation wavelength of ~360 nm.

Photocatalytic activity (PCA) of core-shell heterojunction nanofibers: Photo induced degradation was analyzed for CSHJ samples (~5.7 mg each) by immersing them individually into quartz cuvettes containing MB aqueous solution (0.25 mM). The cuvettes were placed at a distance of ~10 cm from the UV source (8 W, UVLMS-38 EL) operating at a wavelength of 365 nm. Dye concentrations in the cuvettes were measured using a UV-Vis-NIR spectrophotometer (Varian Cary 5000) at regular time intervals. Each CSHJ sample was immersed down to the bottom of the cuvette during the UV-Vis measurement and therefore did not interfere with the data acquisition.

4.6.2. Results and Discussion

Figure 115 is the schematic diagram depicting the fabrication of CSHJ nanofibers, where various processes and sequence of the steps are described. ZnO-TiO_2 and TiO_2-ZnO CSHJ were fabricated *via* a three-step process where electrospinning was followed by ALD and calcination. In the first step, we prepared

precursors *via* electrospinning [7, 10, 312, 397] for the cores of the CSHJ nanofibers, where the precursors were mixtures of PVP and ZnAc or TTIP. In the second step, these nanofibers were used as substrates and TiO_2 or ZnO shell was grown through ALD. Finally, nanofibers were calcined to yield the CSHJ where the organic component (PVP) is removed to form ZnO or TiO_2 in the core of the CSHJ. The present calcination temperature and duration yielded single phase and high quality samples.

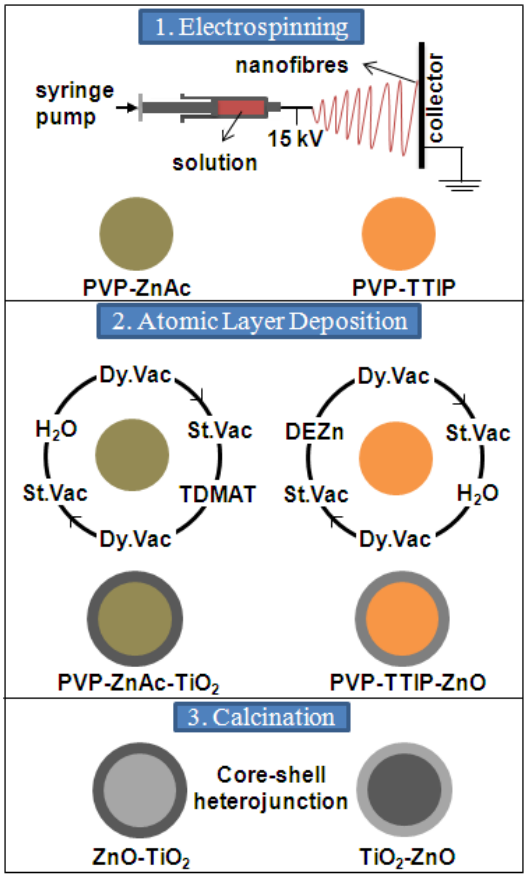

Figure 115. Schematic diagram depicting the fabrication of core-shell structured heterojunction nanofibers. Dy.Vac and St.Vac stand for dynamic and static vacuum conditions, respectively. (Copyright © 2014, Royal Society of Chemistry. Reprinted with permission from Ref.[153])

In any ALD process, it is important to consider the compatibility between the precursor and polymer as the former can degrade the latter by chemically reacting with it; see the case with ALD of Al_2O_3 on nylon-6 polymer [123]. On the other

hand, in the case of poly (propylene) fibers, Al_2O_3 base layer is employed to deposit ZnO, where the former protects the diffusion of DEZn into the polymer [398]. Apart from these limitations ALD in fact can yield coral, [122] core-shell [116] like complex nanostructures, which are potential materials for photocatalytic applications [186, 399]. Hence we applied this technique in combination with electrospinning to produce core-shell structured nano-entities.

The SEM images of the nanofibers before and after calcination are depicted in Figure 116. After the calcination, the structural integrity of the nanofibers was preserved, while we note a decrease in the AFD values which is expected due to the decomposition and removal of PVP. Prior to the calcination and after the ALD process, the AFD are 320 ± 120 and 600 ± 340 nm for PVP-ZnAc-TiO_2 and PVP-TTIP-ZnO nanofibers, respectively (Figure 116a, b).

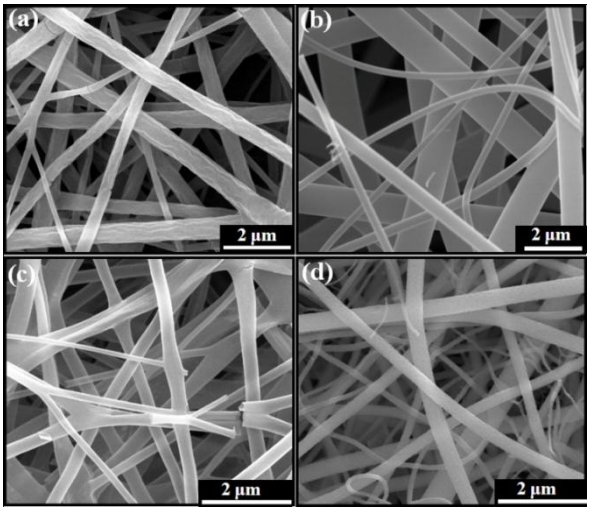

Figure 116. Representative SEM images of (a) PVP-ZnAc-TiO_2, (b) PVP-TTIP-ZnO, (c) ZnO-TiO_2 and (d) TiO_2-ZnO core-shell heterojunction nanofibers. (Copyright © 2014, Royal Society of Chemistry. Reprinted with permission from Ref.[153])

It is generally accepted that the electrospun polymer fibers do possess wide range of diameters, while the rough surface occurs for certain polymers in electrospinning depending upon the solvent and its characteristics [7, 10, 312, 397]. Final CSHJ, ZnO-TiO_2 and TiO_2-ZnO have diameters in the range of 100-650 nm and 50-740 nm with AFD of 270 ± 110 and 200 ± 120 nm (Figure 116c, d). If we compare the AFD before and after calcination, the differences across ZnO-TiO_2 and

TiO_2-ZnO can be attributed to the varying PVP content. In the present case the morphological appearances and changes after the calcination are similar to earlier observations [11, 130, 397]. After calcination CSHJ nanofibers have shown rough surface, see Figure 117. We will see the similarity in the next section, where the samples were analyzed under TEM.

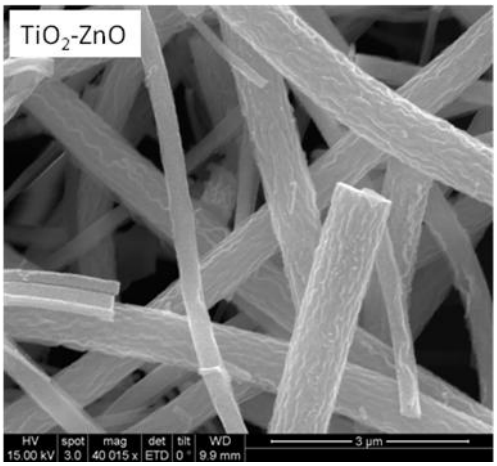

Figure 117. SEM image of TiO_2-ZnO core-shell heterojunction nanofibers depicting the rough surface. (Copyright © 2014, Royal Society of Chemistry. Reprinted with permission from Ref.[153])

The CSHJ samples were subjected to TEM characterization (Figure 118). The core-shell structure can be seen rather explicitly for both of the samples, where uniformities of the TiO_2 and ZnO shell layers need to be pointed out, despite of the relatively large surface area of the nanofibers. We have measured the thickness of the shell from these TEM images yielding ~50 nm and ~70 nm of TiO_2 and ZnO, respectively. Furthermore, the grainy structure of shell is explicit from the TEM images, which has been shown to possess single crystallinity as evidenced by the high resolution TEM (HRTEM) images (Figure 118c, d). The interplanar distances were measured for the shell regions, and the values match with the literature. We have annotated these values on Figure 118c and d for TiO_2 and ZnO, respectively [151, 168, 425]. We have also recorded EDX from TEM on CSHJ and the results are given in Figure 119. For both the cases signal from Zn and Ti is seen as expected, however, the signal from the shell region dominates. From these spectra, the presence of Ti and Zn is confirmed. The quantification of the elements occurred in

the spectra are not given as the signal level from the 'core' part of the structure depends on the characteristics of 'shell' material as the latter encloses the former completely.

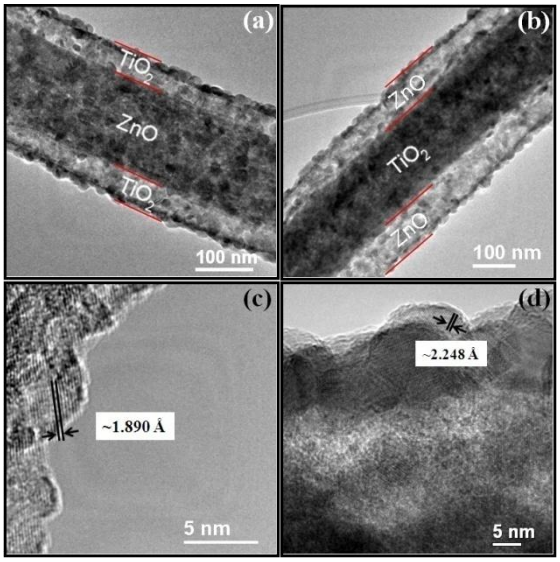

Figure 118. Representative TEM images of core-shell heterojunction nanofibers (a) ZnO-TiO_2, (b) TiO_2-ZnO; (c) and (d) HRTEM images of the 'shell' regions of (a) and (b), respectively. (Copyright © 2014, Royal Society of Chemistry. Reprinted with permission from Ref.[153])

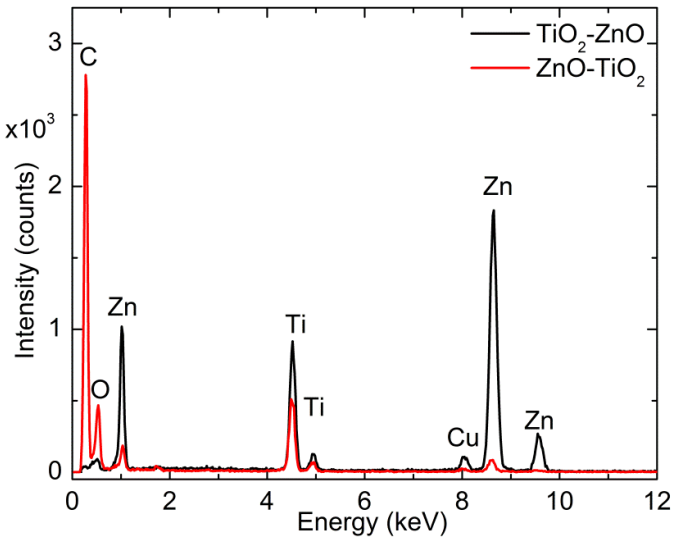

Figure 119. EDX spectra of core-shell heterojunction ZnO-TiO_2 and TiO_2-ZnO nanofibers. (Copyright © 2014, Royal Society of Chemistry. Reprinted with permission from Ref.[153])

The crystalline phase of TiO_2 should be identified as precisely as possible, by given the type II band alignment (band gaps of rutile and anatase are 3.03 eV and 3.20 eV, respectively) and its influence on PCA [426-427]. Importantly by given the penetration depth of X-rays, the XRD data contain ZnO and TiO_2 characteristic peaks in both of the heterojunction nanofibers. A list containing the peak positions and the corresponding Miller indices, (*hkl*), for the three cases (anatase TiO_2, rutile TiO_2 and ZnO) has been tabulated in S3 of ESI. XRD pattern relevant to TiO_2 will be discussed for ZnO-TiO_2 CSHJ (Figure 120a). We have annotated the Miller indices for anatase and rutile phases of TiO_2 on Figure 120a and the peaks corresponding to ZnO are identified on Figure 120b for brevity. For example (010), (002) and (011) reflections of ZnO can be seen in Figure 120a, dotted arrows. Furthermore, the diffraction pattern on log scale (not shown here) is scrutinized for shape changes and asymmetries. A careful inspection of peak positions and the data (Figure 120a) suggests that the pattern matches well with the anatase phased polycrystalline TiO_2 within the detection limits of XRD. Investigation on pure TiO_2 nanofibers (results not shown here) confirmed the formation of anatase phase (i.e. without ZnO shell, subjected to the same thermal treatments). The peaks in the diffraction pattern are consistent with the literature [158, 428]. While the lattice parameters were calculated for tetragonal TiO_2 (a = b = 3.7847 Å, and c = 9.5173 Å) and yielded a crystal volume of 136.33 $Å^3$, which is comparable to the standard value of 135.25 $Å^3$ [428].[428][413][413][413][412] However, in literature lattice contraction is evidenced under the influence of V_O's [429]. In the case of TiO_2 when an O atom is removed, the three nearest Ti atoms tend to relax away from the vacancy in the process of strengthening their bonding with the rest of the lattice [429-430]. In the present case, most probably because of the low density of V_O's, a negligible effect on the bond lengths/cell volume can be seen. Moving onto the XRD pattern of TiO_2-ZnO CSHJ sample, we have identified reflections of the hexagonal (or wurtzite) ZnO and annotated the corresponding Miller indices on Figure 120b. Note that it contains peaks from anatase TiO_2 which were not annotated on Figure 120b. The XRD pattern indicated polycrystalline ZnO which found to be consistent with the literature [151, 167-168, 428]. The lattice parameters were derived and the *c/a* ratio of ~1.6 further supports the wurtzite structure and successful formation of ZnO. Since we have

collected the nanofibers on Al foil and calcined after the ALD process. Hence a background of aluminum oxide is evidenced in TiO_2-ZnO CSHJ (designated with * on Figure 120b).

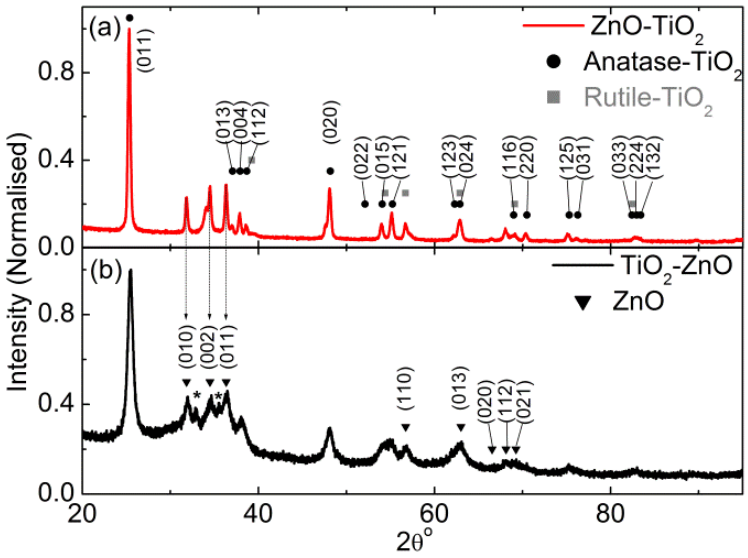

Figure 120. XRD patterns of core-shell heterojunction nanofibers within the 2θ range of 20-100˚ (a) ZnO-TiO_2 and (b) TiO_2-ZnO. Standard reflections for TiO_2 (anatase & rutile) and ZnO are annotated. * represents the peaks from aluminium oxide. (Copyright © 2014, Royal Society of Chemistry. Reprinted with permission from Ref.[153])

The surface characterization of the semiconductors such as ZnO [151, 167-168] and TiO_2 [159-160] is of prime importance not only in the context of PL but also in conjunction with PCA. Interestingly, both of these properties are dependent on the ionic state of the chemisorbed surface oxygen, [151, 159-160, 167-168, 173] which can be realized precisely with XPS. Note that the physisorbed oxygen can be desorbed under ultra high vacuum conditions. CSHJ samples were subjected to XPS analysis for Ti 2*p* or Zn 2*p*, O 1*s* and VB. The spectral locations of the deconvoluted peaks are annotated on the image for each of the spectra. Ti 2*p* core-level spectrum obtained from ZnO-TiO_2 CSHJ is shown in Figure 121a. The spectral locations of the peaks corresponding to Ti $2p_{3/2}$ and Ti $2p_{1/2}$ are consistent with the literature and expected spin-orbit splitting of 5.7 eV is observed [431]. It is also notable that we have not noticed any signatures of Ti^{4+} or Ti^{3+} in the Ti 2*p* spectrum. Core-level

spectrum of Zn 2*p* from the ZnO-TiO_2 CSHJ is shown in Figure 121b and the peaks $2p_{3/2}$ and $2p_{1/2}$ indicated wurtzite structured ZnO where spin orbit splitting and satellite peak are consistent with the literature [168, 431].

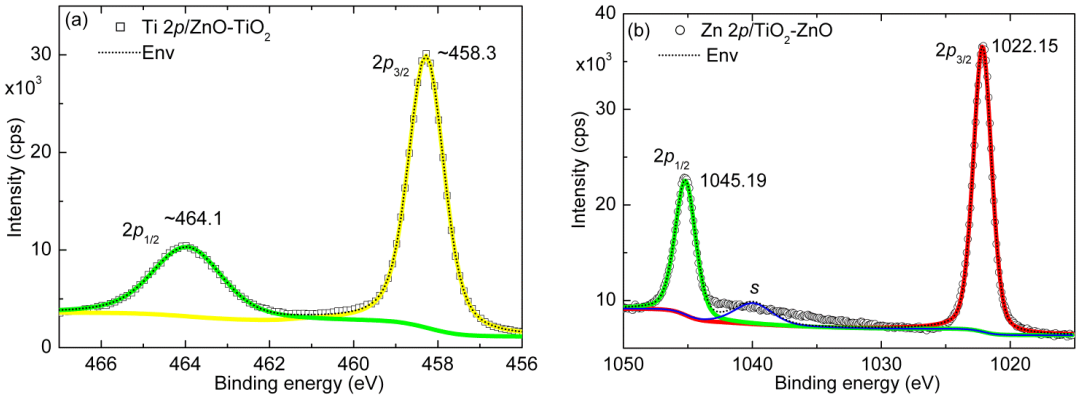

Figure 121. Core-level XPS spectra of core-shell heterojunction nanofibers (a) Ti 2*p* region for ZnO-TiO_2 and (b) Zn 2*p* region for TiO_2-ZnO. (Copyright © 2014, Royal Society of Chemistry. Reprinted with permission from Ref.[153])

In the context of core-level spectrum of O 1*s* from TiO_2 (ZnO-TiO_2 CSHJ), a major peak centered at ~530.4 eV and a minor peak at ~532.2 eV can be seen which correspond to the oxygen [431] in TiO_2 and chemisorbed oxygen, respectively (Figure 122). The presence of oxygen species such as –OH, –CO, adsorbed H_2O and/or O_2 on the surface generally produce a peak at 532.3 eV. [367, 403-404] Similar to the earlier case, the O 1*s* spectrum of ZnO (TiO_2-ZnO CSHJ) can be deconvoluted into two peaks as shown in Figure 122. The spectrum obtained from the ZnO 'shell' has shown a major peak centered at ~530.5 eV corresponding to the oxygen in zinc oxide, which is in line with the literature [431]. The other minor peak appeared at ~531.9 eV corresponds to the chemisorbed oxygen at the lattice defect sites. The peak at 531.5 eV is attributed to O^- and O^{-2} ions in the oxygen deficient regions on the surface [367, 403-404].

Due to the fact that TiO_2 and ZnO possess typical oxygen related defects, the defect sites are subjected to the chemisorption of the above ions while sharing the lattice *electron(s)* [367, 403-404]. Furthermore, the grain boundaries (as seen in the TEM images) are obvious locations for electron deficient species to chemisorb. Depending on the availability of free *electron(s)*, the sharing can be partial with the

above species which has produced relatively broad binding energies peaked at ~532.2 eV or ~531.9 eV. Among these two samples, it can be seen that the chemisorbed oxygen related to the ZnO-TiO_2 sample has shown relatively higher binding energy, obviously because of the differences in the origin of chemisorbed oxygen. While keeping these differences aside, a variation in the relative area of peaks is explicit where TiO_2-ZnO CSHJ has shown nearly 2.6 times higher area than its complimentary CSHJ. This concludes that a larger fraction of oxygen-defect regions is present in the surface layer [367, 403] for TiO_2-ZnO compared to ZnO-TiO_2.

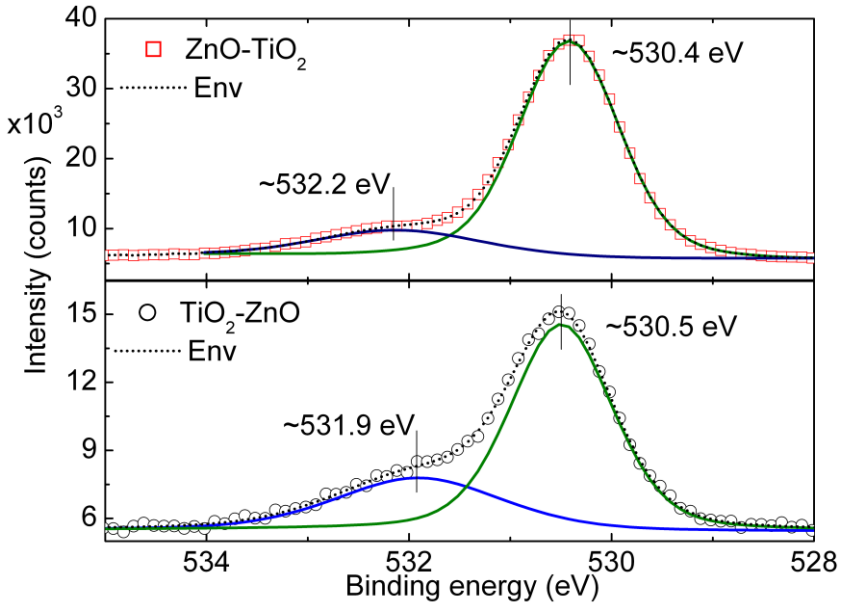

Figure 122. Core-level XPS spectra of O 1*s* from ZnO-TiO_2 and TiO_2-ZnO core-shell heterojunction nanofibers with peak deconvolution. The spectral locations of the peaks are annotated on the image, where the major peak corresponds to the oxygen in the shell material and the minor peak to chemisorbed oxygen. (Copyright © 2014, Royal Society of Chemistry. Reprinted with permission from Ref.[153])

Furthermore, VB spectra (Figure 123) of both CSHJ were investigated for any alterations in the edge of the band corresponding to the 'shell' semiconductor. The VB edges were at ~2.35 eV and ~2.42 eV for ZnO-TiO_2 and TiO_2-ZnO, respectively. By the given TiO_2-anatase phase band gap of 3.20 eV, the CB edge should be placed around –0.85 eV. It is notable that the VB edges were found to be

in the range of 2.4–3.1 eV with band gaps within the range of 3.67–3.2 eV. [432-434] In the case of ZnO, the CB edge was found to be around –0.88 eV according to its typical band gap of 3.3 eV.

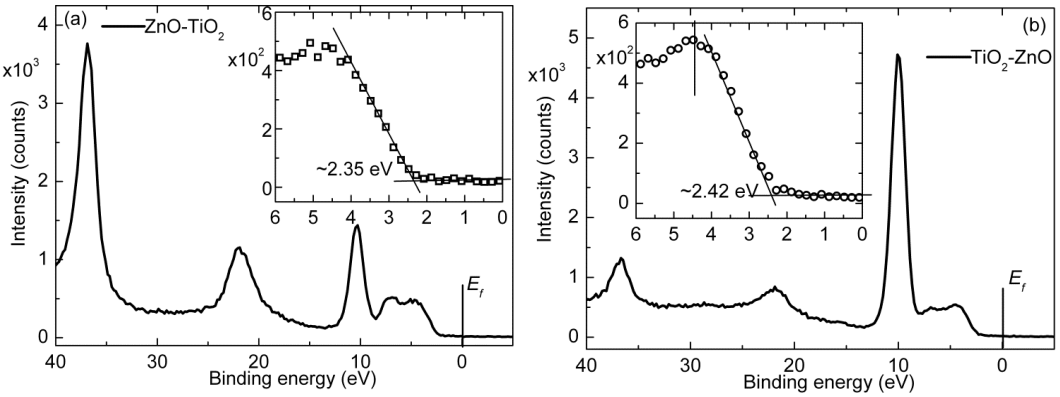

Figure 123. Valance band XPS spectra of core-shell heterojunction nanofibers (a) ZnO-TiO_2 and (b) TiO_2-ZnO. (Copyright © 2014, Royal Society of Chemistry. Reprinted with permission from Ref.[153])

A number of studies [138, 148, 155, 158-161] have already shown the importance of the lattice defects in conjunction with PCA either in the case of pristine or heterojunction catalysts, where they can be identified through optical properties. We have performed PL spectroscopy on the CSHJ nanofibers (Figure 124) and the origin of defects-related emission is overlaid on the corresponding spectrum. When CSHJ were illuminated with energy higher than its band gap, majority of the absorption takes place within the 'shell' region. Hence the emission from CSHJ is majorly due to the shell region of the heterojunction, where the visible emission occurs from the surface recombination [151, 409-410]. In both the cases, a largely similar visible emission indicates a dominant defect density such as V_O's. Importantly, despite the visible emission peaks at almost the same wavelength for both the CSHJ, the energetic location of the V_O's for TiO_2 and ZnO are not the same. These spectra will be discussed independently with reference to the plausible defects in the following and subsequently juxtaposed with PCA. Although majority of the emission is from the 'shell', it should be noted that the emission and its intensity are influenced by the presence of 'core' where there might be a recombination route (radiative/non-radiative) of the photo-generated charge.

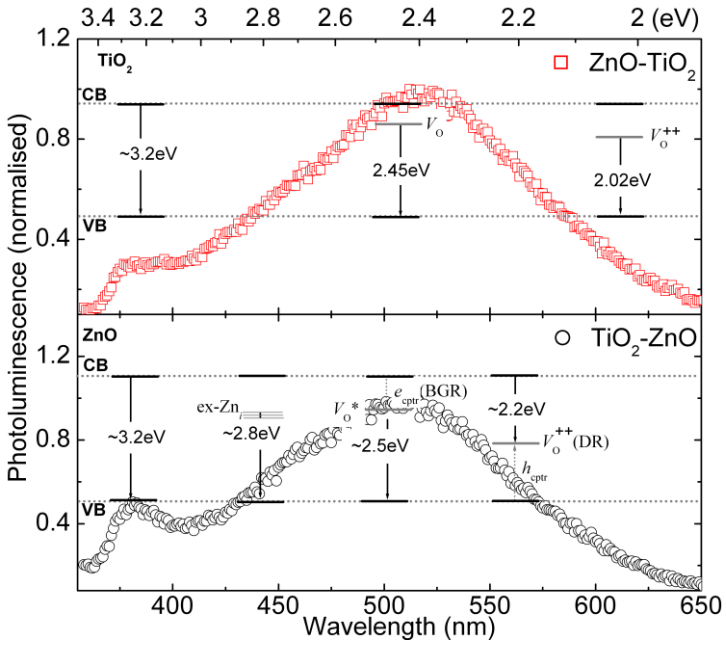

Figure 124. Photoluminescence spectra of ZnO-TiO_2 and TiO_2-ZnO core-shell heterojunction nanofibers. (Copyright © 2014, Royal Society of Chemistry. Reprinted with permission from Ref.[153])

In the case of ZnO-TiO_2 sample the emission from the interband transition can be seen at ~3.2 eV. This band arises due to the *e/h* recombination across the band gap of TiO_2, while the broad visible emission centered at ~2.4 eV is due to the surface recombination associated with V_O defects [158, 160]. XPS has indicated the chemisorbed oxygen on the surface of CSHJ which further supports the defects related to oxygen vacancies. The energetic locations of these defects are discussed in the literature, [158, 160] which were schematized on the emission spectrum (Figure 6). The *electrons* in V_O's (also known as F centers) are localized because of Madelung potential of the highly ionic crystal [435]. This state can be occupied by the O^{2-} by capturing one or two "free" *electrons* from the crystal, and hence the energetic cost of the vacancy is minimized [435]. This localized *electrons* form a donor level 0.75–1.18 eV below the CB of TiO_2, [158, 436] specifically the donor level at 1.18 eV below the CB is due to V_O^{++} [160]. Furthermore, the band because of V_O's can be broad enough which may merge with CB in the case of sufficiently high defective TiO_2 of either anatase or rutile phase, [437] and hence a significant shift in Fermi level toward high energy can be expected. We believe that this has not

happened in the present case where an explicit peak corresponding to the interband transition from TiO_2 and relatively low concentration of V_O's (as evidenced in XPS measurements). On the other hand, the V_O's can cause redistribution of excess charge among the nearest neighboring Ti atoms ($Ti^{4+}/V_O \rightarrow Ti^{3+}$ or Ti^{2+}) which form a shallow donor state below the CB [438-439]. However in the core-level XPS analysis of Ti 2*p* spectrum (Figure 121a) no explicit indication of these ionic states is present as mentioned previously.

In the case of TiO_2-ZnO, emission spectrum from ZnO consists of the least controversial UV-emission (interband transition) which occurred at ~3.2 eV and debatable visible emission centered at ~2.5 eV. Interestingly, the visible emission is attributed to the V_O's similar to the TiO_2 case. However, this green emission consists of two transitions as depicted in Figure 124. The V_O's exists in the bulk grain region (BGR) [409] as well as depletion regions (DR) [410] with different ionic states. In the BGR, V_O^+ captures an *electron* from CB and forms V_O* 0.86 eV below the CB and in DR, V_O^+ captures a *hole* from VB and forms V_O^{++} 1.16 eV above the VB. *cf.* the energetic locations of V_O in TiO_2 range from 0.75 eV to 1.18 eV below the CB, [158, 436] however, notably V_O^{++} is 1.18 eV below the CB [158, 160]. In the context of TiO_2-ZnO, the BGR of ZnO is not accessible to the PCA, hence only the DR, which is on the surface of the CSHJ, takes part in PCA by capturing a *hole* from the VB. The optical quality can be compared across the CSHJ by taking the intensity ratios of interband transition to the visible (I_{UV}/I_{Vis}) [167-168] yielding ~0.3 for TiO_2 and ~0.5 for ZnO for ZnO-TiO_2 and TiO_2-ZnO CSHJ, respectively. These ratios suggest that the optical quality of ZnO is better than TiO_2.

In the case of TiO_2 various chemical species (–OH, –CO, H_2O or O_2) were found to be chemisorbed on the surface which are not the same for ZnO case (O^- and O^{-2}). Although the species those adsorbed on either of the surfaces were not exactly identified, it is clear that for TiO_2 chemisorption occurred at higher energy than ZnO. i.e the surface adsorbents of TiO_2 bind to the lattice stronger than those of ZnO, which explains the differences in the relative intensities of visible emission among TiO_2 and ZnO. In the case of TiO_2, since the surface adsorbents are strongly bound to

the lattice they can successfully capture an *electron* from CB and give rise to visible emission. In contrast, for the case of ZnO, despite of their relatively high density, the surface adsorbents are loosely bound and hence under equilibrium, they have relatively lower probability to stay at the defect site to give visible emission.

Furthermore, we would like to comment on the visible emission from the CSHJ. Within the interfacial region between the semiconductors, there is a certain possibility of so called 'interfacial states' which may arise due to the lattice mismatch or other related effects. These states can be radiative or non-radiative in nature, which can enhance or subdue the visible-intensity, respectively. We have not considered the possible emission from the interface, as the oxide hetero-interfaces are not completely understood yet [382]. Nevertheless, the present design enables the future studies to identify the role of each charge-carrier for oxidation processes of various organic compounds, see Ref 50, 72-81 in Ref.[138] and the recent study as well [177].

Having discussed the influence of defects on the optical properties, involvement and role of V_O's in the interface of heterojunction is still debatable, [159] on the other hand since no catalysis takes place at the interface, the dynamics and consequent charge exchange process are out of the scope of the present article. Essentially if V_O's in TiO_2 exist inside the lattice then they may serve as recombination centers, however this may reduce the PCA [440]. In a recent article, the importance of oxygen vacancies in TiO_2 and their influence on the PCA is emphasized [159]. Prior to the discussion on PCA, it should be noted that no charge carrier is excited to the defect states directly as we have employed monochromatic UV source (365 nm) and hence the defect sites can capture *electron* or *hole* depending on their energetic location within the band gap.

It is useful to revisit the photocatalysis mechanism [139-140] to which we will be referring in the context of PCA for each CSHJ. This process has already shown in Chapter 1 (1.4)

Moving on to the context of CSHJ, its functionality depends on the fundamental physical parameters such as band offset, where there exists a profound effect on the carrier confinement and electronic transport along and across the interface [382]. Further complicating the process of charge transfer the oxide hetero-interfaces are not well understood yet [382]. While in the present case initially precursor nanofibers of ZnO or TiO_2 were produced, then the counter semiconductor is deposited. This intermediate level heterostructure was subjected to calcination, producing the hetero-oxide interface with a structural distortion along with a probability of chemical bonds and charge distribution across the junction. The present calcination parameters yielded anatase TiO_2 in both of the heterojunction. On the other hand, it is acknowledged that the mixed phase TiO_2 yields higher PCA; [426-427, 441] however, we aim to determine individual roles of *electron* and *hole* in the process of catalysis. In the mixed phase TiO_2, the energetic alignment of band edges suggests a flow of conduction *electrons* from rutile to anatase [427]. Keeping this in the background, we chose to produce a single phase TiO_2 to study the catalytic mechanism. On the other hand, defect disorder in either TiO_2 or ZnO plays a significant role in the PCA. Hence we refer to the discussion of PL fromTiO_2 and ZnO, and correlate it with the PCA of ZnO-TiO_2 and TiO_2-ZnO CSHJ, respectively.

PCA is compared across the CSHJ while considering the degradation of MB without any catalyst (Figure 125). Photodegradation of chemical compounds on the surface of a semiconductor most often follows [138] Langmuir sorption isotherms, [424] where a single molecule deep monolayer is adsorbed at a distance of ~1 Å. The exponential decay behavior (Figure 125) suggests a pseudo-first-order kinetics according to the Langmuir–Hinshelwood model. In any photocatalysis involving semiconductor, the efficiency of the process depends on the balance between the interfacial charge transfer (semiconductor to dye) and charge carrier recombination life time [138]. In the present investigation, the degradation time constants yielded from an exponential fit for each CSHJ is given on the Figure 125. In the absence of a catalyst, MB did not show any degradation at noticeable level while ZnO-TiO_2 and TiO_2-ZnO CSHJ yielded ~3.11 h and ~1.95 h of decay times, respectively. These decay times indicate how fast the catalysts can oxidize the dye which is under test.

Interestingly, the time constant shown by TiO_2-ZnO CSHJ is nearly 1.6 times faster than that of ZnO-TiO_2 CSHJ. It is vital to understand the diffusion of *electron* or *hole* across the CSHJ prior to the explanation of the variation observed in PCA.

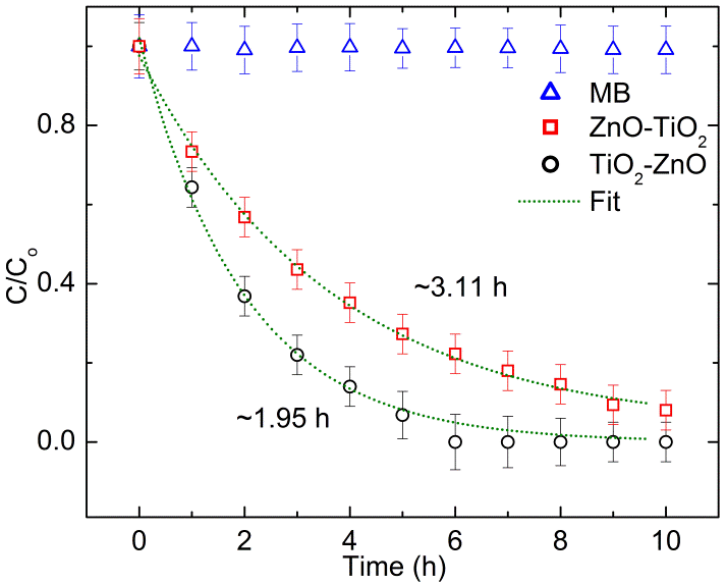

Figure 125. PCA of the ZnO-TiO_2 and ZnO-TiO_2 core-shell heterojunction nanofibers. Exponential decay fits and constants are shown when compared with the pristine methylene blue (MB) without any catalyst. (Copyright © 2014, Royal Society of Chemistry. Reprinted with permission from Ref.[153])

In Figure 126 we have shown the schematic diagram which replicates the semiconductors with energetic locations with respect to vacuum for both the CSHJ. Previously discussed processes are annotated on the figure, i.e. (a) and (b) while considering the nature of defect. In the context of ZnO and TiO_2, these defect-related bands are shown to depict improved catalytic activity [138, 148, 155, 158-161].

Role of electrons: Under illumination of ZnO-TiO_2 CSHJ, *electron* and *hole* pairs are created in the TiO_2 shell region. If we consider the alignments of the band as shown in Figure 126 (left panel), it is clear that the *holes* can be diffused into core (ZnO), while the *electrons* can participate in PCA at the CB, or V_O states of TiO_2. However, there is also a possibility that e^-_{CB} can be transferred to V_O* (BGR) and/or V_O^{++} (DR if exists) states of ZnO directly or after they have been captured by V_O states of TiO_2. In the present context, we are discussing the V_O's those are limited to

the surface of the TiO_2 and the *electrons* at such defects have almost no mobility to reach the V_O^{++}'s or V_O*'s of ZnO. Photo-generated *electron* in the VB of TiO_2 finds the V_O* state energetically favourable, however physically not reachable, because V_O* lies in the bulk of the ZnO. Hence the *electron* has to take part in the PCA before the recombination. However the *electrons* in V_O's of TiO_2 can reach the DR (grain boundaries of ZnO), which might hinder the PCA. Furthermore, if V_O's exist inside the lattice then they may serve as recombination centres [440]. Since the *holes* are most likely diffuse into ZnO, they may not play a major role in the PCA. The above argument assumes that *e/h* pairs are not created in ZnO, where TiO_2 absorbs almost all of the UV illumination. However, in case if they are generated in ZnO dominantly, e_{CB}^- may migrate to the CB of TiO_2 and participate in the PCA. Hence the active sites for the PCA at the TiO_2 surface are CB and V_O's as designated with process (a) on Figure 126, left panel. In the case of TiO_2, the existence of V_O's creates unpaired *electrons* or Ti^{3+} centres (though not evidenced in the XPS), which could form donor levels [160] and also *e*/*h* recombination process is affected causing a change in chemical rates [161]. If we look at the mechanism of catalysis for pure TiO_2, under suitable illumination the photo-generated *electrons* either at CB or V_O's are captured by O_2, producing O_2^- radical groups where the adsorption energies are -0.94 and -2.52 eV, respectively [442]. As discussed earlier, these radical groups are the key for the oxidation of test dye. Notably, high density of V_O's can induce vacancy electronic states below the CB [443] and an improved PCA is noticed under the visible light. Since charge migration is a physical process, it may be possible that some of the *holes*, which are not migrated to the core, can participate in the PCA as indicated with (b)* on Figure 126, left panel, however with negligible activity. Deconvolution of visible emission (not shown here) from TiO_2 suggests that the emission from the optical transition from V_O^{++} to VB has relatively lower intensity when compared to that from V_O (which are 0.75 eV below the CB) to VB, which implies that the defect density of V_O^{++} is relatively less. Hence the *electron* capture from the CB is dominated by V_O, which is 1.18 eV below the CB, [158, 160, 436] see left panel of Figure 126, black coloured (a). Furthermore, similar to the molecular oxygen, H_2O can involve in the PCA when disassociated at a defect site, e.g. V_O

(energetically more favourable [444]), while on a perfect TiO_2 surface H_2O is physically adsorbed [445-447].

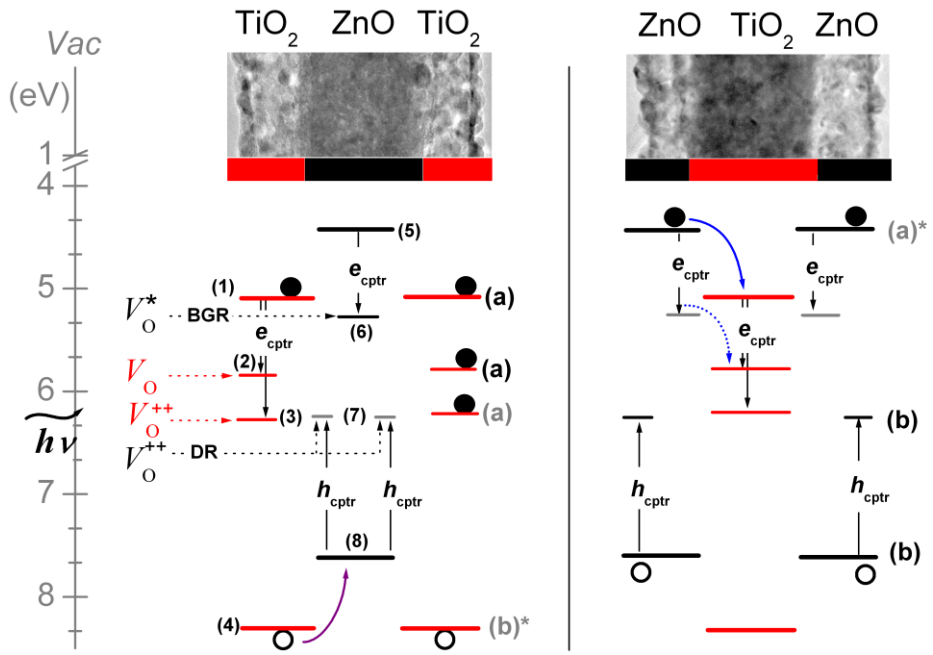

Figure 126. Proposed catalysis mechanism, where either *electrons* from the TiO_2 or *holes* from the ZnO are engaged from the ZnO-TiO_2 (left panel) and TiO_2-ZnO (right panel) core-shell heterojunction nanofibers. e_{cptr} and h_{cptr} stand for *electron* and *hole* capture, respectively. (Copyright © 2014, Royal Society of Chemistry. Reprinted with permission from Ref.[153])

Role of holes: In contrast to the previous CSHJ, the present heterojunction favours *electrons* to migrate to the TiO_2-core leaving the *holes* at the VB to participate in the PCA. Otherwise, this photo-generated *electron* can be captured by V_O* which can further diffuse into the TiO_2-core by accessing V_O's there in, as shown in the Figure 126, right panel. Hence the active *holes* at the surface of ZnO-shell take part in PCA and the above-discussed mechanism can be taken into account to understand the oxidation process. Since the surface layer is only ZnO, it has been revealed that V_O's can behave as important adsorption and active sites for catalysis, which strongly influence the reactivity of metal oxides [448]. Notably, V_O^{++} forms after capturing a *hole* from the VB. Hence by involving H_2O to form $^{\bullet}OH$ oxidizes the dye as shown earlier in equations (b-1) and (b-2). Similar to the earlier case, it may be possible that some of the *electrons*, which are not migrated to the core, can participate in the PCA.

However, the activity with such *electrons* can be negligible and shown with grey coloured (a)* on Figure 126, right panel.

Higher PCA for TiO_2-ZnO CSHJ can be because of various reasons, including high density of surface defects and lower binding energy of the surface adsorbents, which can exchange the charge carrier and participate in PCA. In ZnO, under biased and illuminated conditions, [150] the mobility of the *hole* (10 cm^2/Vs) would be much lower when compared to unbiased condition such as the present. From the earlier described processes (a) and (b), it is clear that $^{\bullet}OH$ radical forms with O_2 (primary)/*electrons* and/or H_2O/*hole*. In the case of ZnO-TiO_2, *electrons* are the majority participants in PCA hence the availability of the O_2 can be a limiting factor. On the other hand, for TiO_2-ZnO CSHJ, the vast availability of H_2O is an advantage to yield higher efficiency. Therefore in the context of an aqueous solution *holes* may yield higher PCA than *electrons.* In the case of TiO_2, charge carrier generation under suitable illumination takes place in the order of fs, and subsequent processes such as charge carrier trapping and recombination take place 0.1-10 ns and 10-100 ns, respectively. We can see that trapping is 10 times faster and the trapped charge has to participate in recombination [138]. Also, it is suggested that the *electron* transfer to oxygen may be the rate determining step, see Ref. 43, 86, 87 in Hoffmann et al. [138]. Depending on the surface chemistry, there is a possibility that there exists more than one type of binding. For example, in the case of $CHCl_3$ interacting with Degussa P25 at pH 5, two different sites of non-uniform binding energies are identified. Stronger binding site dominates sorption at concentrations <1 mM, and weaker binding state is attributed mostly for concentrations >1 mM, see Ref 50 in Hoffmann et al. [138]. It is thought that high density of defects would lead to higher PCA; however, it is the case only when we have loosely bound species at the lattice. Like in the case of TiO_2, although there are significant defects, they are occupied with strongly bound adsorbents and hence may not be easily brought into the catalysis process where an exchange of charge is required. Although we have not considered the effect of pH, it is notable that water disassociation equilibrium depends on the pH of the solution, which is quite complex in the context of UV-irradiated TiO_2. On the other hand, pH also determines the surface charge of TiO_2

with respect to its point of zero charge (pzc, ~6.5), as well as the ionization state of the organic reactant and of its metabolites [449]. If the pH is higher than the pzc the surface becomes negatively charged, the opposite is valid for pH < pzc. In the present case, since MB is a cationic dye, most favorable adsorption occurs at pH < pzc, where the adsorption is the basic requirement [424] for the reaction to take place [138]. We believe that the integral effect of above reasons caused photogenerated *holes* from ZnO to depict higher efficiency than *electrons* from TiO_2.

4.6.3. Conclusions

In this study we have attempted to determine the individual roles of *electron* and *hole* in photocatalysis, which are photo-derived from a core-shell structured semiconducting heterojunction where the design enables only the 'shell' part of the CSHJ to be exposed for PCA. These CSHJ were characterized for their structural integrity, which revealed the formation of pure, single-phase anatase TiO_2 in both CSHJ. TEM analysis suggested well-developed grains, which in principle influence the PCA by forming grain boundaries. XPS has evidenced typical V_O's on the surface hosting various oxygen-related species. The optical properties of the CSHJ were studied and discussed with reference to the intrinsic defects. We have not considered the interfacial defects between core and shell regions, however, the interface is not directly accessible for PCA anyway. In the case of ZnO the visible emission occurs from the surface, and hence considering the defects limited to the surface does not undermine the analysis. Crucially, under suitable illumination, *e*/*h* pairs are created majorly in the shell region of the CSHJ, and *holes* and *electrons* migrate to the core of the structure for ZnO-TiO_2 and TiO_2-ZnO structures, respectively, as governed by the band alignment. In ZnO-TiO_2 CSHJ *e/h* pairs are created in TiO_2 and *electrons* take part in catalysis at the CB of TiO_2 while *holes* migrate to the core of the structure. The PCA in this heterojunction is an integral effect of catalysis taking place at VB and V_O sites on the surface, where the photo-generated *holes* are eliminated. In the TiO_2-ZnO CSHJ, *e/h* pairs are created majorly in ZnO, and *electrons* are diffused into the core while *holes* at the VB of ZnO involve in PCA (see Figure 127). The results suggested that TiO_2-ZnO CSHJ has shown higher PCA

than the other combination. It might be becasue of surface chemistry and the intrinsic characteristics of the photo-generated charge carriers. The density of the V_O's for ZnO-shell is higher than TiO_2-shell (XPS), which might have enhanced the *hole* capture process thereby contributing to the PCA. The densities of oxygen related defects differ by a factor of 2.6, causing an improvement of nearly 1.6 times in the PCA. Appearantly, this is not linear scaling because of the differences in the chemical nature of the defects. Finally the higher PCA for ZnO shell can be because of high density of defects, lower binding energy of surface adsorbents, comparatively lower mobility of the *holes* in the VB. This study was published in Nanoscale as a cover page (see Figure 128).

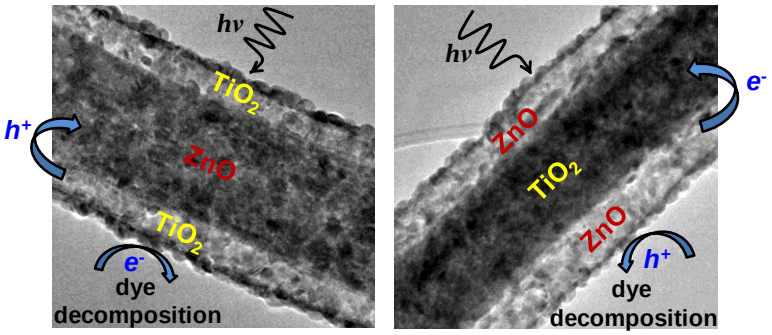

Figure 127. PCA mechanism for CSHJ nanofibers. (Copyright © 2014, Royal Society of Chemistry. Reprinted with permission from Ref.[153])

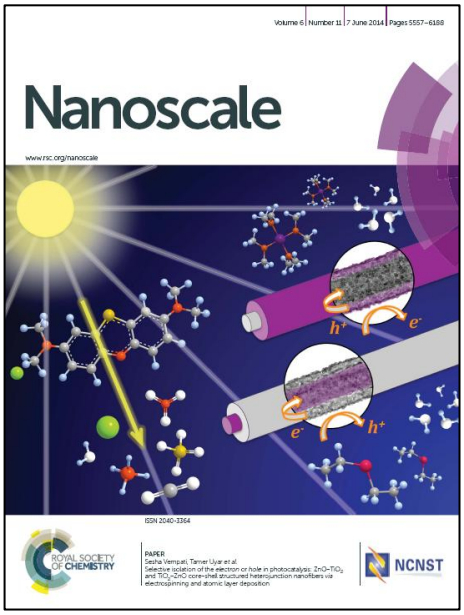

Figure 128. Outside Front Cover of Nanoscale belong to our paper. (Copyright © 2014, Royal Society of Chemistry. Reprinted with permission from Ref.[153])

CHAPTER 5

5. EPILOGUE

The research studies in my dissertation are regarding with the development of multifunctional electrospun nanofibers using different approaches for food packaging, and controlled/slow release systems, volatile organic compounds (VOCs) treatment, water purification and waste treatment. Therefore, we functionalized nanofibers with cyclodextrin inclusion complexes (CD-IC) for food packaging, and controlled/slow release systems, or cyclodextrins (CD) for removal of VOCs from the environment, or cyclodextrin polymer (CDP) for molecular filtration of organic wastes in aqueous solution. In addition, we combined electrospinning and atomic layer deposition (ALD) processes to produce novel materials having photocatalytic activity (PCA) for organic pollutants treatment in water purification.

In Chapter 2, the incorporation of CD-IC of active compounds that are widely used in food industry due to their antioxidant and antibacterial properties, into electrospun polymeric nanofibrous matrix was reported. Our aim was to enhance functionality, thermal stability and sustained release of the active compounds such as vanillin, eugenol, geraniol and triclosan by inclusion complexation, and combine high surface area and nanoporous structure of nanofibers with specific properties of CD-IC.

- In our first study of this chapter (2.2) reports the production of polyvinyl alcohol (PVA) nanofibers containing vanillin/CD-IC via electrospinning technique. The vanillin/CD-IC was prepared with three types of CDs; α-CD, β-CD and γ-CD to find out the most favorable CD type for the stabilization of vanillin. PVA/vanillin/CD-IC nanofibers, having fiber diameters around ~200 nm, were successfully electrospun from aqueous solution mixture of PVA and vanillin/CD-IC. Our results indicated that vanillin with enhanced durability and high temperature stability was achieved for PVA/vanillin/CD-IC nanowebs due to complexation of vanillin with CD, whereas the PVA nanofibers without the CD-IC could not effectively preserve the vanillin. Additionally, we observed that PVA/vanillin/γ-CD-IC nanoweb was more effective for the stabilization and slow release of vanillin suggesting that the strength of interaction between vanillin and the γ-CD cavity is stronger when compared to α-CD and β-CD.
- In order to achieve high thermal stability and slow release of eugenol (EG), electrospun PVA nanofibers encapsulating EG/CD-IC were produced in next study (2.3) using α-CD, β-CD and γ-CD. In the case of PVA/EG/α-CD nanofibers, uncomplexed EG was detected indicating that α-CD is not a proper host for EG/CD-IC formation. However, for PVA/EG/β-CD-IC and PVA/EG/γ-CD-IC nanofibers, enhanced durability and high temperature stability for EG was achieved due to the inclusion complexation.
- One of our studies (2.4), solid geraniol/cyclodextrin inclusion complexes (geraniol/CD-IC) were successfully prepared using three types of native CD (α-CD, β-CD and γ-CD). The modeling studies for inclusion complexation between CD and geraniol were performed by using ab initio techniques. Both experimentally and theoretically, the complexation efficiency between geraniol and γ-CD was higher; therefore, geraniol/γ-CD-IC was chosen and then incorporated into PVA nanofibers via electrospinning. The SEM imaging elucidated that the aggregates of geraniol/γ-CD-IC crystals were distributed in the PVA nanofibers, whereas bead-free and uniform PVA and PVA/geraniol nanofibers without CD-IC were electrospun. Higher thermal stability of geraniol was observed in the electrospun PVA/geraniol/γ-CD-IC

nanofibers. However, geraniol molecules having volatile nature could not be preserved without CD-IC during electrospinning or during storage; therefore, the complete evaporation of geraniol in PVA/geraniol nanofibers was unavoidable even after one day of its production. On the contrary, the loss of geraniol was minimal (~10%) for PVA/geraniol/γ-CD-IC nanofibers even after storage of these nanofibers for two years owing to inclusion complexation.

- In another study (2.5), solid TR/CD-IC were obtained and then incorporated in polylactic acid (PLA) nanofibers via electrospinning. α-CD, β-CD and γ-CD were tested for the formation of TR/CD-IC by co-precipitation method, however, our findings indicated that α-CD could not form inclusion complex with TR, whereas β-CD and γ-CD were successfully formed TR/CD-IC crystals and the molar ratio of TR:CD was found 1:1. The structural and thermal characteristics of the TR/CD-IC were investigated. Then, the encapsulation of TR/β-CD-IC and TR/γ-CD-IC in PLA nanofibers was achieved. Electrospun PLA and PLA/TR nanofibers obtained for comparison were uniform; whereas the TR/CD-IC crystals were present, and distributed within the PLA fiber matrix as confirmed. We have investigated antibacterial activity of these nanofibrous webs. Our results indicated that PLA nanofibers incorporating TR/CD-IC have shown better antibacterial activity against *S. aureus* and *E. coli* bacteria compared to PLA nanofibers containing only TR without CD-IC.

Our studies mentioned in the Chapter 2 shows that the functional electrospun nanofibers/nanowebs incorporating CD-IC are very effective for achieving long-term shelf-life and high thermal stability for volatile flavors/fragrances (vanillin, geraniol, eugenol) as well as efficient antibacterial property for triclosan, hence these functional nanofibrous webs having not only these specific functionalities but also very high surface area and nanoporous structure may be quite applicable in active food packaging in order to prevent foodborne diseases, provide safety/quality of nutrition and extend shelf life of food. The studying with food components would be very interesting to confirm the real applicability of these functional nanofibers.

In Chapter 3, there is an overview of the our researches in which we obtained multifunctional nanofibrous materials using CD and CDP to combine inclusion complexation capability of CD and high surface area and nanoporous structure of nanofibers to promote molecular filtration from air (by nanofibers incorporating CD) or aqueous environment (through CDP functionalized nanofibers).

- Initially (3.2), zein nanofibers containing CD (zein/CD) were produced via electrospinning. Three types of CD (α-CD, β-CD and γ-CD) having 10%, 25% and 50% (w/w) were individually incorporated into zein nanofibers. SEM imaging elucidated that the morphologies of the electrospun zein/CD nanofibers were significantly depend on the CD types and weight percentage. The incorporation of CD in zein improved the electrospinnability and bead-free nanofibers were obtained at lower zein concentrations. Zein/CD nanofibers having fiber diameters ~100 thru 400 nm were obtained depending on the zein concentration, CD type and weight percentage. XRD studies revealed that CD were mostly distributed without forming crystalline aggregates for zein/CD nanofibers containing lower weight percentage of CDs. ATR-FTIR and XPS studies of zein/β-CD nanofibers indicated that some of the CD were present on the fiber surface. Thermal analyses elucidated that zein/β-CD nanofibers have shown higher glass transition temperature and higher degradation temperature with increasing CD content.
- In the next study (3.3), functional nylon 6,6 nanofibers incorporating CD were developed via electrospinning for organic vapor waste treatment. α-CD, β-CD and γ-CD with different weight loadings (25% and 50% (w/w), with respect to polymer matrix) were successfully distributed in nylon 6,6 nanofibers without forming any crystalline aggregates. Enhanced thermal stability of the nylon 6,6/CD nanofibers samples was observed due to interaction between CD and nylon 6,6. XPS and ATR-FTIR studies indicated the existence of some CD molecules on the surface of the nylon 6,6/CD nanofibers, which is essential for the entrapping of organic vapors from the environment. Electrospun nylon 6,6 nanofibers without having CD were ineffective for entrapment of toluene vapor from the environment, whereas

nylon 6,6/CD nanofibrous membranes can effectively entrap toluene vapor from the surrounding by taking advantage of the high surface-volume ratio of nanofibers with the added advantage of inclusion complexation capability of CD presenting on the nanofiber surface. Our findings indicated that not only the amount of surface associated CD molecules but also CD types were important factors for toluene entrapment efficiency. The modeling studies for formation of inclusion complex between CD and toluene were also performed by using ab initio techniques.

- In another study (3.4), polyester (PET) nanofibers incorporating CD were successfully obtained via electrospinning for entrapment of aniline as a model volatile organic compound (VOC). α-CD, β-CD and γ-CD were used to functionalize PET nanofibers. Bead-free PET/CD nanofibers were obtained from lower polymer concentration indicating that the incorporation of CD in polymer solution improved the electrospinnability of the PET nanofibers. XRD studies indicated that CD were distributed into nanofiber matrix without forming any crystalline aggregates. FTIR peak shift was observed possibly due to interaction between CD and PET. TGA data confirmed that the initial CD loading (25%, w/w) in the polymer solution was preserved for the PET/CD nanofibers without any loss of CD after the electrospinning. The presence of most of CD on the surface of PET/CD nanofibers was confirmed by XPS analysis and contact angle measurement. Our studies showed that PET/CD nanofibrous webs can effectively entrap aniline vapor from surrounding owing to their very large surface area and inclusion complexation capability of CD presented on the nanofiber surface. DMA results indicated that CD improve the mechanical property of the nanofibers. The entrapment efficiency of aniline vapor was found to be better for PET/γ-CD nanofibers when compared to PET/α-CD and PET/β-CD nanofibers.
- In the last study of Chapter 3 (3.5) reports surface modified electrospun PET nanofibers with CDP (PET/CDP). CDP formation onto electrospun PET nanofibers was achieved by polymerization between citric acid (CTR, crosslinking agent) and CD. Three different types of native CD (α-CD, β-CD and γ-CD) were used to form CDP. Water-insoluble crosslinked CDP coating

was permanently adhered onto the PET nanofibers. SEM imaging indicated that the nanofibrous structure of PET mats was preserved after CDP surface modification process. PET/CDP nanofibers have shown rougher/irregular surface and larger fiber diameter when compared to untreated PET nanofibers. The surface analyses of PET/CDP nanofibers by XPS elucidated that CDP was present on the fiber surface. DMA analyses revealed the enhanced mechanical properties for PET/CDP where PET/CDP nanofibers have shown higher storage modulus and higher glass transition temperature compared to untreated PET nanofibers. It was observed that PET/CDP nanofibers can efficiently remove the polycyclic aromatic hydrocarbon (PAH) (e.g. phenanthrene) from aqueous solution.

These studies mentioned in the Chapter 3 shows that CD functionalized electrospun nanofibers/nanowebs can be very effective for molecular filtration due to the high surface-to-volume ratio, nanoporous structure and high adsorptive capacity of nanofibers, as well as inclusion complexation property of surface associated CD. The application area of these functional nanofibers can be altered depend on the used polymer type. For example, zein is a useful food packaging material, and therefore, zein/CD nanofibers and their nanowebs may have the potentials to be used as active food packaging materials since removal of unpleasant odors from the surroundings can be achieved by complexation with surface associated CD. In our study, we mainly focused the optimization of electrospinning of zein/CD nanofibers and their morphological, structural, surface and thermal characterizations. In order to show the applicability of these functional nanofibers for food packagaing, the studying with food components would be very interesting. On the other hand, nylon 6,6 and PET are suitable polymer types for filtration application, and our results suggest that nylon 6,6/CD and PET/CD nanofibrous membranes are well suited filtering materials for removal of VOC such as toluene, aniline in air filtration. Moreover, efficiently removal of a model PAH (phenanthrene) from aqueous solution by PET/CDP nanofibers indicated that they can be very good candidate as a filtering material for water purification and waste treatment owing to their very large surface area as well as inclusion complexation capability of surface associated CDP.

In the studies reported in Chapter 4, functional nanofibrous materials showing PCA properties which facilitate the degradation of organic contaminants in water under visible or UV light were obtained using electrospinning and ALD techniques. Since used low-temperatures make ALD technique more attractive for inorganic deposition on temperature-sensitive organic substrates, we produced polymer-ZnO nanofibers to obtain easily handled and folded free standing material that is useful for water filtration application. Furthermore, TiO_2-ZnO/ZnO-TiO_2 core-shell heterojunction (CSHJ) nanofibers were also obtained by combination of electrospinning and ALD to investigate of PCA of these novel samples.

- The study mentioned in the second part of Chapter 4 (4.2), polymer-inorganic core-shell nanofibers were produced by two-step approach; electrospinning and ALD. First, nylon 6,6 (polymeric core) nanofibers were obtained by electrospinning, and then, ZnO (inorganic shell) with precise thickness control, was deposited onto electrospun nylon 6,6 nanofibers using ALD technique. The bead-free and uniform nylon 6,6 nanofibers having different average fiber diameters (~80, ~240 and ~650 nm) were achieved by using two different solvent systems and polymer concentrations. ZnO layer of about 90 nm, having uniform thickness around the fiber structure, was successfully deposited onto the nylon 6,6 nanofibers. Due to the low deposition temperature utilized (200 ºC), ALD process did not deform the polymeric fiber structure, and highly conformal ZnO layer with precise thickness and composition over a large scale were accomplished regardless of the differences in fiber diameters. ZnO shell layer was found to have a polycrystalline nature with hexagonal wurtzite structure. The core-shell nylon 6,6-ZnO nanofiber mats were flexible due to the polymeric core component. Photocatalytic activity of the core-shell nylon 6,6-ZnO nanofiber mats were tested by following the photocatalytic decomposition of rhodamine-B dye. It was found that nylon 6,6-ZnO nanofiber mat, having thinner fiber diameter, has shown better photocatalytic efficiency due to higher surface area of this sample. These nylon 6,6-ZnO nanofiber mats have also shown structural stability and kept their photocatalytic activity for the 2nd cycle test.

- We report on the synthesis and PCA of electrospun poly (acrylonitrile) (PAN) nanofibrous mat decorated with nanoneedles of zinc oxide (ZnO) in the third part of Chapter 4 (4.3). Apart from a detailed morphological and structural characterization, the PCA has been carefully monitored and the results are discussed elaborately when juxtaposed with the photoluminescence. The present hierarchal homoassembled nanostructures are a combination of two types of ZnO with diverse optical qualities, i.e. (a) controlled deposition of ZnO coating on nanofibers with dominant oxygen vacancies and significant grain boundaries by ALD, and (b) growth of single crystalline ZnO nanoneedles with high optical quality on the ALD seeds via hydrothermal process. The needle structure (~25 nm in diameter with an aspect ratio of ~24) also supports the vectorial transport of photo-charge carriers, which is crucial for high catalytic activity. Furthermore, it is shown that enhanced PCA is because of the catalytic activity at surface defects (on ALD seed), valance band, and conduction band (of ZnO nanoneedles). PCA and durability of the PAN/ZnO nanofibrous mat has also been tested with aqueous solution of methylene blue and the results showed almost no decay in the catalytic activity of this material when reused.
- Oxygen vacancies (V_Os) in ZnO are well known to enhance the PCA, despite of various other intrinsic crystal defects. In this study we aim to elucidate the effect of zinc interstitials (Zn_i) and V_Os on the PCA, which has applied as well as fundamental interest. In order to achieve this one needs to overcome the major hurdle of fabricating ZnO with controlled defect density, where it is acknowledged that the defect level control in ZnO significantly hard. In the present context (4.4), we have fabricated nanostructures and thoroughly characterized for their morphological (SEM, TEM), structural (XRD, TEM), chemical (XPS) and optical (PL) properties. To fabricate the nanostructures, we have adopted ALD, a powerful bottom-up approach. However to control defects, we have chosen polysulfone electrospun nanofibers as a substrate on which non-uniform adsorption of ALD precursors is inevitable due to the differences in the hydrophilic nature of the functional groups. For the first 100 cycles, Zn_i are predominant to yield ZnO quantum dots (QDs), while the

presence of *V*os is negligible. As the ALD cycle number increases *V*os are introduced whereas the density of Zn_i is unchanged. We have employed photoluminescence (PL) spectra to identify and quantify the density of each defect for all samples. PCA studies are performed on all samples, and the percent change in the decay constant for each sample is juxtaposed with the relative densities of Zn_is and V_Os. A logical comparison on the relative defect densities of Zn_i and V_O suggested that the former are less efficient than the latter. This is because of the differences in the intrinsic nature and physical accessibility of the defects, while other reasons are elaborated

- On the other hand, heterojunction is a well-studied material combination in photocatalysis studies, majority of which aims to improve the efficacy of the catalysts. Architecting novel catalysts begs the question of which photo-generated charge carrier is more efficient in the process of catalysis and the associated mechanism. To address this issue we have fabricated CSHJ nanofibers from ZnO and TiO_2 in two combinations where only the 'shell' part of the heterojunction is exposed to the environment to participate in the photocatalysis. Core and shell structures were fabricated *via* electrospinning and atomic layer deposition, respectively which were then subjected to calcination. These CSHJ were characterized and studied for the photocatalytic activity (PCA). These two combinations expose *electrons* or *holes* selectively to the environment. Under suitable illumination of ZnO-TiO_2 CSHJ *e/h* pairs are created majorly in TiO_2 and *electrons* take part in catalysis (i.e. reduce the organic dye) at the conduction band or oxygen vacancy sites of 'shell' while *holes* migrate to the core of the structure. Conversely *holes* take part in catalysis and *electrons* diffuse to the core in the case of TiO_2-ZnO CSHJ. The results further revealed that TiO_2-ZnO CSHJ shows ~1.6 times faster PCA when compared to the ZnO-TiO_2 CSHJ because of efficient *hole* capture by oxygen vacancies, and lower mobility of *holes*.

Our findings mentioned in Chapter 4 suggested that the resulting nanofibers obtained by the combination of electrospinning and ALD are well suited and potential candidates for waste water treatment with solar energy where their

performance, structural stability and reusability are worth mentioning.can be a very good candidate as a filter material for water purification and organic waste treatment owing to their PCA properties. Our studies also deepen the understanding of PCA which lead the development of novel materials having high efficient PCA. On the other hand, the combination of electrospinning and ALD techniques offers a promising alternative approach for the fabrication of functional nanofibrous structures for filtration, catalysis, sensors, photonics, electronics, energy, and biotechnology, depending on the selection of polymer type and inorganic components.

Briefly, by functionalization of electrospun nanofibers using different approaches (incorporation of CD-IC or CD into nanofibers, surface modification of nanofibers by CDP, deposition of metal oxide onto surface of nanofibers via ALD), multifunctional nanofibrous materials that are suitable candidates for food packaging, and controlled/slow release systems, organic vapor treatment, water purification and waste treatment have been developed in this dissertation.

LIST OF PUBLICATIONS

20) ***F. Kayaci****, H. S. Sen, E. Durgun and T. Uyar "Electrospun Nylon 6,6 Nanofibers Functionalized with Cyclodextrins for Removal of Toluene Vapor"* ***Journal of Applied Polymer Science****.(submitted)*

19) *A. Haider, C. Ozgit-Akgun,* ***F. Kayaci****, A. K. Okyay, T. Uyar, N. Biyikli "Fabrication of AlN/BN Core/Shell Hollow Nanofibers by Electrospinning and Atomic Layer Deposition"* ***APL Materials*** 2, 096109, ***2014***. DOI: 10.1063/1.48947820

18) ***F. Kayaci****, S. Vempati, I. Donmez, N. Biyikli and T. Uyar "Role of Zinc Interstitials and Oxygen Vacancies of Zno in Photocatalysis: A Bottom-Up Approach to Control the Defect Density"* ***Nanoscale 2014***. DOI: 10.1039/c4nr01887g.

17) ***F. Kayaci****, H. S. Sen, E. Durgun and T. Uyar "Functional Electrospun Polymeric Nanofibers Incorporating Geraniol-Cyclodextrin Inclusion Complexes: High Thermal Stability and Enhanced Durability of Geraniol"* ***Food Research International*** *62C, 424-431,* ***2014***. DOI: 10.1016/j.foodres.2014.03.033.

16) *S. U. Demirci,* ***F. Kayaci****, T. Uyar, S. Timur and L. Toppare "Bioactive Surface Design Based on Functional Composite Electrospun Nanofibers for Biomolecule Immobilization and Biosensor Applications"* ***ACS Applied Materials & Interfaces*** *6(7), 5235-43,* ***2014***. DOI: 10.1021/am5005927.

15) ***F. Kayaci,*** *S. Vempati, C. Ozgit-Akgun, N. Biyikli and T. Uyar "Enhanced Photocatalytic Activity of Homoassembled ZnO Nanostructures on Electrospun Polymeric Nanofibres: A Combination of Atomic Layer Deposition and Hydrothermal Growth"* ***Applied Catalysis B: Environmental*** *156-157, 173-183,* ***2014***. DOI: 10.1016/j.apcatb.2014.03.004.

14) ***F. Kayaci,*** *S. Vempati, C. Ozgit-Akgun, I. Donmez, N. Biyikli and T. Uyar "Selective Isolation of Electron or Hole in Photocatalysis: ZnO-TiO2 and TiO_2-ZnO Core-Shell Structured Heterojunction Nanofibers via Electrospinning and Atomic Layer Deposition"* ***Nanoscale*** *6, 5735–5745,* ***2014 (FRONT COVER)***. DOI: 10.1039/C3NR06665G.

13) ***F. Kayaci*** *and T. Uyar "Electrospun Polyester/Cyclodextrin Nanofibers for Entrapment of Volatile Organic Compounds"* ***Polymer Engineering & Science*** *54, 7,* ***2014***. DOI: 10.1002/pen.23858.

12) ***F. Kayaci****, Y. Ertas and T. Uyar "Enhanced Thermal Stability of Eugenol by Cyclodextrin Inclusion Complex Encapsulated in Electrospun Polymeric*

Nanofibers" ***Journal of Agricultural and Food Chemistry*** *61 (34), 8156–8165,* ***2013****.* *DOI: 10.1021/jf402923c*.

11) F. Kayaci*, Z. Aytac and T. Uyar "Surface Modification of Electrospun Polyester Nanofibers with Cyclodextrin Polymer for the Removal of Phenanthrene from Aqueous Solution"* ***Journal of Hazardous Materials*** *261, 286-294,* ***2013****.* *DOI: 10.1016/j.jhazmat.2013.07.04*.

10) *B. Ortaç,* ***F. Kayaci****, H. A. Vural, A. E. Deniz, and T. Uyar "Photoluminescent electrospun polymeric nanofibers incorporating germanium nanocrystals"* ***Reactive and Functional Polymers*** *73, 1262-1267,* ***2013****.* *DOI: 10.1016/j.reactfunctpolym.2013.06.007*.

9) F. Kayaci*, O.C.O. Umu, T. Tekinay and T. Uyar "Antibacterial Electrospun Polylactic acid (PLA) Nanofibrous Webs Incorporating Triclosan/Cyclodextrin Inclusion Complexes"* ***Journal of Agricultural and Food Chemistry*** *61, 3901-3908,* ***2013****.* *DOI: 10.1021/jf400440b.*

8) F. Kayaci*, C. Ozgit-Akgun, N. Biyikli and T. Uyar "Surface-Decorated ZnO Nanoparticles and ZnO Nanocoating on Electrospun Polymeric Nanofibers by Atomic Layer Deposition for Flexible Photocatalytic Nanofibrous Membranes"* ***RSC Advances*** *3 (19), 6817–6820,* ***2013****.* *DOI: 10.1039/C3RA40359A.*

7) *I. Donmez,* ***F. Kayaci****, C.Ozgit-Akgun, T. Uyar and N. Biyikli "Fabrication of Hafnia Hollow Nanofibers by Atomic Layer Deposition Using Electrospun Nanofiber Templates"* ***Journal of Alloys and Compounds*** *559, 146-151,* ***2013****.* *DOI: 10.1016/j.jallcom.2013.01.064.*

6) *C. Ozgit-Akgun,* ***F. Kayaci****, I. Donmez, N. Biyikli and T. Uyar "Template-Based Synthesis of AlN Hollow Nanofibers via Plasma-Enhanced Atomic Layer Deposition"* ***Journal of the American Ceramic Society*** *96, 916-922,* ***2013****.* *DOI: 10.1111/jace.12030.*

5) F. Kayaci*, C. Ozgit-Akgun, I. Donmez, N. Biyikli and T. Uyar "Polymer-Inorganic Core-Shell Nanofibers by Electrospinning and Atomic Layer Deposition: Flexible Nylon-ZnO Core-Shell Nanofiber Mats and Their Photocatalytic Activity",* ***ACS Applied Materials & Interfaces*** *4, 6185-6194,* ***2012****.* *DOI: 10.1021/am3017976.*

4) F. Kayaci *and T. Uyar "Electrospinning of Zein Nanofibers Incorporating Cyclodextrins"* ***Carbohydrate Polymers*** *90, 558-568,* ***2012.*** *DOI: 10.1016/j.carbpol.2012.05.078.*

3) F. Kayaci *and T. Uyar "Encapsulation of Vanillin/Cyclodextrin Inclusion Complex in Electrospun Polyvinyl Alcohol (PVA) Nanowebs: Prolonged*

Shelf-Life and High Temperature Stability of Vanillin" ***Food Chemistry*** *133, 641-649,* ***2012****.* *DOI: 10.1016/j.foodchem.2012.01.040.*

2) F. Kayaci *and T. Uyar "Solid Inclusion Complexes of Vanillin with Cyclodextrins: Their Formation, Characterization, and High-Temperature Stability"* ***Journal of Agricultural and Food Chemistry*** *59 (21), 11772–11778,* ***2011****.* *DOI: 10.1021/jf202915c.*

1) *A.E. Deniz, A. Celebioglu,* ***F. Kayaci*** *and T. Uyar "Electrospun Polymeric Nanofibrous Composites Containing* TiO_2 *Short Nanofibers"* ***Materials Chemistry and Physics*** *129, 701-704,* ***2011****.* *DOI: 10.1016/j.matchemphys.2011.06.018.*

BIBLIOGRAPHY

1. Lu, X., C. Wang, and Y. Wei, *One-Dimensional Composite Nanomaterials: Synthesis by Electrospinning and Their Applications.* Small, 2009. **5**(21): p. 2349-2370.
2. Ramakrishna, S., et al., *Science and engineering of electrospun nanofibers for advances in clean energy, water filtration, and regenerative medicine.* Journal of materials science, 2010. **45**(23): p. 6283-6312.
3. Xia, Y., et al., *One-dimensional nanostructures: synthesis, characterization, and applications.* Advanced materials, 2003. **15**(5): p. 353-389.
4. Agarwal, S., A. Greiner, and J.H. Wendorff, *Electrospinning of manmade and biopolymer nanofibers—progress in techniques, materials, and applications.* Advanced functional materials, 2009. **19**(18): p. 2863-2879.
5. Celebioglu, A. and T. Uyar, *Electrospinning of nanofibers from non-polymeric systems: polymer-free nanofibers from cyclodextrin derivatives.* Nanoscale, 2012. **4**(2): p. 621-631.
6. Greiner, A. and J.H. Wendorff, *Electrospinning: a fascinating method for the preparation of ultrathin fibers.* Angewandte Chemie International Edition, 2007. **46**(30): p. 5670-5703.
7. Ramakrishna, S., et al., *An introduction to electrospinning and nanofibers*. Vol. 90. 2005: World Scientific.
8. Teo, W.-E. and S. Ramakrishna, *Electrospun nanofibers as a platform for multifunctional, hierarchically organized nanocomposite.* Composites Science and Technology, 2009. **69**(11): p. 1804-1817.
9. Agarwal, S. and A. Greiner, *On the way to clean and safe electrospinning—green electrospinning: emulsion and suspension electrospinning.* Polymers for Advanced Technologies, 2011. **22**(3): p. 372-378.
10. Wendorff, J.H., S. Agarwal, and A. Greiner, *Electrospinning: materials, processing, and applications*. 2012: John Wiley & Sons.
11. Kayaci, F., et al., *Polymer–inorganic core–shell nanofibers by electrospinning and atomic layer deposition: Flexible nylon–ZnO core–shell nanofiber mats and their photocatalytic activity.* ACS applied materials & interfaces, 2012. **4**(11): p. 6185-6194.
12. Li, D. and Y. Xia, *Electrospinning of nanofibers: reinventing the wheel?* Advanced materials, 2004. **16**(14): p. 1151-1170.
13. Deniz, A.E., et al., *Electrospun polymeric nanofibrous composites containing TiO_2 short nanofibers.* Materials Chemistry and Physics, 2011. **129**(3): p. 701-704.
14. Ortaç, B., et al., *Photoluminescent electrospun polymeric nanofibers incorporating germanium nanocrystals.* Reactive and Functional Polymers, 2013. **73**(9): p. 1262-1267.
15. Andrew, J. and D. Clarke, *Enhanced ferroelectric phase content of polyvinylidene difluoride fibers with the addition of magnetic nanoparticles.* Langmuir, 2008. **24**(16): p. 8435-8438.

16. Anitha, S., et al., *Optical, bactericidal and water repellent properties of electrospun nano-composite membranes of cellulose acetate and ZnO.* Carbohydrate Polymers, 2012. **87**(2): p. 1065-1072.
17. Dong, H., et al., *Assembly of metal nanoparticles on electrospun nylon 6 nanofibers by control of interfacial hydrogen-bonding interactions.* Chemistry of Materials, 2008. **20**(21): p. 6627-6632.
18. He, D., et al., *Large-scale synthesis of flexible free-standing SERS substrates with high sensitivity: electrospun PVA nanofibers embedded with controlled alignment of silver nanoparticles.* ACS nano, 2009. **3**(12): p. 3993-4002.
19. Roso, M., et al., *Multifunctional membranes based on spinning technologies: the synergy of nanofibers and nanoparticles.* Nanotechnology, 2008. **19**(28): p. 285707.
20. Zhang, P., et al., *In situ assembly of well-dispersed Ag nanoparticles (AgNPs) on electrospun carbon nanofibers (CNFs) for catalytic reduction of 4-nitrophenol.* Nanoscale, 2011. **3**(8): p. 3357-3363.
21. Xie, J., X. Li, and Y. Xia, *Putting electrospun nanofibers to work for biomedical research.* Macromolecular Rapid Communications, 2008. **29**(22): p. 1775-1792.
22. Sahay, R., et al., *Electrospun composite nanofibers and their multifaceted applications.* Journal of Materials Chemistry, 2012. **22**(26): p. 12953-12971.
23. Thavasi, V., G. Singh, and S. Ramakrishna, *Electrospun nanofibers in energy and environmental applications.* Energy & Environmental Science, 2008. **1**(2): p. 205-221.
24. Demirci Uzun, S., et al., *Bioactive Surface Design Based on Functional Composite Electrospun Nanofibers for Biomolecule Immobilization and Biosensor Applications.* ACS applied materials & interfaces, 2014. **6**(7): p. 5235-5243.
25. Yoon, K., B.S. Hsiao, and B. Chu, *Functional nanofibers for environmental applications.* Journal of Materials Chemistry, 2008. **18**(44): p. 5326-5334.
26. Kriegel, C., et al., *Fabrication, functionalization, and application of electrospun biopolymer nanofibers.* Critical reviews in food science and nutrition, 2008. **48**(8): p. 775-797.
27. Ignatova, M., N. Manolova, and I. Rashkov, *Electrospun Antibacterial Chitosan-Based Fibers.* Macromolecular bioscience, 2013. **13**(7): p. 860-872.
28. Torres-Giner, S., E. Gimenez, and J.M. Lagarón, *Characterization of the morphology and thermal properties of zein prolamine nanostructures obtained by electrospinning.* Food Hydrocolloids, 2008. **22**(4): p. 601-614.
29. Mascheroni, E., et al., *Encapsulation of volatiles in nanofibrous polysaccharide membranes for humidity-triggered release.* Carbohydrate Polymers, 2013. **98**(1): p. 17-25.
30. Kuan, C.-Y., et al., *Physicochemical characterization of alkali treated fractions from corncob and wheat straw and the production of nanofibres.* Food research international, 2011. **44**(9): p. 2822-2829.
31. Stijnman, A.C., I. Bodnar, and R. Hans Tromp, *Electrospinning of food-grade polysaccharides.* Food Hydrocolloids, 2011. **25**(5): p. 1393-1398.
32. Ge, L., et al., *Immobilization of glucose oxidase in electrospun nanofibrous membranes for food preservation.* Food Control, 2012. **26**(1): p. 188-193.

33. Kriegel, C., et al., *Nanofibers as carrier systems for antimicrobial microemulsions. Part I: fabrication and characterization.* Langmuir, 2008. **25**(2): p. 1154-1161.
34. Li, Y., L.T. Lim, and Y. Kakuda, *Electrospun Zein Fibers as Carriers to Stabilize (−)-Epigallocatechin Gallate.* Journal of food science, 2009. **74**(3): p. C233-C240.
35. Vega-Lugo, A.-C. and L.-T. Lim, *Controlled release of allyl isothiocyanate using soy protein and poly (lactic acid) electrospun fibers.* Food research international, 2009. **42**(8): p. 933-940.
36. Brahatheeswaran, D., et al., *Hybrid fluorescent curcumin loaded zein electrospun nanofibrous scaffold for biomedical applications.* Biomedical Materials, 2012. **7**(4): p. 045001.
37. Fernandez, A., S. Torres-Giner, and J.M. Lagaron, *Novel route to stabilization of bioactive antioxidants by encapsulation in electrospun fibers of zein prolamine.* Food Hydrocolloids, 2009. **23**(5): p. 1427-1432.
38. Neo, Y.P., et al., *Encapsulation of food grade antioxidant in natural biopolymer by electrospinning technique: A physicochemical study based on zein–gallic acid system.* Food chemistry, 2013. **136**(2): p. 1013-1021.
39. Fung, W.-Y., K.-H. Yuen, and M.-T. Liong, *Agrowaste-based nanofibers as a probiotic encapsulant: fabrication and characterization.* Journal of agricultural and food chemistry, 2011. **59**(15): p. 8140-8147.
40. Lagaron, J.M., *Multifunctional and nanoreinforced polymers for food packaging*. 2011: Elsevier.
41. Barhate, R. and S. Ramakrishna, *Nanofibrous filtering media: filtration problems and solutions from tiny materials.* Journal of Membrane Science, 2007. **296**(1): p. 1-8.
42. Dai, Y., et al., *Sorption of polycyclic aromatic hydrocarbons on electrospun nanofibrous membranes: Sorption kinetics and mechanism.* Journal of Hazardous Materials, 2011. **192**(3): p. 1409-1417.
43. Ahn, Y., et al., *Development of high efficiency nanofilters made of nanofibers.* Current Applied Physics, 2006. **6**(6): p. 1030-1035.
44. Balamurugan, R., S. Sundarrajan, and S. Ramakrishna, *Recent trends in nanofibrous membranes and their suitability for air and water filtrations.* Membranes, 2011. **1**(3): p. 232-248.
45. Barhate, R., C.K. Loong, and S. Ramakrishna, *Preparation and characterization of nanofibrous filtering media.* Journal of Membrane Science, 2006. **283**(1): p. 209-218.
46. Gopal, R., et al., *Electrospun nanofibrous filtration membrane.* Journal of Membrane Science, 2006. **281**(1): p. 581-586.
47. Huang, Z.-M., et al., *A review on polymer nanofibers by electrospinning and their applications in nanocomposites.* Composites Science and Technology, 2003. **63**(15): p. 2223-2253.
48. Patanaik, A., V. Jacobs, and R.D. Anandjiwala, *Performance evaluation of electrospun nanofibrous membrane.* Journal of Membrane Science, 2010. **352**(1): p. 136-142.

49. Podgórski, A., A. Bałazy, and L. Gradoń, *Application of nanofibers to improve the filtration efficiency of the most penetrating aerosol particles in fibrous filters.* Chemical Engineering Science, 2006. **61**(20): p. 6804-6815.
50. Ramaseshan, R. and S. Ramakrishna, *Zinc titanate nanofibers for the detoxification of chemical warfare simulants.* Journal of the American Ceramic Society, 2007. **90**(6): p. 1836-1842.
51. Ramaseshan, R., et al., *Functionalized polymer nanofibre membranes for protection from chemical warfare stimulants.* Nanotechnology, 2006. **17**(12): p. 2947.
52. Scholten, E., et al., *Electrospun polyurethane fibers for absorption of volatile organic compounds from air.* ACS applied materials & interfaces, 2011. **3**(10): p. 3902-3909.
53. Sundarrajan, S. and S. Ramakrishna, *Fabrication of nanocomposite membranes from nanofibers and nanoparticles for protection against chemical warfare stimulants.* Journal of materials science, 2007. **42**(20): p. 8400-8407.
54. Uyar, T., et al., *Cyclodextrin functionalized poly (methyl methacrylate)(PMMA) electrospun nanofibers for organic vapors waste treatment.* Journal of Membrane Science, 2010. **365**(1): p. 409-417.
55. Subramanian, S. and R. Seeram, *New directions in nanofiltration applications—Are nanofibers the right materials as membranes in desalination?* Desalination, 2013. **308**: p. 198-208.
56. Neghlani, P.K., M. Rafizadeh, and F.A. Taromi, *Preparation of aminated-polyacrylonitrile nanofiber membranes for the adsorption of metal ions: comparison with microfibers.* Journal of Hazardous Materials, 2011. **186**(1): p. 182-189.
57. Niu, J., et al., *Immobilization of horseradish peroxidase by electrospun fibrous membranes for adsorption and degradation of pentachlorophenol in water.* Journal of Hazardous Materials, 2013. **246**: p. 119-125.
58. Szejtli, J., *Introduction and general overview of cyclodextrin chemistry.* Chemical reviews, 1998. **98**(5): p. 1743-1754.
59. Del Valle, E.M., *Cyclodextrins and their uses: a review.* Process biochemistry, 2004. **39**(9): p. 1033-1046.
60. Hedges, A.R., *Industrial applications of cyclodextrins.* Chemical reviews, 1998. **98**(5): p. 2035-2044.
61. Marques, H.M.C., *A review on cyclodextrin encapsulation of essential oils and volatiles.* Flavour and fragrance journal, 2010. **25**(5): p. 313-326.
62. Vyas, A., S. Saraf, and S. Saraf, *Cyclodextrin based novel drug delivery systems.* Journal of inclusion phenomena and macrocyclic chemistry, 2008. **62**(1-2): p. 23-42.
63. Yang, G.-F., et al., *Bioactive permethrin/β-cyclodextrin inclusion complex.* The Journal of Physical Chemistry B, 2006. **110**(13): p. 7044-7048.
64. Zhu, X.-L., et al., *Preparation and characterization of inclusion complex of iprodione and β-cyclodextrin to improve fungicidal activity.* Journal of agricultural and food chemistry, 2007. **55**(9): p. 3535-3539.

65. Buschmann, H.-J., D. Knittel, and E. Schollmeyer, *New textile applications of cyclodextrins.* Journal of inclusion phenomena and macrocyclic chemistry, 2001. **40**(3): p. 169-172.
66. Nostro, P.L., L. Fratoni, and P. Baglioni, *Modification of a cellulosic fabric with β-cyclodextrin for textile finishing applications.* Journal of inclusion phenomena and macrocyclic chemistry, 2002. **44**(1-4): p. 423-427.
67. Szejtli, J., *Cyclodextrins in the textile industry.* Starch-Stärke, 2003. **55**(5): p. 191-196.
68. Samperio, C., et al., *Enhancement of plant essential oils' aqueous solubility and stability using alpha and beta cyclodextrin.* Journal of agricultural and food chemistry, 2010. **58**(24): p. 12950-12956.
69. Kant, A., et al., *Effect of β-cyclodextrin on aroma release and flavor perception.* Journal of agricultural and food chemistry, 2004. **52**(7): p. 2028-2035.
70. Kayaci, F. and T. Uyar, *Solid inclusion complexes of vanillin with cyclodextrins: their formation, characterization, and high-temperature stability.* Journal of agricultural and food chemistry, 2011. **59**(21): p. 11772-11778.
71. Huang, D., et al., *Development and validation of oxygen radical absorbance capacity assay for lipophilic antioxidants using randomly methylated β-cyclodextrin as the solubility enhancer.* Journal of agricultural and food chemistry, 2002. **50**(7): p. 1815-1821.
72. Koontz, J.L., et al., *Cyclodextrin inclusion complex formation and solid-state characterization of the natural antioxidants α-tocopherol and quercetin.* Journal of agricultural and food chemistry, 2009. **57**(4): p. 1162-1171.
73. Du Preez, J. and W. Yang, *Improving the aqueous solubility of triclosan by solubilization, complexation, and in situ salt formation.* J. Cosmet. Sci, 2003. **54**: p. 537-550.
74. Duan, M.S., et al., *Cyclodextrin solubilization of the antibacterial agents triclosan and triclocarban: formation of aggregates and higher-order complexes.* International journal of pharmaceutics, 2005. **297**(1): p. 213-222.
75. Guan, Y., L. Qian, and H. Xiao, *Novel Anti-Microbial Host-Guest Complexes Based on Cationic β-Cyclodextrin Polymers and Triclosan/Butylparaben.* Macromolecular Rapid Communications, 2007. **28**(23): p. 2244-2248.
76. Jug, M., et al., *Analysis of triclosan inclusion complexes with β-cyclodextrin and its water-soluble polymeric derivative.* Journal of pharmaceutical and biomedical analysis, 2011. **54**(5): p. 1030-1039.
77. Qian, L., Y. Guan, and H. Xiao, *Preparation and characterization of inclusion complexes of a cationic β-cyclodextrin polymer with butylparaben or triclosan.* International journal of pharmaceutics, 2008. **357**(1): p. 244-251.
78. Veiga, M., et al., *Comparative study on triclosan interactions in solution and in the solid state with natural and chemically modified cyclodextrins.* Journal of inclusion phenomena and macrocyclic chemistry, 2005. **53**(1-2): p. 77-83.
79. Laekeman, G., et al., *Eugenol a valuable compound for in vitro experimental research and worthwhile for further in vivo investigation.* Phytotherapy Research, 1990. **4**(3): p. 90-96.

80. Wang, T., et al., *Release characteristics and antibacterial activity of solid state eugenol/β-cyclodextrin inclusion complex.* Journal of inclusion phenomena and macrocyclic chemistry, 2011. **71**(1-2): p. 207-213.
81. Badr, T., K. Hanna, and C. De Brauer, *Enhanced solubilization and removal of naphthalene and phenanthrene by cyclodextrins from two contaminated soils.* Journal of Hazardous Materials, 2004. **112**(3): p. 215-223.
82. Crini, G. and M. Morcellet, *Synthesis and applications of adsorbents containing cyclodextrins.* J. Separ. Sci., 2002. **25**(13): p. 789-813.
83. Szejtli, J., *β-cyclodextrin enhanced biological detoxification of industrial wastewaters.* Water Res., 1988. **22**(11): p. 1345-1351.
84. Szente, L., É. Fenyvesi, and J. Szejtli, *Entrapment of iodine with cyclodextrins: potential application of cyclodextrins in nuclear waste management.* Environ. Sci.Technol., 1999. **33**(24): p. 4495-4498.
85. Uyar, T., et al., *Crystalline cyclodextrin inclusion compounds formed with aromatic guests: guest-dependent stoichiometries and hydration-sensitive crystal structures.* Crystal growth & design, 2006. **6**(5): p. 1113-1119.
86. Yudiarto, A., et al., *Separation of structural isomers using soluble β-cyclodextrin polymer by ultrafiltration.* Separation and purification technology, 2001. **24**(1): p. 243-253.
87. Morin-Crini, N. and G. Crini, *Environmental applications of water-insoluble β-cyclodextrin–epichlorohydrin polymers.* Progress in Polymer Science, 2013. **38**(2): p. 344-368.
88. Connors, K.A., *The stability of cyclodextrin complexes in solution.* Chemical reviews, 1997. **97**(5): p. 1325-1358.
89. Reineccius, T.A., G.A. Reineccius, and T.L. Peppard, *The effect of solvent interactions on α-, β-, and γ-cyclodextrin/flavor molecular inclusion complexes.* Journal of agricultural and food chemistry, 2005. **53**(2): p. 388-392.
90. Rekharsky, M.V. and Y. Inoue, *Complexation thermodynamics of cyclodextrins.* Chemical reviews, 1998. **98**(5): p. 1875-1918.
91. Vacca, P., et al., *Patterned organic and inorganic composites for electronic applications.* The Journal of Physical Chemistry C, 2009. **113**(14): p. 5777-5783.
92. Kim, P., et al., *High energy density nanocomposites based on surface-modified $BaTiO_3$ and a ferroelectric polymer.* ACS nano, 2009. **3**(9): p. 2581-2592.
93. Lu, P.-P., et al., *Processing–Structure–Property Correlations of Polyethersulfone/Perfluorosulfonic Acid Nanofibers Fabricated via Electrospinning from Polymer–Nanoparticle Suspensions.* ACS applied materials & interfaces, 2012. **4**(3): p. 1716-1723.
94. Zhu, J., et al., *Electrospun Polyimide Nanocomposite Fibers Reinforced with Core− Shell Fe-FeO Nanoparticles.* The Journal of Physical Chemistry C, 2010. **114**(19): p. 8844-8850.
95. Liu, L., et al., *Synthesis and white-light emission of ZnO/HfO_2: Eu nanocables.* Nanoscale research letters, 2010. **5**(9): p. 1418-1423.

96. Fragalà, M., et al., *Core–shell Zn-doped TiO_2–ZnO nanofibers fabricated via a combination of electrospinning and metal–organic chemical vapour deposition.* CrystEngComm, 2010. **12**(11): p. 3858-3865.
97. Zhou, X., et al., *Mesoporous Coaxial Titanium Nitride-Vanadium Nitride Fibers of Core–shell Structures for High-Performance Supercapacitors.* ACS applied materials & interfaces, 2011. **3**(8): p. 3058-3063.
98. Sun, Z., et al., *Compound Core–Shell Polymer Nanofibers by Co-Electrospinning.* Advanced materials, 2003. **15**(22): p. 1929-1932.
99. Zhang, Y., et al., *Preparation of core-shell structured PCL-r-gelatin bi-component nanofibers by coaxial electrospinning.* Chemistry of Materials, 2004. **16**(18): p. 3406-3409.
100. Chen, M., et al., *Thermo-responsive core− sheath electrospun nanofibers from poly (N-isopropylacrylamide)/polycaprolactone blends.* Chemistry of Materials, 2010. **22**(14): p. 4214-4221.
101. Gong, B. and G.N. Parsons, *Quantitative in situ infrared analysis of reactions between trimethylaluminum and polymers during Al_2O_3 atomic layer deposition.* Journal of Materials Chemistry, 2012. **22**(31): p. 15672-15682.
102. Hyde, G., et al., *Atomic layer deposition and biocompatibility of titanium nitride nano-coatings on cellulose fiber substrates.* Biomedical Materials, 2009. **4**(2): p. 025001.
103. Jur, J., et al., *Atomic Layer Deposition of Conductive Coatings on Cotton, Paper, and Synthetic Fibers: Conductivity Analysis and Functional Chemical Sensing Using "All-Fiber" Capacitors.* Advanced functional materials, 2011. **21**(11): p. 1993-2002.
104. Jur, J.S., et al., *Temperature-dependent subsurface growth during atomic layer deposition on polypropylene and cellulose fibers.* Langmuir, 2010. **26**(11): p. 8239-8244.
105. Kemell, M., et al., *Atomic layer deposition in nanometer-level replication of cellulosic substances and preparation of photocatalytic TiO_2/cellulose composites.* Journal of the American Chemical Society, 2005. **127**(41): p. 14178-14179.
106. Hyde, G.K., et al., *Atomic layer deposition and abrupt wetting transitions on nonwoven polypropylene and woven cotton fabrics.* Langmuir, 2009. **26**(4): p. 2550-2558.
107. Hyde, G.K., et al., *Atomic layer deposition of conformal inorganic nanoscale coatings on three-dimensional natural fiber systems: effect of surface topology on film growth characteristics.* Langmuir, 2007. **23**(19): p. 9844-9849.
108. Korhonen, J.T., et al., *Inorganic hollow nanotube aerogels by atomic layer deposition onto native nanocellulose templates.* ACS nano, 2011. **5**(3): p. 1967-1974.
109. Leskelä, M. and M. Ritala, *Atomic Layer Deposition Chemistry: Recent Developments and Future Challenges.* Angewandte Chemie International Edition, 2003. **42**(45): p. 5548-5554.
110. Detavernier, C., et al., *Tailoring nanoporous materials by atomic layer deposition.* Chemical Society Reviews, 2011. **40**(11): p. 5242-5253.

111. George, S.M., *Atomic layer deposition: an overview.* Chemical reviews, 2009. **110**(1): p. 111-131.
112. Hakim, L.F., S.M. George, and A.W. Weimer, *Conformal nanocoating of zirconia nanoparticles by atomic layer deposition in a fluidized bed reactor.* Nanotechnology, 2005. **16**(7): p. S375.
113. Peng, Q., et al., *Atomic layer deposition on electrospun polymer fibers as a direct route to Al_2O_3 microtubes with precise wall thickness control.* Nano letters, 2007. **7**(3): p. 719-722.
114. Peng, Q., et al., *Bi-directional Kirkendall effect in coaxial microtube nanolaminate assemblies fabricated by atomic layer deposition.* ACS nano, 2009. **3**(3): p. 546-554.
115. Kim, G.-M., et al., *Nanostructured pure anatase titania tubes replicated from electrospun polymer fiber templates by atomic layer deposition.* Chemistry of Materials, 2008. **20**(9): p. 3085-3091.
116. Santala, E., et al., *The preparation of reusable magnetic and photocatalytic composite nanofibers by electrospinning and atomic layer deposition.* Nanotechnology, 2009. **20**(3): p. 035602.
117. Cho, S., et al., *Ethanol sensors based on ZnO nanotubes with controllable wall thickness via atomic layer deposition, an O_2 plasma process and an annealing process.* Sensors and Actuators B: Chemical, 2012. **162**(1): p. 300-306.
118. Park, J.Y., S.-W. Choi, and S.S. Kim, *A synthesis and sensing application of hollow ZnO nanofibers with uniform wall thicknesses grown using polymer templates.* Nanotechnology, 2010. **21**(47): p. 475601.
119. Lee, B.-S., et al., *Fabrication of SnO_2 nanotube microyarn and its gas sensing behavior.* Smart Materials and Structures, 2011. **20**(10): p. 105019.
120. Ozgit-Akgun, C., et al., *Template-Based Synthesis of Aluminum Nitride Hollow Nanofibers Via Plasma-Enhanced Atomic Layer Deposition.* Journal of the American Ceramic Society, 2013. **96**(3): p. 916-922.
121. Donmez, I., et al., *Fabrication of hafnia hollow nanofibers by atomic layer deposition using electrospun nanofiber templates.* Journal of Alloys and Compounds, 2013. **559**: p. 146-151.
122. Heikkilä, P., et al., *High surface area nanostructured tubes prepared by dissolution of ALD-coated electrospun fibers.* Journal of materials science, 2012. **47**(8): p. 3607-3612.
123. Oldham, C.J., et al., *Encapsulation and chemical resistance of electrospun nylon nanofibers coated using integrated atomic and molecular layer deposition.* Journal of The Electrochemical Society, 2011. **158**(9): p. D549-D556.
124. Park, J.Y., et al., *Synthesis and Gas Sensing Properties of TiO_2–ZnO Core-Shell Nanofibers.* Journal of the American Ceramic Society, 2009. **92**(11): p. 2551-2554.
125. Choi, S.-W., J.Y. Park, and S.S. Kim, *Synthesis of SnO_2–ZnO core–shell nanofibers via a novel two-step process and their gas sensing properties.* Nanotechnology, 2009. **20**(46): p. 465603.

126. Li, Q., et al., *Antimicrobial nanomaterials for water disinfection and microbial control: potential applications and implications.* Water research, 2008. **42**(18): p. 4591-4602.
127. Meng, F., et al., *Recent advances in membrane bioreactors (MBRs): membrane fouling and membrane material.* Water research, 2009. **43**(6): p. 1489-1512.
128. Chen, T.-T., et al., *The exceptional photo-catalytic activity of ZnO/RGO composite via metal and oxygen vacancies.* Applied Catalysis B: Environmental, 2013. **142**: p. 442-449.
129. Hotchandani, S. and P.V. Kamat, *Charge-transfer processes in coupled semiconductor systems. Photochemistry and photoelectrochemistry of the colloidal cadmium sulfide-zinc oxide system.* The Journal of Physical Chemistry, 1992. **96**(16): p. 6834-6839.
130. Kayaci, F., et al., *Surface-decorated ZnO nanoparticles and ZnO nanocoating on electrospun polymeric nanofibers by atomic layer deposition for flexible photocatalytic nanofibrous membranes.* RSC Advances, 2013. **3**(19): p. 6817-6820.
131. Lee, H.U., et al., *Highly photocatalytic performance of flexible 3 dimensional (3D) ZnO nanocomposite.* Applied Catalysis B: Environmental, 2014. **144**: p. 83-89.
132. LingáYeh, C., *Photocatalytic CdSe QDs-decorated ZnO nanotubes: an effective photoelectrode for splitting water.* Chemical Communications, 2011. **47**(12): p. 3493-3495.
133. Pei, Z., et al., *Defect and its dominance in ZnO films: A new insight into the role of defect over photocatalytic activity.* Applied Catalysis B: Environmental, 2013. **142**: p. 736-743.
134. Pelaez, M., et al., *A review on the visible light active titanium dioxide photocatalysts for environmental applications.* Applied Catalysis B: Environmental, 2012. **125**: p. 331-349.
135. Xu, D.-X., et al., *Advanced near-infrared-driven photocatalyst: Fabrication, characterization, and photocatalytic performance of β-$NaYF_4$: Yb^{3+}, Tm^{3+}@ TiO_2 core@ shell microcrystals.* Applied Catalysis B: Environmental, 2013. **142**: p. 377-386.
136. Xu, F., et al., *Enhanced photocatalytic activity of hierarchical ZnO nanoplate-nanowire architecture as environmentally safe and facilely recyclable photocatalyst.* Nanoscale, 2011. **3**(12): p. 5020-5025.
137. Zuo, Y., et al., *Double-sided ZnO nanorod arrays on single-crystal Ag holed microdisks with enhanced photocataltytic efficiency.* Nanoscale, 2013. **5**(10): p. 4388-4394.
138. Hoffmann, M.R., et al., *Environmental applications of semiconductor photocatalysis.* Chemical reviews, 1995. **95**(1): p. 69-96.
139. Izumi, I., et al., *Heterogeneous photocatalytic oxidation of hydrocarbons on platinized titanium dioxide powders.* The Journal of Physical Chemistry, 1980. **84**(24): p. 3207-3210.
140. Matthews, R.W., *Photocatalytic oxidation of chlorobenzene in aqueous suspensions of titanium dioxide.* Journal of catalysis, 1986. **97**(2): p. 565-568.

141. Khin, M.M., et al., *A review on nanomaterials for environmental remediation.* Energy Environ. Sci., 2012. **5**(8): p. 8075-8109.
142. Chang, Z., *"Firecracker-shaped" ZnO/polyimide hybrid nanofibers via electrospinning and hydrothermal process.* Chemical Communications, 2011. **47**(15): p. 4427-4429.
143. Johnson, K.T., et al., *Self-assembled nanofibers from leucine derived amphiphiles as nanoreactors for growth of ZnO nanoparticles.* Chemical Communications, 2010. **46**(10): p. 1757-1759.
144. Liu, H., et al., *ZnO Nanofiber and Nanoparticle Synthesized Through Electrospinning and Their Photocatalytic Activity Under Visible Light.* Journal of the American Ceramic Society, 2008. **91**(4): p. 1287-1291.
145. Sugunan, A., et al., *Radially Oriented ZnO Nanowires on Flexible Poly-l-Lactide Nanofibers for Continuous-Flow Photocatalytic Water Purification.* Journal of the American Ceramic Society, 2010. **93**(11): p. 3740-3744.
146. Ochiai, T. and A. Fujishima, *Photoelectrochemical properties of TiO_2 photocatalyst and its applications for environmental purification.* Journal of Photochemistry and Photobiology C: Photochemistry Reviews, 2012. **13**(4): p. 247-262.
147. Shang, M., et al., *General Strategy for a Large-Scale Fabric with Branched Nanofiber–Nanorod Hierarchical Heterostructure: Controllable Synthesis and Applications.* Chemistry-A European Journal, 2010. **16**(37): p. 11412-11419.
148. Tada, H., T. Kiyonaga, and S.-i. Naya, *Rational design and applications of highly efficient reaction systems photocatalyzed by noble metal nanoparticle-loaded titanium (IV) dioxide.* Chemical Society Reviews, 2009. **38**(7): p. 1849-1858.
149. Zhao, T., et al., *Multichannel TiO_2 hollow fibers with enhanced photocatalytic activity.* Journal of Materials Chemistry, 2010. **20**(24): p. 5095-5099.
150. Vempati, S., et al., *Unusual photoresponse of indium doped ZnO/organic thin film heterojunction.* Applied physics letters, 2012. **100**(16): p. 162104.
151. Vempati, S., J. Mitra, and P. Dawson, *One-step synthesis of ZnO nanosheets: a blue-white fluorophore.* Nanoscale research letters, 2012. **7**(1): p. 1-10.
152. Daneshvar, N., D. Salari, and A. Khataee, *Photocatalytic degradation of azo dye acid red 14 in water on ZnO as an alternative catalyst to TiO_2.* Journal of Photochemistry and Photobiology A: Chemistry, 2004. **162**(2): p. 317-322.
153. Kayaci, F., et al., *Selective isolation of the electron or hole in photocatalysis: ZnO-TiO_2 and TiO_2-ZnO core-shell structured heterojunction nanofibers via electrospinning and atomic layer deposition.* Nanoscale, 2014. **6**(11): p. 5735-5745.
154. Zhang, N. and Y.-J. Xu, *Aggregation-and leaching-resistant, reusable, and multifunctional Pd@ CeO2 as a robust nanocatalyst achieved by a hollow core–shell strategy.* Chemistry of Materials, 2013. **25**(9): p. 1979-1988.
155. Zhang, N., S. Liu, and Y.-J. Xu, *Recent progress on metal core@ semiconductor shell nanocomposites as a promising type of photocatalyst.* Nanoscale, 2012. **4**(7): p. 2227-2238.

156. Yu, C., et al., *Novel hollow Pt-ZnO nanocomposite microspheres with hierarchical structure and enhanced photocatalytic activity and stability.* Nanoscale, 2013. **5**(5): p. 2142-2151.
157. Kayaci, F., et al., *Enhanced photocatalytic activity of homoassembled ZnO nanostructures on electrospun polymeric nanofibers: A combination of atomic layer deposition and hydrothermal growth.* Applied Catalysis B: Environmental, 2014. **156-157**: p. 173-183.
158. Nakamura, I., et al., *Role of oxygen vacancy in the plasma-treated TiO_2 photocatalyst with visible light activity for NO removal.* Journal of Molecular Catalysis A: Chemical, 2000. **161**(1): p. 205-212.
159. Pan, X., et al., *Defective TiO 2 with oxygen vacancies: synthesis, properties and photocatalytic applications.* Nanoscale, 2013. **5**(9): p. 3601-3614.
160. Nowotny, M., et al., *Defect chemistry of titanium dioxide. Application of defect engineering in processing of TiO2-based photocatalysts.* The Journal of Physical Chemistry C, 2008. **112**(14): p. 5275-5300.
161. Wang, J., et al., *Relationship between oxygen defects and the photocatalytic property of ZnO nanocrystals in nafion membranes.* Langmuir, 2008. **25**(2): p. 1218-1223.
162. Yu, C., et al., *Phase transformation synthesis of novel Ag_2O/Ag_2CO_3 heterostructures with high visible light efficiency in photocatalytic degradation of pollutants.* Advanced materials, 2014. **26**(6): p. 892-898.
163. Zeng, H., et al., *Blue Luminescence of ZnO Nanoparticles Based on Non-Equilibrium Processes: Defect Origins and Emission Controls.* Advanced functional materials, 2010. **20**(4): p. 561-572.
164. *Vacancies on cation and anion sublattices can be paired to form neutral (Schottky) defect, or a vacancy can be compensated by an interstitial of same atom. A paired vacancy and interstitial can also form a neutral defect (Frenkel).Hence the ionicity of intrinsic defect is controlled by the lattice, in contrast to doping where a successful doping depends on the ionicity of the dopant.*
165. Athauda, T.J., U. Butt, and R.R. Ozer, *One-dimensional hierarchical composite materials based on ZnO nanowires and electrospun blend nanofibers.* RSC Advances, 2013. **3**(44): p. 21431-21438.
166. Li, G., et al., *Morphology− Function Relationship of ZnO: Polar Planes, Oxygen Vacancies, and Activity.* The Journal of Physical Chemistry C, 2008. **112**(31): p. 11859-11864.
167. Vempati, S., et al., *Cobalt-doped ZnO nanowires on quartz: synthesis by simple chemical method and characterization.* Journal of Crystal Growth, 2012. **343**(1): p. 7-12.
168. Vempati, S., et al., *Solution-based synthesis of cobalt-doped ZnO thin films.* Thin Solid Films, 2012. **524**: p. 137-143.
169. Özgür, Ü., et al., *A comprehensive review of ZnO materials and devices.* Journal of Applied Physics, 2005. **98**(4): p. 041301.
170. Schmidt-Mende, L. and J.L. MacManus-Driscoll, *ZnO–nanostructures, defects, and devices.* Materials Today, 2007. **10**(5): p. 40-48.
171. Tuomisto, F., et al., *Evidence of the Zn vacancy acting as the dominant acceptor in n-type ZnO.* Physical Review Letters, 2003. **91**(20): p. 205502.

172. Ahn, C.H., et al., *A comparative analysis of deep level emission in ZnO layers deposited by various methods.* Journal of Applied Physics, 2009. **105**(1): p. 013502-013505.
173. Ye, J., et al., *Correlation between green luminescence and morphology evolution of ZnO films.* Applied Physics A, 2005. **81**(4): p. 759-762.
174. Choi, S.K., et al., *Photocatalytic comparison of TiO_2 nanoparticles and electrospun TiO_2 nanofibers: effects of mesoporosity and interparticle charge transfer.* The Journal of Physical Chemistry C, 2010. **114**(39): p. 16475-16480.
175. Vitchuli, N., et al., *Multifunctional ZnO/Nylon 6 nanofiber mats by an electrospinning–electrospraying hybrid process for use in protective applications.* Science and technology of advanced materials, 2011. **12**(5): p. 055004.
176. Bedford, N. and A. Steckl, *Photocatalytic self cleaning textile fibers by coaxial electrospinning.* ACS applied materials & interfaces, 2010. **2**(8): p. 2448-2455.
177. Agiral, A., H.S. Soo, and H. Frei, *Visible Light Induced Hole Transport from Sensitizer to Co_3O_4 Water Oxidation Catalyst across Nanoscale Silica Barrier with Embedded Molecular Wires.* Chemistry of Materials, 2013. **25**(11): p. 2264-2273.
178. Cho, S., et al., *Porous ZnO–ZnSe nanocomposites for visible light photocatalysis.* Nanoscale, 2012. **4**(6): p. 2066-2071.
179. Jiang, T., et al., *Carrier concentration-dependent electron transfer in Cu 2 O/ZnO nanorod arrays and their photocatalytic performance.* Nanoscale, 2013. **5**(7): p. 2938-2944.
180. Liu, L., et al., *In situ loading of ultra-small Cu 2 O particles on TiO 2 nanosheets to enhance the visible-light photoactivity.* Nanoscale, 2012. **4**(20): p. 6351-6359.
181. Wang, S., et al., *Synthesis and photocatalysis of hierarchical heteroassemblies of ZnO branched nanorod arrays on Ag core nanowires.* Nanoscale, 2012. **4**(19): p. 5895-5901.
182. Zhu, H., et al., *General synthesis of a mesoporous composite of metal oxide and silicate nanoparticles from a metal salt and laponite suspension for catalysis.* Chemistry of Materials, 2006. **18**(17): p. 3993-4001.
183. Zong, X., et al., *Enhancement of photocatalytic H_2 evolution on CdS by loading MoS_2 as cocatalyst under visible light irradiation.* Journal of the American Chemical Society, 2008. **130**(23): p. 7176-7177.
184. Athauda, T.J., P. Hari, and R.R. Ozer, *Tuning physical and optical properties of ZnO nanowire arrays grown on cotton fibers.* ACS applied materials & interfaces, 2013. **5**(13): p. 6237-6246.
185. Athauda, T.J. and R.R. Ozer, *Nylon fibers as template for the controlled growth of highly oriented single crystalline ZnO nanowires.* Crystal growth & design, 2013. **13**(6): p. 2680-2686.
186. Gong, B., et al., *Highly active photocatalytic ZnO nanocrystalline rods supported on polymer fiber mats: Synthesis using atomic layer deposition and hydrothermal crystal growth.* Applied Catalysis A: General, 2011. **407**(1): p. 211-216.

187. Caleb, O.J., et al., *Modified Atmosphere Packaging Technology of Fresh and Fresh-cut Produce and the Microbial Consequences—A Review.* Food and Bioprocess Technology, 2013. **6**(2): p. 303-329.
188. Majeed, K., et al., *Potential materials for food packaging from nanoclay/natural fibres filled hybrid composites.* Materials & Design, 2013. **46**: p. 391-410.
189. Appendini, P. and J.H. Hotchkiss, *Review of antimicrobial food packaging.* Innovative Food Science & Emerging Technologies, 2002. **3**(2): p. 113-126.
190. Del Nobile, M., et al., *Antimicrobial efficacy and release kinetics of thymol from zein films.* Journal of Food Engineering, 2008. **89**(1): p. 57-63.
191. Rodriguez, A., C. Nerin, and R. Batlle, *New cinnamon-based active paper packaging against Rhizopusstolonifer food spoilage.* Journal of agricultural and food chemistry, 2008. **56**(15): p. 6364-6369.
192. de Oliveira, T.M., et al., *Development and evaluation of antimicrobial natamycin-incorporated film in gorgonzola cheese conservation.* Packaging Technology and Science, 2007. **20**(2): p. 147-153.
193. Schirmer, B.C., et al., *A novel packaging method with a dissolving CO_2 headspace combined with organic acids prolongs the shelf life of fresh salmon.* International journal of food microbiology, 2009. **133**(1): p. 154-160.
194. Appendini, P. and J.H. Hotchkiss, *Immobilization of lysozyme on food contact polymers as potential antimicrobial films.* Packaging Technology and Science, 1997. **10**(5): p. 271-279.
195. Wang, J., et al., *Physicochemical and release characterisation of garlic oil-β-cyclodextrin inclusion complexes.* Food chemistry, 2011. **127**(4): p. 1680-1685.
196. Uyar, T., J. Hacaloglu, and F. Besenbacher, *Electrospun polystyrene fibers containing high temperature stable volatile fragrance/flavor facilitated by cyclodextrin inclusion complexes.* Reactive and Functional Polymers, 2009. **69**(3): p. 145-150.
197. Uyar, T., J. Hacaloglu, and F. Besenbacher, *Electrospun polyethylene oxide (PEO) nanofibers containing cyclodextrin inclusion complex.* Journal of nanoscience and nanotechnology, 2011. **11**(5): p. 3949-3958.
198. Uyar, T., et al., *Electrospinning of functional poly (methyl methacrylate) nanofibers containing cyclodextrin-menthol inclusion complexes.* Nanotechnology, 2009. **20**(12): p. 125703.
199. Kayaci, F., Y. Ertas, and T. Uyar, *Enhanced thermal stability of eugenol by cyclodextrin inclusion complex encapsulated in electrospun polymeric nanofibers.* Journal of agricultural and food chemistry, 2013. **61**(34): p. 8156-8165.
200. Kayaci, F., et al., *Functional electrospun polymeric nanofibers incorporating geraniol–cyclodextrin inclusion complexes: High thermal stability and enhanced durability of geraniol.* Food research international, 2014. **62**: p. 424-431.
201. Kayaci, F., et al., *Antibacterial electrospun poly (lactic acid)(PLA) nanofibrous webs incorporating triclosan/cyclodextrin inclusion complexes.* Journal of agricultural and food chemistry, 2013. **61**(16): p. 3901-3908.

202. Kayaci, F. and T. Uyar, *Encapsulation of vanillin/cyclodextrin inclusion complex in electrospun polyvinyl alcohol (PVA) nanowebs: prolonged shelf-life and high temperature stability of vanillin.* Food chemistry, 2012. **133**(3): p. 641-649.
203. Anklam, E., S. Gaglione, and A. Müller, *Oxidation behaviour of vanillin in dairy products.* Food chemistry, 1997. **60**(1): p. 43-51.
204. Karathanos, V.T., et al., *Study of the solubility, antioxidant activity and structure of inclusion complex of vanillin with β-cyclodextrin.* Food chemistry, 2007. **101**(2): p. 652-658.
205. Tai, A., et al., *Evaluation of antioxidant activity of vanillin by using multiple antioxidant assays.* Biochimica et Biophysica Acta (BBA)-General Subjects, 2011. **1810**(2): p. 170-177.
206. Astray, G., et al., *Factors controlling flavors binding constants to cyclodextrins and their applications in foods.* Food research international, 2010. **43**(4): p. 1212-1218.
207. Divakar, S., *Structure of a. beta.-cyclodextrin-vanillin inclusion complex.* Journal of agricultural and food chemistry, 1990. **38**(4): p. 940-944.
208. Divakar, S. and M. Maheswaran, *Structural studies on inclusion compounds of β-cyclodextrin with some substituted phenols.* Journal of inclusion phenomena and molecular recognition in chemistry, 1997. **27**(2): p. 113-126.
209. Pîrnau, A., M. Bogdan, and C.G. Floare. *NMR spectroscopic characterization of β-cyclodextrin inclusion complex with vanillin*. in *Journal of Physics: Conference Series*. 2009: IOP Publishing.
210. DeMerlis, C. and D. Schoneker, *Review of the oral toxicity of polyvinyl alcohol (PVA).* Food and Chemical Toxicology, 2003. **41**(3): p. 319-326.
211. Cheng, S.-S., et al., *Antifungal activity of cinnamaldehyde and eugenol congeners against wood-rot fungi.* Bioresource technology, 2008. **99**(11): p. 5145-5149.
212. Atsumi, T., S. Fujisawa, and K. Tonosaki, *A comparative study of the antioxidant/prooxidant activities of eugenol and isoeugenol with various concentrations and oxidation conditions.* Toxicology in vitro, 2005. **19**(8): p. 1025-1033.
213. Shimoda, K., et al., *Biotransformation of thymol, carvacrol, and eugenol by cultured cells of Eucalyptus perriniana.* Phytochemistry, 2006. **67**(20): p. 2256-2261.
214. Choi, M.-J., et al., *Physical and light oxidative properties of eugenol encapsulated by molecular inclusion and emulsion–diffusion method.* Food research international, 2009. **42**(1): p. 148-156.
215. Chun, J.-Y., et al., *Characterization of β-cyclodextrin self-aggregates for eugenol encapsulation.* Journal of Food Engineering, 2012. **8**(2): p. 17.
216. Gomes, C., R.G. Moreira, and E. Castell-Perez, *Microencapsulated antimicrobial compounds as a means to enhance electron beam irradiation treatment for inactivation of pathogens on fresh spinach leaves.* Journal of food science, 2011. **76**(6): p. E479-E488.
217. Zhan, H., et al., *Molecular microcapsules and inclusion interactions of eugenol with β-cyclodextrin and its derivatives.* European Food Research and Technology, 2008. **227**(5): p. 1507-1513.

218. Solórzano-Santos, F. and M.G. Miranda-Novales, *Essential oils from aromatic herbs as antimicrobial agents.* Current opinion in biotechnology, 2012. **23**(2): p. 136-141.
219. Chen, W. and A. Viljoen, *Geraniol—A review of a commercially important fragrance material.* South African Journal of Botany, 2010. **76**(4): p. 643-651.
220. Lapczynski, A., et al., *Fragrance material review on geraniol.* Food and Chemical Toxicology, 2008. **46**(11): p. S160-S170.
221. Holm, V.K., G. Mortensen, and J. Risbo, *Quality changes in semi-hard cheese packaged in a poly (lactic acid) material.* Food chemistry, 2006. **97**(3): p. 401-410.
222. Siracusa, V., et al., *Poly (lactic acid)-modified films for food packaging application: Physical, mechanical, and barrier behavior.* Journal of applied polymer science, 2012. **125**(S2): p. E390-E401.
223. Vink, E.T., et al., *Applications of life cycle assessment to NatureWorks™ polylactide (PLA) production.* Polymer Degradation and stability, 2003. **80**(3): p. 403-419.
224. Peng, H., et al., *Vanillin cross-linked chitosan microspheres for controlled release of resveratrol.* Food chemistry, 2010. **121**(1): p. 23-28.
225. Lin, S.-Y., C.-H. Hsu, and M.-T. Sheu, *Curve-fitting FTIR studies of loratadine/hydroxypropyl-β-cyclodextrin inclusion complex induced by co-grinding process.* Journal of pharmaceutical and biomedical analysis, 2010. **53**(3): p. 799-803.
226. Singh, R., et al., *Characterization of cyclodextrin inclusion complexes—a review.* J. Pharm. Sci. Technol, 2010. **2**(3): p. 171-183.
227. Harata, K., *Structural aspects of stereodifferentiation in the solid state.* Chemical reviews, 1998. **98**(5): p. 1803-1827.
228. Saenger, W., et al., *Structures of the common cyclodextrins and their larger analogues beyond the doughnut.* Chemical reviews, 1998. **98**(5): p. 1787-1802.
229. Harada, A., et al., *Preparation and characterization of inclusion complexes of poly (propylene glycol) with cyclodextrins.* Macromolecules, 1995. **28**(24): p. 8406-8411.
230. Rusa, C.C., et al., *Inclusion compound formation with a new columnar cyclodextrin host.* Langmuir, 2002. **18**(25): p. 10016-10023.
231. Celebioglu, A. and T. Uyar, *Electrospinning of polymer-free nanofibers from cyclodextrin inclusion complexes.* Langmuir, 2011. **27**(10): p. 6218-6226.
232. Giordano, F., C. Novak, and J.R. Moyano, *Thermal analysis of cyclodextrins and their inclusion compounds.* Thermochimica Acta, 2001. **380**(2): p. 123-151.
233. Uyar, T., et al., *The solid channel structure inclusion complex formed between guest styrene and host γ-cyclodextrin.* Journal of inclusion phenomena and macrocyclic chemistry, 2006. **55**(1-2): p. 109-121.
234. Marcolino, V.A., et al., *Interaction of curcumin and bixin with β-cyclodextrin: complexation methods, stability, and applications in food.* Journal of agricultural and food chemistry, 2011. **59**(7): p. 3348-3357.

235. Chiellini, E., et al., *Environmentally Degradable Bio-Based Polymeric Blends and Composites.* Macromolecular bioscience, 2004. **4**(3): p. 218-231.
236. Tripathi, S., G. Mehrotra, and P. Dutta, *Physicochemical and bioactivity of cross-linked chitosan–PVA film for food packaging applications.* International Journal of Biological Macromolecules, 2009. **45**(4): p. 372-376.
237. Wu, J.G., P.J. Wang, and S.C. Chen, *Antioxidant and Antimicrobial Effectiveness of Catechin-Impregnated PVA–Starch Film on Red Meat.* Journal of Food Quality, 2010. **33**(6): p. 780-801.
238. Taepaiboon, P., U. Rungsardthong, and P. Supaphol, *Drug-loaded electrospun mats of poly (vinyl alcohol) fibres and their release characteristics of four model drugs.* Nanotechnology, 2006. **17**(9): p. 2317.
239. Ren, G., et al., *Electrospun poly (vinyl alcohol)/glucose oxidase biocomposite membranes for biosensor applications.* Reactive and Functional Polymers, 2006. **66**(12): p. 1559-1564.
240. Park, J.H., et al., *Electrospinning fabrication and characterization of poly (vinyl alcohol)/montmorillonite/silver hybrid nanofibers for antibacterial applications.* Colloid and Polymer Science, 2010. **288**(1): p. 115-121.
241. Bhardwaj, N. and S.C. Kundu, *Electrospinning: a fascinating fiber fabrication technique.* Biotechnology advances, 2010. **28**(3): p. 325-347.
242. Uyar, T. and F. Besenbacher, *Electrospinning of uniform polystyrene fibers: The effect of solvent conductivity.* Polymer, 2008. **49**(24): p. 5336-5343.
243. Paramera, E.I., S.J. Konteles, and V.T. Karathanos, *Stability and release properties of curcumin encapsulated in Saccharomyces cerevisiae, β-cyclodextrin and modified starch.* Food chemistry, 2011. **125**(3): p. 913-922.
244. Tsai, Y., et al., *Preparation, characterisation and activity of the inclusion complex of paeonol with β-cyclodextrin.* Food chemistry, 2010. **120**(3): p. 837-841.
245. Nuchuchua, O., et al., *Physicochemical investigation and molecular modeling of cyclodextrin complexation mechanism with eugenol.* Food research international, 2009. **42**(8): p. 1178-1185.
246. Sajomsang, W., et al., *Water-soluble β-cyclodextrin grafted with chitosan and its inclusion complex as a mucoadhesive eugenol carrier.* Carbohydrate Polymers, 2012. **89**(2): p. 623-631.
247. Chahal, R.P., et al., *γ-Irradiated PVA/Ag nanocomposite films: Materials for optical applications.* Journal of Alloys and Compounds, 2012. **538**: p. 212-219.
248. Yang, Y. and L.X. Song, *Study on the inclusion compounds of eugenol with α-, β-, γ-and heptakis (2, 6-di-O-methyl)-β-cyclodextrins.* Journal of inclusion phenomena and macrocyclic chemistry, 2005. **53**(1-2): p. 27-33.
249. Locci, E., et al., *13C-CPMAS and 1H-NMR Study of the Inclusion Complexes of β-Cyclodextrin with Carvacrol, Thymol, and Eugenol Prepared in Supercritical Carbon Dioxide.* Chemistry & biodiversity, 2004. **1**(9): p. 1354-1366.
250. Hernández, R., et al., *Controlling PVA hydrogels with γ-cyclodextrin.* Macromolecules, 2004. **37**(25): p. 9620-9625.
251. Hohenberg, P. and W. Kohn, *Inhomogeneous electron gas.* Physical review, 1964. **136**(3B): p. B864.

252. Kohn, W. and L.J. Sham, *Self-consistent equations including exchange and correlation effects.* Physical review, 1965. **140**(4A): p. A1133.
253. Kresse, G. and J. Furthmüller, *Efficiency of ab-initio total energy calculations for metals and semiconductors using a plane-wave basis set.* Computational Materials Science, 1996. **6**(1): p. 15-50.
254. Kresse, G. and J. Furthmüller, *Efficient iterative schemes for ab initio total-energy calculations using a plane-wave basis set.* Physical Review B, 1996. **54**(16): p. 11169.
255. Perdew, J.P., et al., *Atoms, molecules, solids, and surfaces: Applications of the generalized gradient approximation for exchange and correlation.* Physical Review B, 1992. **46**(11): p. 6671.
256. Grimme, S., *Semiempirical GGA-type density functional constructed with a long-range dispersion correction.* Journal of computational chemistry, 2006. **27**(15): p. 1787-1799.
257. Blöchl, P.E., *Projector augmented-wave method.* Physical Review B, 1994. **50**(24): p. 17953.
258. Manor, P.C. and W. Saenger, *Topography of cyclodextrin inclusion complexes. III. Crystal and molecular structure of cyclohexaamylose hexahydrate, the water dimer inclusion complex.* Journal of the American Chemical Society, 1974. **96**(11): p. 3630-3639.
259. Puliti, R., C.A. Mattia, and L. Paduano, *Crystal structure of a new α-cyclodextrin hydrate form. Molecular geometry and packing features: disordered solvent contribution.* Carbohydrate Research, 1998. **310**(1): p. 1-8.
260. Lindner, K. and W. Saenger, *Crystal and molecular structure of cyclohepta-amylose dodecahydrate.* Carbohydrate Research, 1982. **99**(2): p. 103-115.
261. Harata, K., *The Structure of the Cyclodextrin Complex. XX. Crystal Structure of Uncomplexed Hydrated'y-Cyclodextrin.* Structure, 1987.
262. Allen, F.H., *The Cambridge Structural Database: a quarter of a million crystal structures and rising.* Acta Crystallographica Section B: Structural Science, 2002. **58**(3): p. 380-388.
263. Snor, W., et al., *Density functional calculations on meloxicam–β-cyclodextrin inclusion complexes.* International journal of pharmaceutics, 2009. **381**(2): p. 146-152.
264. Lu, J., et al., *Formation of antibiotic, biodegradable polymers by processing with Irgasan DP300R (triclosan) and its inclusion compound with β-cyclodextrin.* Journal of applied polymer science, 2001. **82**(2): p. 300-309.
265. Li, L. and Y.-L. Hsieh, *Ultra-fine polyelectrolyte fibers from electrospinning of poly (acrylic acid).* Polymer, 2005. **46**(14): p. 5133-5139.
266. Uyar, T., et al., *Functional electrospun polystyrene nanofibers incorporating α-, β-, and γ-cyclodextrins: comparison of molecular filter performance.* ACS nano, 2010. **4**(9): p. 5121-5130.
267. Uyar, T., et al., *Molecular filters based on cyclodextrin functionalized electrospun fibers.* Journal of Membrane Science, 2009. **332**(1): p. 129-137.
268. Zhang, W., M. Chen, and G. Diao, *Electrospinning β-cyclodextrin/poly (vinyl alcohol) nanofibrous membrane for molecular capture.* Carbohydrate Polymers, 2011. **86**(3): p. 1410-1416.

269. Bai, J., et al., *Preparation of composite nanofibers containing gold nanoparticles by using poly (N-vinylpyrrolidone) and β-cyclodextrin.* Materials Chemistry and Physics, 2008. **111**(2): p. 205-208.
270. Chae, H.H., et al., *Synthesis and antibacterial performance of size-tunable silver nanoparticles with electrospun nanofiber composites.* Synthetic Metals, 2011. **161**(19): p. 2124-2128.
271. Kayaci, F. and T. Uyar, *Electrospun polyester/cyclodextrin nanofibers for entrapment of volatile organic compounds.* Polymer Engineering & Science, 2014.
272. Paraman, I. and B.P. Lamsal, *Recovery and characterization of α-zein from corn fermentation coproducts.* Journal of agricultural and food chemistry, 2011. **59**(7): p. 3071-3077.
273. Selling, G.W. and K.K. Woods, *Improved isolation of zein from corn gluten meal using acetic acid and isolate characterization as solvent.* Cereal chemistry, 2008. **85**(2): p. 202-206.
274. Alkan, D., et al., *Development of flexible antimicrobial packaging materials against Campylobacter jejuni by incorporation of gallic acid into zein-based films.* Journal of agricultural and food chemistry, 2011. **59**(20): p. 11003-11010.
275. Parris, N., P.H. Cooke, and K.B. Hicks, *Encapsulation of essential oils in zein nanospherical particles.* Journal of agricultural and food chemistry, 2005. **53**(12): p. 4788-4792.
276. Sanchez-Garcia, M.D., L. Hilliou, and J.M. Lagaron, *Nanobiocomposites of carrageenan, zein, and mica of interest in food packaging and coating applications.* Journal of agricultural and food chemistry, 2010. **58**(11): p. 6884-6894.
277. Shi, K., J.L. Kokini, and Q. Huang, *Engineering zein films with controlled surface morphology and hydrophilicity.* Journal of agricultural and food chemistry, 2009. **57**(6): p. 2186-2192.
278. Zhong, Q., et al., *Sustained release of lysozyme from zein microcapsules produced by a supercritical anti-solvent process.* Food chemistry, 2009. **115**(2): p. 697-700.
279. Jiang, H., P. Zhao, and K. Zhu, *Fabrication and Characterization of Zein-Based Nanofibrous Scaffolds by an Electrospinning Method.* Macromolecular bioscience, 2007. **7**(4): p. 517-525.
280. Jiang, Q., N. Reddy, and Y. Yang, *Cytocompatible cross-linking of electrospun zein fibers for the development of water-stable tissue engineering scaffolds.* Acta biomaterialia, 2010. **6**(10): p. 4042-4051.
281. Jiang, Q. and Y. Yang, *Water-stable electrospun zein fibers for potential drug delivery.* Journal of Biomaterials Science, Polymer Edition, 2011. **22**(10): p. 1393-1408.
282. Miyoshi, T., K. Toyohara, and H. Minematsu, *Preparation of ultrafine fibrous zein membranes via electrospinning.* Polymer international, 2005. **54**(8): p. 1187-1190.
283. Selling, G.W., et al., *Impact of solvent on electrospinning of zein and analysis of resulting fibers.* Macromolecular Chemistry and Physics, 2007. **208**(9): p. 1002-1010.

284. Selling, G.W., et al., *Electrospun zein fibers using glutaraldehyde as the crosslinking reagent: Effect of time and temperature.* Macromolecular Chemistry and Physics, 2008. **209**(10): p. 1003-1011.
285. Yao, C., et al., *Biodegradable nanofibrous membrane of zein/silk fibroin by electrospinning.* Polymer international, 2009. **58**(4): p. 396-402.
286. Yao, C., X. Li, and T. Song, *Fabrication of zein/hyaluronic acid fibrous membranes by electrospinning.* Journal of Biomaterials Science, Polymer Edition, 2007. **18**(6): p. 731-742.
287. Kayaci, F. and T. Uyar, *Electrospun zein nanofibers incorporating cyclodextrins.* Carbohydrate Polymers, 2012. **90**(1): p. 558-568.
288. Homaeigohar, S. and M. Elbahri, *Nanocomposite Electrospun Nanofiber Membranes for Environmental Remediation.* Materials, 2014. **7**(2): p. 1017-1045.
289. Mo, J., et al., *Photocatalytic purification of volatile organic compounds in indoor air: a literature review.* Atmos. Environ., 2009. **43**(14): p. 2229-2246.
290. Organization, W.H., *Indoor air quality: organic pollutants.* 1989.
291. Wang, S., H. Ang, and M.O. Tade, *Volatile organic compounds in indoor environment and photocatalytic oxidation: state of the art.* Environ. Int., 2007. **33**(5): p. 694-705.
292. Kim, Y.M., S. Harrad, and R.M. Harrison, *Concentrations and sources of VOCs in urban domestic and public microenvironments.* Environ. Sci.Technol., 2001. **35**(6): p. 997-1004.
293. Gopal, R., et al., *Electrospun nanofibrous polysulfone membranes as pre-filters: particulate removal.* J. Membr. Sci., 2007. **289**(1): p. 210-219.
294. Matsumoto, H. and A. Tanioka, *Functionality in electrospun nanofibrous membranes based on fiber's size, surface area, and molecular orientation.* Membranes, 2011. **1**(3): p. 249-264.
295. Celebioglu, A., S. Demirci, and T. Uyar, *Cyclodextrin-Grafted Electrospun Cellulose Acetate Nanofibers via "Click" Reaction for Removal of Phenanthrene.* Appl. Surf. Sci., 2014.
296. Dasari, A., et al., *Antifouling membranes prepared by electrospinning polylactic acid containing biocidal nanoparticles.* Journal of Membrane Science, 2012. **405**: p. 134-140.
297. Kim, H.J., et al., *Composite electrospun fly ash/polyurethane fibers for absorption of volatile organic compounds from air.* Chem. Eng. J. , 2013. **230**: p. 244-250.
298. Kaur, S., et al., *Oligosaccharide functionalized nanofibrous membrane.* International Journal of Nanoscience, 2006. **5**(01): p. 1-11.
299. Kayaci, F., Z. Aytac, and T. Uyar, *Surface modification of electrospun polyester nanofibers with cyclodextrin polymer for the removal of phenanthrene from aqueous solution.* Journal of Hazardous Materials, 2013. **261**: p. 286-294.
300. Kim, H. and A.H. Jadhav, *Preparation and application of supramolecular assembled β-cyclodextrin/polyacrylonitrile composite nanofibers as a highly efficient adsorbent for dye removal*, in *Advanced Materials Research*. 2013. p. 827-832.

301. Zhang, W., et al., *Correlation of polymer-like solution behaviors with electrospun fiber formation of hydroxypropyl-β-cyclodextrin and the adsorption study on the fiber.* Physical Chemistry Chemical Physics, 2012. **14**(27): p. 9729-9737.
302. Heikkilä, P., et al., *Electrospinning of polyamides with different chain compositions for filtration application.* Polymer Engineering & Science, 2008. **48**(6): p. 1168-1176.
303. Huang, L. and J.R. McCutcheon, *Hydrophilic nylon 6, 6 nanofibers supported thin film composite membranes for engineered osmosis.* Journal of Membrane Science, 2014. **457**: p. 162-169.
304. Abdel-Halim, E., et al., *Incorporation of chlorohexidin diacetate into cotton fabrics grafted with glycidyl methacrylate and cyclodextrin.* Carbohydrate Polymers, 2010. **79**(1): p. 47-53.
305. Martel, B., et al., *Grafting of cyclodextrins onto polypropylene nonwoven fabrics for the manufacture of reactive filters. III. Study of the sorption properties.* Journal of applied polymer science, 2002. **85**(8): p. 1771-1778.
306. Nostro, P.L., et al., *Surface treatments on Tencel fabric: Grafting with β-cyclodextrin.* Journal of applied polymer science, 2003. **88**(3): p. 706-715.
307. Romi, R., et al., *Bioengineering of a cellulosic fabric for insecticide delivery via grafted cyclodextrin.* Biotechnology progress, 2005. **21**(6): p. 1724-1730.
308. Blanchemain, N., et al., *Vascular prostheses with controlled release of antibiotics: Part 1: Surface modification with cyclodextrins of PET prostheses.* Biomolecular engineering, 2007. **24**(1): p. 149-153.
309. Blanchemain, N., et al., *In vitro study of a HPγ-cyclodextrin grafted PET vascular prosthesis for application as anti-infectious drug delivery system.* Journal of inclusion phenomena and macrocyclic chemistry, 2007. **57**(1-4): p. 675-681.
310. Ducoroy, L., et al., *Ion exchange textiles from the finishing of PET fabrics with cyclodextrins and citric acid for the sorption of metallic cations in water.* Journal of inclusion phenomena and macrocyclic chemistry, 2007. **57**(1-4): p. 271-277.
311. Martel, B., et al., *Finishing of polyester fabrics with cyclodextrins and polycarboxylic acids as crosslinking agents.* Journal of inclusion phenomena and macrocyclic chemistry, 2002. **44**(1-4): p. 443-446.
312. Uyar, T., et al., *The formation and characterization of cyclodextrin functionalized polystyrene nanofibers produced by electrospinning.* Nanotechnology, 2009. **20**(12): p. 125605.
313. Uyar, T., et al., *Electrospinning of cyclodextrin functionalized poly (methyl methacrylate)(PMMA) nanofibers.* Polymer, 2009. **50**(2): p. 475-480.
314. Uyar, T. and F. Besenbacher, *Electrospinning of cyclodextrin functionalized polyethylene oxide (PEO) nanofibers.* European Polymer Journal, 2009. **45**(4): p. 1032-1037.
315. Rusa, C.C., et al., *Conformational Changes Induced in Bombyx m ori Silk Fibroin by Cyclodextrin Inclusion Complexation.* Macromolecules, 2005. **38**(13): p. 5640-5646.

316. López-de-Dicastillo, C., et al., *Immobilization of β-cyclodextrin in ethylene-vinyl alcohol copolymer for active food packaging applications.* Journal of Membrane Science, 2010. **353**(1): p. 184-191.
317. López-de-Dicastillo, C., et al., *Development of active polyvinyl alcohol/β-cyclodextrin composites to scavenge undesirable food components.* Journal of agricultural and food chemistry, 2011. **59**(20): p. 11026-11033.
318. Torres-Giner, S., M.J. Ocio, and J.M. Lagaron, *Novel antimicrobial ultrathin structures of zein/chitosan blends obtained by electrospinning.* Carbohydrate Polymers, 2009. **77**(2): p. 261-266.
319. Torres-Giner, S. and J.M. Lagaron, *Zein-based ultrathin fibers containing ceramic nanofillers obtained by electrospinning. I. Morphology and thermal properties.* Journal of applied polymer science, 2010. **118**(2): p. 778-789.
320. Woods, K.K., G.W. Selling, and P.H. Cooke, *Compatible blends of zein and polyvinylpyrrolidone.* Journal of Polymers and the Environment, 2009. **17**(2): p. 115-122.
321. Chang, H.-H., et al., *Preparation of bi-continuous Nylon-66 porous membranes by coagulation of incipient dopes in soft non-solvent baths.* Desalination, 2013. **313**: p. 77-86.
322. Leo, C., et al., *Effects of γ-aminopropyltriethoxylsilane on morphological characteristics of hybrid nylon-66-based membranes before electron beam irradiation.* J. Appl. Polym. Sci., 2011. **122**(5): p. 3339-3350.
323. Linggawati, A., A. Mohammad, and C. Leo, *Effects of APTEOS content and electron beam irradiation on physical and separation properties of hybrid nylon-66 membranes.* Mater. Chem. Phys., 2012. **133**(1): p. 110-117.
324. Mehrabanian, M., M. Nasr-Esfahani, and M. Jafari, *A novel method for in situ synthesis of nanostructure hydroxyapatite–nylon 66 composites in tissue engineering.* Int. J. Polym. Mater., 2012. **61**(7): p. 558-570.
325. Murthy, N., et al., *Premelting crystalline relaxations and phase transitions in nylon 6 and 6, 6.* Macromolecules, 1991. **24**(11): p. 3215-3220.
326. Sanatgar, R.H., et al., *The influence of solvent type and polymer concentration on the physical properties of solid state polymerized PA66 nanofiber yarn.* J. Appl. Polym. Sci., 2012. **126**(3): p. 1112-1120.
327. Giller, C.B., et al., *Effect of solvent evaporation rate on the crystalline state of electrospun nylon 6.* Polymer, 2010. **51**(18): p. 4225-4230.
328. Huang, L., E. Allen, and A.E. Tonelli, *Inclusion compounds formed between cyclodextrins and nylon 6.* Polymer, 1999. **40**(11): p. 3211-3221.
329. Wei, M., et al., *Unique morphological and thermal behaviors of reorganized poly (ethylene terephthalates).* Journal of Polymer Science Part B: Polymer Physics, 2004. **42**(3): p. 386-394.
330. Wei, M., et al., *Partial miscibility in a nylon-6/nylon-66 blend coalesced from their common α-cyclodextrin inclusion complex.* J. Polym. Sci. Part B Polym. Phys., 2004. **42**(8): p. 1369-1378.
331. Kojima, Y., T. Matsuoka, and H. Takahashi, *Preparation of nylon 66/mesoporous molecular sieve composite under high pressure.* J. Appl. Polym. Sci., 1999. **74**(13): p. 3254-3258.

332. Wei, M., et al., *Manipulation of Nylon-6 crystal structures with its α-Cyclodextrin inclusion complex.* Macromolecules, 2002. **35**(21): p. 8039-8044.
333. Rusa, C.C., et al., *An intimate polycarbonate/poly (methyl methacrylate)/poly (vinyl acetate) ternary blend via coalescence from their common inclusion compound with γ-cyclodextrin.* J. Polym. Sci. Part B Polym. Phys., 2004. **42**(22): p. 4182-4194.
334. Sambasevam, K.P., et al., *Synthesis and Characterization of the Inclusion Complex of β-cyclodextrin and Azomethine.* Int. J. Mol. Sci., 2013. **14**(2): p. 3671-3682.
335. Gardner, S.D., et al., *Surface characterization of carbon fibers using angle-resolved XPS and ISS.* Carbon, 1995. **33**(5): p. 587-595.
336. Hariharan, A., S.K. Kumar, and T.P. Russell, *A lattice model for the surface segregation of polymer chains due to molecular weight effects.* Macromolecules, 1990. **23**(15): p. 3584-3592.
337. Hunley, M.T., et al., *Effect of Hyperbranched surface-migrating additives on the electrospinning behavior of poly (methyl methacrylate).* Langmuir, 2008. **24**(3): p. 654-657.
338. Walton, D. and A. Mayes, *Entropically driven segregation in blends of branched and linear polymers.* Physical Review E, 1996. **54**(3): p. 2811.
339. Walton, D., et al., *Creation of stable poly (ethylene oxide) surfaces on poly (methyl methacrylate) using blends of branched and linear polymers.* Macromolecules, 1997. **30**(22): p. 6947-6956.
340. Chakraborty, M., P. Ivanova-Mitseva, and H.-J. Bart, *Selective Separation of Toluene from n-Heptane via Emulsion Liquid Membranes Containing Substituted Cyclodextrins as Carrier.* Sep. Sci. Technol., 2006. **41**(16): p. 3539-3552.
341. Chalumot, G., et al., *Determining the stoichiometry and binding constants of inclusion complexes formed between aromatic compounds and β-cyclodextrin by solid-phase microextraction coupled to high-performance liquid chromatography.* J. Chromatogr. A, 2009. **1216**(27): p. 5242-5248.
342. Schwartz, A. and R. Bar, *Cyclodextrin-enhanced degradation of toluene and p-toluic acid by Pseudomonas putida.* Appl. Environ. Microbiol., 1995. **61**(7): p. 2727-2731.
343. Schneiderman, E. and A.M. Stalcup, *Cyclodextrins: a versatile tool in separation science.* J. Chromatogr. B Biomed. Sci. Appl., 2000. **745**(1): p. 83-102.
344. Bullions, T., et al., *Intimate blend of poly (ethylene terephthalate) and poly (ethylene 2, 6-naphthalate) via formation with and coalescence from their common inclusion compound with γ-cyclodextrin.* Journal of Polymer Science Part B: Polymer Physics, 2003. **41**(2): p. 139-148.
345. Djebara, M., et al., *FTIR analysis of polyethylene terephthalate irradiated by MeV He^+.* Nuclear Instruments and Methods in Physics Research Section B: Beam Interactions with Materials and Atoms, 2012. **274**: p. 70-77.
346. Hayes, N.W., et al., *Crystallisation of PET from the Amorphous State: Observation of Different Rates for Surface and Bulk Using XPS and FTIR.* Surface and Interface Analysis, 1996. **24**(10): p. 723-728.

347. Amor, S.B., et al., *XPS characterisation of plasma treated and zinc oxide coated PET.* Applied Surface Science, 2009. **255**(9): p. 5052-5061.
348. Ben Amor, S., et al., *A ZnO/PET assembly study: Optimization and investigation of the interface region.* Materials Chemistry and Physics, 2010. **119**(1): p. 158-168.
349. Ektessabi, A. and K. Yamaguchi, *Changes in chemical states of PET films due to low and high energy oxygen ion beam.* Thin Solid Films, 2000. **377**: p. 793-797.
350. Cho, Y., et al., *Preparation and characterization of amphiphilic triblock terpolymer-based nanofibers as antifouling biomaterials.* Biomacromolecules, 2012. **13**(5): p. 1606-1614.
351. Özçam, A.E., et al., *Responsive PET Nano/microfibers via surface-initiated polymerization.* ACS applied materials & interfaces, 2012. **4**(1): p. 59-64.
352. Jacobs, T., et al., *Plasma surface modification of biomedical polymers: influence on cell-material interaction.* Plasma Chemistry and Plasma Processing, 2012. **32**(5): p. 1039-1073.
353. Martel, B., et al., *Water-soluble polymers and gels from the polycondensation between cyclodextrins and poly (carboxylic acid) s: A study of the preparation parameters.* Journal of applied polymer science, 2005. **97**(2): p. 433-442.
354. Bednarz, S., et al., *Chemical structure of poly (β-cyclodextrin-co-citric acid).* Journal of applied polymer science, 2011. **119**(6): p. 3511-3520.
355. Zhao, D., et al., *Synthesis and properties of water-insoluble β-cyclodextrin polymer crosslinked by citric acid with PEG-400 as modifier.* Carbohydrate Polymers, 2009. **78**(1): p. 125-130.
356. Zhao, D., et al., *Water-insoluble β-cyclodextrin polymer crosslinked by citric acid: synthesis and adsorption properties toward phenol and methylene blue.* Journal of inclusion phenomena and macrocyclic chemistry, 2009. **63**(3-4): p. 195-201.
357. El Ghoul, Y., et al., *Improved dyeability of polypropylene fabrics finished with β-cyclodextrin–citric acid polymer.* Polymer journal, 2010. **42**(10): p. 804-811.
358. Hebeish, A., A. El Shafei, and S. Shaarawy, *Synthesis and characterization of multifunctional cotton containing cyclodextrin and butylacrylate moieties.* Polymer-Plastics Technology and Engineering, 2009. **48**(8): p. 839-850.
359. Bou, M., et al., *Chemistry of the interface between aluminium and polyethyleneterephthalate by XPS.* Applied Surface Science, 1991. **47**(2): p. 149-161.
360. Uchida, E., H. Iwata, and Y. Ikada, *Surface structure of poly (ethylene terephthalate) film grafted with poly (methacrylic acid).* Polymer, 2000. **41**(10): p. 3609-3614.
361. Gawish, S., et al., *Synthesis and characterization of novel biocidal cyclodextrin inclusion complexes grafted onto polyamide-6 fabric by a redox method.* Journal of applied polymer science, 2006. **99**(5): p. 2586-2593.
362. Shown, I. and C. Murthy, *Grafting of cotton fiber by water-soluble cyclodextrin-based polymer.* Journal of applied polymer science, 2009. **111**(4): p. 2056-2061.

363. Huang, F., et al., *Surface structures and contact angles of electrospun poly (vinylidene fluoride) nanofiber membranes.* International Journal of Polymer Analysis and Characterization, 2008(13): p. 292-301.
364. Gómez, J., et al., *Soil washing using cyclodextrins and their recovery by application of electrochemical technology.* Chemical Engineering Journal, 2010. **159**(1): p. 53-57.
365. Kayaci, F., et al., *Role of zinc interstitials and oxygen vacancies of ZnO in photocatalysis: A bottom-up approach to control the defect density.* Nanoscale, 2014.
366. Zhu, C., et al., *A simple method for the preparation of hollow ZnO nanospheres for use as a high performance photocatalyst.* Nanoscale, 2012. **4**(10): p. 3060-3064.
367. Ansari, S.A., et al., *Oxygen Vacancy Induced Band Gap Narrowing of ZnO Nanostructure by Electrochemically Active Biofilm.* Nanoscale, 2013.
368. Zheng, Y., et al., *Luminescence and photocatalytic activity of ZnO nanocrystals: correlation between structure and property.* Inorganic chemistry, 2007. **46**(16): p. 6675-6682.
369. Mei, Y., et al., *Surface modification of polyacrylonitrile nanofibrous membranes with superior antibacterial and easy-cleaning properties through hydrophilic flexible spacers.* Journal of Membrane Science, 2012. **417**: p. 20-27.
370. Scharnagl, N. and H. Buschatz, *Polyacrylonitrile (PAN) membranes for ultra- and microfiltration.* Desalination, 2001. **139**(1): p. 191-198.
371. Yang, S. and Z. Liu, *Preparation and characterization of polyacrylonitrile ultrafiltration membranes.* Journal of Membrane Science, 2003. **222**(1): p. 87-98.
372. Zhang, L., et al., *Antimicrobial nano-fibrous membranes developed from electrospun polyacrylonitrile nanofibers.* Journal of Membrane Science, 2011. **369**(1): p. 499-505.
373. Vlasenko, L. and G. Watkins, *Optical detection of electron paramagnetic resonance for intrinsic defects produced in ZnO by 2.5-MeV electron irradiation in situ at 4.2 K.* Physical Review B, 2005. **72**(3): p. 035203.
374. Janotti, A. and C.G. Van de Walle, *Native point defects in ZnO.* Physical Review B, 2007. **76**(16): p. 165202.
375. Zeng, H., et al., *Composition/structural evolution and optical properties of ZnO/Zn nanoparticles by laser ablation in liquid media.* The Journal of Physical Chemistry B, 2005. **109**(39): p. 18260-18266.
376. Zeng, H., et al., *Microstructure control of Zn/ZnO core/shell nanoparticles and their temperature-dependent blue emissions.* The Journal of Physical Chemistry B, 2007. **111**(51): p. 14311-14317.
377. Hagemark, K.I. and L.C. Chacka, *Electrical transport properties of Zn doped ZnO.* Journal of Solid State Chemistry, 1975. **15**(3): p. 261-270.
378. Tomlins, G.W., J.L. Routbort, and T.O. Mason, *Zinc self-diffusion, electrical properties, and defect structure of undoped, single crystal zinc oxide.* Journal of Applied Physics, 2000. **87**(1): p. 117-123.

379. Wuensch, B.J. and H.L. Tuller, *Lattice diffusion, grain boundary diffusion and defect structure of ZnO*. Journal of Physics and Chemistry of Solids, 1994. **55**(10): p. 975-984.
380. Halliburton, L., et al., *Production of native donors in ZnO by annealing at high temperature in Zn vapor*. Applied physics letters, 2005. **87**(17): p. 172108.
381. Han, J., P. Mantas, and A. Senos, *Defect chemistry and electrical characteristics of undoped and Mn-doped ZnO*. Journal of the European Ceramic Society, 2002. **22**(1): p. 49-59.
382. Seo, H., et al., *Band alignment and electronic structure of the anatase TiO 2/SrTiO 3 (001) heterostructure integrated on Si (001).* Physical Review B, 2012. **86**(7): p. 075301.
383. Agrawal, M., et al., *A Facile Approach to Fabrication of ZnO− TiO_2 Hollow Spheres.* Chemistry of Materials, 2009. **21**(21): p. 5343-5348.
384. Li, L., et al., *Visible light photochemical activity of heterostructured $PbTiO_3$–TiO_2 core–shell particles.* Catalysis Science & Technology, 2012. **2**(9): p. 1945-1952.
385. Li, L., G.S. Rohrer, and P.A. Salvador, *Heterostructured ceramic powders for photocatalytic hydrogen production: nanostructured TiO_2 shells surrounding microcrystalline (Ba, Sr) TiO_3 cores.* Journal of the American Ceramic Society, 2012. **95**(4): p. 1414-1420.
386. Zhang, Z., et al., *ZnO hollow nanofibers: fabrication from facile single capillary electrospinning and applications in gas sensors.* The Journal of Physical Chemistry C, 2009. **113**(45): p. 19397-19403.
387. Elam, J., Z. Sechrist, and S. George, *ZnO/Al_2O_3 nanolaminates fabricated by atomic layer deposition: growth and surface roughness measurements.* Thin Solid Films, 2002. **414**(1): p. 43-55.
388. Pan, K.Y., et al., *Synthesis of SnO_2-ZnO core-shell nanowires and their optoelectronic properties.* Journal of Nanomaterials, 2012. **2012**.
389. Li, W., H. Li, and Y.M. Zhang, *Preparation and investigation of PVDF/PMMA/TiO_2 composite film.* Journal of materials science, 2009. **44**(11): p. 2977-2984.
390. Shi, J., et al., *Effects of coupling agents on the impact fracture behaviors of T-ZnOw/PA6 composites.* Composites Science and Technology, 2008. **68**(6): p. 1338-1347.
391. Li, J., et al., *Preparation and characterization of nano-hydroxyapatite/polyamide 66 composite GBR membrane with asymmetric porous structure.* Journal of Materials Science: Materials in Medicine, 2009. **20**(5): p. 1031-1038.
392. Zhang, Q.-X., et al., *Multiple melting and crystallization of nylon-66/montmorillonite nanocomposites.* Journal of Polymer Science Part B: Polymer Physics, 2003. **41**(22): p. 2861-2869.
393. Min, Y.-S., et al., *ZnO nanoparticle growth on single-walled carbon nanotubes by atomic layer deposition and a consequent lifetime elongation of nanotube field emission.* Applied physics letters, 2007. **90**(26): p. 263104.

394. Min, Y.-S., et al., *Botryoidal growth of crystalline ZnO nanoparticles on a forest of single-walled carbon nanotubes by atomic layer deposition.* CrystEngComm, 2011. **13**(10): p. 3451-3454.
395. Libera, J., J. Elam, and M. Pellin, *Conformal ZnO coatings on high surface area silica gel using atomic layer deposition.* Thin Solid Films, 2008. **516**(18): p. 6158-6166.
396. Vempati, S., et al., *Non-universal behavior well above the percolation threshold and thermal properties of core-shell-magnetite-polymer fibers.* Journal of Applied Physics, 2011. **110**(11): p. 113718.
397. VingeáNygaard, J., *Characterisation of internal morphologies in electrospun fibers by X-ray tomographic microscopy.* Nanoscale, 2011. **3**(9): p. 3594-3597.
398. Sweet III, W.J., J.S. Jur, and G.N. Parsons, *Bi-layer Al_2O_3/ZnO atomic layer deposition for controllable conductive coatings on polypropylene nonwoven fiber mats.* Journal of Applied Physics, 2013. **113**(19): p. 194303.
399. Szilágyi, I.M., et al., *Photocatalytic Properties of WO_3/TiO_2 Core/Shell Nanofibers prepared by Electrospinning and Atomic Layer Deposition.* Chemical Vapor Deposition, 2013. **19**(4-6): p. 149-155.
400. Liu, P., et al., *Preparation of continuous porous alumina nanofibers with hollow structure by single capillary electrospinning.* Colloids and Surfaces A: Physicochemical and Engineering Aspects, 2013. **436**: p. 489-494.
401. Zhang, Z., et al., *A convenient route to polyacrylonitrile/silver nanoparticle composite by simultaneous polymerization–reduction approach.* Polymer, 2001. **42**(19): p. 8315-8318.
402. Cullity, B.D. and S.R. Stock, *Elements of X-ray Diffraction*. 2001: Pearson.
403. Chen, M., et al., *X-ray photoelectron spectroscopy and auger electron spectroscopy studies of Al-doped ZnO films.* Applied Surface Science, 2000. **158**(1): p. 134-140.
404. Stănoiu, A., C.E. Simion, and S. Somăcescu, *NO_2 sensing mechanism of ZnO–Eu_2O_3 binary oxide under humid air conditions.* Sensors and Actuators B: Chemical, 2013. **186**(0): p. 687-694.
405. Djurišić, A., et al., *Photoluminescence and electron paramagnetic resonance of ZnO tetrapod structures.* Advanced functional materials, 2004. **14**(9): p. 856-864.
406. Bylander, E., *Surface effects on the low-energy cathodoluminescence of zinc oxide.* Journal of Applied Physics, 1978. **49**(3): p. 1188-1195.
407. Lin, B., Z. Fu, and Y. Jia, *Green luminescent center in undoped zinc oxide films deposited on silicon substrates.* Applied physics letters, 2001. **79**(7): p. 943-945.
408. Xu, P., et al., *The electronic structure and spectral properties of ZnO and its defects.* Nuclear Instruments and Methods in Physics Research Section B: Beam Interactions with Materials and Atoms, 2003. **199**: p. 286-290.
409. Vanheusden, K., et al., *Mechanisms behind green photoluminescence in ZnO phosphor powders.* Journal of Applied Physics, 1996. **79**(10): p. 7983-7990.
410. Van Dijken, A., et al., *Identification of the transition responsible for the visible emission in ZnO using quantum size effects.* Journal of Luminescence, 2000. **90**(3): p. 123-128.

411. Prahsarn, C., W. Klinsukhon, and N. Roungpaisan, *Electrospinning of PAN/DMF/H_2O containing TiO_2 and photocatalytic activity of their webs.* Materials Letters, 2011. **65**(15–16): p. 2498-2501.
412. Baruah, S., et al., *Photoreactivity of ZnO nanoparticles in visible light: Effect of surface states on electron transfer reaction.* Journal of Applied Physics, 2009. **105**(7): p. 074308.
413. Warule, S.S., et al., *Novel sonochemical assisted hydrothermal approach towards the controllable synthesis of ZnO nanorods, nanocups and nanoneedles and their photocatalytic study.* CrystEngComm, 2009. **11**(12): p. 2776-2783.
414. Yang, Y., et al., *Shape control of colloidal Mn doped ZnO nanocrystals and their visible light photocatalytic properties.* Nanoscale, 2013. **5**(21): p. 10461-10471.
415. Wang, J., et al., *Oxygen vacancy induced band-gap narrowing and enhanced visible light photocatalytic activity of ZnO.* ACS applied materials & interfaces, 2012. **4**(8): p. 4024-4030.
416. Puurunen, R.L., *Surface chemistry of atomic layer deposition: A case study for the trimethylaluminum/water process.* Journal of Applied Physics, 2005. **97**(12): p. 121301.
417. Ischenko, V., et al., *Zinc oxide nanoparticles with defects.* Advanced functional materials, 2005. **15**(12): p. 1945-1954.
418. *NIST X-ray Photoelectron Spectroscopy Database, Version 4.1 (National Institute of Standards and Technology, Gaithersburg, 2012); http://srdata.nist.gov/xps/.*
419. Wu, J.-J. and S.-C. Liu, *Low-temperature growth of well-aligned ZnO nanorods by chemical vapor deposition.* Advanced materials, 2002. **14**(3): p. 215.
420. Zhang, W.-H., et al., *Preparation and characterization of ZnO clusters inside mesoporous silica.* Chemistry of Materials, 2000. **12**(5): p. 1408-1413.
421. Jeong, S.-H., B.-S. Kim, and B.-T. Lee, *Photoluminescence dependence of ZnO films grown on Si (100) by radio-frequency magnetron sputtering on the growth ambient.* Applied physics letters, 2003. **82**(16): p. 2625-2627.
422. Ley, L., et al., *Total valence-band densities of states of III-V and II-VI compounds from x-ray photoemission spectroscopy.* Physical Review B, 1974. **9**(2): p. 600.
423. Oba, F., et al., *Energetics of native defects in ZnO.* Journal of Applied Physics, 2001. **90**(2): p. 824-828.
424. Langmuir, I., *The adsorption of gases on plane surfaces of glass, mica and platinum.* Journal of the American Chemical Society, 1918. **40**(9): p. 1361-1403.
425. Masuda, Y., T. Ohji, and K. Kato, *Multineedle TiO_2 nanostructures, self-assembled surface coatings, and their novel properties.* Crystal growth & design, 2009. **10**(2): p. 913-922.
426. Li, G. and K.A. Gray, *The solid–solid interface: Explaining the high and unique photocatalytic reactivity of TiO_2-based nanocomposite materials.* Chemical physics, 2007. **339**(1): p. 173-187.

427. Scanlon, D.O., et al., *Band alignment of rutile and anatase TiO2.* Nat Mater, 2013. **12**(9): p. 798-801.
428. *HighScorePlus-Version-3.0e(3.0.5), PANalytical B.V., 30-02-2012 edn., 2012.*
429. Naldoni, A., et al., *Effect of nature and location of defects on bandgap narrowing in black TiO2 nanoparticles.* Journal of the American Chemical Society, 2012. **134**(18): p. 7600-7603.
430. Janotti, A., et al., *Hybrid functional studies of the oxygen vacancy in TiO 2.* Physical Review B, 2010. **81**(8): p. 085212.
431. Naumkin, A., et al., *NIST X-Ray Photoelectron Spectroscopy Database, NIST Standard Reference Database 20, Version 4.1 (2013), 2012 copyright by the US Secretary of Commerce on behalf of the United States of America.*
432. Nishikawa, T., T. Nakajima, and Y. Shinohara, *An exploratory study on effect of the isomorphic replacement of Ti^{4+} ions by various metal ions on the light absorption character of TiO_2.* Journal of Molecular Structure: THEOCHEM, 2001. **545**(1): p. 67-74.
433. Xiao, G., et al., *$InVO_4$-sensitized TiO_2 photocatalysts for efficient air purification with visible light.* Journal of Photochemistry and Photobiology A: Chemistry, 2008. **193**(2): p. 213-221.
434. Xu, Y. and M.A. Schoonen, *The absolute energy positions of conduction and valence bands of selected semiconducting minerals.* American Mineralogist, 2000. **85**(3-4): p. 543-556.
435. Pacchioni, G., *Oxygen vacancy: The invisible agent on oxide surfaces.* ChemPhysChem, 2003. **4**(10): p. 1041-1047.
436. Cronemeyer, D., *Infrared Absorption of Reduced Rutile TiO_2 Single Crystals.* Physical review, 1959. **113**(5): p. 1222.
437. von Oertzen, G.U. and A.R. Gerson, *The effects of O deficiency on the electronic structure of rutile TiO_2.* Journal of Physics and Chemistry of Solids, 2007. **68**(3): p. 324-330.
438. Liu, G., et al., *Electron field emission of a nitrogen-doped TiO_2 nanotube array.* Nanotechnology, 2008. **19**(2): p. 025606.
439. Serpone, N., *Is the band gap of pristine TiO_2 narrowed by anion-and cation-doping of titanium dioxide in second-generation photocatalysts?* The Journal of Physical Chemistry B, 2006. **110**(48): p. 24287-24293.
440. Zuo, F., et al., *Self-doped Ti^{3+} enhanced photocatalyst for hydrogen production under visible light.* Journal of the American Chemical Society, 2010. **132**(34): p. 11856-11857.
441. Zhao, L., M. Han, and J. Lian, *Photocatalytic activity of TiO_2 films with mixed anatase and rutile structures prepared by pulsed laser deposition.* Thin Solid Films, 2008. **516**(10): p. 3394-3398.
442. Muhich, C.L., et al., *Effect of surface deposited Pt on the photoactivity of TiO_2.* The Journal of Physical Chemistry C, 2012. **116**(18): p. 10138-10149.
443. Justicia, I., et al., *Designed Self-Doped Titanium Oxide Thin Films for Efficient Visible-Light Photocatalysis.* Advanced materials, 2002. **14**(19): p. 1399-1402.
444. Schaub, R., et al., *Oxygen vacancies as active sites for water dissociation on rutile TiO_2 (110).* Physical Review Letters, 2001. **87**(26): p. 266104.

445. Gercher, V.A. and D.F. Cox, *Water adsorption on stoichiometric and defective SnO_2(110) surfaces.* Surface Science, 1995. **322**(1): p. 177-184.
446. Henderson, M.A., *Structural sensitivity in the dissociation of water on TiO_2 single-crystal surfaces.* Langmuir, 1996. **12**(21): p. 5093-5098.
447. Hugenschmidt, M.B., L. Gamble, and C.T. Campbell, *The interaction of H_2O with a TiO_2(110) surface.* Surface Science, 1994. **302**(3): p. 329-340.
448. Polarz, S., et al., *On the role of oxygen defects in the catalytic performance of zinc oxide.* Angewandte Chemie International Edition, 2006. **45**(18): p. 2965-2969.
449. Lachheb, H., et al., *Photocatalytic degradation of various types of dyes (Alizarin S, Crocein Orange G, Methyl Red, Congo Red, Methylene Blue) in water by UV-irradiated titania.* Applied Catalysis B: Environmental, 2002. **39**(1): p. 75-90.